GIRT BY $\vec{B}$: RADIO POLARIMETRIC OBSERVATIONS OF KILOPARSEC-SCALE MAGNETIC FIELDS

JANE F. KACZMAREK

A THESIS SUBMITTED IN FULFILMENT OF THE REQUIREMENTS
FOR THE DEGREE OF DOCTOR OF PHILOSOPHY

2017

SCHOOL OF PHYSICS
FACULTY OF SCIENCE
THE UNIVERSITY OF SYDNEY

ABSTRACT

In this thesis I address some of the central questions regarding the growth of magnetic fields from the confines of galaxies into the large-scale pervasive fields observed today. Specifically, I have used radio polarisation data, acquired primarily with the Australia Telescope Compact Array, and large surveys to carry out four individual investigations into the evolution of magnetic fields on kiloparsec scales.

I carry out an investigation into the magnetic field structure in the Magellanic Bridge, a nearby tidal remnant, which was conducted through the observation of Faraday rotation towards 167 polarised background radio sources. Comparing measured Faraday depth values of sources 'on' and 'off' the Bridge, I find that the two populations are different. Assuming that this difference in populations is due to a coherent field in the Magellanic Bridge, the observed Faraday depths indicate a median line-of-sight magnetic-field strength of $B_{\parallel} \simeq 0.3\,\mu$G directed uniformly away from us. This is the first detection of a coherent magnetic field spanning the entirety of the Magellanic Bridge and I argue that this is a direct probe of a 'pan-Magellanic' field.

I present broadband polarisation observations of the radio galaxy NGC 612 (PKS B0131-637). By fitting complex polarisation models to the polarised spectrum of each pixel, I find that a single polarisation component can adequately describe the observed signal for most of the radio galaxy. I argue that the bulk of the Faraday rotation must be taking place very near, or at, the location of the polarised emission, yielding an estimated total magnetic field strength of $4\,\mu$G. If the location of the bulk polarised emission is located cospatially with a coherent magnetic field, the implied thermal mass of the two lobes is of the order $10^9\,\mathrm{M}_{\odot}$.

I carry out a broadband polarisation investigation into the lobes of radio galaxy MSH 05−3*13* (ESO363 G−027). After correcting for the dominant Galactic Faraday component, I reveal gradients in the Faraday depth across the outer lobes. Using derived age estimates in conjunction with magnetic field strength estimates, I show that Kelvin-Helmholtz instabilities could serve as a plausible explanation for the observed Faraday depth patterns. I go on to argue that the thermal material responsible for the observed Faraday rotation is likely to be swept up material from the surrounding intergalactic medium.

Finally, I combine the GAMA galaxy group catalogue with a large radio catalogue of

rotation measures to cross-correlate galaxy group locations with the positions of known background polarised radio sources. I identify 64 instances where the line of sight to a polarised radio source passes through the angular projection of a galaxy group, but find no significant excess in residual rotation measure with respect to a number of different galaxy group parameters. Restricting the sample to radio-optical pairs with impact parameters less than the inner radius of a group, I calculate a 3σ upper detection limit of $B_{\parallel} \leq 2.0\ \mu$G.

DECLARATION

I, Jane Frances Kaczmarek, certify that the content of this thesis is my own work and has been carried out in close collaboration with my supervisors: Bryan Gaensler, Naomi McClure-Griffiths and Richard Hunstead. Throughout my candidature, I benefitted from the patient mentorship of Cormac Purcell, who wrote the bulk of the qu-fitting code used throughout this thesis. Here I detail other, or more significant contributions that have been made to some chapters of this work and by whom they were made.

- **Chapter 2**: This chapter shows few deviations from Kaczmarek et al. (2017). All observations for the publication were taken by myself and Jamie Stevens. The initial polarised source finding took advantage of archival data observed and detailed in Muller et al. (2003). Polarisation source finding was carried out using a 'polarisation pipeline' that was built by Cormac Purcell.
- **Chapter 3**: Data for this chapter were part of the ATCA project, C2776, which I led and observed in its entirety. This chapter has benefitted from the detailed insight of Robert Laing and Jamie Stevens, which led to the eventual abandonment of the 5500 MHz polarisation dataset. Discussions with Larry Rudnick led to the interpretation and discussion of the hot spot.
- **Chapter 4**: All data for this chapter were part of ATCA project, C2776, for which all observations were made by myself. This chapter has benefitted from detailed discussions with Craig Anderson and Shane O'Sullivan, who both added credence to the final analysis of Kelvin-Helmholtz instabilities.
- **Chapter 5**: Much of the analysis and discussion for this chapter was finalised in part with the help of Ilana Feain, who was my co-supervisor when the work for this chapter was first completed.

Jane F. Kaczmarek
July 20, 2017

DEDICATION

To Thomas W. Glowienka, for teaching me that the most important thing one can have is an education.

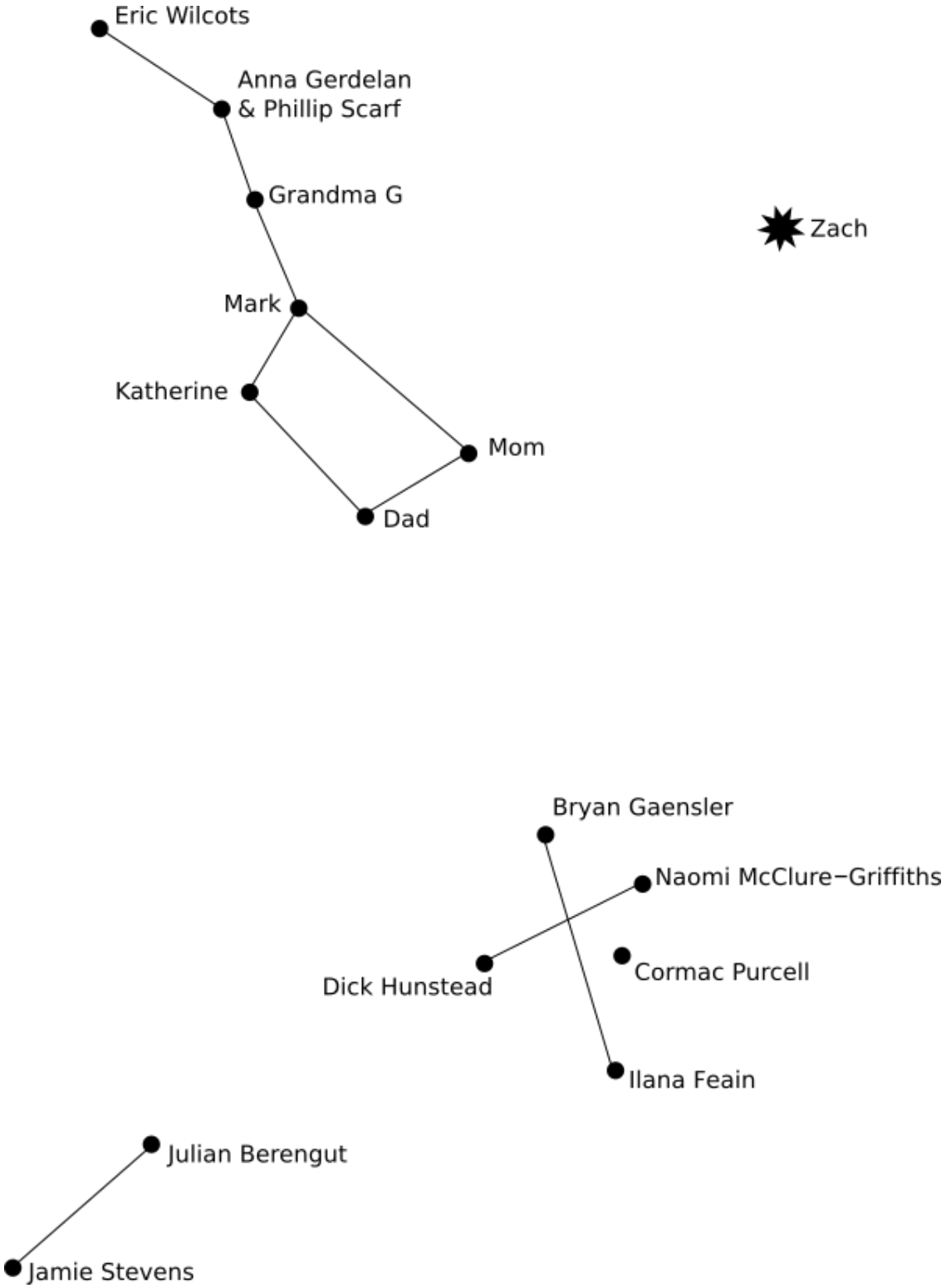
Eric Wilcots
Anna Gerdelan
& Phillip Scarf
Grandma G
Zach
Mark
Katherine
Mom
Dad
Bryan Gaensler
Naomi McClure−Griffiths
Cormac Purcell
Dick Hunstead
Ilana Feain
Julian Berengut
Jamie Stevens

ACKNOWLEDGEMENTS

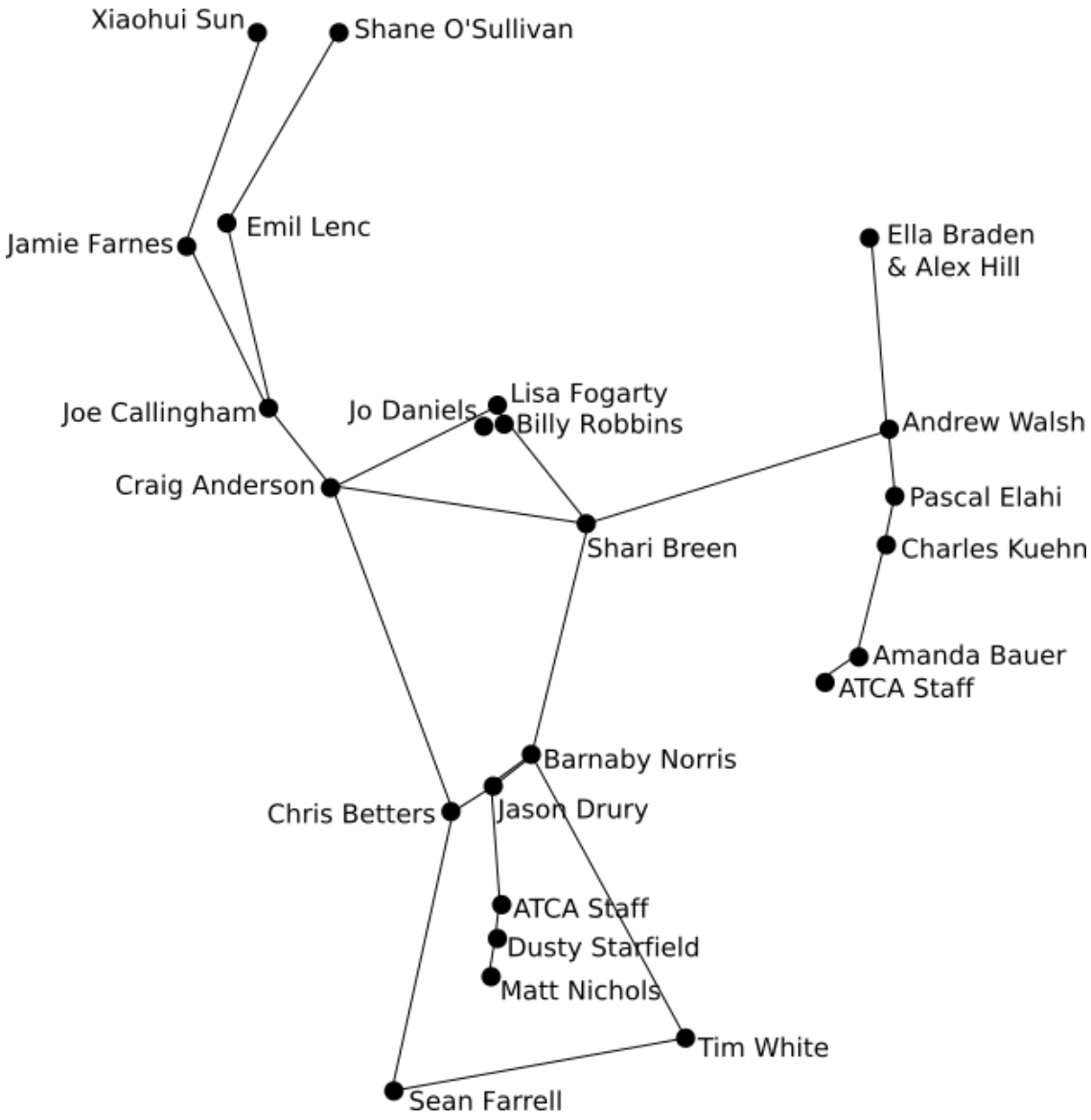

Contents

List of Figures

List of Tables

Astronomers all let us rejoice,
For thermal emission is free-free;
Though observer's toil, RFI does foil;
The Milky Way is girt by $\vec{B}$;*
Distant quasars at large redshifts
Probe sightlines rich and rare;
Here I engage, on every page,
P*'s dependence on* λ^2.
(Adapted from 'Advance Australia Fair')

1 INTRODUCTION

1.1 PREFACE

Magnetic fields are ubiquitous throughout the Universe, but despite their pervasiveness, fundamental questions relating to their origin and evolution remain unanswered. Without answers to these key questions, we cannot fully understand how the Universe itself evolved.

As magnetic fields exist everywhere, it is no surprise that they play an important role in the evolution of astrophysical structures. We know that magnetism is essential on stellar scales to facilitate the accretion of protostellar disks onto stars. Even during the violent death of stars, magnetic field strengths are an influential parameter during a supernova's expansion into the surrounding interstellar medium (ISM). Magnetic fields throughout the ISM play a multitude of roles – including, but not limited to, molecular cloud collapse and star-formation. Invoking magnetic fields facilitates cold gas accretion onto galaxies, as the field lines may act to preserve the gas clump. Magnetic fields are also necessary for the accretion of material onto supermassive blackholes and are ultimately involved with the launch and collimation of the resultant jets stemming from active galactic nuclei (AGN). Looking to larger and larger scales, we find that even galaxy clusters, the largest gravitationally bound objects in the visible Universe, host strong magnetic fields that inevitably play a fundamental role in the evolution of the large scale structure of the Universe.

While it is clear that the roles magnetic fields play in an ever-evolving Universe are vital and varied, little is known of how the magnetic field themselves evolve. Without an understanding of how magnetic fields have grown from the confines of galaxies into the pervasive large-scale fields that we observe today, our understanding of the Universe is limited. It is therefore of primary importance that we learn how magnetic fields come to evolve on the scales that bridge the evolutionary gap between individual galaxies and the

* girt, *v. t.* [/gɛt/] to encircle with a belt or girdle. Macquarie dictionary: the national dictionary. 2nd ed. Macquarie Library, 1991.

large-scale structure of the Universe.

Cosmic magnetic fields are predominantly observed at radio wavelengths, with additional insight being offered at optical, infrared, and X-ray wavelengths. Historically, our knowledge of the magnetised Universe has been limited partially by the sensitivity of available instruments and partially by an inability to disentangle complex polarised sightlines. New interferometric telescopes with increased sensitivities have largely overcome the former limitation. Of the latter impediment, limitations have been predominantly caused by observations in narrow frequency ranges. However, the development of broad observing bandwidths in recent years has the potential to decipher contributions from individual magneto-ionic structures along the line of sight. In this regard, current research is leading to a radical and rapid change in our knowledge of cosmic magnetism.

Motivated by this latter technological advancement, my thesis is aimed broadly at exploring and exploiting the power and potential of broadband polarisation observations in order to shed light on some of the mechanisms responsible for the evolution of cosmic magnetic fields.

In this chapter, I begin by discussing the mechanisms and methods used to study cosmic magnetic fields (§1.2). This is followed by §1.3, in which I introduce the phenomenon known as Faraday rotation and describe how it can be used to probe magneto-ionic structures. In §1.4, I present the mathematical concepts that provide a framework for all subsequent polarisation analysis in this thesis. This chapter will also introduce the various terms that are used in discussing magnetic fields. A description of the various polarisation analysis techniques that are used extensively in this thesis and in the literature are presented in §1.5. In §1.6, I summarise what is currently known about the various strengths and morphologies of magnetic fields associated with galactic and larger-scale structures in order to build a foundation that this thesis strives to build upon, the specific aims of which are outlined in §1.7.

1.2 OBSERVING THE MAGNETISED UNIVERSE

Research into polarisation is often motivated by cosmic magnetic fields. For a monochromatic electromagnetic wave propagating in the z-direction, the wave can be described by two orthogonal components E_x and E_y, given by

$$E_x = a_x(t)\cos[\omega t + \delta_x] \tag{1.1}$$

$$E_y = a_y(t)\cos[\omega t + \delta_y], \tag{1.2}$$

where E_i is magnitude of the electric field vector, $a_i(t)$ is the amplitude as a function of time and δ_i is the phase of the electromagnetic wave in the i-direction. Light is considered to be polarised if the electric field vector has a preferred direction, i.e., it is not random.

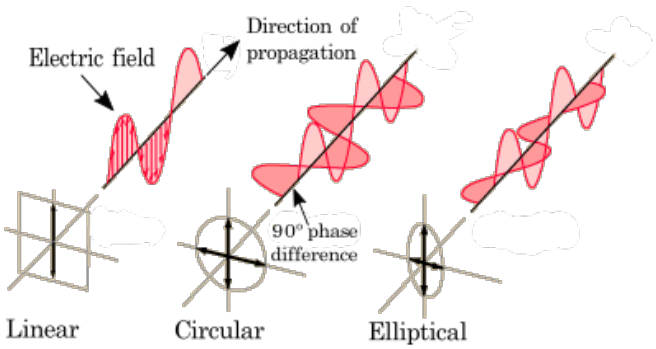

Figure 1.1: Orientation of the electric field vector for different polarisation states. Given propagation in the $z-$direction, any wave that is confined to a single plane is considered to be linearly polarised (left). Circularly polarised light (centre) consists of two perpendicular plane waves of equal amplitude. If the wave oscillates equally in the $\hat{x}$ and $\hat{y}$-directions, it is considered to be circularly polarised (middle). If the wave oscillates in some combination of the two, it is considered to be elliptically polarised (right). This figure has been adapted from http://hyperphysics.phy-astr.gsu.edu/hbase/phyopt/polclas.html

Figure 1.1 shows the different polarisation states that exist due to varying orientations of the electric field vector. If the field vector oscillates in a single plane, the resultant emission is considered to be linearly polarised, while if the direction of oscillation rotates as a function of time, the light is considered to be circularly polarised. Commonly, the electric field vector will trace out an elliptical pattern, that is, the wave oscillates in the xy-plane. In this case, the light is considered to be elliptically polarised.

In general, an individual electro-magnetic wave can be described by one of the three polarisation states (i.e. linear, circular, elliptical). However, astrophysical observations do not concern individual waves, but rather an ensemble of radiation from some source. Most astrophysical sources emit light that exhibits all possible orientations of the electric field, leading to the superposition of the radiation to have no preferred orientation. In this instance, the light is considered to be unpolarised. By contrast, if the ensemble of EM waves has a preferred orientation, one can describe the polarisation state as some combination of linear and circularly polarised light. Circular polarisation tends to be very low in the vast majority of astronomical sources, with values typically ranging from 0.1 - 0.5 per cent (Saikia and Salter 1988). By contrast, many objects exhibit linear polarisation at radio frequencies (e.g. Cotton et al. 2003).

Observations at radio wavelengths have proven to be an essential tracer of polarisation. In the radio regime, dust and ionised gas and cosmic rays can all be used as tracers of the total magnetic field strength and orientation. One of the dominant mechanisms for producing polarised emission is synchrotron radiation. Synchrotron radiation is gen-

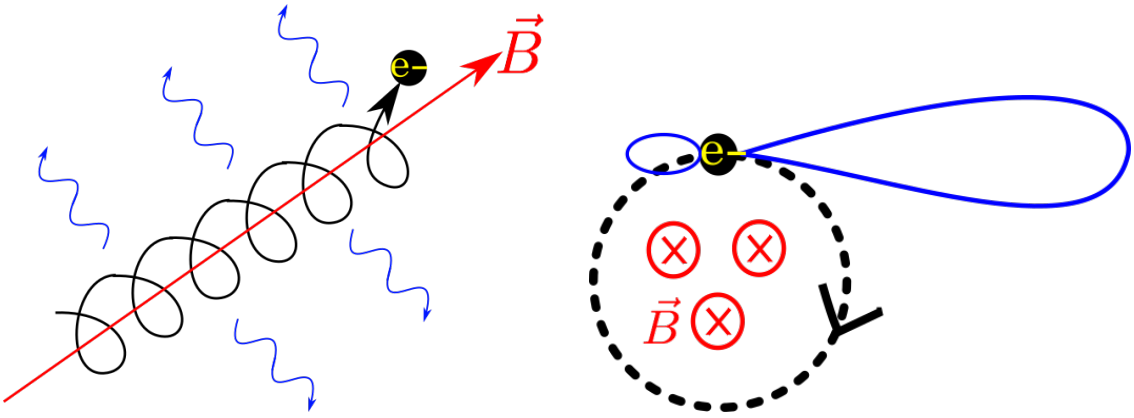

(a) (b)

Figure 1.2: Illustrations of the synchrotron emission process. Figure (a) shows that as a electron (or proton) spirals along a magnetic field line (red), the constant acceleration generates synchrotron emission (blue). Figure (b) shows this process, as viewed along a field line, in that the synchrotron emission will appear beamed perpendicular to the direction of movement.

erated via the spiralling of relativistic electrons and cosmic rays around magnetic field lines (Figure 1.2(a)). The intensity of the emission will be highest in the direction of the particle's motion that is perpendicular to the magnetic field (Figure 1.2(b)).

For a power-law distribution of cosmic ray electron energies, $N(E)dE \propto E^{-p}dE$, the total emission spectrum will also follow a power-law distribution (Figure 1.3), with the slope of the distribution, α, referred to as the spectral index, and defined by $\alpha = -(p-1)/2$. Therefore, for an optically-thin source, the measured surface brightness (S_ν) is a result of integrated radiation from an ensemble of relativistic electrons with a power-law distribution of energies (e.g. $S_\nu \propto \nu^\alpha$).

Observations of radio synchrotron emission serve as a useful probe for cosmic magnetic field structure, since the properties of linearly polarised radiation reflect the geometry and strength of the incident magnetic field. Due to the geometry required to produce synchrotron emission, measurements of the electric vector polarisation angle can be used to deduce the orientation of the magnetic field vector on the sky (i.e. $B_\perp = E + 90°$). Therefore, the polarisation position angle is a key property of linearly polarised radiation.

1.2.1 RADIO INTERFEROMETRY

When faced with insufficient angular resolution in the 1950s, radio astronomers built interferometers in order to gain spatial resolution without the expense and difficulty of building enormous dishes or antennae. A radio interferometer is a telescope in which an array of widely separated radio antennas, separated by some distance, simultaneously ob-

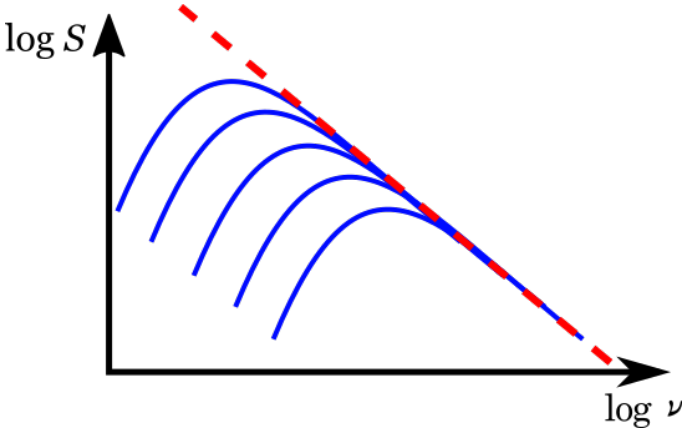

Figure 1.3: For a given synchrotron electron, the characteristic energy spectrum may appear as any of the blue lines, where the x-axis is the log of some arbitrary frequency and the y-axis represents arbitrary log-brightness. When summed over an entire population of cosmic ray electrons, the total emission spectrum follows the power law distribution traced by the red dashed line.

serve an astrophysical target (Figure 1.4). The array of antennas is used to simulate parts of a whole, larger telescope. The resolution of the synthesised beam of an interferometer is a function of the longest baseline of the array (d), with the angular distance to the first null in an Airy disk/beam given by

$$\text{beamwidth} = \frac{1.22\lambda}{d}, \tag{1.3}$$

where λ is the observing wavelength. Interferometers have a limited number of baselines and only sample the sky over a limited range of spatial scales and act as a spatial filter. In order to be sensitive to polarisation emission on sufficiently small angular scales, a radio interferometer must be used.

As radiation emitted from an astrophysical source propagates through space, it remains coherent on the sampling scales of the interferometer. At each telescope element, measurements of the incoming electromagnetic wave front are converted into a voltage response. The responses of each pair of antenna are then cross-correlated to pick out the common signal.

The Van Cittert-Zernicke (van Cittert 1934; Zernike 1938) theorem states that the Fourier transform of the sky brightness results in a sample of the spatial coherence function. The correlation between two antennas forms a visibility of the total sky that is a function of the baseline projection on the sky ($\mathrm{V}(u, v)$). The two-dimensional intensity distribution is measured by taking the Fourier transform of all visibilities, making it possible to determine the properties of the source of emission. Due to sky intensities

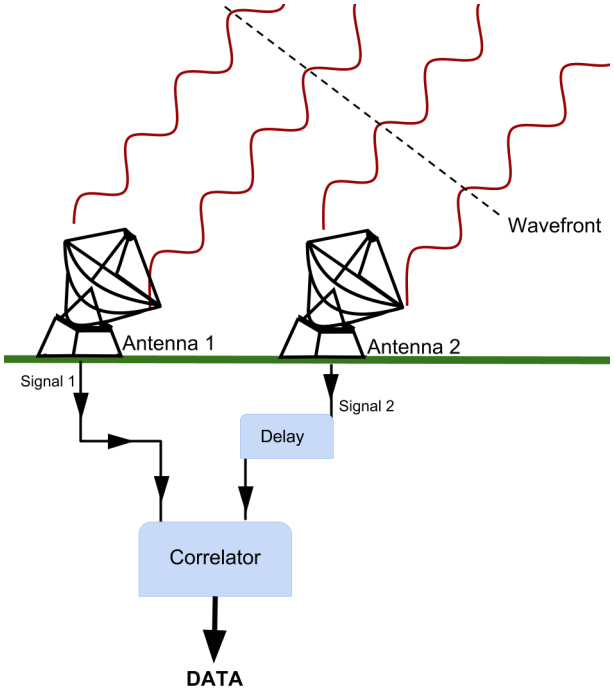

Figure 1.4: Schematic of a basic, two-element interferometer. A coherent wavefront is observed by two array elements with some time delay that is a function of the direction of propagation and separation of the two antennas. The correlator takes the signal from both array elements and combines them to form the final data product.

being real-valued, each discrete sampling of a baseline in visibility-space is Hermitian and corresponds to two samples in uv-space, one of which is a complex conjugate. In an array with sufficiently numerous antennas, correlating all baseline pairs results in a well-sampled spatial coherence function, thus allowing an accurate image of the radio sky to be made.

The polarisation radiation is first detected by a 'feed horn'. The feed-horn detectors of classical radio telescopes can exist as either two circular elements, or two linear elements, with each element sensitive to the plane of polarisation orthogonal to its counterpart. This thesis has made extensive use of the Australia Telescope Compact Array, a radio interferometer operated by the Commonwealth Scientific and Industrial Research Organisation (CSIRO). As this telescope has orthogonal linear feeds, the following description of polarisation characteristics will follow a linearly-polarised definition.

Historically, the instantaneous observable frequency-range and frequency-resolution of many of the world's interferometers were limited to values of ~ 100 MHz and ~ 10 MHz. However, in the past decade two of the leading radio interferometers, the Australia Telescope Compact Array (ATCA) and the Karl G. Jansky Very Large Array (VLA), received major upgrades to their hardware leading to substantial increases each telescope's

Figure 1.5: The Australia Telescope Compact Array, at Paul Wilde Observatory in Narrabri, New South Wales, Australia. Photo credit: Ed Hurst. Copyright: Spiffing Pics. Printed here with express permission.

capabilities. I discuss the ATCA and CABB in greater detail in the following section; however,2 it is fair to remark on the successes of the Wideband Interferometer Digital ARchitecture (WIDAR) correlator on the VLA (Perley et al. 2011), which allowed the telescope able to observe in full polarisation over an 8 GHz instantaneous bandwidth from 1 to 40 GHz.

Australia Telescope Compact Array

The Australia Telescope Compact Array (ATCA, Figure 1.5) consists of six 22-metre diameter radio antennas located at the Paul Wild Observatory in Narrabri, New South Wales, Australia. The telescope is positioned primarily as an east-west array with a maximum baseline of 6 km. Five array elements are mobile along a 3 km track while the sixth dish remaining stationary with a maximum baseline of 6km. A short North-South arm is also used for compact, hybrid configurations. Arrays of this nature were not used in this thesis.

For observations made post-April 2009, one of the main advantages in observing with the ATCA is the 2048 MHz instantaneous bandwidth operation. Such observations were made possible with the installation of the Compact Array Broadband Backend (CABB, Wilson et al. 2011). The CABB correlator provides independent channel sampling, which eliminates any cross-talk between channels/frequencies, meaning each channel is completely independent with no correlation to adjacent channels.The wideband feed horn

design, in conjunction with front-end electronics, serves to increase the instantaneous uv-coverage through multi-frequency synthesis imaging. The use of CABB ensures that well-designed observations will result in a dataset with high continuum sensitivity and spectral resolution.

The receiver system on the ATCA allows observations to consist of two independent frequency bands each with two independent polarisation measurements. This is a consequence of a the signal 'mixing' process, in that signal from the receiver are mixed with a local oscillator signal in order to convert to a slower sampling rate. This results in upper and lower side bands and the simultaneous observation of two unique frequency windows. For the majority of observations used in this thesis, the dual-frequency receiver was used to observe at frequencies centred at 2100, 5500 and 9000 MHz, each with a bandwidth of 2048 MHz.

Signal from one axis of the feed are noted as 'X' and the other as 'Y' e.g. for baseline Ant(1→2), 'XX' translates to the correlated visibility between the X-direction of antenna 1 with the X-direction of antenna 2. The linear polarisation feeds installed in each antenna are fixed such that the position angle of the polarisation splitter is stationary with respect to the antenna and therefore rotates as a function of sky-position. Output from the linear feeds result in independent measurement of the two orthogonal polarisations at each observing frequency. The ATCA with CABB provides all polarisation parameters for all cross-correlation products where the resultant cross-correlations for each baseline ij are recorded as X_iX_j, Y_iY_j, X_iY_j and Y_iX_j.

All observations undertaken for this thesis used the full 2048 MHz bandwidth with a spectral resolution of 1 MHz. Combined with high sensitivity and well-characterised polarised response, the ATCA serves as an ideal instrument for spectropolarimetric studies.

1.2.2 The Convenience of Stokes Parameters

Recalling from Section 1.2, an electromagnetic wave can be broken down into two orthogonal components and summarised by two amplitudes (E_x, E_y) and phases (δ_x, δ_y). The polarisation state of such a wave can also be conveniently described using the four observable Stokes parameters, as was first defined by Stokes (1852), and were later adopted for astronomical use by Chandrasekhar (1947).

In the case of an idealised radio interferometer with linear orthogonal feeds, the Stokes parameters represent the auto-correlation and cross-correlation products that a combination of array elements measure

$$\begin{aligned} I &= \langle E_{xi}E_{xj}\rangle + \langle E_{yi}E_{yj}\rangle \\ Q &= \langle E_{xi}E_{xj}\rangle - \langle E_{yi}E_{yj}\rangle \\ U &= \langle E_{xi}E_{yj}\rangle + \langle E_{xj}E_{yi}\rangle \\ V &= i(\langle E_{xi}E_{yj}\rangle - \langle E_{xj}E_{yi}\rangle) \end{aligned} \tag{1.4}$$

where E_{xi}, E_{yi}, E_{xj} and E_{yj} are now indicative of the voltage responses of the X and Y linear feeds for the i^{th} and j^{th} antennas forming baseline ij. The angle brackets denote time averaging.

The flux density of all four Stokes parameters are measured in janskys (Jy), where 1 Jy is equivalent to 10^{-26} W/m^2/Hz. The Stokes parameters are four real numbers, where only Q, U and V are allowed to have negative sky brightnesses. Stokes I is the sum of two orthogonal polarisations and describes the total intensity. Linear polarisation is completely characterised by Stokes Q and U, whereas Stokes V characterises circular polarisation. The linear polarisation state of a radio wave can be expressed as a complex vector (Gardner and Whiteoak 1966)

$$\vec{\mathbf{P}} = Q + iU \tag{1.5}$$

Q and U then relate to the angle of the electric vector relative to the plane of polarisation (Ψ) as

$$\Psi = \frac{1}{2}\tan^{-1}\frac{U}{Q} \tag{1.6}$$

where Ψ is measured in radians.

Measurements of $\mathbf{P}$, Q and U are all impacted by spectral effects in total intensity (I). Additionally, synchrotron emission associated with astrophysical processes emits only partially polarised radiation. Since this thesis focuses on the observed changes to these variables due to an intervening cosmic magnetic field, we attempt to decouple the measured polarisation parameters from spectral effects by working in terms of fractional polarisation. The majority of this thesis discusses polarisation levels as fractions of the total intensity, denoted by

$$\begin{aligned} q = \frac{Q}{I}; \quad u = \frac{U}{I}; \quad v = \frac{V}{I} \\ p = \frac{\sqrt{Q^2+U^2}}{I} \\ \Pi = \frac{\sqrt{Q^2+U^2+V^2}}{I} \end{aligned} \tag{1.7}$$

where q, u and v are the fractional Stokes parameters, p is the fractional linear polarisation and Π is the total fractional polarisation. Since Stokes V fully represents the circular polarisation of a electromagnetic wave, v is also indicative of the fractional circular polarisation of a source. However, as the majority of astrophysical objects have very little or no circular polarisation, it is common to assume that $V = v = 0$, with p used interchangeably with Π to represent the total fractional polarisation.

1.2.3 Polarisation Calibration

The scenario described in §1.2.2 was for an idealised case. Realistically, there are aspects of the interferometer hardware and environment that may cause information from the total intensity component to 'leak' into the polarised components and vice versa (e.g the X direction of a signal feed is also sensitive to some fraction of the Y direction). Without calibration of ATCA data, the measured fractional Stokes parameters (i.e. q, u and v) can be systematically erroneous by about 3%, 1.6% and 3% at the 2100 MHz, 5500 MHz and 9000 MHz bands, when measured on-axis. These errors can significantly increase in magnitude for sources that have been observed off-axis. As many astronomical sources are only linearly polarised to a few percent, additional polarisation-specific calibration must be carried out in order to characterise and correct for these 'leakages.' Sault and Cornwell (1999) showed that in order to carry out polarisation calibration for a source with unknown polarisation levels, observations of such a source must be made at at least three parallactic angles.

1.3 Faraday Rotation

When linearly polarised radiation passes through a magnetised plasma, the polarisation angle will be rotated from its intrinsic value (Ψ_0) by an amount that is proportional to the square of the observed wavelength (Figure 1.6). This effect is known as Faraday rotation.

Knowledge of the amount of Faraday rotation experienced by the electric field vector polarisation angle makes it possible to analyse the magnetic field properties of the synchrotron emitting source as well as the intervening magneto-ionic structure. This section will discuss the methods for characterising the Faraday structure along a polarised sightlines, namely the rotation measure (RM) and Faraday depth (ϕ).

1.3.1 Rotation Measure

Polarised emission can be expressed simply as

$$p = p_0 e^{2i\Psi} \tag{1.8}$$

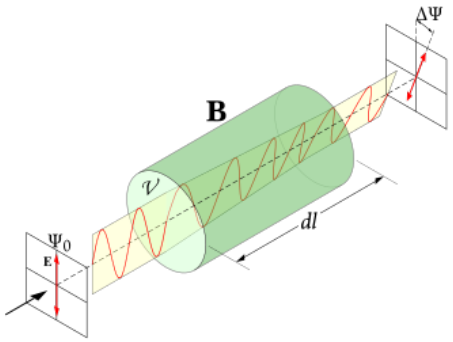

Figure 1.6: Depiction of Faraday rotation where the electric field (**E**) at frequency ν passing through a magnetised medium of strength **B** and length dl is rotated by some amount $\Delta\Psi$. Adapted from https://commons.wikimedia.org/wiki/File:Faraday-effect.svg CC-ASA 3.0

where p_0 is the intrinsic fractional polarisation and Ψ is the polarisation angle of the emission. The simplest scenario for Faraday rotation is one in which linearly polarised emission encounters a single, non-emitting magnetised screen, i.e., a parcel of thermal electrons threaded by a magnetic field. In such an instance, Ψ_0 will be rotated from its initial position according to

$$\Psi = \Psi_0 + \mathrm{RM}\lambda^2, \tag{1.9}$$

where λ is the observed wavelength and RM is the rotation measure, in units of rad m^{-2}. Combining equations 1.8 and 1.9 results in an adapted expression for the observed polarisation,

$$p = p_0\, e^{2i(\Psi_0 + \mathrm{RM}\lambda^2)}. \tag{1.10}$$

In this instance, the polarisation fraction would remain constant for all λ^2 and the slope of Ψ versus λ^2 would be a constant (Figure 1.7a).

The RM is related to physical quantities via,

$$\mathrm{RM} = \frac{e^3}{2\pi {m_e}^2 c^4} \int_{source}^{0} n_e B_{\parallel} dl \tag{1.11}$$

where n_e is the density of free electrons, $B_{\parallel}$ is the net line-of-sight magnetic field strength. The integral is taken over the entire line-of-sight pathlength; e, m_e and c are constants representing the charge of an electron, the mass of an electron and the speed of light in a vacuum, respectively.Historically, the RM could be calculated as the slope of Ψ versus λ^2 such that

$$\mathrm{RM} = \frac{d\Psi}{d\lambda^2}. \tag{1.12}$$

The RM can be either positive or negative and has been defined such that a positive RM indicates a magnetic field that is oriented towards the observer. In conjunction with

being used to reconstruct the intrinsic polarisation angle, the RM can be a useful tool for studying various properties of the intervening magnetic screen.

The relationship between RM, Ψ_0 and λ^2 make the study of Faraday rotation ideal for radio frequency observations. While measurements of RM cannot be made from a single frequency, attempts to recover the correct RM and Ψ_0 can be made from observations at two or more frequencies. Historically, observations of the polarisation angle had been made at two, or three, discrete frequencies, with a single, straight-line fit representing the RM. For example, Figure 1.8 shows three observations of an arbitrary polarised sightline at 750, 1400 and 5500 MHz –frequencies which were often used in historical RM studies. The black dashed line is the true polarisation angle ($\Psi(\lambda^2)$) while the solid blue line represents the line of best fit to the observations. Astronomers were keenly aware that sampling at discrete frequencies was unlikely to return the true complex polarised sightline and that the analysis of a true Faraday rotation along the line of sight was not as straightforward as fitting a straight line (e.g. Burn 1966; Brentjens and de Bruyn 2005). Following the construction of more advanced radio telescopes, wider λ^2 ranges were made possible as was the observation of complex $\Psi(\lambda^2)$. Figure 1.8 compares the contiguous λ^2 coverage offered by the ATCA and highlights the relative polarisation signal that can be observed. The orange shaded region represents the λ^2 coverage available before the CABB upgrade. Once CABB was installed, the red and teal shaded regions represent the λ^2 coverage for frequency bands centred on 2100 and 5500 MHz, respectively.

1.3.2 Faraday Depth

Analysis of RMs offer an overly simplistic description of the structure of the magnetoionic material along the line of sight, as $\mathbf{P}$ is often observed to change as a function of λ^2 and $\Psi(\lambda^2)$ exhibits non-linear behaviour (e.g. O'Sullivan et al. 2012; Anderson et al. 2016). Observations of polarised sightlines that exhibit this behaviour are considered to be Faraday complex. These observations can arise as a result of an inhomogeneous foreground Faraday screen, multiple emitting and rotating components along the line-of-sight, the emitting and rotating regions being cospatial, multiple unresolved components existing on the plane of the sky and any combination of these scenarios.

In an attempt to disentangle complex Faraday sightlines, Burn (1966) proposed the more general term 'Faraday depth' (ϕ) to incorporate Faraday complexity. It wasn't until Brentjens and de Bruyn (2005) that the concept was fully developed. Before defining Faraday depth, we redefine RM to explicitly represent the slope $d\Psi/d\lambda^2$. The Faraday depth of a polarised source is now defined such that at a given distance L, the Faraday depth is

$$\phi(L) = \frac{e^3}{2\pi {m_e}^2 c^4} \int_L^0 n_e B_\parallel dl, \tag{1.13}$$

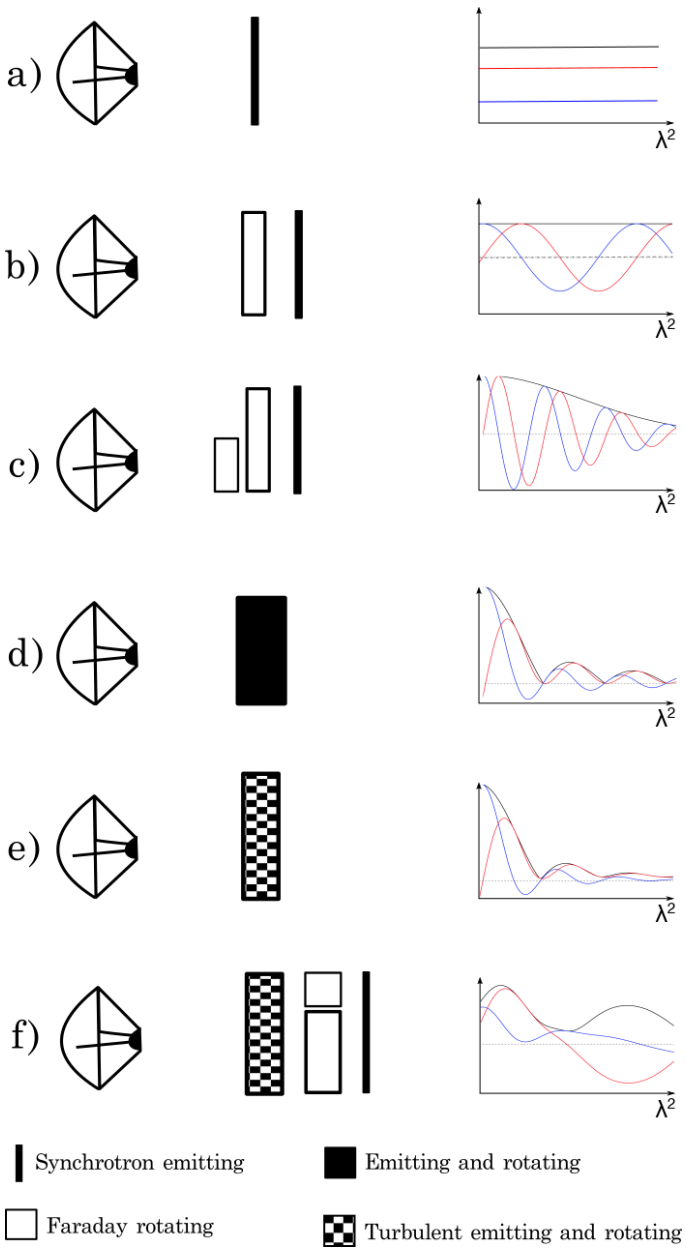

Figure 1.7: Various Faraday rotation mechanisms and the resultant polarisation spectra shown on the right. Blue and red lines represent the arbitrary Stokes Q and U spectra and black shows the total polarised intensity. We assume that each element displayed is within one synthesised beam of the telescope (represented on the left). Example a) represents a pure synchrotron emitting source, b) a single Faraday rotating in front of the source of emission (§1.3.1). In both of these examples, we see a constant polarisation fraction. Examples c), d) and e) represent the three depolarisation mechanisms discussed in this chapter, EFD (§1.4.1), DFR (§1.4.2), and IFD (§1.4.3), respectively. Example f) represents an arbitrary complex polarised sightline with multiple Faraday rotators and depolarisation mechanisms (§1.4.4).

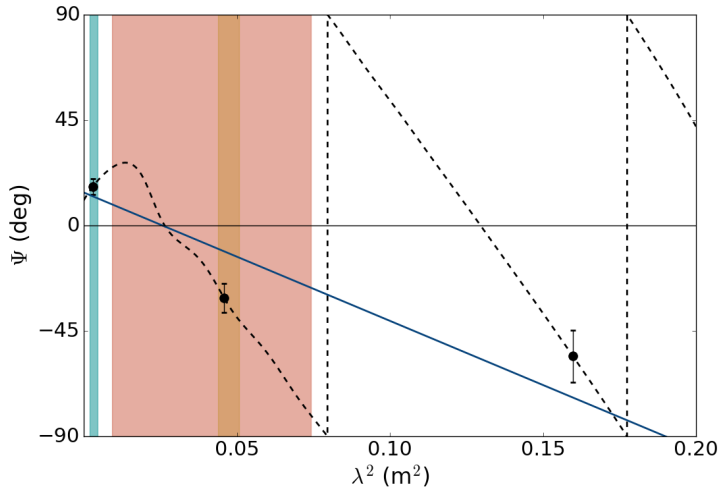

Figure 1.8: Figure comparing the relative λ^2 coverage sampled by different observing techniques. The black dashed line shows an arbitrary complex polarisation angle ($\Psi(\lambda^2)$) and the black points represent observations at 750, 1400 and 5500 MHz with an assumed uncertainty of 8%. The best-fit RM is given by the solid blue line. The orange shaded region represents the λ^2 coverage offered by the ATCA before the CABB upgrade and the red and teal shaded regions represent the λ^2 coverage for frequency bands centred on 2100 and 5500 MHz, respectively.

where L now designates the progressive position along the line-of-sight, in contrast to the integral definition of RM (Equation 1.11). It follows from this definition of ϕ that multiple polarised sources at different line-of-sight depths can exist at different Faraday depths. It is worth stressing that an object's Faraday depth does not correspond to a physical depth.

1.4 DEPOLARISATION

In the instance of a single magnetised slab in the sightline, the polarisation fraction would remain constant for all λ^2 (Figure 1.7b) . However, observations of such a scenario in nature is highly unlikely. It is much more common to observe a polarisation spectrum that appears to depolarise, i.e. $dp/d\lambda^2 < 0$ for an arbitrary λ^2 (e.g. Figures 1.7c-f). Farnsworth et al. (2011) argue that in all physically realistic descriptions of a polarised line-of-sight, there exist multiple complexities that cause the $p(\lambda^2)$ spectra to exhibit non-linear behaviour. There are typically four mechanisms that can lead to depolarisation, all of which are presented with complete discussion by Sokoloff et al. (1998). Below we summarise these mechanisms and outline their physical implications and limitations.

1.4.1 External Faraday Dispersion

All polarisation studies have an intrinsic spatial resolution, as determined by the angular size of the resolution element, or beam, and the redshift (z) , or distance, of the source. If, within the observing beam, there exists an external, non-emitting slab of material threaded by an ordered magnetic field that varies in strength and/or direction, or by a turbulent magnetic field, the polarised emission will undergo different amounts of rotation along the different lines of sight. This slab of material is often referred to as a Faraday screen. In this scenario, the polarised emission will experience depolarisation that results from the smoothing out and subsequent cancellation of the polarisation vectors (including their fluctuations) under the footprint of the beam. This will cause the measured polarisation to be less than that at the source of emission. An example of such smoothing is given in Figure 1.7c).

When observed over multiple wavelengths, depolarisation of this type will have the form (Burn 1966),

$$p = p_0 \, e^{2i(\Psi_0 + \phi\lambda^2)} \, e^{(-2\sigma_\phi^2 \lambda^4)}, \tag{1.14}$$

where σ_ϕ^2 is the RMS of the Faraday depth fluctuations on scales smaller than the synthesised beam. Polarised emission that is experiencing this type of depolarisation has a characteristic dependence on λ^4. This strong dependence on observing wavelength leads to beam depolarisation often dominating radio polarisation observations, causing many targets to appear completely depolarised at sufficiently low frequencies. There is no way to correct for the lost polarisation signal other than to observe a polarised target at higher angular resolution or higher frequency.

Due to the purely external dependence of this type of depolarisation, and its dependence on the observing beam, this type of depolarisation is often referred to as 'beam depolarisation' and has more recently been referred to as '*external Faraday dispersion*.' We adopt the latter nomenclature and will refer to any depolarisation of this kind accordingly.

1.4.2 Differential Faraday Rotation

If the synchrotron emitting and Faraday rotating regions are cospatial in the presence of a uniform magnetic field, then polarised emission at different depths will experience different relative amounts of Faraday rotation. Assuming a symmetric uniform slab, Burn (1966) describes this scenario as resulting in depolarisation of the form

$$p \; = \; p_0 \, e^{2i(\Psi_0 + \frac{1}{2}\phi\lambda^2)} \, \frac{\sin(\phi\lambda^2)}{\phi\lambda^2}, \tag{1.15}$$

when integrated over the entire line-of-sight. As the observed amount of depolarisation is a function of the physical depth of the source, this mechanisms is often referred to as

depth depolarisation. However, it is more correctly referred to as *'differential Faraday rotation'* (DFR) in the literature (Gardner and Whiteoak 1966) and I will adopt the same naming convention. One such example of a DFR polarisation signal is given in Figure 1.7d).

The sinc function dependence allows for polarisation levels to increase at certain values of λ^2; however, p will never be greater than p_0. Observations of such repolarising spectra are rare (e.g. O'Sullivan et al. 2012; Farnes et al. 2014; Anderson et al. 2016), but the existence of a such an occurrence immediately lends insight into the internal distribution of the polarising medium. The classical RM-value for Faraday rotation due to this mechanism will be equivalent to half of the resultant Faraday depth value (RM $= \frac{1}{2}\phi$).

1.4.3 Internal Faraday Dispersion

Similarly to DFR, if the emitting and rotating regions are cospatial in a region with a turbulent magnetic field, the amount of rotation experienced by waves emitted at different depths will experience a random walk as they propagate through the medium. In the literature, depolarisation of this nature is referred to as internal Faraday dispersion (IFD), since any mechanism responsible for the observed depolarisation is located locally to the source of synchrotron emission.

The simplest case of IFD is one where the synchrotron emissivity, the regular component of the magnetic field, and standard deviation of the random component are all symmetric as a function of depth of the magneto-ionic material and the distribution of the random and regular components are identical. Polarised emission of this form can be expressed as

$$p \;=\; p_0\, e^{2i\Psi_0} \frac{1 \;-\; e^{(2i\phi\lambda^2 \,-\, 2\zeta^2\lambda^4)}}{2\zeta^2\lambda^4 \;-\; 2i\phi\lambda^2}, \tag{1.16}$$

where ζ is the standard deviation of the random magnetic field component along the line of sight. Figure 1.7e) represents a typical polarisation spectrum associated with the described geometry.

A consequence of this depolarisation mechanism is that polarisation levels are inversely related to the source depth. In cases of high turbulence, emission will only appear polarised from the front of the source, with a physical depth approximately equivalent to the size of the turbulent cell. In such an occasion, the entire turbulent field component can be neglected, as it will already be depolarised and the observed polarisation level can be quite significant.

1.4.4 Multiple Faraday Components

In real situations, multiple Faraday active components may coexist, either within the synthesised beam or along the line of sight (e.g. O'Sullivan et al. 2012; Anderson et al. 2016). Characterising each source of Faraday rotation is an important step towards understanding the polarised sightline, however it is difficult for a number of reasons. Firstly, each component has an intrinsic Faraday depth, which varies between sources. Schnitzeler (2010) find a spread in intrinsic Faraday depth values equivalent to 6 rad m^{-2}. This spread in intrinsic Faraday depth would ideally be accounted for. Furthermore, each individual component can themselves be subject to any of the aforementioned depolarisation mechanisms potentially making the observed polarisation spectra especially complex (e.g. Figure 1.7f).

For example, contributions from the Earth's ionosphere exist towards all sightlines and while the estimated Faraday rotation contribution is low it is non-negligible at low radio frequencies and/or for sources with low Faraday depth values. The scale of the ionospheric magnetic field varies little on the timescales typical of radio observations (Cotton 1993). However, changes in the total electron content of the ionosphere can augment the observed Ψ by ~ 1 rad m^{-2}. Taking this effect into account will increase the overall uncertainty in the Faraday depth.

The Milky Way lies foreground to all sources of polarisation outside of our Galaxy. In fact, Faraday rotation was first used to study astronomical sources by Cooper and Price (1962), who found that the amount of Faraday rotation observed had a strong dependence on Galactic latitude. It became clear that the Faraday depth of the Milky Way is highly dependent on position, with the strongest dependence on Galactic latitude, as expected from electron and magnetic field scale heights. Faraday depth magnitudes have been measured to vary between $\gtrsim 100$ rad m^{-2} near the Galactic Plane (e.g. Schnitzeler 2010; Oppermann et al. 2012, 2015) to $\lesssim 6$ rad m^{-2} near the Galactic poles (Mao et al. 2010). Significant effort has been made to model the magnetic field structure of the Galaxy (e.g. Sun and Reich 2010; Jansson and Farrar 2012), which has revealed the field to be very complex, with typical field strengths $< 10\,\mu$G (Manchester 1974; Han et al. 2006). The work of Taylor et al. (2009) showed that the Galaxy has a major influence on the measured RM towards the majority of polarised extragalactic radio sources such that these sightlines can be seen to probe local Galactic structures (Figure 1.9). Extending the work of Taylor et al. (2009), Oppermann et al. (2015) carried out an extensive study to separate the Milky Way's contribution and map the Galactic Faraday depth across the sky.

Further complicating polarisation studies, differing amounts of material that comprise the large-scale structure (LSS) lay foreground to many extragalactic polarised sources. Characterising the potential magnetic field strength within the LSS filaments, and thus the Faraday depth contributions, is an area of intense research. At present, the contributions

from the LSS are believed to manifest as a deviation in intrinsic Faraday depth of order $1 - 10$ rad m^{-2} (Akahori and Ryu 2010, 2011).

Historically, astronomers would often approximate a line of sight as having one dominant Faraday rotation component. However, it is increasingly clear that secondary components may have non-negligible effects on the science. A key issue for polarimetry work is to characterise and remove these unwanted Faraday contributions that alter the polarisation measurements of the target of interest. Often constructing models containing multiple components is necessary to extract parameters of interest.

For example, a common case would be an extragalactic radio source containing two unresolved lobes of a radio galaxy. The observed signal will be the summation of the two individual Faraday components and emission from the various components will experience different amounts of Faraday rotation leading to constructive and deconstructive interferences that varies a function of λ^2. In the instance of two independent, Faraday-thin components within the observing beam, the polarisation will follow

$$p(\lambda^2) = p_{0,1}\, e^{2i(\Psi_{0,1}+\phi_1\lambda^2)} \quad + \quad p_{0,2}\, e^{2i(\Psi_{0,2}+\phi_2\lambda^2)}, \tag{1.17}$$

where the subscripts '1' and '2' refers to the two lobes of the radio galaxy.

Here we note that polarised sightlines can be affected by the foreground Faraday rotation due to the Galaxy. If the Galaxy itself were to be a source of polarised emission and rotation, the scenario can be approximated as two polarised Faraday components at different physical depths such that the expression for the total observed polarisation becomes

$$p(\lambda^2) = p_{0,a}\, e^{2i(\Psi_{0,a}+(\phi_a+\phi_b)\lambda^2)} \quad + \quad p_{0,b}\, e^{2i(\Psi_{0,b}+\phi_2\lambda^2)}, \tag{1.18}$$

where variables pertaining to the more distant Faraday component are denoted with a subscript 'a' and those of the closer component, 'b'.

In such instances of multiple emitting and rotating components, nothing is known about the differing spectral indices of individual components since neither source can be independently observed. Often analysis of such models is unable to decouple spectral dependencies within the fractional polarised spectra. In such instances, spectral analysis has often been carried out as a function of P, rather than in the fractional domain. However, as we will discuss in Section 1.5.2, certain developments into new spectropolarimetric analysis methods have made it possible to decouple total intensity flux from polarised flux.

In order to carry out analysis towards extragalactic polarised sources, we must confidently measure the magnetic field strength, and thus the Faraday depth of, external galaxies. Disentangling the signal from interfering magnetoionic emission has been an essential step. As ionospheric effects are relatively small at the frequencies of our observations when compared to other contributions, our corrections have been primarily

for the Milky Way foreground, environmental effects (i.e. intergalactic medium) and the intrinsic Faraday depth at the source of emission.

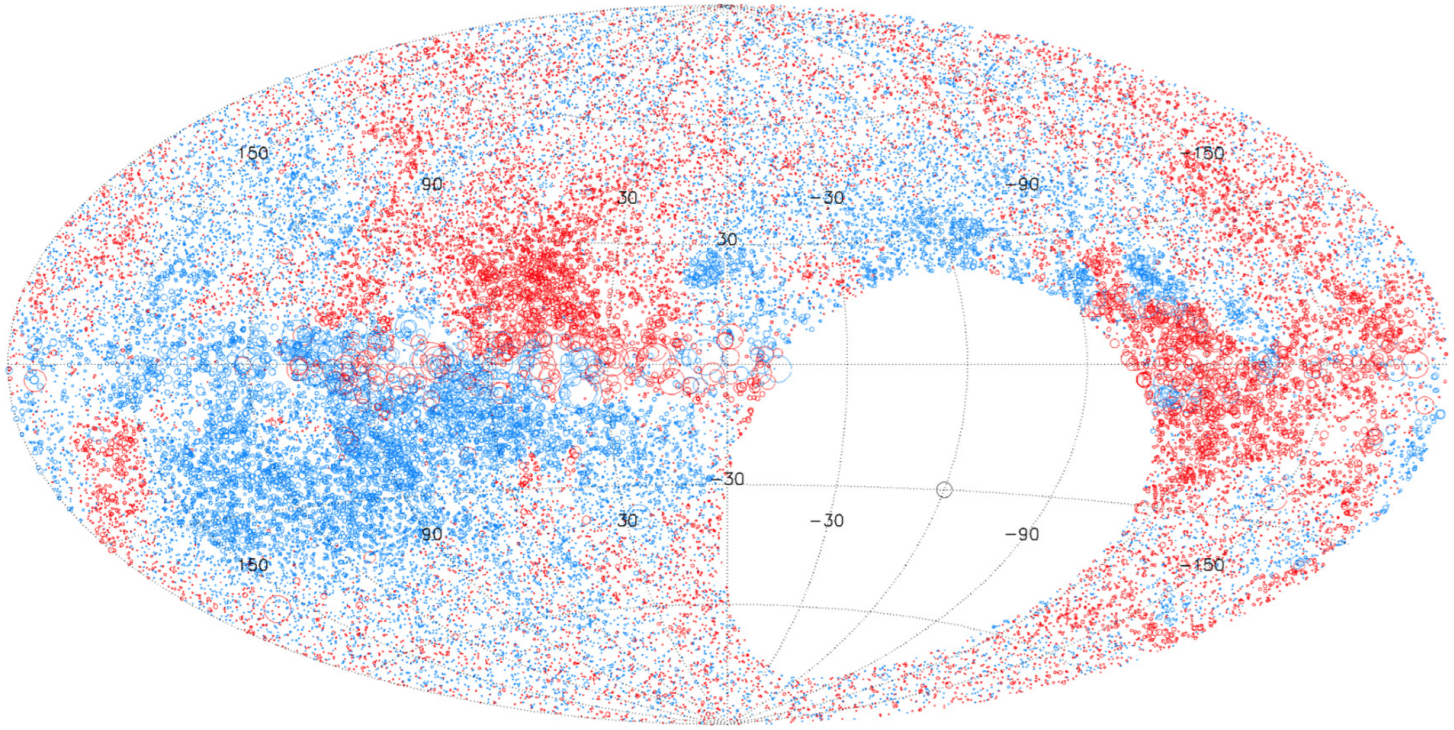

Figure 1.9: Aitoff projection of 37,543 RM values towards extragalactic polarised radio sources north of $\delta = -40°$ from Taylor et al. (2009), shown in Galactic coordinates. The colour of each circle is indicative of a positive (red) and negative (blue) RM. The size of the circles scales with the magnitude of the RM. It has been shown that much of the Faraday rotation signal displayed in this map trace Galactic contributions.

1.5 SPECTROPOLARIMETRY

The Faraday rotation complexities described in previous sections only add to the difficulty in recovering true Faraday depth measurements. The broad bandwidth advancements of recent telescopes have brought Faraday rotation studies into a new era of research by opening up areas of contiguous λ^2-coverage that were previously unattainable. It has become clear that use and analysis of simple straight-line fits to $d\Psi/d\lambda^2$ no longer suffice in describing the complex Faraday structure along a given line-of-sight and new, more robust methods need to be developed. Recalling that p can be expressed in terms of the observable quantities q and u, it becomes possible to solve for the various polarimetric variables through analysis of the fractional Stokes spectra.

One of the major advantages to spectropolarimetry is the ability to derive accurate Faraday depths of all contributions to a set of observations of $\mathbf{P}(\lambda^2)$). At the present time, there are two major methods of recovering the Faraday depth spectrum and analysing polarised spectra for Faraday complexity, *rotation-measure synthesis* and *qu-fitting*.

1.5.1 ROTATION-MEASURE SYNTHESIS

The concept of rotation-measure synthesis (RM synthesis) was first postulated by Burn (1966) and fully developed by Brentjens and de Bruyn (2005), and is based on the notion that complex polarisation can be expressed in a functional form analogous to Fourier analysis. That is, it is possible to express complex polarised intensity as

$$\mathbf{P}(\lambda^2) = \int_{-\infty}^{+\infty} \mathbf{F}(\phi) e^{2i\phi\lambda^2} d\phi, \tag{1.19}$$

where $\mathbf{P}(\lambda^2)$ is the complex polarised intensity and $\mathbf{F}(\phi)$ is the complex polarised flux per unit Faraday depth, often referred to as the Faraday dispersion function. The Faraday dispersion function characterises all Faraday depth contributions along a given line-of-sight. The major exception to the similarities between Equation 1.19 and a true Fourier transform is that for Equation 1.19, $\mathbf{P}(\lambda^2)$ can only be measured for positive λ^2. However, as argued by Burn (1966), by assuming that radio sources exhibit certain characteristic traits, the Fourier transform can be calculated from limited observations where $\lambda^2 > 0$ (Brentjens and de Bruyn 2005). The transform results in a finite point spread function, referred to as the rotation measure spread function (RMSF), which acts as a sampling window in Faraday space. Typical RMSF for observations with ATCA are shown in Figure 1.10.

RM synthesis serves as a means to visualise polarisation data and categorise the λ^2-sampling limitations. The major advantage of RM synthesis is that in order to implement the technique, no prior knowledge of the source structure is required. The ability for RM

synthesis to reconstruct the true distribution of Faraday depths can be characterised by three quantities defined by Brentjens and de Bruyn (2005): the resolution in Faraday-depth space ($\delta(\phi)$), the maximum observable Faraday depth ($\phi_{\rm max}$), and the maximum scale of Faraday structures ($L_{\rm max}(\phi)$).

- Just as there is an angular resolution limit in interferometric imaging, there exists an inherent resolution limit in Faraday depth ($\delta(\phi)$) space for a given set of observations, as determined by the width ($\Delta\lambda^2$) of the coverage in λ^2, i.e.

$$\delta(\phi) = \frac{2\sqrt{3}}{\Delta\lambda^2}. \tag{1.20}$$

  This implies that if there exist one or more components separated by a Faraday depth less than, or equal to $\delta(\phi)$, it will not be possible to distinguish these components from one another. Therefore, in order to achieve high-resolution ϕ-measurements, one requires polarisation observations over a wide range of λ^2.

- Any spectropolarimetric dataset will have a maximum ϕ to which it is sensitive. The maximum observable $|\phi|$ is dependent on the width of the spectropolarimetric channels such that

$$|\phi_{\rm max}| = \frac{\sqrt{3}}{\delta\lambda^2}, \tag{1.21}$$

  where $\delta(\lambda^2)$ is the average channel width in λ^2-space. Spectropolarimetric observations that are well separated in λ^2 space, but have no intermediate samplings will not be strong probes of complex Faraday structures. When observing sources typical of hosting large magnitude Faraday depths (e.g. accretion disks, jets, ICM), it is imperative that one samples the polarised spectra at sufficiently small channel widths. Historically, the channel width of spectropolarimetric observations was so large that many structures were invisible in Faraday space.

- Finally, in order to achieve sensitivity to extended structures in Faraday space, well-sampled, low λ^2 data must be available. The maximum detectable Faraday-depth scale is determined by

$$L_{\rm max}(\phi) = \frac{\pi}{\lambda^2_{\rm min}} \tag{1.22}$$

Over the past decade, RM synthesis has proven to be a powerful tool for understanding the magnetised Universe. However, it has limited application for data with limited bandwidth sampling, which is characteristic of the vast majority of earlier Faraday studies. With the upgrade of ATCA to the CABB system, many of these sampling limitations have been vastly improved. However, realistic radio observations are subject to radio-frequency interference (RFI), which results in non-uniform sampling and sensitivity in

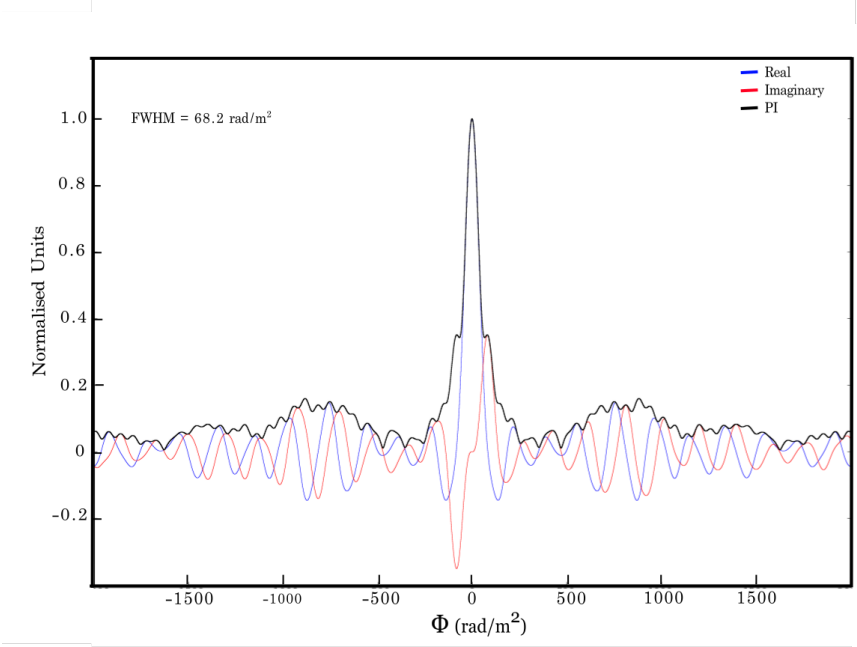

(a) 2100 MHz band

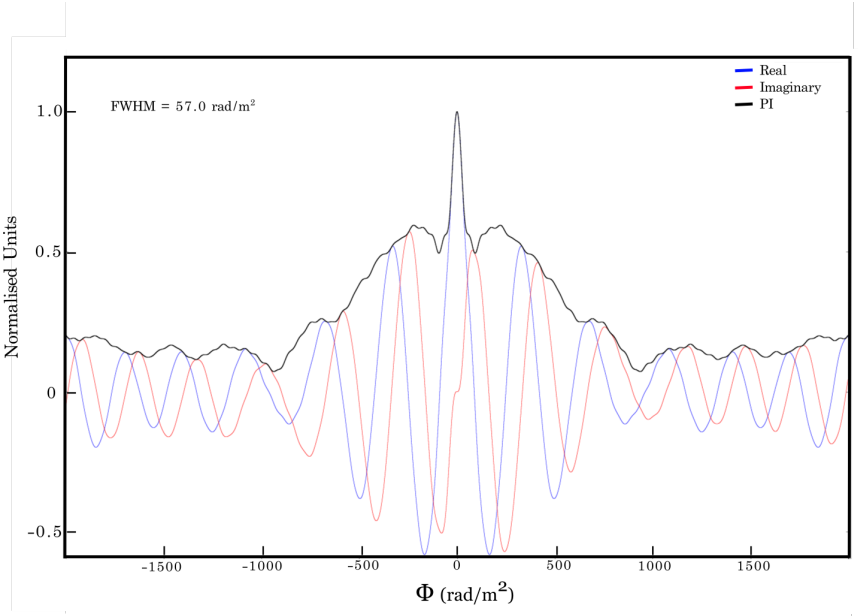

(b) 2100, 5500, and 9000 MHz observing bands.

Figure 1.10: RMSF for CABB observing bands centred at 2100 MHz (top) and the combined 2100, 5000 and 9000 MHz bands (bottom). Each observing band covers 2048 MHz.

λ^2-space. Limited sampling of $\mathbf{P}(\lambda^2)$ introduces severe side lobes into the RMSF (e.g. Figure 1.10). These complex-valued sidelobes can cause interference between one or more Faraday components and make the reconstruction of the true Faraday depth distribution erroneous (Farnsworth et al. 2011; Sun et al. 2015). Additionally, in the low signal-to-noise regime, false peaks can emerge in the FDF, which can often be interpreted as a real component (Schnitzeler and Lee 2017). Therefore, the interpretation of the data is complicated as the FDF does not impart the intrinsic polarisation attributes, nor can it robustly return the number of real Faraday components. These features of RM synthesis make it difficult to expand the analysis to physical properties of the magnetised plasma.

1.5.2 QU-FITTING

The second commonly-used approach is qu-fitting where a model to the Faraday depth structure is constructed and fit to the observed Q and U spectra (e.g. Farnsworth et al. 2011; O'Sullivan et al. 2012). Using a minimisation procedure, this method simultaneously fits the $q(\lambda^2)$ and $u(\lambda^2)$ spectra (Figure 1.11). Through direct comparison of various spectropolarimetric analysis techniques, Sun et al. (2015) show that qu-fitting is the most accurate method currently available.

One of the distinct advantages to qu-fitting is that with the careful construction of polarisation models, this method has the potential to offer significant insight into the nature of observed magnetised plasma. Supplied with good signal-to-noise data, the qu-fitting method can return accurate and precise measurements of the intrinsic polarisation fraction, initial polarisation angle, Faraday depth and Faraday dispersion of each Faraday component along the line-of-sight, provided the model is realistic.

qu-fitting can be extended to overcome many of the drawbacks of RM synthesis, such as incomplete frequency sampling and non-zero spectral indices by fitting with maximum-likelihood methods (Schnitzeler and Lee 2017). Observational limitations due to RFI incur less-severe penalties to the success of the algorithm, by taking into account frequency-dependent uncertainties of the Stokes Q and U spectra. If the fractional polarisation spectra are derived via a higher order function that takes into account variations as a function of wavelength, it breaks the dependence on spectral index information for all emission components. Therefore, it can be possible to recover accurate polarimetric properties for the entire line of sight.

While qu-fitting has its strengths, it also has its limitations. In order to use qu-fitting, one must impose certain assumptions on any tested model. Therefore, qu-fitting's main disadvantages are centred around the fact that in order to test a polarisation model, simplifications are often made to the assumed line-of-sight. This thesis primarily uses the polarisation models from Sokoloff et al. (1998), but as those authors notes, each model has been derived to meet specific conditions. While some of these assumptions can be

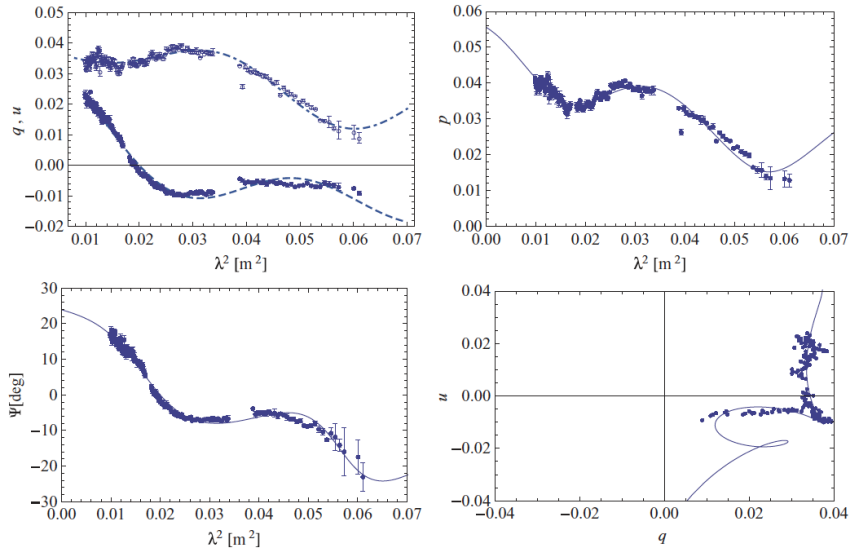

Figure 1.11: A qu-fitting example from O'Sullivan et al. (2012) in which a three component polarisation model is fitted to the source PKS B1039−47. The top left panel gives the fraction q and u spectra versus λ^2 and the resultant model fit, the top right panel shows the fractional polarisation, p, spectra and fit versus λ^2. The observed and model Ψ versus λ^2 is given in the bottom left and a plot of $q(\lambda^2)$ versus $u(\lambda^2)$ is shown in the bottom right.

minor, real sources are often much more complex then the assumed model geometry. In this way, qu-fitting often imposes significant limitations to the interpretation of the best-fitting model.

As previously discussed in Section 1.4, there exist degeneracies between depolarisation mechanisms. Thus, a well-fitted solution to a depolarisation model does not guarantee an accurate description of the true polarised line of sight. However, it may be possible in some cases to break these degeneracies with additional data and logical arguments.

Confidently fitting using maximum-likelihood methods requires the full exploration of each parameter space in a model and modelling complex expressions for polarisation requires intensive data processing. Solutions to the best-fitting polarisation parameters have often be found via brute force and repetition (e.g. O'Sullivan et al. 2012; Wehus et al. 2013). While new techniques to minimise data-processing time are currently being explored (Purcell et al., *In prep.*), time and computing restraints are perhaps the most limiting drawbacks to current qu-fitting routines.

Motivated by its potential to probe the physical nature of various magnetised cosmic structures and its ability to return accurate fits to an observed polarised spectrum, qu-fitting is the primary method used for spectropolarimetric analysis and interpretation in this thesis.

1.6 COSMIC MAGNETIC FIELDS

I now present a brief discussion of polarimetric observation across various evolving structures typical of the kpc-scale regime. In each section that follows, I summarise some of the scientific arguments made in the literature and highlight a few open questions that remain in each field of research.

1.6.1 GALAXIES

Magnetic fields in galaxies can be observed at optical, infrared and radio wavelengths. Observing at radio wavelengths has an added advantage when compared to other wavelengths since radio continuum emission typically exhibits higher fractional polarisation and therefore is easier to detect at high significance. Observations of total and polarised intensities also allow for the study of the magnetic field strengths both along the line of sight, through the analysis of observed Faraday rotation, as well as in the plane of the sky, through synchrotron emission. In this thesis, I hold that the term 'galaxy' pertains to the gravitationally bound systems identified through their optical emission. While research into the magnetic properties of individual galaxies is a rapidly growing area of study in its own right, this thesis does not carry out any detailed investigation of optical hosts of radio galaxies.

The Milky Way

Due to its close proximity, the Milky Way can serve as an ideal laboratory for investigating many aspects of galaxy evolution. All-sky observations have been carried out towards nearly every phase of the ISM, and such investigations have revealed a complex, dynamic structure with bubbles and loops of gas distributed throughout the Galaxy. These fractal structures are created by supernova explosions and clusters of OB-stars, potentially driving material out of the Galactic disk into the halo (Shapiro and Field 1976; Bregman 1980; Norman and Ikeuchi 1989; Dove et al. 2000; Reynolds et al. 2001). Simulations predict that magnetic fields play an integral role in the evolution of these structures, but in contrast to our understanding of the Galactic ISM, our knowledge of polarisation and magnetism in the Galaxy is still limited. Our lack of understanding is in part due to difficulty in imaging diffuse, magnetoionic plasma on such large angular scales.

Yet, the Milky Way lies in the foreground to all of extragalactic polarisation research, and the severity to which it impacts observations depends heavily on the Galactic latitude of a target source, with the Milky Way dominating at low Galactic latitude (Leahy 1987; Schnitzeler 2010). A seminal example of this was presented in Taylor et al. (2009), in which RM measurements towards extragalactic polarised sources were shown to trace some of the magnetised structures within the Milky Way (Figure **??**). Following this,

Oppermann et al. (2012) and Oppermann et al. (2015) assembled an all-inclusive list of measured RMs in order to reconstruct the Galactic Faraday depth across the whole sky. Confidently accounting and correcting for the Faraday rotation contribution from the Milky Way is a deciding factor in much of the analysis presented in this thesis.

Galaxy Interactions

Close encounters, collisions and interactions between galaxies have the potential to trigger bursts of star-formation and feed active galactic nuclei (detailed in the next section). Additionally, interactions drive the deformation and evolution of galaxies, leading to the creation of tails, bridges and rings. These tidal features are believed to play an important role in the magnetisation of the intergalactic medium (IGM) (Cesarsky 1980; Ptuskin 2006) and may affect local magnetic field structures. In interacting galaxies, increased star-formation triggered by the encounter can lead to the destruction of field regularity (e.g. Chyży and Beck 2004). In tidal streams and bridges, there is evidence of magnetic fields being pulled out of the parent galaxies and potentially amplified (e.g. Condon et al. 1993; Basu et al. 2017). It is even possible to trace the interaction of an individual galaxy with the surrounding intergalactic medium (IGM) through the observation of compressed field lines and/or strongly polarised ridges (e.g. Hummel and Beck 1995; Soida et al. 1996).

Galaxy interactions are an important cosmological phenomenon due in part to their role as an catalyst for the evolution of the visible Universe. But as pointed out in the previous paragraph, galaxy interactions also have the potential to influence the evolution of large-scale magnetic fields. Few detailed investigations into the magnetic field structure of tidal structures have been carried out to date (e.g. Condon et al. 1993; Chyży and Beck 2004; Basu et al. 2017). This is partially due to limited bandwidth observations and, in part, to the relatively small angular scale of the majority of tidal features. Therefore, in order understand the evolutionary history of cosmic magnetism, it is imperative that we understand the extent to which galaxy interactions affect galactic-scaled magnetic fields.

1.6.2 Radio Galaxies

Radio galaxies are the most powerful sources of radio emission in the Universe. The Milky Way exhibits radio emission at a level of 10^{30} W, typical of most optical galaxies. By comparison, the power associated with radio galaxies is typically of order $10^{34} - 10^{38}$ W. This makes radio galaxies of significant importance when considering the relationship between galaxies and their environment. In addition, their huge brightnesses make it possible to observe them across the visible Universe. Combined with their large physical size ($10\text{s} - 1,000\text{s}$ kpc), the relatively long timescales over which radio emission is detectable ($\sim 10^8$ yr, Komissarov and Gubanov 1994) and high fractional polarisation

levels, radio galaxies have been a natural target for polarimetric observations.

The central engine of a radio galaxy is the active galactic nucleus (AGN), from which collimated jets (Bridle and Perley 1984) and extended radio lobes emanate. Diffuse radio lobes are inflated with magnetised, synchrotron plasma (Begelman et al. 1984; Xu et al. 2003). The radio jet is the main mechanism through which material and energy is transported from the host galaxy into the surrounding medium. Radio galaxies are typically broken down into two categories, defined by Fanaroff and Riley (1974), as low-luminosity Fanaroff-Riley type I (FR I) and high-luminosity Fanaroff-Riley type II (FR II). FR I galaxies host jets that flare into large, diffuse, radio lobes. In contrast, FR II galaxies host narrow jets that are highly-collimated. These jets typically terminate in hot spots, where the jet is believed to intersect a higher-density environment. The plasma then flows backwards, creating the radio lobes.

AGN may be responsible for the entrainment and large scale distribution of metal-rich interstellar gas into radio lobes (Simionescu et al. 2009; Kirkpatrick et al. 2011) and the lobes themselves inject this thermal material and subsequent magnetic fields into the surrounding environment (Reuland et al. 2007). As thermal gas acts as a Faraday-rotating medium, observations of Faraday rotation towards radio galaxies have attempted to shed light on the thermal and non-thermal content of radio lobes. However, disentangling the different Faraday components from one another has proven difficult. As such, refining the thermal gas content in radio lobes is currently a particularly active area of research. Laing (1988), Taylor et al. (2009) and Kronberg et al. (2008) modelled the Faraday rotation associated with radio galaxies as the result of foreground material from a large scale, diffuse intracluster medium (ICM).

In contrast, other authors have argued that a significant portion of the observed Faraday rotation is intrinsic to the radio lobe itself. In the latter case, there is even more debate as to where in the lobe the Faraday rotation takes place. Rudnick and Blundell (2003) and Laing et al. (2008) make a case that the Faraday rotating material forms a thin skin encompassing the purely synchrotron lobes. In a somewhat similar argument, Guidetti et al. (2011) and Guidetti et al. (2012) argue that large-scale Faraday depth structures seen in the lobes of two radio galaxies may be a result of interactions at the interface between the synchrotron lobe and surrounding medium. Contrasting these geometric arguments, there are authors who fit their observations by modelling radio lobes as a mixture of relativistic synchrotron plasma and magnetised, thermal gas (O'Sullivan et al. 2013, using narrow-band radio observations and Seta et al. 2013, using X-ray observations).

As the majority of the previous studies into Faraday rotation towards radio lobes were carried out over narrow observing bandwidths, it is possible that new broadband observations, such as those possible with the ATCA, may be able to provide sensitive enough measurements of the polarised signal and subsequent Faraday rotation that the true geometry and structure of the magneto-ionic medium can be revealed.

1.6.3 Cosmic Environments

The Universe is built up of a complex network of dark matter, gas and galaxies in the form of low-density filaments that lead to high-density clusters of galaxies. These different environments in which galaxies are embedded play a significant role in the evolutionary timescales and ultimate fate of each galaxy.

Galaxy Groups

Galaxy groups are a unique class of cosmic environment: they host up to 60% of galaxies in the Universe and have halo masses that span the range between that of the largest galaxies ($10^{12}\,M_{\odot}$) to that of galaxy clusters ($10^{15}\,M_{\odot}$). As a consequence, interactions give rise to increased star formation rates and a smattering of tidal debris diffused throughout the intragroup medium (IGrM) (Donahue et al. 1995; Freeland and Wilcots 2011). These phenomena, along with galactic winds and AGN, have been suggested as mechanisms by which magnetic fields can be expelled from a galaxy into their surrounding medium (Menon 1995; Chyży and Beck 2004; Kronberg et al. 1999; Bertone et al. 2006). Observing these phenomena conveniently offers astronomers insight as to how magnetic fields can affect, and be affected by, galaxy evolution.

However, magnetism of the intragroup medium remains one of the least studied aspects of galaxy groups. Detailed investigations have been hindered by the relatively low thermal electron density comprising the diffuse IGrM, making it difficult for telescopes to confidently detect any existing field. To date, investigation into magnetic fields in galaxy groups has been limited to the observations of tidal bridges at discrete and/or narrow bandwidths (Condon et al. 1993; Xu et al. 2003; Nikiel-Wroczyński et al. 2013a,b; Basu et al. 2017). Due to a recent increase in observing bandwidth as well as improved surface brightness sensitivity of instruments, detailed and systematic studies of magnetism in galaxy groups are becoming possible for the first time.

Galaxy Clusters

Galaxy clusters are the largest gravitationally bound structures in the Universe that form via the accretion of less massive structures. The existence of magnetic fields in clusters has been confirmed using a number of different approaches, including investigation of inverse Compton X-ray emission from cluster centres (Jaffe 1977; Bonafede et al. 2009), extended synchrotron emission from radio halos and relics (Govoni et al. 2011; Bonafede et al. 2013), and analysis of background and embedded Faraday rotation measures (Clarke et al. 2001; Johnston-Hollitt et al. 2004). Large-scale magnetic fields such as these play a significant role in the propagation of cosmic rays (e.g. Murase et al. 2008; Das et al. 2008) as well as the production of powerful radio emission (Feretti et al. 2012). Feedback simulations from large-scale structure formation has been shown to drive the

creation and maintenance of these extremely large-scale magnetic fields (Dolag et al. 2002), yet feedback from cluster formation, such as shocks and turbulence, can act to destroy any coherent, primordial magnetic field structure indicating that the exact creation mechanism for a coherent field on such a large scale is still poorly understood.

Large Scale Structure Filaments

The various feedback mechanisms in galaxy clusters likely erase signatures of magnetic-field evolution. Therefore, in order to answer questions pertaining to the evolution of magnetic fields in the early Universe, one must look to more pristine, low-turbulence volumes. One such environment that has the potential to host information on the origin of cosmic magnetic fields are large scale structure filaments.

The Universe is constructed out of a complex network of filaments and voids. The large-scale gas filaments can be found connecting galaxies, groups and clusters (Cen and Ostriker 1999; Kang et al. 2005). When compared to galaxy clusters, the evolutionary history of filaments is thought to be much less complex. Therefore, information pertaining to primordial magnetic field origin and evolution may still exist within the low-density environment.

The detection of magnetic fields within filaments has the potential to answer key formation questions pertaining to cosmic magnetism, and it may be possible to measure the strength and structure of the primordial seed fields. Estimates of the magnetic field strength in filaments is of order $B \sim 1$ nG and the resultant Faraday depths would be of order $1-10$ rad m^{-2} (Akahori and Ryu 2010, 2011). To date, the existence of such fields has yet to be definitively determined, but future telescopes such as the Square Kilometre Array (SKA) will be sensitive enough to begin to search for these weak, information-packed magnetic fields. As research into this area is largely theoretical at present, I do not carry out any investigations into large-scale filamentary magnetic fields in this thesis, but it is worthy of inclusion on merits of completeness.

1.7 THESIS GOALS

With the advent of broadband observations and large surveys, astronomers have only recently gained the capability to seek answers to fundamental questions pertaining to cosmic magnetic fields. In doing so, it appears that our knowledge of the polarised Universe is entering a new era and we are able to disentangle and characterise complex polarised sightlines with unprecedented precision.

As the polarisation revolution is still young, a multitude of questions remain to be answered, especially in the realm of the evolution of large-scale magnetic fields. While it is not feasible to wholly investigate this topic in a single body of work, this thesis has

been structured to investigate the mechanisms by which galaxies can magnetise their immediate environment, and thus affect the evolution of magnetic fields onto larger scales. Specifically, this thesis aims to answer the following questions:

(1) To what extent do magnetic fields in tidal remnants remain coherent?

(2) What are the magneto-ionic properties of radio galaxies and their outflows?

(3) Is the diffuse intragroup medium magnetised?

I have carried out four separate studies which aim to address the above questions. In Chapter 2, I address the first question while I search for a magnetic field spanning the entirety of the Magellanic Bridge and address possible origins for the subsequently discovered field. In Chapter 3, I carry out a detailed spectropolarimetric study of the radio galaxy, NGC 612, and endeavour to determine the polarisation mechanism responsible for the observed Faraday rotation, thus addressing question 2. Chapter 4 continues addressing question 2 through an additional investigation into the extended radio lobes of MSH 05−3*13*. In this chapter, we explore the possibility for environmental impacts to explain complex Faraday structures spanning the synchrotron radio lobes. The radio galaxies studied in chapters 3 and 4 are each imbedded within a galaxy group. Therefore, by studying the Faraday structures associated with their radio lobes, we are also able to explore the density of magneto-ionic material in the surrounding environment, potentially answering question 3. Chapter 5 presents a statistical approach towards question 3, in that I present a blind study into magnetic field strengths and morphologies associated with the diffuse medium of a sample of galaxy groups. To conclude, Chapter 6 summarises the results presented in this thesis. I also discuss the possible directions of future work into the study of magnetic field evolution and how they may augment the findings of this thesis.

2

Detection of a Coherent Magnetic Field in the Magellanic Bridge through Faraday Rotation

This chapter has also appeared published as Kaczmarek et al. (2017), "Detection of a coherent magnetic field in the Magellanic Bridge through Faraday rotation", MNRAS, 467 (2), 1776-1794.

2.1 Introduction

The Large Magellanic Cloud (LMC) and Small Magellanic Cloud (SMC) are a highly-studied galaxy pair. Due to their close proximity to the Milky Way (MW), the Magellanic Clouds allow astronomers to study galaxy interactions and evolution in unprecedented detail. The on-going interaction between the galaxy pair, and possibly the MW, have led to the creation of the Magellanic Bridge (MB), the Magellanic Stream, and the Leading Arm (see Besla et al. 2010 and D'Onghia and Fox 2016 for a complete review)– each of which can be identified through the presence of HI gas. Most prominent of these features is perhaps the MB (Hindman et al. 1963) – a contiguous, gaseous tidal feature that spans the region between the LMC and SMC. We assume that the MB is located at a distance of 55 kpc, the mean distance to the LMC and SMC (Walker 1999). We also assume that the bulk of the HI emission has a radial velocity in the range $100\,\mathrm{km\,s^{-1}} \leq v_{\mathrm{HI}} \leq 300\mathrm{km\,s^{-1}}$ (Putman et al. 2003; Muller et al. 2003). The tidal remnant is thought to have formed $\sim$200 Myr ago when the LMC and SMC were at their closest approach to one another (Gardiner and Noguchi 1996; Besla et al. 2012).

Tidal tails, streams and bridges play an important role in the evolution of the parent galaxies as well as the host environment, as they serve as a siphon for galactic material to be dispensed into the diffuse intergalactic medium. It can be posited that a pre-existing

magnetic field could follow the movement of neutral gas into the intergalactic medium. The stretching and compressing of tidally stripped gas may then serve as a mechanism for the amplification of any existing magnetic fields (Kotarba et al. 2010). Thus, the stripping of tidal debris may be partially responsible for the distribution of magnetic fields over large volumes. What remains unclear is the importance and role of magnetic fields within tidal features.

The association between tidal remnants and magnetic fields has been studied for nearly two decades. Classically, the radio continuum tidal bridge connecting the 'Taffy' galaxies (Condon et al. 1993) was estimated as having a similar magnetic-field strength to the pre-collision galaxies and the field lines appeared to be stretching across the space between the galaxy pair. More recently, tidal dwarfs within the Leo Triplet and Stephan's Quintet have been shown to possess coherent magnetic fields and have total magnetic-field strengths of $B_T = 3.3 \pm 0.5\,\mu$G and $B_T = 6.5 \pm 1.9\,\mu$G, respectively (Nikiel-Wroczyński et al. 2013a, Nikiel-Wroczyński et al. 2013b).

Decades of research using optical polarized starlight has shown that polarization vectors in the plane of the sky trace out a path from the SMC along the western Bridge oriented in the direction of the LMC (Mathewson and Ford 1970b,a; Schmidt 1970, 1976; Magalhaes et al. 1990; Wayte 1990; Lobo Gomes et al. 2015). Due to the limited number of stars with which one can carry out optical polarimetry studies, all previous claims of the existence of a coherent magnetic field spanning the entire Magellanic System have had to be speculative due to the lack of information stemming from the diffuse MB.

Studies of Faraday rotation of background polarized radio sources towards the LMC have determined that the galaxy has a coherent magnetic field of strength $\sim 1\,\mu$G (Gaensler et al. 2005). Mao et al. (2008) observed the SMC using both Faraday rotation measures and polarized starlight. Through careful consideration of the Galactic foreground they constructed 3D models for the magnetic field and showed that the orientation of the field has a possible alignment with the MB.

A similar investigation into Faraday rotation towards extragalactic polarized sightlines has shown that a high-velocity cloud (HVC) in the Leading Arm hosts a coherent magnetic field (McClure-Griffiths et al. 2010). In such an instance, a magnetic field would work to prolong the structural lifetime of the HVC as it is accreted onto the MW disk. While the exact origin of the magnetic field in this HVC remains unclear, it is plausible that the HVC fragmented from a magnetized Leading Arm. Therefore, the observed magnetic field in the HVC would be a consequence of the initial seed field followed by compression and amplification due to the MW halo.

Although magnetic fields have been found in the SMC, LMC, and some HVCs, none of the previous investigations of magnetism in the Magellanic System have directly confirmed the existence of the *Pan-Magellanic Field* – a coherent magnetic field connecting the two Magellanic Clouds.

2.1.1 FARADAY ROTATION

Complex linear polarization is an observable quantity and can be defined as

$$\mathcal{P} \;=\; Q + iU = p_0\, e^{2i\Psi}, \tag{2.1}$$

where Q, and U are the observed linearly polarized Stokes parameters, p_0 is the polarization fraction intrinsic to the source and Ψ is the observed polarization angle, also defined as:

$$\Psi = \frac{1}{2}\, arctan\, \frac{U}{Q}. \tag{2.2}$$

The polarization angle is rotated from its intrinsic value (Ψ_0) any time the emission passes through a magneto-ionic material. This effect is known as Faraday rotation. The total observed Faraday rotation, defined $\Delta\Psi/\Delta\lambda^2$, is known as the rotation measure (RM).

When the rotating material is located along the line-of-sight, Faraday rotation can serve as a powerful tool to analyse magnetism. In the simple case of a thermal plasma threaded by a single magnetic field, the intrinsic polarization angle is rotated by $\Delta\Psi = \mathrm{RM}\lambda^2$ radians. However, recent studies have shown that the RM may offer an incomplete, or misleading diagnostic of the actual polarization properties along the line-of-sight (O'Sullivan et al. 2012; Anderson et al. 2016) and that many sources cannot be described by a single RM. It is therefore more robust to discuss the polarized signal in terms of its Faraday Depth (ϕ), as first derived by Burn (1966). The Faraday depth encodes the electron density (n_e, in cm^{-3}) and magnetic-field strength along the line-of-sight ($B_\parallel$, in μG) according to

$$\phi(L) \;=\; 0.812 \int_L^0 n_e B_\parallel dl, \tag{2.3}$$

where L is the distance through the magneto-ionic material in parsecs. The sign of the Faraday depth is indicative of the orientation of the magnetic field with a positive ϕ signifying the field to be oriented towards the observer and a negative ϕ implying a field that is pointing away.

The measured ϕ_{obs} for a extragalactic source behind the MB is a summation of the various Faraday depth components along the line-of-sight and can be broken down into its constituent parts as follows:

$$\phi_{\mathrm{obs}} \;=\; \phi_{\mathrm{intrinsic}} \;+\; \phi_{\mathrm{IGM}} \;+\; \phi_{\mathrm{MB}} \;+\; \phi_{\mathrm{MW}}, \tag{2.4}$$

where $\phi_{\mathrm{intrinsic}}$ is the Faraday depth that is associated with the polarized emitting source, ϕ_{IGM} is any rotation due to the intergalactic medium, ϕ_{MB} is our targeted Faraday depth due to the posited MB magnetic field and ϕ_{MW} is the Faraday rotation due to the foreground MW. Although $\phi_{\mathrm{intrinsic}}$, ϕ_{IGM} and ϕ_{MW} are present along all sightlines, ϕ_{MW} is

Table 2.1: Summary of the observations. Column 1 gives the array configuration; Column 2 gives the regions targeted (as defined in §2) ; Column 3 lists the length of the observing run and Column 4 gives an approximation for the total integration time per source. Column 5 gives the UT date of the commencement of the observations.

Array Config.	Obs. Targets	Obs. Length (hrs)	Time On-Source (min)	Obs. Date
6C	Wing, West	12	2.5	2015 Mar 14
6A	Wing, West	15	1.5	2015 Apr 30
6A	Join, North, South	15	3	2015 Apr 30
1.5B	Wing (subset)	3	5	2016 Jun 11

likely to dominate the observed signal. This assumption appears to have been well justified in Taylor et al. (2009), whereby mapping the rotation measures of extragalactic polarized sources from the NRAO VLA Sky Survey (NVSS) revealed local structures in the Galaxy. Therefore, by observing polarized sources with sightlines that do not intersect the MB, we will be able to correct for the Galactic foreground, leaving the residual ϕ to represent the intrinsic properties of the background source and the MB contribution. The intrinsic polarized properties of each polarized source are random and considered to have a negligible effect on the overall statistics for a large sample.

If there exists a coherent magnetic field threading the MB, observations of linearly polarized background radio sources may hold the key to its discovery. In this work, we use detailed measurements of the Faraday depth of background, extragalactic polarized sources to investigate the existence of a coherent magnetic field spanning the MB. We describe our source selection process and observations in Section 2.2, followed by data reduction and processing in Section 2.3. We present our results in Section 2.4, which include the fitting and subtraction of the MW foreground. Section 2.5 motivates different distributions of ionized gas and the subsequently derived magnetic-field strengths. In Section 2.6 we discuss the possible origins and implications of the pan-Magellanic Field. A summary is presented in Section 2.7.

2.2 Observations & Data

2.2.1 Source Selection

For this investigation, we observed a subset of polarized sources that were originally identified through the reduction and re-processing of archival continuum data of the western MB (see Muller et al. (2003) for a summary of observations). In the literature, this region has been referred to usually as either the 'Wing' or 'Tail' (Lehner et al. 2008; Brüns et al. 2005), and we make reference to this region as the 'Wing,' exclusively (See Figure 2.1 for location). The HI observations of the 'Wing' had simultaneously observed the

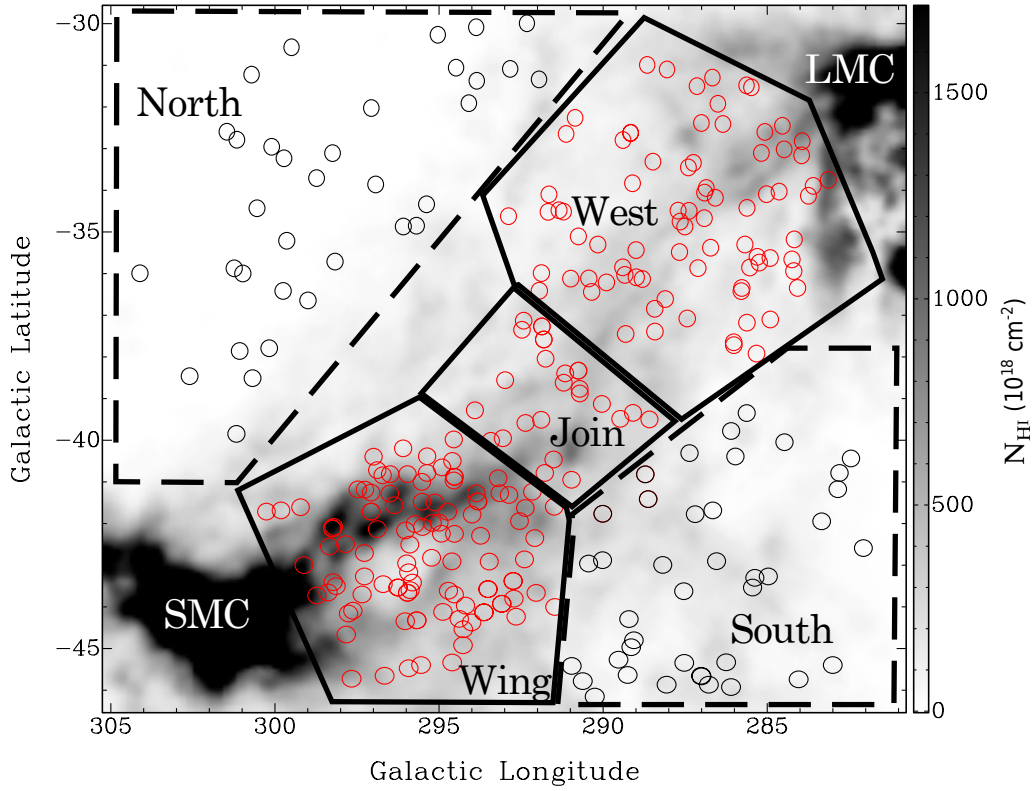

Figure 2.1: Neutral hydrogen column density for the velocity range of $+100 \leq v_{\rm HI} \leq +300\,{\rm km\,s^{-2}}$ of the MB region from the GASS survey (McClure-Griffiths et al. 2009, Kalberla et al. 2010), over-plotted with the positions of observed radio sources. Each pointing is associated with a region name denoted by the text in the enclosed areas. Red circles (pointings enclosed by a solid line) are sources where the MB is considered to intersect the background source's line-of-sight, whereas sources marked by black circles (pointings enclosed by a dashed line) are considered as having lines-of-sight that are not contaminated by the MB. These latter sources were observed in order to subtract the Faraday rotation contribution from foregrounds and backgrounds.

continuum emission associated with this region. The source-finding algorithm *Aegean* (Hancock et al. 2012) was used to identify sources in the final, deconvolved continuum images. A brief description of the source finding method in addition to a table of the identified sources is given in Appendix A. From this original sample, we targeted 101 polarized sources for follow-up observations.

An additional 180 radio sources were targeted in order to extend the investigation across the entirety of the MB and surrounding area. Motivated by the changing morphology and kinematics of the Bridge, we separate these additional sources into regions 'West', 'Join', 'North', and 'South'. These additional radio sources were selected from the Sydney University Molonglo Sky Survey (SUMSS, Mauch et al. 2003) as having a Stokes I flux $\geq$ 100 mJy at 843 MHz for the region labelled 'West' and $\geq$ 150 mJy for regions 'Join,' 'North' and 'South'. Figure 2.1 gives a summary of the pointing regions observed overlaid on a map of neutral Hydrogen (HI) of the region from the Galactic All Sky Survey (GASS; McClure-Griffiths et al. 2009; Kalberla et al. 2010).

2.2.2 Observations

Observations of the 281 radio sources were taken over 3 days with the Australia Telescope Compact Array under project C3043. Taking advantage of the instantaneous broad bandwidths of the Compact Array Broadband Backend (CABB, Wilson et al. 2011), the observations spanned the continuous frequency range of 1100 – 3100 MHz. Each pointing was observed as a series of snapshots in order to improve uv-coverage. Phase calibrators were observed at least every 40 minutes. The bandpass and flux calibrator PKS B1934-638 was observed on 14 March 2015 and 30 April 2015 and PKS B0823-500 was observed as the bandpass calibrator on 11 June 2016. polarization leakage calibrations were carried out using the aforementioned primary calibrators. On average, each pointing was observed for a total of 3 minutes. Due to the nature of the source selection associated with the 'Wing' and the possibility that sources could be weak in total intensity, the initial 3 minutes of observation was sometimes not enough to reach a sufficient signal-to-noise. Additional observations were made as a single hour-angle uv-cut on 11 June 2016 in order to improve our sensitivity limits for points that were not bright enough in polarization nor total intensity to be confidently detected with our initial observations. A summary of the observations is listed in Table 2.1 and the representative uv-coverage for any source in each region is shown in Figure 2.2.

2.3 Data Reduction and Extraction

Observations were calibrated and imaged in the MIRIAD software package (Sault et al. 1995) using standard routines. Flagging of the data was done largely with the auto-

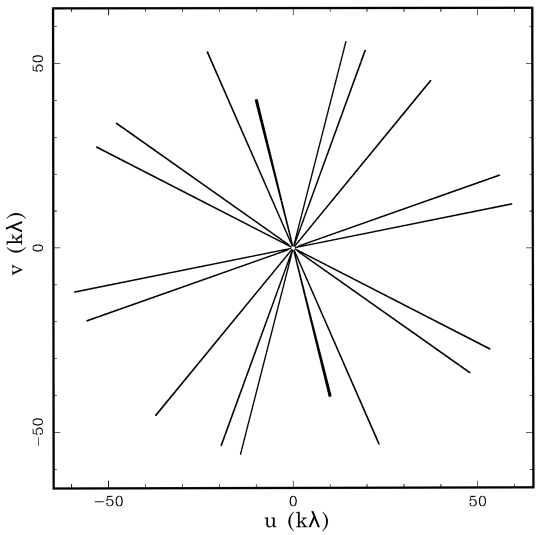

(a) Wing and West regions

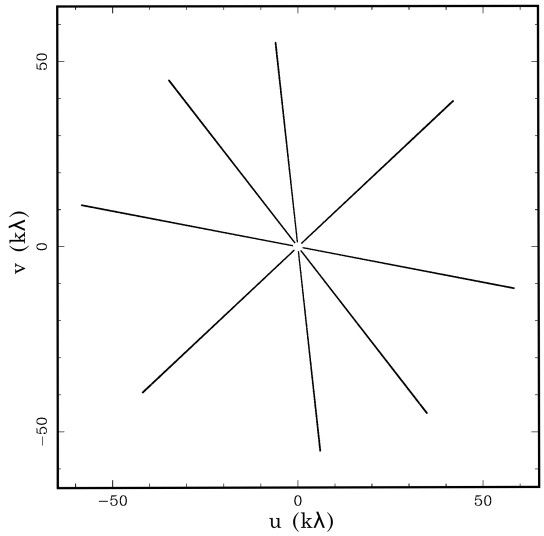

(b) Join, North and South regions

Figure 2.2: Typical uv-coverage of a single radio source associated with (a) the 'Wing' and 'West' and (b) 'Join', 'North', 'South'.

Region	Observed	Polarized	Accepted fraction (%)
Wing	101	69	68
West	83	40	48
Join	23	15	65
North	34	22	65
South	40	21	53
	281	167	59

Table 2.2: Summary of total number of points observed per region and total number of polarized sources accepted. In order to be accepted, a source must be detected to at least 8σ in the full bandwidth polarized intensity image. The 'Wing' region returns a higher fraction of polarized sources due to our previous knowledge of the polarization in this region.

mated task PGFLAG, with minor manual flagging being carried out with tasks BLFLAG and UVFLAG. Naturally-weighted Stokes I, Q, U and V maps were made using the entire 2 GHz bandwidth. Deconvolution of the multi-frequency dataset was performed on the dirty maps with the task MFCLEAN. Cleaning thresholds were set to be 3 times the rms Stokes V levels ($3\sigma_V$) for Stokes Q and U, and $5\sigma_V$ for Stokes I. Images were convolved to a common resolution of 8 arcseconds, which corresponds to a linear scale of 2 pc at the assumed distance to the MB of 55 kpc.

From the broadband 2 GHz images, images of linearly polarized intensity ($\mathcal{P}$) were made with the task MATH. The total polarized flux of a target was extracted from an aperture 8 arcseconds in diameter centred on the peak polarization pixel with noise estimates ($\sigma_{\mathcal{P}}$) measured as the rms residuals from a source-extracted image. A target was considered 'polarized' if the integrated polarized flux was greater than $8\sigma_{\mathcal{P}}$. This method of imaging will lead to bandwidth depolarization for sources with absolute Faraday depths greater than $\sim 90\,\mathrm{rad\,m^{-2}}$; however, we consider the number of sources rejected due to high Faraday rotation to be negligible and has no impact on our final science goals.

Imaging with narrow bandwidths decreases the signal-to-noise in addition to reducing the resolution in Faraday depth space, while broad bandwidths decrease the maximum observable scale in Faraday space, as well as the maximum observable Faraday depth. In order to minimise the bandwidth depolarization and maintain a desirable signal-to-noise ratio, Stokes I, Q, U images were made every 64 MHz - resulting in 27 channel maps spanning 1312 - 3060 MHz.

As with the broadband $\mathcal{P}$ images, integrated fluxes were extracted from each map from an equivalent beam area centred on the pixel corresponding to the peak in $\mathcal{P}$. Error measurements were estimated as the rms-noise level from images created from the residual of the Stokes maps after the source aperture was blanked. With the exception of

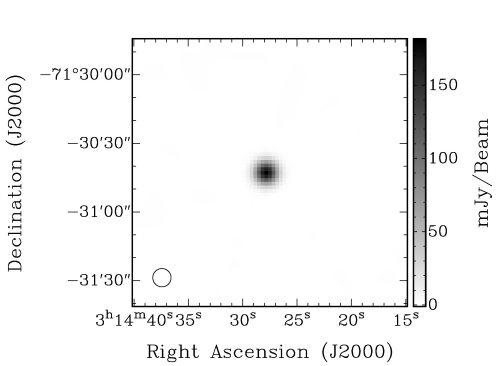

(a) Total intensity for source Join_08.

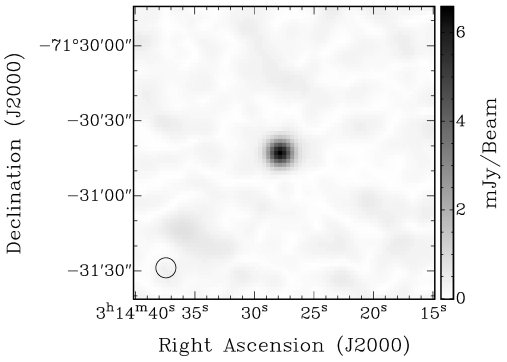

(b) Polarized intensity for source Join_08.

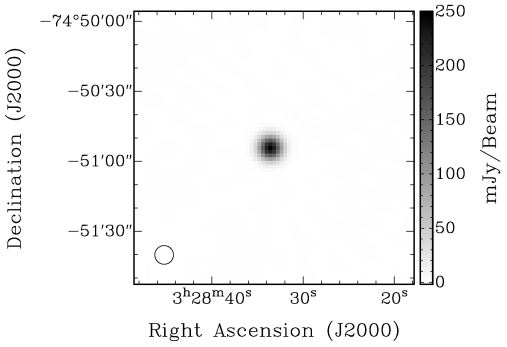

(c) Total intensity for source West_02.

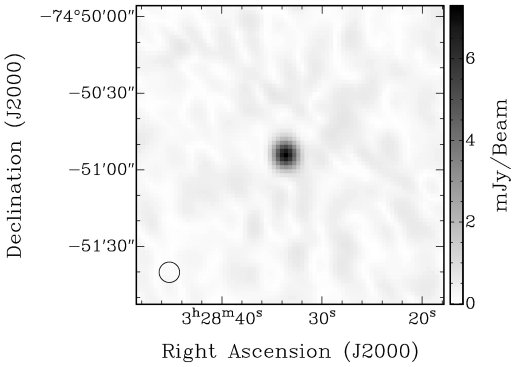

(d) Polarized intensity for source West_02.

Figure 2.3: Example of two polarized sources detected in our survey: points 'Join_08' (a) and (b) and 'West_02' (c) and (d). Multi-frequency images for total intensity (Stokes I) are shown in (a) and (c) and polarized intensity ($\mathcal{P}$) in (b) and (d). Both sources have been imaged using the full bandwidth available and the restoring beam is shown in the bottom left of each image.

Table 2.3: A subset of measured and calculated source parameters. Columns (1) and (2) give the source location in Galactic longitude and latitude, respectively. Column (3) lists the integrated total intensity (I) over the full 2 GHz bandwidth with uncertainties. Integrated polarized flux ($\mathcal{P}$) with uncertainty is listed in Column (4). Columns (5 - 8) give the best-fit parameters returned from qu-fitting: namely, the intrinsic polarization fraction (Column (5)), the intrinsic polarization angle (Column (6)), the total Faraday depth along the line-of-sight (Column (7)) and the Faraday dispersion (Column (8)).

(1) l (°)	(2) b (°)	(3) I (mJy)	(4) $\mathcal{P}$ (mJy)	(5) p_0 (%)	(6) Ψ_0 (°)	(7) $\phi_{\rm obs}$ rad m^{-2}	(8) σ_ϕ rad m^{-2}
291.778	-40.785	104.9 ± 0.2	3.2 ± 0.3	$5.8^{+0.7}_{-0.6}$	37^{+4}_{-4}	$+6^{+3}_{-4}$	21^{+2}_{-2}
288.589	-39.501	258.4 ± 0.07	3.9 ± 0.3	$1.66^{+0.09}_{-0.08}$	82^{+3}_{-3}	-0.2^{+2}_{-2}	3^{+2}_{-2}
290.958	-45.418	215 ± 3	7.1 ± 0.4	$2.8^{+0.3}_{-0.3}$	49^{+5}_{-5}	$+13^{+4}_{-4}$	23^{+2}_{-2}
285.625	-39.347	123.8 ± 0.2	1.6 ± 0.2	$6.38^{+0.07}_{-0.07}$	$143.9^{+0.5}_{-0.5}$	$+26.8^{+0.3}_{-0.3}$	$13.9^{+0.2}_{-0.2}$
296.659	-45.653	73.0 ± 0.2	6.8 ± 0.3	$10.1^{+0.4}_{-0.4}$	71^{+2}_{-2}	$-13.1^{+0.9}_{-1}$	$10.7^{+0.8}_{-0.8}$

sources associated with the 'Wing', all targets are expected to be bright in total intensity. A further 10σ cut-off was imposed, and extracted spectra with fewer than 10 channels were discarded.

The procedures described above result in 167 sources with spectra in I, Q and U. Table 2.2 has a summary of the fraction of sources accepted per region. The 'Wing' region has an advantage in returning a higher number of polarized sources due to our previous knowledge of the polarized detections in the region. However, our data extraction method rejected multiple targets in the 'Wing' region for falling below the sensitivity threshold. Figure 2.3 gives two examples of total ((a) and (c)) and polarized intensity ((b) and (d)) detected from extragalactic radio sources.

2.3.1 qu-FITTING AND ϕ DETERMINATION

We adopt the fractional notation such that $q = Q/I$ and $u = U/I$, where the observable polarized fraction can be expressed as

$$p = \sqrt{q^2 + u^2}. \tag{2.5}$$

In working with fractional Stokes parameters the wavelength dependent depolarization effects are decoupled from spectral index effects.

To create our fractional polarized spectra, the Q and U spectra are divided by a model fit to the Stokes I spectrum. This approach avoids creating non-Gaussian noise and the propagation of small-scale spectral errors that may be present in the Stokes I spectrum. Using a bootstrap approach with 10,000 iterations, we fit a second-order polynomial to

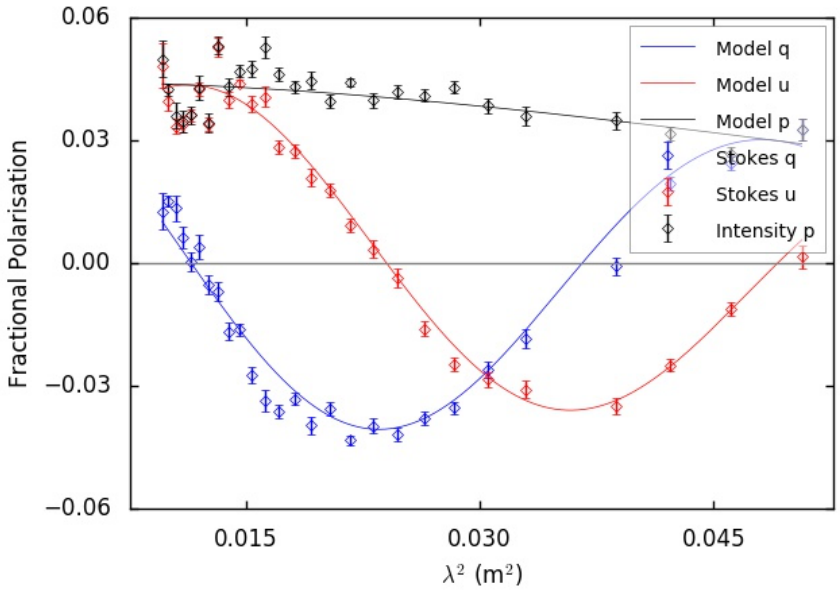

(a)

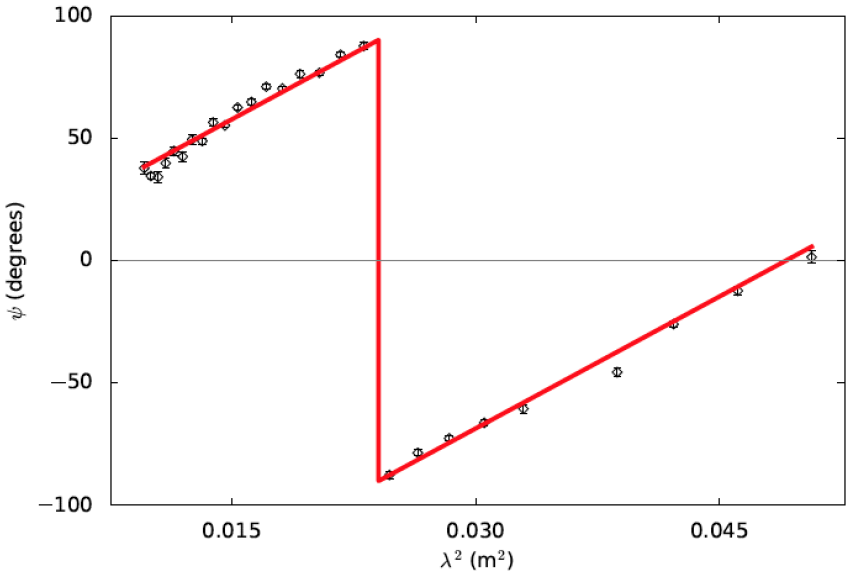

(b)

Figure 2.4: (a) Observed data and best-fit solution for qu-fitting to a point in the 'West' region. Observed fractional Stokes q and u are shown as blue and red points, respectively, whereas the model solution is shown as blue and red lines. The observed and model polarized fraction is shown as black points and a black line for reference. (b) Corresponding fit to polarization angle (Ψ) versus λ^2 for the aforementioned solution from qu-fitting.

the Stokes I spectrum of each polarized source and calculate the standard deviation of the resultant q and u values for each frequency channel. The total error is considered to be the standard deviation of the bootstrapped values of q and u added in quadrature to the measured noise from the cleaned Stokes Q and U maps. The bootstrap method is necessary to correctly propagate the uncertainty due to the fit and has the overall effect of increasing the magnitude of the errors from what can be measured from the Stokes maps.

In order to extract the observed Faraday depth from our polarized signal, we must motivate a polarization model for the MB environment. External Faraday dispersion (Burn 1966) can be used as a proxy to measure fluctuations in the free-electron density or magnetic-field strength. This model has been used in numerous past studies of the polarization of galaxies, galaxy groups and clusters (Gaensler et al. 2005; Laing et al. 2008). Without an observed continuum-emission component of the MB, a single-component external Faraday dispersion model serves as an appropriate approximation to the polarization signal associated with the MB.

Polarization of this form displays a decreasing polarization fraction as a function of λ^2. This depolarization can be defined as p/p_0, where p is the observed polarization. This effect is most evident towards long wavelengths. Due to the purely external dependence of external Faraday dispersion, and its dependence on the size of the observing beam, this depolarization model is often referred to as *'beam depolarization'*. In this scenario, averaging the fluctuations across the entire beam area, the result is polarization of the form

$$\mathcal{P} \;=\; p_0 \, e^{2i(\Psi_0+\phi_{\rm obs}\lambda^2)} \, e^{-2\sigma_\phi^2\lambda^4}, \tag{2.6}$$

where $\phi_{\rm obs}$ is the total observed Faraday-depth value (Equation 2.4) and σ_ϕ^2 characterises the variance in Faraday depth on scales smaller than our beam.

We calculate the best-fit $\phi_{\rm obs}$, σ_ϕ and Ψ_0 for each point source by fitting an external Faraday dispersion model (Equation 2.6) simultaneously to the extracted $q(\lambda^2)$ and $u(\lambda^2)$ data. This technique is called qu-fitting and Sun et al. (2015) show it to be the best algorithm currently available for minimising scatter in derived polarization parameters. We take a Monte Carlo Markov chain (MCMC) approach to fitting our complex polarization parameters by employing the EMCEE *Python* module (Foreman-Mackey et al. 2013). Compared to Levenburg-Marquardt fitting, MCMC better explores the parameter space, and returns numerically-determined uncertainties for the model parameters. The log-likelihood of the complex polarization model of the joint qu chi-squared (χ^2) is minimised to find the best-fitting parameters. For each pointing, we initialise a set of 200 parallel samplers that individually and randomly explore the n-dimensional parameter space (where n is the degrees of freedom). Each of these samplers – called 'walkers' – iteratively calculate the likelihood of a given location in parameter space and in doing so map out a probability distribution for a set of parameters.

We initialise the walkers to random values of the free parameters and run three 300 it-

eration 'burn-in' phases where the samples settle on a parameter set of highest likelihood. The position history of the walkers is removed before initiating a 300-step exploration of the new parameter sub-space. The best fit model is calculated as the mean of the marginalised posterior distribution for each parameter. The parameter uncertainties are measured from the 1σ deviation of the walkers above and below the resultant best-fit.

Figure 2.4 gives an example solution from qu-fitting. The fractional Stokes spectra (p, q and u) versus λ^2 is shown in the top panel (a). Observed values are shown as black, blue and red points for p, q and u, respectively. The best-fit solution is shown to trace the observed data. The best fit solution to Ψ versus λ^2 is given in the bottom panel (b). We attribute any deviation from the model to Faraday complexity of the source or a line-of-sight component that is not accounted for in the simple polarization model we assume (Equation 2.6).

2.4 RESULTS

In addition to fitting the observed Faraday depth ($\phi_{\rm obs}$), our fitting routine also returns best-fit values for all polarization parameters defined in Equation 2.6, namely p_0, Ψ_0 and σ_ϕ. A subsample of sources with the resultant best-fit parameters is given in Table 2.3, with the full dataset available in Appendix 2.6 .

Figure 2.5 shows the best-fit $\phi_{\rm obs}$ of every polarized radio source plotted over the HI emission of the region from GASS (McClure-Griffiths et al. 2009; Kalberla et al. 2010). Red circles indicate a positive $\phi_{\rm obs}$ and a field that is oriented towards the observer; blue circles, the opposite. Black crosses signify a $\phi_{\rm obs}$ that is consistent with zero to $2\times d\phi$ where $d\phi$ is the returned uncertainty in Faraday depth from qu-fitting.

We divide the observed polarized sources into two populations – those where the MB intersects the sightline to the polarized source and those with sightlines that are unaffected by the MB. We define an 'on-Bridge' region to be the area defined by a non-extinction corrected Hα intensity of $I_{\rm H\alpha} = 0.06$ R, shown as the lowest contour in Figure 2.8. The Hα dataset and subsequent analysis is discussed in more detail in Section §2.5.1. All sources associated with the 'Wing,' 'West' and 'Join' regions meet this criterion. The 'North' and 'South' regions are considered to be 'off-Bridge' and serve as a probe of the MW's Faraday depth structure in the region.

Of all the $\phi_{\rm obs}$-values in the imaged region, 84% are positive (red), and all of the negative (blue) and null (cross) Faraday depths are associated with the on-Bridge region (Figure 2.5). Figure 2.6 shows the $\phi_{\rm obs}$ population of all on- and off-Bridge sources as a cumulative histogram and highlights the clear discrepancy in Faraday depths for each population. We test the statistical likelihood that the Faraday depths associated with points on and off the Bridge come from a single population by performing a K-sample Anderson-Darling test on the best-fit $\phi_{\rm obs}$-values for all sources that have been detected

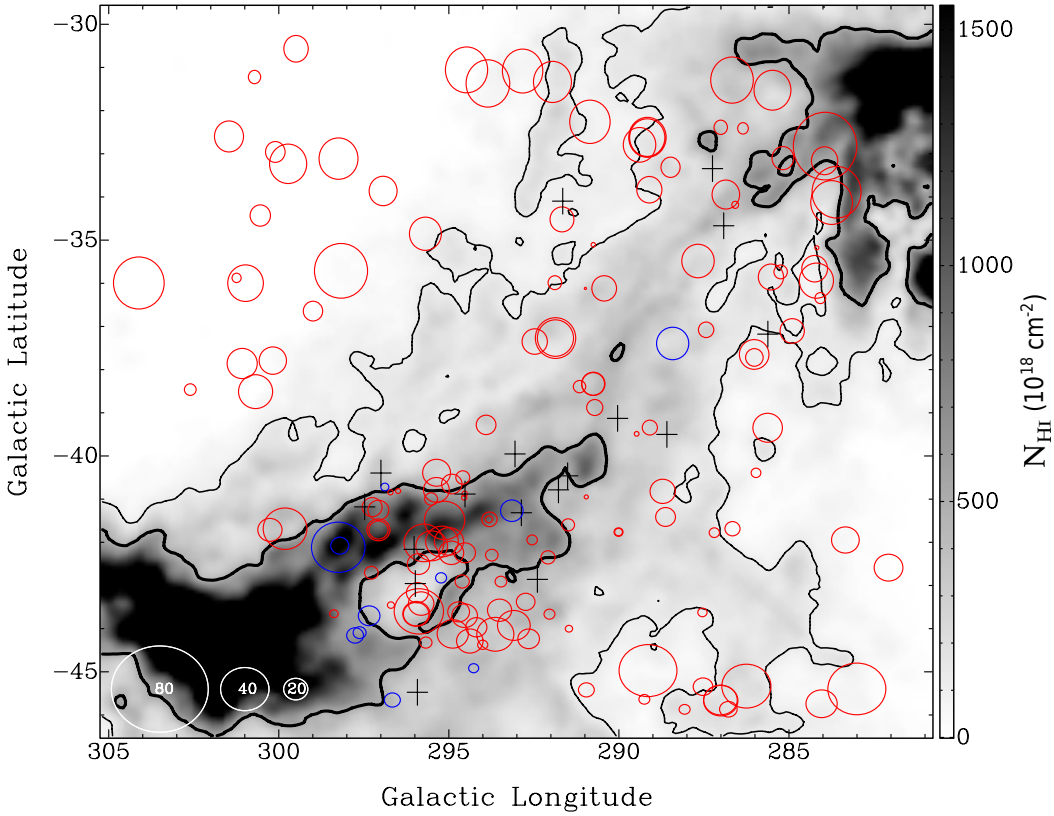

Figure 2.5: $\phi_{\rm obs}$ values fit to an external Faraday dispersion model overlaid on a map of HI intensity from GASS (Kalberla et al. 2010) in the velocity range of $+100 \leq v_{\rm LSR} \leq +300\,{\rm km\,s^{-2}}$. No correction for the Galactic contribution to Faraday depth has been made in this figure. Black contours represent HI emissivity of 1.2 and $5.0\times10^{20}\,{\rm cm^{-2}}$. The size of each circle is representative of the magnitude of ϕ, with scale-circles shown in the bottom left corner. Red circles represent a line-of-sight magnetic field pointing towards the observer (positive ϕ), and blue circles show a field that is pointing away (negative ϕ). Black crosses show ϕ values consistent with zero to $2\times d\phi$.

to $8\sigma_{\mathcal{P}}$ or higher in polarized intensity. The returned normalised test statistic allows us to reject the null hypothesis with a 99.992% confidence level. The difference in Faraday depths between the populations of $\phi_{\rm obs}$-values indicate that the polarized radiation on and off the MB probe distinctly different magnetic environments.

2.4.1 Correcting for Faraday Rotation due to the MW Foreground

The amount of Faraday rotation observed towards an extragalactic point source ($\phi_{\rm obs}$) will always include some contribution from the MW. Therefore, before the line-of-sight magnetic-field strength can be estimated, the Galaxy's contribution to the observed Faraday depth must be fit and corrected for. The 43 off-Bridge $\phi_{\rm obs}$ can be described by a tilted-plane $\phi_{\rm MW}$-model, whose parameters are obtained using a non-linear least-squares fit to the data. The best-fit solution was found to be of the form

$$\phi_{\rm MW} = -0.511\ell + 1.28b + 225, \tag{2.7}$$

where l and b are the coordinates in Galactic longitude and latitude, respectively. The plane is shown in Figure 2.7. By subtracting the resultant Faraday depth surface from all $\phi_{\rm obs}$, the residual Faraday depths ($\phi_{\rm corr}$ are considered to be foreground-corrected).

We compare our MW Faraday depth model with similar models from Mao et al. (2008) and Oppermann et al. (2015). Testing a point in the centre of the 'Join' region ($\ell = 290°, b = -38°$), our fit returns a $\phi_{\rm MB}$-value of $+28\,{\rm rad\,m^{-2}}$. At the same position, MW models from Mao et al. (2008) and Oppermann et al. (2015) return values of $+28\,{\rm rad\,m^{-2}}$ and $+25\,{\rm rad\,m^{-2}}$, respectively. The close agreement amongst all three MW models adds confidence to our MW correction.

We further test the validity of the foreground $\phi_{\rm MW}$-model by comparing the distributions of the uncorrected and corrected ϕ-values ($\phi_{\rm obs}$ and $\phi_{\rm MB}$, respectively) for points in the 'North' and 'South' regions. If the assumptions made to create the foreground model were valid, the distribution of Faraday depths should become more similar after the foreground correction has been applied. We test this theory by conducting two separate Anderson-Darling tests on the $\phi_{\rm obs}$ and $\phi_{\rm corr}$ distributions for the two off-Bridge regions. We find that before the foreground correction is applied there is $\sim 98\%$ confidence that the two background samples are drawn from different populations. Once our model is subtracted from the raw, observed Faraday depths, the likelihood that the two populations are unique drops to 67%. At this level there is no longer sufficient confidence to say they are not drawn from the same parent distribution. We therefore consider our simplified tilted-plane assumption of the Faraday depth distribution of the MW-foreground to be justifiable.

Figure 2.8 shows the foreground-subtracted Faraday depths across the imaged region. We expect that after our foreground correction, the majority of off-Bridge sources

would have values near zero, but this is not observed. We assume that the major cause for this discrepancy is that our foreground model is an oversimplification of the likely complex Faraday structure of the MW (Oppermann et al. 2015). We test the merit of a higher-order foreground Faraday depth model, but it produces minimal improvement while increasing the degrees of freedom. If our foreground fit was well founded, we would expect to have a mean $\phi_{\rm corr}$-value of off-Bridge points near zero: our sample returns $\overline{\phi}_{\rm off,\,corr} = 0.3\,{\rm rad\,m^{-2}}$ with a standard deviation of $12.0\,{\rm rad\,m^{-2}}$, compared to $\overline{\phi}_{\rm off,\,obs} = 25\,{\rm rad\,m^{-2}}$ before subtracting the foreground. We note that the foreground $\phi_{\rm MW}$ fit does not attempt to fit and subtract the Faraday rotation that is intrinsic to the background source. Schnitzeler (2010) estimates the spread in intrinsic Faraday depths of extragalactic sources to be $\simeq 6\,{\rm rad\,m^{-2}}$, which can account for much of the large standard deviation of the off-Bridge, foreground-corrected Faraday depths.

The uncertainty in the foreground Faraday depth subtraction must be included the error in the Faraday depth of the on-Bridge sources. The magnitude of the increased error was determined through bootstrapping the foreground $\phi_{\rm MW}$ surface 10,000 times with the standard deviation of the correction at each location ($\sigma_{\phi_{\rm MW}}$). The mean uncertainty in Faraday depths through this method is $\overline{\sigma}_{\phi_{\rm MW}} = 0.21\,{\rm rad\,m^{-2}}$. The expression for the total uncertainty in the Faraday depth of a background radio source therefore becomes

$$d\phi(l,b)^2 = d\phi^2_{\rm MCMC} + \sigma^2_{\phi_{\rm MW}}(l,b), \tag{2.8}$$

where (l, b) are the coordinates of the point source.

We infer that the MB Faraday rotation, $\phi_{\rm MB}$, accounts for the majority of the residual rotation seen in points associated with the MB and assume for all further analysis that $(\phi_{\rm obs} - \phi_{\rm MW}) = \phi_{\rm corr} = \phi_{\rm MB}$. A map of foreground-corrected $\phi_{\rm MB}$ is given in Figure 2.8, which shows negative Faraday depths spanning the entirety of the MB. Analysis of this trend shows that 68% of the polarized sources follow this trend to $2 \times d\phi$, where $d\phi$ is the calculated error in our Faraday depth measurement.

$\phi_{\rm MB}$ may contain contributions from localised enhancements – such as HII and star formation regions – that may influence the observed magnetic field on scales to which we are sensitive ($\sim 2\,{\rm pc}$). In order to identify any phenomena that could influence the small-scale magnetic field fluctuations in the MB, we cross-reference our region of sky with Simbad (Wenger et al. 2000) and find 7 molecular clouds (Chen et al. 2014) and 4 HII regions (Meaburn 1986; Bica et al. 2008) that are located in the 'Wing' region. Three of the molecular clouds and three HII regions are near the small patch of positive ϕ-values near $l = 295°, b = -42°$. These individual molecular clouds do not directly align with any of the background sources at our physical-scale sensitivity of 8 arcseconds.

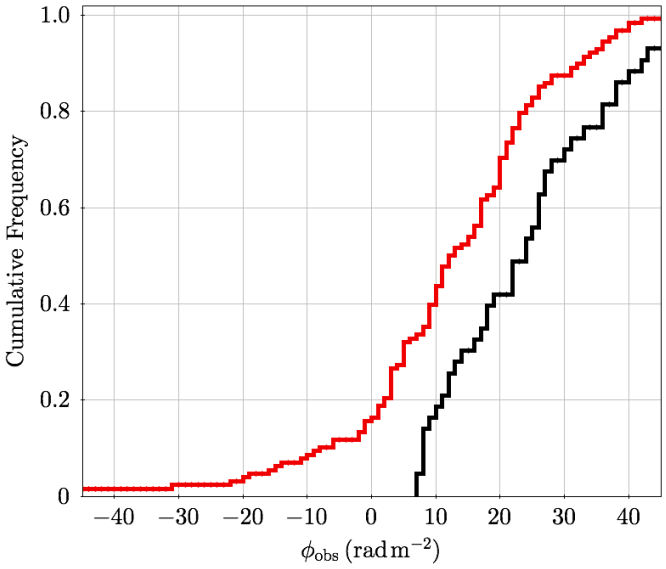

Figure 2.6: Cumulative histogram of ϕ_{obs} values for on-Bridge (red) and off-Bridge (black) sources. The figure is truncated at $\phi = \pm 45$ rad m^{-2} for clarity.

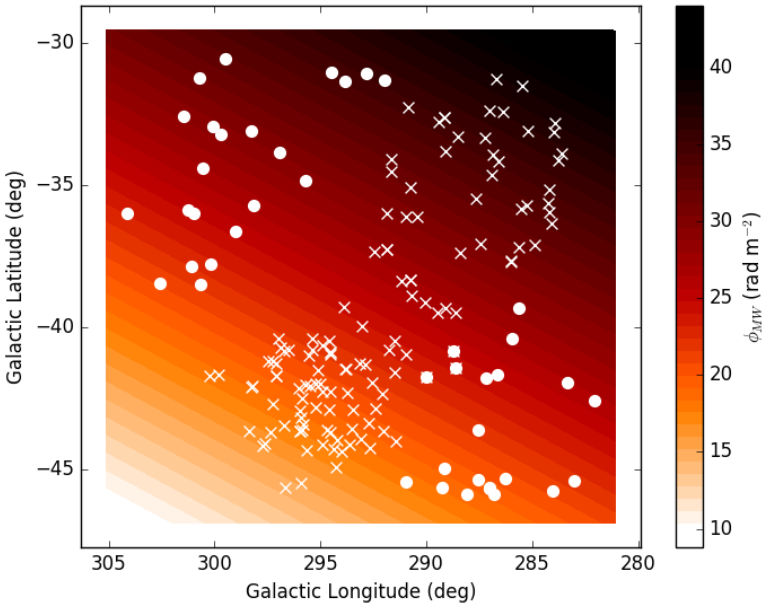

Figure 2.7: An estimation of the foreground- and background-ϕ covering our field of view, assuming the Faraday depth varies as a tilted plane across our imaged region. The fit used the 43 off-Bridge sources which are shown as white dots. The location of the on-Bridge sources are shown as white crosses.

2.5 THE LINE-OF-SIGHT MAGNETIC-FIELD STRENGTH

2.5.1 EMISSION MEASURES

Our objective is to calculate the line-of-sight magnetic field ($B_{\parallel}$) associated with the MB; however, $B_{\parallel}$ is degenerate with estimates of electron density (n_e). Therefore an independent estimate of n_e is required. By making some assumptions about the line-of-sight depth of the ionized medium, it is possible to use observed Hα intensities as a means to independently estimate n_e^2 by taking advantage of the implied emission measure (EM). The EM is defined as the integral of the square of the electron density along the pathlength of ionized gas (L_{H^+}) and can be derived from the measured Hα intensity ($I_{\mathrm{H}\alpha}$) in rayleighs (R)*

$$\mathrm{EM} = \int_0^L n_e(l)^2 dl = 2.75\, T_4^{0.92} I_{\mathrm{H}\alpha} \ \ \mathrm{pc\,cm^{-6}}. \tag{2.9}$$

We utilise the work carried out by the Wisconsin Hα Mapper (WHAM) survey (Haffner et al. 2003). Barger et al. (2013) offer kinematically resolved intensities of the Hα emission across our entire imaged region with sensitivities of a few hundredths of a rayleigh. WHAM has a 1° beam, which is equivalent to a diameter of nearly 1 kpc at the assumed average distance to the MB of 55 kpc. While the WHAM beam is considerably larger than the final resolution of our radio data, at this size it is less sensitive to small-scale Hα emission stemming from individual HII regions and is optimised to detect faint emission from diffuse ionized gas. For simplicity, we assume an electron temperature of $T_e = 10^4$ K (denoted T_4), as assumed in Barger et al. (2013). Figure 2.8 shows the MB region with white contours indicating levels of uncorrected Hα emission from the WHAM Northern Sky Survey (Haffner et al. 2003). Contours mark the 0.06, 0.15 and 1.0 R intensity levels.

Observed Hα intensities are reduced from their intrinsic values due to dust contained within the MB itself and in the MW. These are known as internal and foreground extinction, respectively. We have corrected for both sources of extinction according to Table 2 from Barger et al. (2013). We assume that the 'Join' and 'West' regions have similar interstellar- and local dust content – and therefore an identical total-extinction correction of 28% has been applied. Hα-intensity correction of 22% has been applied to all 'Wing' points. For all future analysis and discussion, Hα intensities have been extinction corrected, unless stated otherwise.

We cross-reference the position of each background polarized source with the WHAM data and accept the pointing with the smallest angular separation from our target as the representative Hα brightness for that particular sightline. Because the WHAM survey

*1 R $= (10^6/4\pi)$ photons cm^{-2} s^{-1} sr^{-1} which is equivalent to 5.7×10^{-18}erg cm^{-2}s^{-1} arcsec^{-2} for Hα.

of the MB is Nyquist sampled, the maximum angular separation allowed is less than 30 arcminutes, which corresponds to $\leq$ 500 pc at our assumed distance to the MB of 55 kpc. EMs are then derived towards each matched sightline. Mean EMs for each region are listed in Table 2.4.

2.5.2 Distribution of ionized Medium

In order to estimate the magnetic-field strength along the line-of-sight through the MB we assume that there is no correlation between electron density and magnetic-field strength. This has been shown to be a reasonable approximation for typical gas densities associated with the diffuse interstellar medium (Crutcher et al. 2003). Rearranging Equation 2.3, it can be shown that the equation for magnetic field along the line-of-sight becomes

$$B_{\parallel} = \frac{\phi_{\rm MB}}{0.812\,\overline{n_e}\,L_{H^+}}, \tag{2.10}$$

where $\phi_{\rm MB}$ is the MW-foreground corrected Faraday depth and $\overline{n_e}$ is the mean electron density along the total pathlength of ionized material (L_{H^+}).

Often, pulsar dispersion measures (DM $= \overline{n_e} L_{H^+}$) can be used to construct well-formed estimates of the pathlength and electron density through the different regions. Unfortunately, there are no known pulsars in the MB and very little is known about the morphology and line-of-sight depth of the MB.

Subramanian and Subramaniam (2009) argue that the SMC is nearly edge-on, indicating a pathlength through the galaxy of $\geq$ 5 kpc. If the bulk of the material in the MB had its origins in the SMC, one might expect the depth of the MB to be equally large. Muller et al. (2004) argue that there are numerous observations throughout the MB that hint at a large line-of-sight depth and Gardiner et al. (1994) estimate the pathlength through regions of the MB 5 kpc $\lesssim L \lesssim$ 10 kpc. For simplicity, we parameterise and evaluate the depth of the MB as $L_5 = 5$ kpc and consider the implications of different pathlengths through this parameter, with $1 \lesssim L_5 \lesssim 2$.

Several independent assumptions corresponding to the distribution and geometry of ionized- and neutral-gas can be made in order to validate our $B_{\parallel}$ measurements. Below, we describe three separate ionized gas distributions and discuss how each might affect derived magnetic-field strengths. In our discussion, all ionized parameters will be denoted with subscript H^+ and all neutral gas parameters will be denoted with subscript HI, unless otherwise noted.

Case 1: Constant Dispersion Measure

When estimating the line-of-sight magnetic field strength, the simplest model of the distribution of material in the MB is one in which the neutral and ionized gas are well-

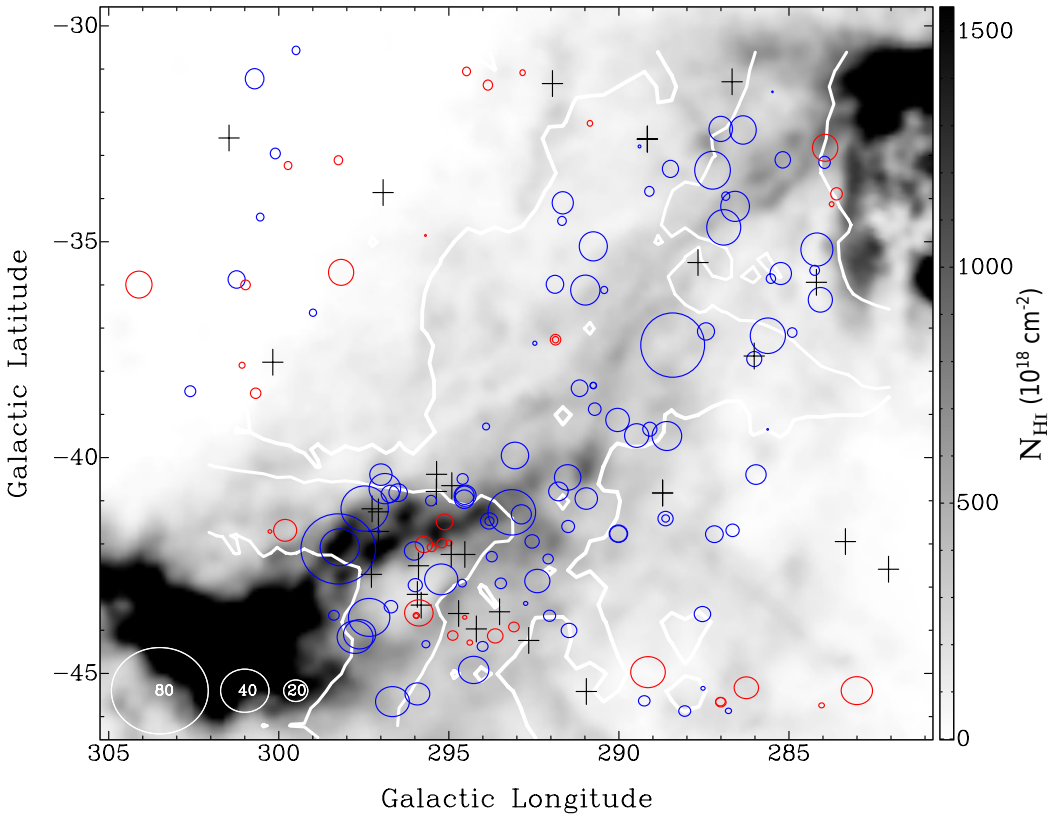

Figure 2.8: Neutral Hydrogen intensity from GASS (Kalberla et al. 2010) in the velocity range of $+100 \leq v_{\rm LSR} \leq +300\,{\rm km\,s^{-2}}$ overlaid with white contours representing non-extinction corrected Hα intensities of 0.06, 0.15 and 1.0 R as measured from WHAM (Barger et al. 2013). Circles represent the foreground-corrected Faraday depth ($\phi_{\rm MB}$) values towards each polarized background source. Red and blue circles represent a line-of-sight magnetic field oriented towards and away from the observer, respectively. Black crosses mark the existence of ϕ values that are consistent with zero to $2\times d\phi$.

mixed. In such a scenario, the bulk of the neutral gas would be distributed across the MB in small clumps, with the ionized medium distributed uniformly amongst the neutral clouds. Therefore, the effective depth of the ionized medium can be expressed as a fraction of the depth of the neutral material, $L_{H^+} = f L_{\rm HI}$, where $L_{\rm HI}$ is the depth of the neutral gas and f is the filling factor of ionized gas along the total line-of-sight (Reynolds 1991).

Little is known of the effective filling factor of ionized gas along the line-of-sight, but a filling factor of $f = 1$ is highly unlikely. Previous work on nearby high-velocity clouds in the Leading Arm (McClure-Griffiths et al. 2010) has assumed a filling factor of $f \sim 0.5$ to describe the distribution of the ionized gas and we assume the same value for our analysis. In Section 2.5.3, we briefly explore the implications of a range of filling factors. Combining the derived EM with our line-of-sight estimates, the DM becomes

$$\mathrm{DM} = (\mathrm{EM}\, f\, L_{\rm HI})^{1/2}. \tag{2.11}$$

Incorporating the above expression for DM with Equation 2.10, estimates of the magnetic field along the line-of-sight can be evaluated as

$$B_{\parallel} = \frac{\phi_{\rm MB}}{0.812\,(\mathrm{EM}\, f\, L_{\rm HI})^{1/2}}. \tag{2.12}$$

This assumption of the geometry of the ionized material in the MB is likely an oversimplification of the actual distribution, which is expected to vary as a function of position along the MB.

Case 2: Constant Regional ionization Fraction

In contrast to Case 1, where we estimated the effective pathlength of the ionized material, we now wish to estimate the free-electron content of a sightline using the ionization fractions (X) across the MB. In order to motivate this approach, a few assumptions must be made. Firstly, we assume that the bulk of the MB material is in the velocity range $+100 \leq v_{\rm LSR} \leq +300\,\mathrm{km\,s^{-2}}$ relative to the Galactic centre (Putman et al. 2003; Muller et al. 2003).

Following from the previous assumption, we also assume that the observed HI depth from GASS (Kalberla et al. 2010) in our selected velocity range probes the entire line-of-sight depth of the MB such that the ionization fraction of a region represents the sum of ionized material in the MB along a given sightline. Previous investigations into the MB have shown this assumption to be reasonable in the diffuse regions of the MB, where observation have shown there to be little dust content (Smoker et al. 2000; Lehner et al. 2008). However there have been observations of molecules in the 'Wing' region (Muller et al. 2004; Mizuno et al. 2006; Lehner et al. 2008) and this assumption will serve as

a lower limit to our estimates of neutral- and ionized-gas densities in this region. This second assumption indirectly implies $f \sim 1$ ($L_{\rm HI} \simeq L_{\rm H^+}$) since any reported ionization fraction is a reflective of the pathlength of neutral gas.

Following from these assumptions, the electron density is calculated simply as the ionization fraction multiplied by the neutral-gas density

$$\overline{n_e} = \frac{X \langle N_{\rm HI} \rangle}{f\, L_{\rm HI}}. \tag{2.13}$$

As with Case 1, the above expression has the underlying premise of $L_{\rm H^+} = f\, L_{\rm HI}$. It follows then that the DM can be written as

$$\mathrm{DM} = \frac{X \langle N_{\rm HI} \rangle}{f\, L_{\rm HI}} L_{\rm H^+} = 3.09 \times 10^{18}\, X \langle N_{\rm HI} \rangle, \tag{2.14}$$

where the constant 3.09×10^{18} is the conversion factor of pc to cm.

With an expression for the DM, it is now possible to estimate the magnetic field along the line-of-sight by combining Equations 2.10 and 2.14,

$$B_{\parallel} = 3.80 \times 10^{18} \left(\frac{\phi_{\rm MB}}{X \langle N_{\rm HI} \rangle} \right). \tag{2.15}$$

The MB is highly ionized with ionization fractions dependent upon location within the MB (Lehner et al. 2008; Barger et al. 2013). Barger et al. (2013) determined the minimum multiphase ionization fraction across the MB and argued that in the region of the diffuse MB, the ionization fraction ranges from $36 - 53\%$; whereas in the region of the 'Wing', the minimum ionization fraction is between $5 - 24\%$. Comparing column densities of various species along three sightlines corresponding to the 'Join' and 'West' regions, Lehner et al. (2008) showed that ionization fractions in the MB may be as high as 90%.

Motivated by the wide variability in ionization fractions, we choose to evaluate the ionization level of the various regions individually. In the region of the Wing, we compare the HI and Hα column densities from Table 3 in Barger et al. (2013), to calculate a multiphase ionization fraction of $\sim 20\%$ in the Wing. We evaluate the 'Join' and 'West' regions at an ionization fraction of 45%, which is within the minimum ionization range cited in Barger et al. (2013) and is half of the maximum ionization fraction reported in Lehner et al. (2008). Evaluation of this ionization level makes it simple to explore the range of possible magnetic field strengths.

In the region of the SMC-Wing, there is a clear variation of HI column densities as well as Hα intensities (Figure 2.8). Following Barger et al. (2013), we choose to break up the Wing into two regions corresponding to the relative Hα brightness. If a

sightline is associated with an uncorrected Hα brightness larger than 0.15 R, this region is classified as the 'Hα-Wing' and assigned a HI column density of 6.8×10^{20} cm^{-2}, else we consider the region to be the 'HI-Wing' and evaluate it as having a HI column density of 3.6×10^{20} cm^{-2}. A summary of region parameters is given in Table 2.4.

This assumed geometry of the distribution of ionized gas is similar to Case 1 (§2.5.2), in that it requires the neutral and ionized media to be well-mixed. However, in this model, our greatest approximation is the mean ionization fraction for a given region of the MB. Although not stated explicitly in Equation 2.15, this $B_\parallel$ estimate does have a dependence on the assumed pathlength of ionized material through the derivative of the total ionized mass of the region and subsequently implied X, which is outlined in Barger et al. (2013).

Case 3: ionized Skin

Ionising photons that have escaped the MW and the Magellanic Clouds have the potential to ionise the outer layers of the MB (Fox et al. 2005; Barger et al. 2013). In this possibility, the distribution of the thermal electrons is that of an ionized skin, rather than mixed with the neutral gas, as we assumed in Cases 1 and 2. In order to explore this third scenario, we assume that the neutral hydrogen is girt by a fully ionized skin at the same temperature and pressure, the density of which will be $\overline{n_e} = \overline{n_{\rm HI}}/2$ (Hill et al. 2009). This condition requires that the neutral and ionized media have had enough time to come into pressure equilibrium, which we assume for our analysis.

In the ionized skin, the line-of-sight depth can be derived from our density assumption combined with Hα brightnesses:

$$L_{H^+} = \mathrm{EM}\, n_e^{-2} = \mathrm{EM} \left(\frac{\overline{n_{\rm HI}}}{2} \right)^{-2} = 4\,\mathrm{EM} \left(\frac{f\, L_{\rm HI}}{\langle N_{\rm HI} \rangle} \right)^2, \tag{2.16}$$

where the discussion for the evaluation of n_e is given in the previous model (Equation 2.13). We can now combine Equation 2.16 with our density estimates (Equation 2.13) to find an expression for DM:

$$\mathrm{DM} = \frac{2\,\mathrm{EM}\, f^2\, L_{\rm HI}}{\langle N_{\rm HI} \rangle}. \tag{2.17}$$

Substituting this expression for DM into Equation 2.10, the equation for the magnetic-field strength along the line-of-sight in an ionized skin becomes

$$B_\parallel = \frac{\phi_{\rm MB}\, \langle N_{\rm HI} \rangle}{1.6\,\mathrm{EM}\, f^2\, L_{\rm HI}} \tag{2.18}$$

where the line-of-sight of the neutral medium is in units of cm.

In the case of an ionized skin, the pathlength of the ionized medium is expressed explicitly in terms of our two assumptions: firstly, that the neutral and ionized media

are in pressure equilibrium and secondly, that the filling factor of the neutral medium is $f_{\rm HI} \simeq 1$ along the effective depth of the MB. Therefore, we argue that for the above thin-skin approximation, $f \simeq 1$.

2.5.3 Summary and Comparison of ionization Cases

We evaluate each of the aforementioned cases for a line-of-sight pathlength of $L_{\rm HI} = L_5 = 5\,$kpc. As shown in Table 2.4 and Figure 2.9, each of the cases results in similar estimates in line-of-sight magnetic-field strengths for the entire MB, with median values all near $B_\parallel \simeq 0.3\,\mu$G. By comparison, individual regions show a larger scatter between derived magnetic-field strengths.

Our sample of Faraday depths is skewed towards the negative (as seen in Figure 2.8); therefore, it follows that the derived field strengths are distributed in kind. By completing a skewness test, we find that the $B_\parallel$ distribution resulting from Case 1 is skewed towards negative values with a $3.2\,\sigma$ confidence level. It follows that Case 2 is skewed negative to 1.7σ and Case 3 to 4.2σ significance. This skew can be seen most clearly in Figure 2.9. Due to this skew towards negative values, the $B_\parallel$ values quoted in Table 2.4 represent the median magnetic-field strengths, where the median statistic is more robust against outliers. Along with the median value, we list the deviation from the first and third quartile ($\mathcal{Q}_1$ and $\mathcal{Q}_3$, respectively), which represents the 25th and 75th percentile values in the distribution. The derived magnetic-field strengths are best summarised by Figure 2.9, where the bound region denotes the interquartile range (IQR), defined as IQR = $\mathcal{Q}_3 - \mathcal{Q}_1$.

As noted in our discussion of the ionization models, the largest uncertainty in our $B_\parallel$ measurements comes from the unknown geometry of the MB along the line-of-sight, namely the uncertainty in $L_{\rm H^+}, X$, and f. With that in mind, we aim to compare all models by their dependence on our depth assumptions and use of measured quantities.

Cases 1 and 2 are built from the same oversimplified picture of well-mixed neutral and ionized gas distributions along the line-of-sight. Case 1 uses only the measured EM with a largely unconstrained filling factor, f. Exploring a range of f for Case 1 shows that a 20% change in f (i.e. $0.3 \leq f \leq 0.7$) results in less than a $0.1\,\mu$G change in the median line-of-sight magnetic field strength. In contrast, Case 2 takes advantage of more information, using both calculated ionization fractions and measured $\langle N_{\rm HI} \rangle$. Contrasting these first two ionized gas distributions, Case 3 has the ionized material distributed as an ionized skin. This geometry requires that the neutral and ionized gas to be in pressure equilibrium in order to be physical. It is possible that this condition could be met in the 'Join' region; however, it is likely that this is inappropriate for regions in the 'Wing' due to ram-pressure effects.

(1) Region	(2) $\langle N_{\rm HI}\rangle$ ($\times 10^{20}$ cm^{-2})	(3) $\langle {\rm EM}\rangle^{\dagger}$ (pc cm^{-6})	(4) $\overline{\phi}_{MB}$ (rad m^{-2})	(5) $\sigma(\phi)$ (rad m^{-2})	(6) X (%)	(7) $B^{*}_{\parallel,1}$ (μG $L_5^{-1/2}$)	(8) $B^{*}_{\parallel,2}$ (μG)	(9) $B^{*}_{\parallel,3}$ (μG L_5^{-1})	(10) B_r (μG)
Join	3.0	0.283	-13.5	9.3	45	$-0.61^{+0.22}_{-0.41}$	$-0.43^{+0.19}_{-0.15}$	$-0.56^{+0.28}_{-0.57}$	0.10
West	2.8	0.603	-12.3	15.4	45	$-0.33^{+0.29}_{-0.44}$	$-0.28^{+0.23}_{-0.42}$	$-0.23^{+0.20}_{-0.25}$	0.84
Wing	5.0	0.823	-8.7	15.4	20	$-0.26^{+0.32}_{-0.45}$	$-0.33^{+0.26}_{-0.51}$	$-0.27^{+0.21}_{-0.57}$	1.0
– HI Wing	3.6	0.295	-8.1	12.5	20	$-0.39^{+0.44}_{-0.40}$	$-0.97^{+1.1}_{-0.82}$	$-0.44^{+0.48}_{-0.50}$	
– Hα Wing	6.8	1.69	-9.7	19.1	20	$-0.06^{+0.14}_{-0.32}$	$-0.08^{+0.17}_{-0.39}$	$-0.08^{+0.17}_{-0.36}$	
Total						$-0.34^{+0.33}_{-0.45}$	$-0.34^{+0.33}_{-0.36}$	$-0.28^{+0.27}_{-0.46}$	

Table 2.4: Table of derived values for polarized sources in all regions of the MB. Column (1) specifies the region of interest, column (2) gives the average HI column density for the region as measured from GASS (Kalberla et al. 2010) and column (3) gives the average extinction-corrected EM from the WHAM dataset (Barger et al. 2013). The mean foreground-corrected Faraday depth is given in column (4). Column (5) gives the standard deviation of the foreground-corrected Faraday depth of the region about the mean. The average ionization fraction for the region, as determined by (Barger et al. 2013), is listed in column (6). Columns (7 - 9) give the median coherent magnetic-field strength along the line-of-sight for each of the ionization geometries discussed in Section §2.5.2. The errors listed represent the deviation from the 25th and 75th percentiles. The implied random magnetic-field strength, as calculated from Equation 2.19 is given in column (10).

We show that Case 2 has least dependence on an assumed pathlength through the MB and filling factor. As we mentioned in §2.5.2, the actual ionization fractions across the MB may be higher than our evaluated estimates. Increasing the ionization fraction by a factor of two implies that the line-of-sight magnetic field strength is half the current value – i.e. $B_{\parallel}(X = 90\%) \simeq -0.17\,\mu$G. The following discussion will be carried out using the magnetic field estimates derived from Case 2 and all parameters reported in Table 2.4, unless specified otherwise.

2.6 DISCUSSION

In this section, we consider the implications of the observed Faraday-depth values and magnetic-field strengths in the MB and explore possible origins of the coherent magnetic structure.

2.6.1 THE TURBULENT MAGNETIC FIELD

On-going star-formation in the MB (e.g. Noël et al. 2015) will make any existent regular magnetic field to become turbulent and random. An increase in random motion would also depolarize any background polarized light, proportional to the level of turbulence. If the magnetic field observed in the MB were sufficiently turbulent, one would expect that the polarization of sources associated with the MB would exhibit higher levels of depolarization, and thus have lower values for the observed fractional polarization.

We explore the consequences of the turbulent field by comparing the observed polarization fraction for populations of sources on and off the MB. Figure 2.10 shows a cumulative histogram comparing the observed polarization fractions. We choose not to include sources associated with the 'Wing' region due to the source selection bias that favours highly-polarized sources. The two source populations show no statistically-significant differences in the observed fractional polarization, indicating there is no correlation between source location and turbulence of the foreground magnetic field.

If the turbulence in the field is not strong enough to depolarize the background signal completely, it is still possible to investigate the mean Faraday dispersion (σ_ϕ) as fitted by our qu-fitting routine. We compare the values for sources on-Bridge and off-Bridge, under the hypothesis that sources on the MB would exhibit higher σ_ϕ if there are more coherent and/or turbulent cells located in the MB when compared to the MW. Figure 2.11 shows a cumulative histogram of the best-fit Faraday dispersion values for all points on and off the MB. We carry out a two-sample Anderson-Darling test with both σ_ϕ populations and find that we cannot reject the null-hypothesis of the two samples being drawn from the same distribution and conclude that any turbulence in the MB magnetic field cannot be differentiated from that in the MW.

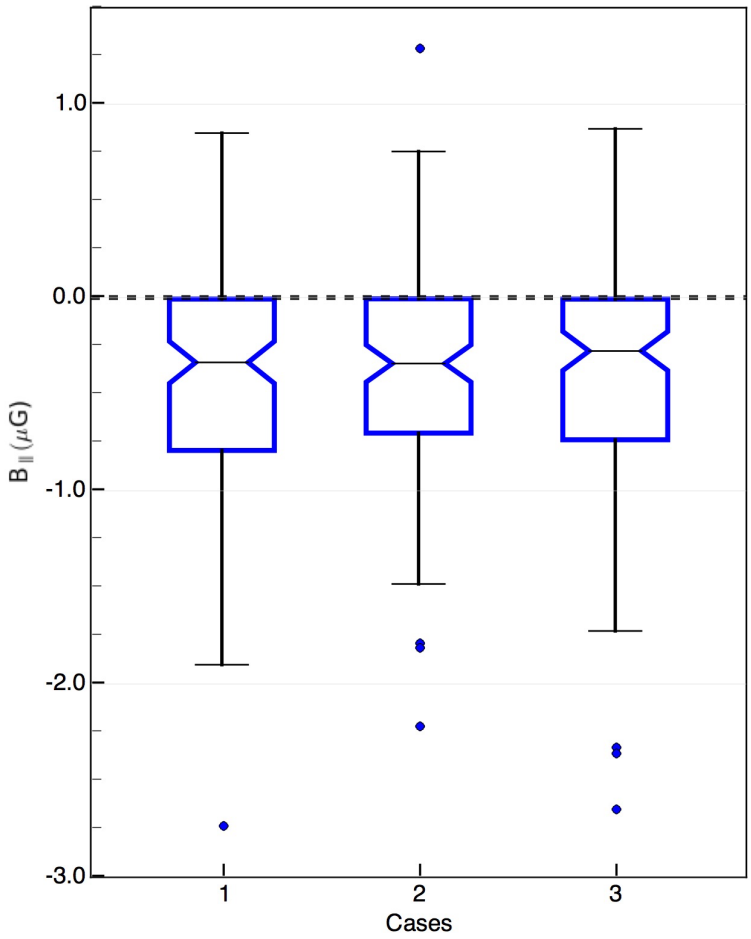

Figure 2.9: Box-and-whisker plots of coherent line-of-sight magnetic field measurements towards all sightlines through the MB for all cases listed in §2.5.2. The height of each box marks the IQR of each distribution while notches mark the median position. The caps at the end of the whiskers represent the 5th and 95th percentiles. The outliers in each population are shown as dots above and below the whiskers. There is a dashed line at $B_{\parallel} = 0$ to clarify the distribution of positive and negative magnetic field orientations.

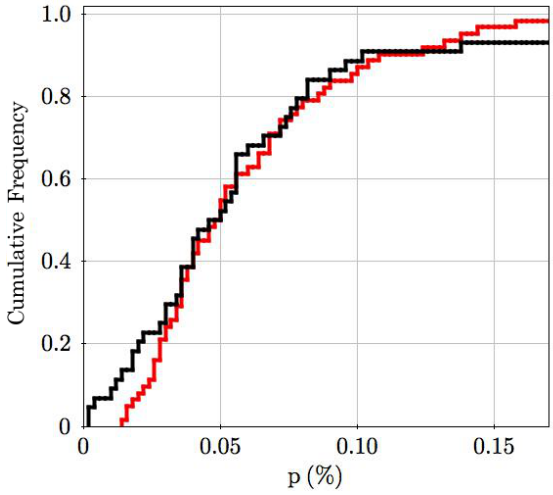

Figure 2.10: Cumulative histogram comparing observed polarization fractions (p) for sources on (red) and off the Bridge (black). Sources associated with the 'Wing' region are not included in this distribution due to the source selection bias towards sources with high polarization. This figure has been truncated at $p = 17\%$ for clarity.

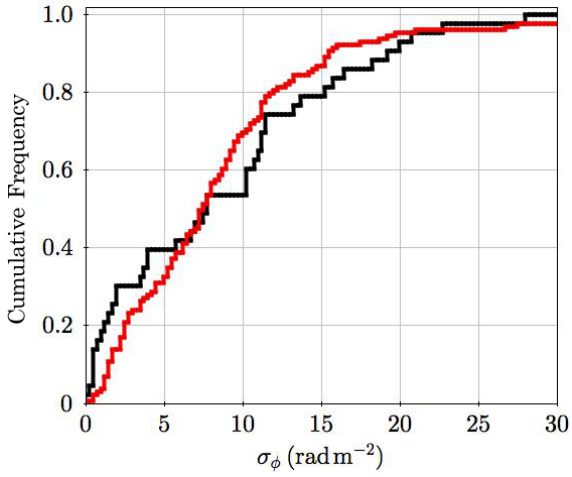

Figure 2.11: Cumulative histogram of best-fit Faraday-dispersion values (σ_ϕ) fitting to a single, simple Faraday-rotating source with foreground depolarization for sources on (red) and off the Bridge (black). The figure has been truncated at $\sigma_\phi = 30\,\mathrm{rad\,m^{-2}}$ for clarity.

In the MW, LMC and SMC, it has been shown that the random component of the magnetic field dominates the total field strength (Beck 2000; Gaensler et al. 2005; Mao et al. 2008). To estimate the random magnetic-field strength, we choose a similar approach to Mao et al. (2008), who assume that the coherent magnetic field does not change as a function of position, but that any change in observed ϕ is due to turbulence. It is then possible to estimate the mean random magnetic-field strength for each observed region as

$$B_r = \frac{3l_0}{L_5}\sqrt{\left(\frac{\sigma(\phi)}{0.812\,\overline{n_e}\,l_0}\right)^2 - \left(\frac{B_\parallel^*\,\Delta L}{l_0}\right)^2}, \tag{2.19}$$

where $\sigma(\phi)$ is the standard deviation of Faraday depths in the region of interest, $\overline{n_e}$ is the average electron density in units of cm^{-3} and $B_\parallel^*$ is the median coherent magnetic-field strength along the line-of-sight in μG. ΔL is the standard deviation of the pathlength through the ionized medium in pcs and characterises the uncertainty in the depth of the MB. l_0 is the linear scale of a 'RM-cell' in units of pc, such that $n \sim L_5/l_0$, where n is the number of cells in a single line-of-sight.

As stressed in our derivation of the coherent magnetic-field strength, little is known about the morphology of the MB, leaving the estimations for pathlength to be our largest uncertainty. We estimate the standard deviation of the width of the MB (ΔL) to be 1 kpc. Gaensler et al. (2005) show that RM-cells in the LMC are of order $\sim$ 100 pc, and we adopt a similar value for our analysis. As we have done in Case 2 (§2.5.2), we consider $\overline{n_e}$ to be related to the column density of HI as $\overline{n_e} = (X\,\langle N_{\rm HI}\rangle)/L_5$ where L_5 is the line-of-sight depth of the MB in cm and X is the ionization fraction of the region.

As discussed in Section §2.4.1, our correction for the foreground MW Faraday depth does not account for the intrinsic Faraday depth of the source. We minimise any resultant effects by subtracting the scatter of intrinsic extragalactic Faraday depths $\sigma(\phi) = 6$ rad m^{-2} (Schnitzeler 2010) from our regional Faraday depth standard deviations.

Using the above estimates and the values listed in Table 2.4 we derive the implied random magnetic-field strengths of each region, the results of which are summarised in Table 2.4. We find that the turbulent field dominates the ordered component in the regions of the 'Wing' and 'West'. Intriguingly, this does not hold in the 'Join' region. Perhaps this is indicative that our pathlength estimates, are unrealistic or that our overarching assumptions are unviable. However, the 'Join' region is furthest from any ongoing star-formation. This fact, combined with with our aforementioned turbulence null-hypotheses, suggests that the random field may not dominate the large-scale magnetic field in the diffuse MB.

[†]The mean EM is not used in the derivation of magnetic-field strengths. It is listed to give the reader an appreciation of the characteristics of the region.

2.6.2 Estimating the Total Magnetic Field of the Wing

Recent work by Lobo Gomes et al. (2015) mapped coherent field lines in the plane-of-the-sky ($B_{c,\perp}$) in the SMC and Wing using optical polarized starlight. They argued that there exists a significant fraction of sightlines that exhibit a magnetic field that points in the direction of the MB towards the LMC of order $B_\perp = (0.947 \pm 0.079)\,\mu$G.

We combine their measurements with our estimations for $B_\parallel$ to estimate the total coherent magnetic-field strength ($B_{c,T}$) in the Wing

$$B^2_{c,T} = B^2_{c,\perp} + B^2_{c,\parallel}. \tag{2.20}$$

We find an implied total magnetic-field strength of $B_{c,T} \simeq 1\,\mu$G in the region of the Wing which implies that the ordered magnetic field in the Wing is dominated by the plane-of-the-sky component. We note that our error estimates imply a large range of coherent field strengths and omit their inclusion with this discussion. This field strength is within the range of magnitudes expected if the field were to have originated from the SMC as Mao et al. (2008) estimated total coherent magnetic field in the SMC to be $B_T \simeq 1.7 \pm 0.4\,\mu$G.

2.6.3 The Pan-Magellanic Field

The possible existence of a large-scale magnetic field that permeates the entire Magellanic System (the 'pan-Magellanic field', pM field) was first introduced by Mathewson and Ford (1970b) and Schmidt (1970). Furthermore, Schmidt (1970) argued that the existence of such a field suggested that the fields observed in the LMC and SMC shared a common origin. Continued investigations into the nature of the magnetism across Magellanic System were carried out (e.g. Schmidt 1976; Mathewson et al. 1979; Wayte 1990) strengthening the case for the existence of the pM field. More recently, Mao et al. (2008) and Lobo Gomes et al. (2015) note the potential alignment of the SMC magnetic field with the MB, and Mao et al. (2012) argue the same for the LMC. However, all previous research has been confined to high density regions in the LMC and SMC.

If the pM field exists, it is expected to be dominated by the plane-of-the-sky component, just as the fields associated with the LMC and SMC have been observed to be (Mao et al. 2012; Lobo Gomes et al. 2015). However, the observation of negative Faraday depths across the MB implies a non-trivial line-of-sight component. We argue that this directional component was anticipated, as the SMC is located further away from the MW than the LMC (~ 60 and ~ 50 kpc, respectively Walker 1999). Therefore, our observation of a Faraday-depth signal spanning the entirety of the MB may be the first direct evidence of the pan-Magellanic field.

Before we can confirm the existence of the pan-Magellanic field, it is important to

understand if the coherent fields associated with the SMC and LMC can account for the observed Faraday depth signal seen to span the entire MB. Below we investigate the possible origins of the observed coherent magnetic field and how it might relate to the 'pan-Magellanic field' hypothesis. We assume that the observed magnetic field has been frozen in to the tidally-stripped gas for this discussion, and address any evidence towards the contrary at the end of this section.

The SMC-Wing Field

Mao et al. (2008) estimate that the SMC has a line-of-sight and total magnetic-field strength of $B_{\parallel} = -0.19 \pm 0.06$ and $B_{Tot,C} = 1.6 \pm 0.4\,\mu$G, respectively. All ionization models discussed in our paper imply a line-of-sight magnetic-field strength that is consistent with this estimate in the 'Wing' region, within the IQR (Table 2.4). We note that our median value of $-0.39\,\mu$G is twice what was observed in the SMC; however, our estimates are again based largely on the assumed geometry of the MB. If the MB is oriented predominantly along the line-of-sight, as is the orientation of the SMC, then the ionized pathlength would be larger than L_5. Doubling the line-of-sight depth through the Bridge ($2L_5$) results in a decreased estimated magnetic-field strength of $-0.33\,\mu$G, a value that deviates from the mean SMC magnetic-field strength by 1.1σ (Mao et al. 2008).

If the SMC magnetic field is responsible for the observed MB field, it is also possible to estimate the expected MB ϕ signal. Using Case 1 (§2.5.2) and an average pathlength of $\overline{L} = L_5$, a filling factor of $f = 0.5$ and estimates of the average electron density from the EMs from Table 2.4, a coherent line-of-sight magnetic field of $B_{\parallel}$ would manifest itself as a Faraday depth of $\phi \sim -7$ and $-4\,\mathrm{rad\,m^{-2}}$ in the 'Wing' and 'Join' regions, respectively. This approximation is roughly consistent with the observed median ϕ in the Wing, but appears to contradict the mean Faraday depth measured in the 'Join' region, which returns an average Faraday depth that has a magnitude more than 3 times the expected value ($\overline{\phi}_{MB} = 12.5\,\mathrm{rad\,m^{-2}}$). To achieve the observed mean Faraday depth in the 'Join' region with the SMC $\overline{B_{\parallel}}$ requires an effective pathlength of $\sim 27\,$kpc, which is unlikely to be physical.

This contradiction can be accounted for if the orientation of the magnetic field changes as a function of position along the MB. If in the 'Join' region, the coherent field has been rotated such that a larger fraction of the total field lies along the line-of-sight, one would observe a larger ϕ_{MW} and derive a stronger $B_{\parallel}$. Indeed, this is what is observed in the 'Join' region.

We argue that the magnetic field present in the 'Wing' region is consistent with a field that was created in the SMC and pulled into the MB. It is possible that the inherited field stretches as far as the 'Join' region. However, it requires that the turbulent field to be less significant than that associated with the 'Wing' region. It is then plausible that the pan-

Magellanic field is governed by the geometry of the coherent field in the SMC. We do not extend this analysis to the 'West' region as the field associated with this region is possibly an extension from the LMC rather than the SMC. We now explore this possibility.

The LMC-West Field

Figure 2.8 shows a nearly consistent, negative ϕ-value in the region nearest the LMC. Leading to this region, Gaensler et al. (2005) show the bulk of the polarized sources in the nearest portion of the LMC also have negative RM-values[‡] after MW-foreground correction. Contrasting this, the majority of the RMs associated with the LMC have positive values.

In the plane-of-the-sky magnetic field, both Wayte (1990) and Mao et al. (2012) note that there are regions of the LMC where the magnetic field appears to align with the direction towards the SMC.

If the MB-field is built from the magnetized material that originated in both Magellanic Clouds, the LMC contribution is likely associated with the tidal filaments ($l \simeq 285.7, b \simeq -33.7$), first identified by Haynes et al. (1991). Mao et al. (2012) estimate that the tidal filaments stemming from the LMC have a magnetic-field strength of $B_T = 11\,\mu$G. They argue that the similar magnitude of off-source and on-source Faraday depths signifies that the line-of-sight magnetic field in this region is negligible.

We measure an average $\overline{\phi}_{MB} = -21\,\mathrm{rad\,m^{-2}}$ in the region of the filament discussed above. Although we have fewer off-source points, we find a scatter of the nearest 10 sources to be $\sigma \sim 2\,\mathrm{rad\,m^{-2}}$. For there to be no line-of-sight magnetic field in this region, the average electron density would have to be zero, which is unphysical. We estimate the $B_\parallel$ of the tidal filament using the same estimated pathlength as Mao et al. (2012), $L_{H^+} = 800\,$pc and Case 1 (§2.5.2). The implied line-of-sight magnetic field in this region is $B_\parallel = 1.2\,\mu$G, a value that is twice as strong as our initial estimates ($L_{H^+} = fL_5$) for the same region.

This exercise demonstrates two things: firstly, it is possible that the Faraday depth values we see in the region nearest the LMC could be a consequence of a coherent magnetic field having been stripped from the LMC. Secondly, with different pathlength estimates, the magnetic field contribution from the LMC could be much higher than our initial estimates, implying a stronger total magnetic field strength in the MB.

Does the pan-Magellanic Field Exist?

We have discussed the implications of the known magnetic fields of the SMC and LMC as they pertain to our observed $\phi_{\rm MB}$ and $B_{\parallel,MB}$ in an attempt to justify the assumption

[‡]Previous studies explicitly use the term rotation measure (RM), rather than Faraday depth, to express the magnitude of observed Faraday rotation.

that the observed MB magnetic field originated from both galaxies. We posit that the dominant magnetic field component is in the plane of the sky, a claim that is consistent with what has been previously argued in all discussions of the pan-Magellanic field.

However, the previous discussions and implications of the SMC- and LMC magnetic fields assumed that the observed MB field is a combination of magnetic fields that have been drawn out of the LMC and SMC. Below, we briefly explore if the observed coherent field in the MB could have been formed in situ.

The $\alpha - \omega$ dynamo – which is believed to be the mechanism responsible for the observation of coherent magnetic fields on the scales of galaxies – requires too large a timescale to explain the existence of a coherent field in the young MB. By comparison, the cosmic-ray driven dynamo works on much shorter timescales. However, both of these dynamos require there to be differential rotation in the MB, which has not been observed. Therefore, these mechanisms cannot be responsible for the magnetic field in the MB. By contrast, the typical amplification time of the fluctuating dynamo is $10^6 - 10^7$ yr, a timescale that is favourable given the age of the MB. However, this mechanism creates turbulent or incoherent magnetic fields and cannot be responsible for the observed ordered field in the MB.

While we do not address the origins of the magnetic fields in the LMC and SMC, the standard magnetic-field creation mechanisms cannot explain the existence of a coherent magnetic field in the young tidal remnant. We therefore conclude that the magnetic field in the MB is a consequence of field lines having been dragged out of the LMC and SMC with an overarching field geometry that has been determined by the orientation of the parent galaxies. This shared magnetic history links the two Magellanic Clouds and establishes the existence of the pan-Magellanic field.

All previous detections of tidal bridges with corresponding polarization have been detected through polarized continuum emission emanating from tidal regions (e.g. Condon et al. 1993; Nikiel-Wroczyński et al. 2013a Nikiel-Wroczyński et al. 2013b). Our detection of a coherent magnetic field in the MB was made using Faraday rotation observations through a non-continuum foreground, and is the first ever such detection for any tidal bridge. This may imply that magnetic fields are an early influence on the evolution of galaxy interactions. If magnetic fields do affect early galaxy interactions, the existence of magnetic fields in tidal remnants could explain the observation of coherent magnetic fields in tidal dwarfs (Nikiel-Wroczyński et al. 2013b) and would suggest the existence of magnetic fields in more diffuse tidal features, such as the Magellanic Stream and Leading Arm.

2.7 SUMMARY

We have presented Faraday rotation data for 167 extragalactic polarized sources and observe a coherent magnetic field towards the MB. Each source in our catalogue has well-determined polarization ($\mathcal{P} \geq 8\sigma_{\mathcal{P}}$). Using a Monte Carlo Markov Chain approach to fitting observed complex polarization spectra, we were able to recover the polarization parameters of each source to high confidence.

We have demonstrated that the observed Faraday depths of sources 'on' and 'off' the MB are inherently different and have attributed this disparity to the existence of a large-scale, coherent magnetic field within the MB. We assumed a line-of-sight depth through the MB of 5 kpc and explored different distributions of ionized gas. The median line-of-sight magnetic field derived from these approximations are all consistent with $B_{\parallel} \simeq 0.3\,\mu$G, where the uniform field is directed away from us. We stress that little is known about the distribution of ionized gas within the MB and the implied magnetic field is dependent upon this constraint.

The MB is a tidal remnant that we argued has no known means for creating a coherent field on the scales observed. Therefore, we concluded that the magnetic fields of the LMC and SMC have been tidally stripped along with the neutral gas emanating from these galaxies to form the MB. The implied line-of-sight magnetic-field strength in the MB region nearest the SMC, which is where the majority of the gas of the MB is believed to have originated, is consistent with observed line-of-sight component of this galaxy. We have argued that the magnetic field associated with the LMC and its polarized filaments has also been pulled into the MB and are likely responsible for the observed Faraday-rotation in the region nearest these features.

This work represents the first observational confirmation of the pan-Magellanic field – a coherent magnetic field spanning the entirety of the MB with a history and evolutionary fate that is tied to that of the Magellanic System.

A1: TABLE OF SYMBOLS

Table 2.5: List of symbols used in this chapter and their meaning.

Symbol	Physical Quantity
$B_{\parallel}$	measured magnetic-field strength along the line-of-sight in units of μG
$B^{*}_{\parallel}$	median magnetic-field strength along the line-of-sight in units of μG
$B_{c,T}$	total coherent magnetic-field strength, in units of μG
B_r	random magnetic-field strength, in units of μG
DM	measured dispersion measure for a specific sightline in units of pc cm^{-3}
$\langle$EM$\rangle$	average emission measure for specified region, in units of pc cm^{-6}
EM	measured emission measure along a specific sightline, pc cm^{-6}
f	volume filling factor of gas such that the effective pathlength of gas with a characteristic density n_0 is $f \times n_0$
X	ionization fraction
I, Q, U, V	observed Stokes parameters, with units of mJy
$I_{\mathrm{H}\alpha}$	intensity of Hα emission, with units of rayleighs
L_5	5000 pc. The nominal line-of-sight depth of the MB.
L_{HI}	estimated line-of-sight depth of neutral hydrogen, in units of pc
$L_{\mathrm{H^+}}$	estimated line-of-sight depth of ionized material, in units of pc
$\Delta\, L$	estimated standard deviation in line-of-sight depth of the MB, in units of pc
IQR	inter-quartile range, defined as the range of values between the 25th and 75th percentiles
l_0	typical cell size along line-of-sight, in units of pc
λ^2	the square of the observed wavelength, in units of m^2
$\langle N_{\mathrm{HI}}\rangle$	average HI column density, in units of cm^{-2}
$\overline{n_{\mathrm{HI}}}$	average neutral-gas density, calculated as $\langle N_{\mathrm{HI}}\rangle / L_{\mathrm{HI}}$ in units of cm^{-3}
$\overline{n_e}$	average free electron density, in units of cm^{-3}
$\mathcal{P}$	polarized intensity in units of mJy/beam
p	observed polarized fraction
p_0	intrinsic polarized fraction
ϕ_{corr}	Faraday depth for which the foreground, MW contribution has been subtracted, in rad m^{-2}
ϕ_{MB}	Faraday depth of the MB, in units of rad m^{-2}
ϕ_{obs}	observed Faraday depth in units of rad m^{-2}
$d\phi$	error estimate in ϕ from fitting algorithm, qu-fitting , in units of rad m^{-2}
$\overline{\phi}$	mean Faraday depth in units of rad m^{-2}
σ^2_{ϕ}	variance of Faraday depths on scales smaller than the synthesised beam, in rad m^{-2}
$\sigma(\phi)$	standard deviation of an ensemble of Faraday depth values for a specified region, in rad m^{-2}
Ψ	observed polarization angle, defined as $0.5\, arctan\frac{U}{Q}$
Ψ_0	intrinsic polarization angle at the source of emission
$\mathcal{Q}_1$, $\mathcal{Q}_2$	first and third quartile, defined as the 25th and 75th population percentile value
RM	the classical rotation measure, defined as $(\Psi_0 - \Psi)/\lambda^2$, in units of rad m^{-2}

$\sigma_{\mathcal{P}}$	rms error in extracted polarized intensity, in units of mJy b^{-1}
q, u	fractional linear polarized Stokes Q and U parameters, units of per cent
T_4	assumed temperature of 10^4 K for the ionized medium

TABLE OF DERIVED FARADAY DEPTHS

Table 2.6: Table of the Faraday depth values for each polarized source used in our analysis. Sources proceeded by a '*' indicate targets that are considered to be off the Bridge, whereas those without an asterisk are considered to be on-Bridge sources. Columns 1 and 2 give the position of the source in galactic longitude and latitude. Columns 3-6 lists the best-fit values returned from the $q - u$ fitting routine, namely the intrinsic polarization fraction, intrinsic polarization angle, observed Faraday depth and Faraday dispersion. Each of the the uncertainties represents the 1σ standard deviation in parameter space. Column 7 lists the corresponding Faraday depth of each source once the Faraday rotation due to the Milky Way foreground has been corrected for. The uncertainty calculation for this value is described in detail §4.1.

l (°)	b (°)	p_0 (%)	Ψ_0 (°)	ϕ_{raw} (rad m^{-2})	σ_ϕ (rad m^{-2})	$\phi_{\rm corr}$ (rad m^{-2})
* 282.073	-42.586	0.025 ± 0.001	10.5 ± 2.7	24.9 ± 1.5	0.9 ± 0.8	-1.2 ± 1.5
* 283.003	-45.398	0.068 ± 0.001	3.1 ± 0.7	47.9 ± 0.5	11.0 ± 0.5	25.9 ± 0.5
* 283.340	-41.945	0.043 ± 0.001	44.0 ± 1.9	24.2 ± 1.1	1.0 ± 0.9	-2.0 ± 1.1
283.601	-33.891	0.078 ± 0.004	0.9 ± 2.7	47.8 ± 1.5	10.0 ± 1.3	11.4 ± 1.6
283.747	-34.130	0.097 ± 0.005	94.9 ± 2.1	40.6 ± 1.2	7.5 ± 1.5	4.6 ± 1.2
283.937	-32.823	0.045 ± 0.001	3.8 ± 0.6	62.7 ± 0.5	9.0 ± 0.4	25.0 ± 0.6
283.953	-33.160	0.060 ± 0.002	16.5 ± 1.9	25.9 ± 1.1	1.1 ± 1.0	-11.3 ± 1.1
* 284.041	-45.740	0.044 ± 0.001	6.2 ± 1.0	25.7 ± 0.7	16.6 ± 0.4	4.6 ± 0.7
284.078	-36.344	0.073 ± 0.004	19.9 ± 2.5	10.2 ± 1.5	11.6 ± 1.1	-22.9 ± 1.5
284.178	-35.180	0.072 ± 0.002	14.7 ± 1.6	3.8 ± 0.9	1.3 ± 1.1	-30.7 ± 0.9
284.193	-35.940	0.032 ± 0.002	93.9 ± 2.2	32.5 ± 1.6	9.7 ± 1.5	-1.0 ± 1.6
284.245	-35.661	0.162 ± 0.015	118.6 ± 4.0	24.6 ± 2.3	13.3 ± 1.6	-9.3 ± 2.4
284.904	-37.103	0.070 ± 0.008	121.7 ± 5.4	22.8 ± 3.2	14.4 ± 1.8	-8.9 ± 3.2
285.180	-33.102	0.053 ± 0.004	43.2 ± 2.9	21.4 ± 1.9	14.5 ± 1.2	-15.2 ± 1.9
285.244	-35.736	0.060 ± 0.003	16.8 ± 1.9	12.8 ± 1.0	5.9 ± 1.6	-20.4 ± 1.1
285.485	-31.527	0.334 ± 0.009	44.5 ± 1.2	37.0 ± 0.7	7.5 ± 0.7	-1.5 ± 0.7
285.532	-35.854	0.133 ± 0.006	42.2 ± 2.0	24.0 ± 1.1	8.0 ± 1.1	-8.9 ± 1.1
285.621	-37.178	0.132 ± 0.007	122.4 ± 2.5	-1.7 ± 1.4	11.6 ± 1.0	-32.9 ± 1.4
* 285.625	-39.347	0.064 ± 0.001	143.9 ± 0.6	26.8 ± 0.3	13.9 ± 0.2	-1.6 ± 0.3
* 285.970	-40.392	0.075 ± 0.007	87.3 ± 3.6	8.7 ± 2.0	7.4 ± 2.6	-18.2 ± 2.0
286.019	-37.718	0.049 ± 0.002	134.3 ± 1.9	16.3 ± 1.4	15.6 ± 0.8	-14.0 ± 1.4
286.022	-37.647	0.248 ± 0.011	12.3 ± 2.9	27.5 ± 1.4	2.5 ± 1.9	-2.9 ± 1.4

Table 2.6 continued...

l (°)	b (°)	p_0 (%)	Ψ_0 (°)	ϕ_{raw} (rad m^{-2})	σ_ϕ (rad m^{-2})	$\phi_{\rm corr}$ (rad m^{-2})
* 286.253	-45.332	0.400 ± 0.035	177.6 ± 7.5	40.6 ± 3.4	3.6 ± 2.5	20.2 ± 3.4
286.352	-32.410	0.158 ± 0.018	147.1 ± 4.2	10.6 ± 2.0	8.8 ± 2.4	-26.3 ± 2.1
286.582	-34.181	0.047 ± 0.001	154.4 ± 0.7	6.6 ± 0.4	1.3 ± 1.0	-27.9 ± 0.5
* 286.660	-41.685	0.101 ± 0.002	118.0 ± 1.1	13.3 ± 0.6	1.8 ± 1.3	-11.6 ± 0.6
286.672	-31.294	0.291 ± 0.013	124.5 ± 2.4	42.8 ± 2.3	30.6 ± 0.9	4.6 ± 2.3
* 286.782	-45.866	0.076 ± 0.001	109.4 ± 0.8	14.4 ± 0.4	3.5 ± 1.1	-5.1 ± 0.4
286.858	-33.944	0.082 ± 0.006	150.3 ± 3.1	26.9 ± 1.6	6.9 ± 2.1	-7.8 ± 1.6
286.919	-34.667	0.324 ± 0.024	71.1 ± 3.2	0.9 ± 1.7	11.5 ± 1.3	-32.9 ± 1.8
* 287.005	-45.668	0.114 ± 0.001	89.0 ± 0.4	28.2 ± 0.2	0.5 ± 0.4	8.6 ± 0.2
287.005	-32.386	0.070 ± 0.002	175.3 ± 2.1	13.3 ± 1.1	1.3 ± 1.1	-23.3 ± 1.1
* 287.015	-45.653	0.117 ± 0.001	88.9 ± 0.4	27.6 ± 0.2	3.8 ± 0.5	7.9 ± 0.2
* 287.195	-41.776	0.070 ± 0.006	73.3 ± 3.8	9.0 ± 2.3	10.9 ± 2.0	-15.5 ± 2.3
287.249	-33.344	0.094 ± 0.003	130.9 ± 1.3	0.2 ± 0.7	11.5 ± 0.5	-35.0 ± 0.8
287.439	-37.078	0.042 ± 0.001	160.9 ± 1.4	14.4 ± 0.8	9.6 ± 0.7	-16.0 ± 0.8
* 287.529	-45.345	0.058 ± 0.001	150.2 ± 1.0	16.2 ± 0.7	13.4 ± 0.4	-3.5 ± 0.7
* 287.545	-43.624	0.087 ± 0.002	3.8 ± 1.0	7.9 ± 0.6	10.3 ± 0.5	-14.0 ± 0.6
287.675	-35.482	0.118 ± 0.007	159.4 ± 2.6	31.1 ± 1.6	12.4 ± 1.1	-1.3 ± 1.6
* 288.067	-45.870	0.111 ± 0.002	146.6 ± 1.2	9.0 ± 0.7	0.9 ± 0.8	-9.8 ± 0.7
288.421	-37.393	0.067 ± 0.003	164.6 ± 2.3	-30.1 ± 1.3	4.7 ± 2.2	-59.6 ± 1.3
288.484	-33.311	0.139 ± 0.008	111.5 ± 4.0	18.8 ± 2.1	2.3 ± 1.9	-15.9 ± 2.2
288.589	-39.501	0.017 ± 0.001	81.8 ± 3.1	-0.2 ± 1.8	2.9 ± 2.2	-26.9 ± 1.8
* 288.627	-41.413	0.084 ± 0.004	133.5 ± 2.1	17.5 ± 2.0	28.2 ± 1.0	-6.8 ± 2.0
* 288.715	-40.820	0.964 ± 0.027	10.7 ± 4.8	22.5 ± 4.3	32.5 ± 1.1	-2.5 ± 4.3
289.090	-39.342	0.127 ± 0.006	49.2 ± 2.1	13.8 ± 1.2	8.2 ± 1.2	-12.9 ± 1.2
289.105	-33.833	0.048 ± 0.004	30.0 ± 3.7	24.6 ± 2.6	15.7 ± 1.9	-9.1 ± 2.6
* 289.145	-44.971	0.080 ± 0.007	174.8 ± 4.8	48.2 ± 4.1	18.4 ± 2.1	28.8 ± 4.1
289.161	-32.618	0.112 ± 0.007	28.2 ± 2.5	37.1 ± 1.3	6.9 ± 1.8	1.8 ± 1.3
289.167	-32.625	0.111 ± 0.006	35.3 ± 2.4	34.9 ± 1.4	10.2 ± 1.3	-0.3 ± 1.4
* 289.253	-45.636	0.168 ± 0.018	83.4 ± 4.4	9.0 ± 2.7	11.1 ± 2.1	-9.5 ± 2.7
289.395	-32.792	0.132 ± 0.006	120.5 ± 1.8	32.1 ± 1.0	5.8 ± 1.6	-2.8 ± 1.0
289.478	-39.488	0.037 ± 0.002	170.7 ± 2.9	4.4 ± 1.5	2.9 ± 2.2	-21.9 ± 1.5
* 290.012	-41.763	0.051 ± 0.001	169.3 ± 0.7	7.9 ± 0.4	10.5 ± 0.3	-15.2 ± 0.4
290.038	-39.129	0.044 ± 0.004	57.1 ± 3.4	4.9 ± 2.6	19.9 ± 1.5	-21.5 ± 2.6
290.434	-36.118	0.165 ± 0.001	43.0 ± 0.5	23.5 ± 0.3	0.3 ± 0.3	-6.6 ± 0.3
290.710	-38.878	0.170 ± 0.017	111.1 ± 4.0	14.8 ± 2.3	12.8 ± 1.7	-11.6 ± 2.3
290.754	-38.330	0.038 ± 0.001	21.3 ± 1.5	21.6 ± 0.8	2.4 ± 1.7	-5.5 ± 0.8
290.754	-35.106	0.074 ± 0.001	107.8 ± 1.1	4.2 ± 0.6	0.6 ± 0.6	-27.0 ± 0.6
290.852	-32.259	0.051 ± 0.002	172.8 ± 1.6	40.2 ± 0.8	6.7 ± 1.1	5.4 ± 0.8
* 290.958	-45.418	0.028 ± 0.003	49.3 ± 4.6	13.1 ± 4.4	22.7 ± 1.9	-4.8 ± 4.4
290.961	-40.949	0.130 ± 0.006	158.0 ± 2.1	3.7 ± 1.1	5.7 ± 1.8	-19.9 ± 1.1
290.986	-36.119	0.058 ± 0.002	35.5 ± 1.3	2.0 ± 0.8	11.0 ± 0.6	-27.8 ± 0.8
291.157	-38.395	0.127 ± 0.001	3.6 ± 0.4	11.4 ± 0.2	1.6 ± 0.9	-15.4 ± 0.3

Table 2.6 continued...

l (°)	b (°)	p_0 (%)	Ψ_0 (°)	ϕ_{raw} (rad m^{-2})	σ_ϕ (rad m^{-2})	$\phi_{\rm corr}$ (rad m^{-2})
291.468	-44.002	0.536 ± 0.026	90.4 ± 3.2	6.2 ± 1.9	2.3 ± 1.9	-13.2 ± 1.9
291.492	-41.596	0.033 ± 0.001	179.4 ± 1.2	11.3 ± 0.6	5.6 ± 0.9	-11.3 ± 0.6
291.508	-40.460	0.199 ± 0.005	54.3 ± 1.3	0.3 ± 0.8	11.8 ± 0.5	-23.7 ± 0.8
291.652	-34.097	0.079 ± 0.006	175.1 ± 5.0	11.5 ± 5.7	39.8 ± 2.0	-20.6 ± 5.7
291.674	-34.518	0.044 ± 0.001	48.1 ± 0.6	23.2 ± 0.4	0.5 ± 0.5	-8.4 ± 0.4
291.778	-40.785	0.059 ± 0.007	37.7 ± 4.6	6.0 ± 3.6	21.1 ± 2.2	-17.4 ± 3.6
291.865	-37.269	0.134 ± 0.010	91.7 ± 2.9	37.7 ± 2.6	26.7 ± 1.5	9.9 ± 2.6
291.865	-37.269	0.114 ± 0.008	95.2 ± 2.8	33.8 ± 2.3	27.6 ± 1.3	5.9 ± 2.3
291.881	-35.986	0.075 ± 0.004	58.2 ± 2.3	12.9 ± 1.2	6.7 ± 1.6	-16.6 ± 1.2
* 291.954	-31.336	0.161 ± 0.006	87.6 ± 2.0	38.1 ± 1.4	19.3 ± 0.7	2.7 ± 1.4
292.041	-43.665	0.193 ± 0.010	50.6 ± 4.5	9.3 ± 2.4	1.4 ± 1.2	-10.3 ± 2.4
292.082	-42.348	0.186 ± 0.012	26.8 ± 2.7	12.2 ± 1.4	7.7 ± 1.8	-9.0 ± 1.4
292.397	-42.859	0.128 ± 0.007	103.2 ± 3.5	-1.2 ± 1.8	3.0 ± 2.2	-21.7 ± 1.8
292.473	-37.351	0.018 ± 0.000	129.6 ± 1.1	23.6 ± 0.6	3.9 ± 1.5	-3.9 ± 0.6
292.550	-41.942	0.545 ± 0.026	65.5 ± 2.1	9.1 ± 1.3	13.2 ± 0.8	-12.5 ± 1.3
292.652	-44.236	0.293 ± 0.003	19.9 ± 0.4	18.2 ± 0.3	15.8 ± 0.2	-0.4 ± 0.4
292.741	-43.379	0.235 ± 0.019	87.9 ± 3.5	15.9 ± 1.8	7.3 ± 2.3	-3.7 ± 1.8
* 292.833	-31.083	0.081 ± 0.003	35.4 ± 2.4	40.7 ± 1.2	2.1 ± 1.7	5.4 ± 1.2
292.868	-41.315	0.320 ± 0.034	175.4 ± 4.6	4.4 ± 2.8	7.9 ± 3.5	-17.8 ± 2.8
293.055	-39.953	0.146 ± 0.012	64.2 ± 3.7	-0.8 ± 2.0	10.2 ± 1.6	-24.7 ± 2.0
293.088	-43.924	0.363 ± 0.033	78.7 ± 5.0	27.7 ± 3.9	8.3 ± 4.9	9.0 ± 3.9
293.148	-41.268	0.089 ± 0.002	13.7 ± 1.5	-20.0 ± 1.1	19.4 ± 0.5	-42.1 ± 1.1
293.471	-42.911	0.178 ± 0.007	122.4 ± 1.7	10.0 ± 1.0	11.2 ± 0.7	-9.8 ± 1.0
293.509	-43.572	0.317 ± 0.014	80.4 ± 1.9	20.6 ± 1.1	7.9 ± 1.2	1.6 ± 1.1
293.635	-44.131	0.229 ± 0.013	25.0 ± 2.4	31.3 ± 1.5	16.1 ± 0.9	13.1 ± 1.5
293.737	-42.296	0.284 ± 0.018	130.6 ± 2.8	10.9 ± 1.6	6.9 ± 2.2	-9.6 ± 1.6
293.807	-41.469	0.129 ± 0.012	61.1 ± 3.9	13.5 ± 2.3	11.8 ± 1.7	-8.0 ± 2.3
293.819	-41.466	0.154 ± 0.012	71.9 ± 3.3	6.4 ± 2.0	14.2 ± 1.4	-15.1 ± 2.0
* 293.851	-31.371	0.035 ± 0.000	98.3 ± 0.3	43.8 ± 0.2	0.1 ± 0.1	9.4 ± 0.2
293.907	-39.279	0.385 ± 0.021	53.0 ± 4.5	17.9 ± 2.1	2.4 ± 2.0	-6.3 ± 2.1
294.006	-44.374	0.200 ± 0.005	4.1 ± 1.2	8.6 ± 0.6	3.9 ± 1.5	-9.1 ± 0.7
294.192	-43.969	0.234 ± 0.019	156.9 ± 3.5	17.8 ± 1.9	6.4 ± 2.8	-0.3 ± 1.9
294.271	-44.918	0.095 ± 0.001	158.1 ± 0.5	-8.4 ± 0.3	3.1 ± 0.7	-25.2 ± 0.4
294.385	-44.286	0.084 ± 0.003	93.6 ± 1.7	22.4 ± 1.0	9.5 ± 0.9	4.7 ± 1.0
* 294.480	-31.056	0.132 ± 0.002	165.5 ± 1.0	42.5 ± 0.5	0.9 ± 0.8	8.0 ± 0.5
294.525	-40.882	0.081 ± 0.004	99.8 ± 1.9	2.4 ± 1.1	8.3 ± 1.2	-19.5 ± 1.1
294.530	-42.244	0.347 ± 0.024	12.2 ± 3.6	18.4 ± 1.8	4.3 ± 2.7	-1.7 ± 1.8
294.535	-40.875	0.063 ± 0.002	95.2 ± 1.5	4.9 ± 0.9	5.7 ± 1.4	-17.0 ± 1.0
294.536	-43.701	0.454 ± 0.019	53.2 ± 1.8	21.9 ± 0.9	7.9 ± 1.0	3.6 ± 0.9
294.548	-40.966	0.107 ± 0.007	21.2 ± 3.1	4.7 ± 1.6	5.0 ± 2.4	-17.1 ± 1.6
294.593	-40.497	0.231 ± 0.007	136.5 ± 1.8	12.4 ± 1.0	2.9 ± 1.9	-10.0 ± 1.0
294.608	-42.908	0.060 ± 0.007	161.1 ± 4.2	12.2 ± 2.5	8.7 ± 3.4	-7.1 ± 2.5

Table 2.6 continued...

l (°)	b (°)	p_0 (%)	Ψ_0 (°)	ϕ_{raw} (rad m^{-2})	σ_ϕ (rad m^{-2})	$\phi_{\rm corr}$ (rad m^{-2})
294.713	-43.612	0.614 ± 0.039	79.3 ± 2.7	18.6 ± 1.6	14.7 ± 0.9	0.2 ± 1.6
294.884	-44.122	0.052 ± 0.001	73.1 ± 1.5	26.3 ± 0.8	2.8 ± 1.8	8.8 ± 0.9
294.912	-40.650	0.027 ± 0.002	21.5 ± 5.5	18.3 ± 2.9	4.0 ± 2.9	-3.7 ± 2.9
294.930	-42.244	0.065 ± 0.002	157.6 ± 2.6	21.7 ± 1.4	1.8 ± 1.5	1.8 ± 1.4
294.995	-41.978	0.051 ± 0.002	49.8 ± 1.7	25.5 ± 1.1	9.5 ± 1.1	5.3 ± 1.1
295.126	-41.492	0.057 ± 0.003	109.3 ± 2.0	35.5 ± 1.1	5.1 ± 1.9	14.7 ± 1.1
295.202	-41.984	0.167 ± 0.014	86.4 ± 3.5	28.6 ± 2.0	9.8 ± 1.8	8.4 ± 2.0
295.226	-42.823	0.294 ± 0.015	92.6 ± 2.2	-9.5 ± 1.2	11.6 ± 1.0	-28.6 ± 1.3
295.361	-40.387	0.121 ± 0.007	54.4 ± 4.1	25.0 ± 2.2	2.6 ± 2.2	2.9 ± 2.2
295.367	-40.785	0.322 ± 0.041	147.4 ± 10.5	22.9 ± 5.1	2.9 ± 2.6	1.3 ± 5.1
295.507	-42.082	0.162 ± 0.009	86.8 ± 2.2	27.7 ± 1.2	7.2 ± 1.7	7.8 ± 1.2
295.524	-40.997	0.062 ± 0.006	85.3 ± 6.4	11.5 ± 3.1	3.7 ± 2.9	-9.8 ± 3.1
295.675	-44.323	0.077 ± 0.007	173.7 ± 5.5	10.3 ± 2.8	5.3 ± 3.0	-6.6 ± 2.8
* 295.688	-34.852	0.130 ± 0.003	9.9 ± 1.4	30.8 ± 0.9	5.7 ± 1.1	1.8 ± 0.9
295.733	-42.013	0.142 ± 0.010	105.0 ± 3.4	34.9 ± 2.0	5.8 ± 2.7	15.1 ± 2.0
295.814	-43.417	0.274 ± 0.030	174.5 ± 5.0	21.8 ± 2.8	8.3 ± 3.2	3.8 ± 2.8
295.881	-43.599	0.022 ± 0.001	72.5 ± 2.7	42.0 ± 1.8	15.8 ± 0.9	24.3 ± 1.8
295.893	-42.505	0.205 ± 0.011	48.4 ± 2.6	19.3 ± 1.6	15.5 ± 0.9	0.2 ± 1.6
295.925	-45.474	0.473 ± 0.037	85.4 ± 3.6	-5.1 ± 2.3	17.5 ± 1.1	-20.4 ± 2.3
295.925	-43.169	0.209 ± 0.014	73.3 ± 3.2	18.8 ± 1.9	9.9 ± 1.6	0.5 ± 1.9
295.956	-43.659	0.044 ± 0.001	37.3 ± 1.4	23.1 ± 0.8	6.6 ± 1.1	5.4 ± 0.9
295.963	-43.664	0.054 ± 0.002	39.0 ± 1.4	21.7 ± 1.0	12.1 ± 0.7	4.1 ± 1.0
295.986	-42.955	0.325 ± 0.054	106.3 ± 7.2	6.3 ± 3.8	9.5 ± 3.9	-12.2 ± 3.8
296.022	-42.163	0.070 ± 0.004	50.4 ± 3.2	2.5 ± 3.4	31.1 ± 1.4	-17.0 ± 3.4
296.491	-40.813	0.226 ± 0.011	157.0 ± 3.4	4.5 ± 1.9	1.6 ± 1.4	-16.4 ± 1.9
296.659	-45.653	0.101 ± 0.004	70.9 ± 1.6	-13.1 ± 1.0	10.6 ± 0.8	-27.8 ± 1.0
296.704	-43.455	0.057 ± 0.006	168.7 ± 3.9	6.0 ± 2.4	9.2 ± 2.7	-11.5 ± 2.4
296.719	-40.842	0.194 ± 0.004	55.0 ± 0.8	4.7 ± 0.5	6.4 ± 0.6	-16.1 ± 0.5
296.882	-40.719	0.237 ± 0.028	52.9 ± 4.7	-7.1 ± 2.3	8.5 ± 2.8	-28.0 ± 2.3
* 296.933	-33.860	0.137 ± 0.011	6.3 ± 4.0	27.3 ± 3.2	20.9 ± 1.4	-2.4 ± 3.2
296.997	-40.395	0.063 ± 0.002	68.3 ± 1.4	1.3 ± 0.7	2.6 ± 1.6	-19.9 ± 0.7
297.068	-41.714	0.043 ± 0.002	125.5 ± 2.3	16.8 ± 1.3	11.3 ± 0.9	-2.8 ± 1.3
297.070	-41.711	0.042 ± 0.002	114.8 ± 2.7	20.2 ± 1.5	10.8 ± 1.0	0.7 ± 1.5
297.070	-41.257	0.063 ± 0.003	145.0 ± 3.4	18.4 ± 1.8	1.7 ± 1.5	-1.7 ± 1.8
297.257	-41.186	0.300 ± 0.013	132.7 ± 2.8	17.6 ± 1.8	2.8 ± 2.2	-2.5 ± 1.8
297.277	-42.705	0.628 ± 0.056	9.5 ± 6.1	11.9 ± 3.7	4.6 ± 3.9	-6.3 ± 3.7
297.344	-43.704	0.233 ± 0.019	67.3 ± 3.4	-18.4 ± 2.1	8.6 ± 2.2	-35.2 ± 2.1
297.476	-41.179	0.766 ± 0.128	150.1 ± 31.9	-21.9 ± 12.1	5.1 ± 3.4	-41.9 ± 12.1
297.624	-44.093	0.170 ± 0.017	76.8 ± 3.9	-11.0 ± 2.1	8.3 ± 2.6	-27.2 ± 2.1
297.758	-44.158	0.097 ± 0.007	33.4 ± 3.2	-14.2 ± 2.1	15.5 ± 1.4	-30.3 ± 2.1
* 298.169	-35.710	0.127 ± 0.003	114.9 ± 1.1	50.7 ± 0.6	4.2 ± 1.3	24.0 ± 0.6
298.209	-42.078	0.177 ± 0.014	15.6 ± 4.4	-15.7 ± 2.4	3.7 ± 2.7	-34.2 ± 2.4

Table 2.6 continued...

l (°)	b (°)	p_0 (%)	Ψ_0 (°)	ϕ_{raw} (rad m^{-2})	σ_ϕ (rad m^{-2})	$\phi_{\rm corr}$ (rad m^{-2})
* 298.247	-33.110	0.125 ± 0.010	25.8 ± 3.1	38.3 ± 1.8	7.1 ± 2.6	8.4 ± 1.8
298.251	-42.116	0.433 ± 0.026	11.8 ± 2.7	-46.6 ± 1.6	7.7 ± 1.9	-65.0 ± 1.6
298.381	-43.653	0.050 ± 0.003	144.7 ± 3.3	7.3 ± 1.8	3.1 ± 2.3	-9.1 ± 1.8
* 298.994	-36.643	0.031 ± 0.002	135.7 ± 2.8	18.3 ± 2.0	15.9 ± 1.1	-6.8 ± 2.0
* 299.493	-30.568	0.021 ± 0.001	2.7 ± 2.0	24.7 ± 1.2	11.6 ± 0.8	-7.9 ± 1.2
* 299.727	-33.232	0.019 ± 0.001	178.4 ± 2.5	36.5 ± 1.5	13.4 ± 0.9	7.5 ± 1.5
299.815	-41.686	0.190 ± 0.003	23.6 ± 1.4	38.4 ± 1.0	0.9 ± 0.8	20.2 ± 1.0
* 300.101	-32.957	0.107 ± 0.002	42.9 ± 1.5	19.3 ± 0.8	1.3 ± 1.1	-9.9 ± 0.8
* 300.176	-37.791	0.083 ± 0.004	156.5 ± 3.2	25.4 ± 1.7	1.8 ± 1.5	2.4 ± 1.7
300.260	-41.713	0.022 ± 0.000	32.5 ± 1.2	21.2 ± 0.6	1.6 ± 1.2	3.3 ± 0.7
* 300.546	-34.430	0.210 ± 0.004	35.0 ± 1.6	19.8 ± 0.9	0.8 ± 0.7	-7.3 ± 0.9
* 300.682	-38.509	0.098 ± 0.004	124.7 ± 1.6	31.4 ± 1.0	11.6 ± 0.7	9.6 ± 1.0
* 300.712	-31.222	0.023 ± 0.001	26.9 ± 1.6	12.4 ± 0.9	5.8 ± 1.3	-18.7 ± 0.9
* 300.977	-35.998	0.096 ± 0.009	60.8 ± 4.0	33.9 ± 3.0	20.0 ± 1.6	9.1 ± 2.9
* 301.077	-37.858	0.378 ± 0.032	144.6 ± 3.6	28.0 ± 1.7	7.7 ± 1.8	5.5 ± 1.7
* 301.241	-35.873	0.042 ± 0.002	157.0 ± 2.3	8.7 ± 1.2	11.3 ± 0.9	-16.2 ± 1.2
* 301.463	-32.596	0.089 ± 0.003	37.9 ± 1.3	28.7 ± 0.8	10.9 ± 0.7	-0.2 ± 0.8
* 302.602	-38.463	0.059 ± 0.002	177.2 ± 1.8	10.8 ± 1.0	7.1 ± 1.2	-10.1 ± 1.0
* 304.115	-35.992	0.041 ± 0.003	138.4 ± 4.0	48.2 ± 2.8	15.4 ± 1.5	25.0 ± 2.8

3

The Broadband Polarisation Signature of Radio Galaxy NGC 612

3.1 Introduction

The synchrotron emission associated with radio lobes can be used to dissect the evolutionary history of the host galaxy as well as that of the surrounding intergalactic medium. Jets that are launched from a central supermassive black hole create, and subsequently inflate, radio lobes (Begelman et al. 1984; Xu et al. 2010). As the lobes expand, they have the potential to interact with the surrounding environment, potentially implanting signatures from the interaction into the generated synchrotron plasma. Additionally, these interactions can enrich the surrounding medium with large amounts of energy and metals (McNamara et al. 2009; Aguirre et al. 2001; Reuland et al. 2007). However, the relative amount of thermal material present in radio lobes is poorly constrained, and it has been shown that the lobes are predominantly inflated with non-thermal, synchrotron-emitting plasma (Begelman et al. 1984). Evidence for thermal material distributed throughout the volumes of radio lobes has been argued in the case of some of the most well-studied radio galaxies, Centaurus A (O'Sullivan et al. 2012) and Fornax A (Fomalont et al. 1989). The key to detecting thermal material in radio lobes may lie in the detailed analysis of the Faraday depth structure, as the Faraday depth encodes the thermal electron density in addition to the line-of-sight magnetic field strength. Therefore, by studying the polarised emission associated with radio lobes we can gain insight towards the origin and density of thermal gas in radio galaxies and the intergalactic medium.

Differentiating between polarisation contributions that are internal and those that are external to the source has proven difficult. Laing (1988), Kronberg et al. (2008) and Guidetti et al. (2010) successfully modelled rotation measures associated with ra-

dio galaxies as a result of foreground emission from the large scale, diffuse intracluster medium (ICM). In contrast, other authors have argued that a significant portion of the observed RM is intrinsic to the radio lobe itself. In the latter case, there is even more debate as to where in the lobe the Faraday rotation takes place. Rudnick and Blundell (2003), Guidetti et al. (2011) and Guidetti et al. (2012) make the case that the Faraday rotating material forms a thin skin encompassing the purely synchrotron lobes. In contrast, O'Sullivan et al. (2013) successfully fit their observations by modelling radio lobes as a mixture of relativistic synchrotron plasma and magnetised, thermal gas.

Each of the aforementioned scenarios may result in a unique polarisation signal stemming from a galaxy. However, a majority of the previous studies have had limited frequency coverage and could not distinguish between the models. Narrow bandwidths greatly reduce the resolution in Faraday depth space, while broad channel widths decrease the maximum observable Faraday depth. Continuous sampling over a large frequency range allows for the recovery of the true polarisation signal.

In this chapter, we present a detailed study of the polarisation properties of the radio galaxy NGC 612 (PKS B0131-367) in an attempt to conclusively determine the physical properties of all Faraday rotating components that contributes to the observed polarisation. This target was selected as part of a larger sample of large angular-scale, Southern hemisphere radio galaxies, with each radio galaxy representing different intrinsic characteristics, radio morphology classifications and environments. Using the Australia Telescope Compact Array (ATCA) and the Compact Array Broad-band Backend (CABB, Wilson et al. 2011), we observe a continuous frequency ranges of $1100 - 3100$ and $4500 - 6500$ MHz, sampled at 1 MHz intervals. With these wide bandwidths and high spatial resolution, we are able to evaluate and model the polarisation properties of the radio emission on a pixel-by-pixel basis, investigate the origin of the polarised signal and attempt to answer whether the rotation we observe is a consequence of magnetic fields adjacent to or within the radio galaxy.

The chapter is structured as follows: we begin with a brief introduction to the galaxy NGC 612 and its local environment (§3.2). The observations and data reduction are described in detail in §3.4, followed by a description of how the polarised signal was recovered from the data. In §3.5, we introduce the different depolarisation mechanisms and how we built and tested models of polarised emission using maximum likelihood and MCMC techniques. Our results are presented in §3.6, which describes the relative success of polarisation models, in addition to introducing the parameter maps created from the best-fit polarisation solutions. The discussion (§3.7) focuses on differentiating between the different depolarisation models and attempts to answer the question of the origin of the observed Faraday rotation signal. Our conclusions are presented in §3.8.

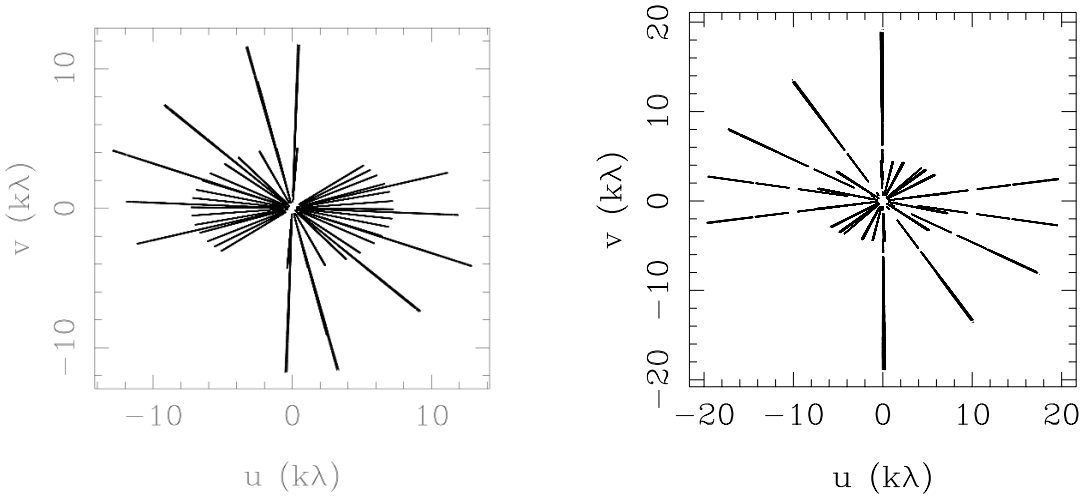

(a) 2100 MHz (b) 5500 MHz

Figure 3.1: Final uv-coverage for our observations of NGC 612 for observing bands centred at 2100 MHz (left) and 5500 MHz (right). As the bright galaxy was observed in short snapshots, there are negligible azimuthal tracks.

3.2 NGC 612

NGC 612 has been studied in great detail at multiple wavelengths. At radio frequencies, the galaxy is known to have two, large-scale lobes (Ekers et al. 1978) and has been classified as having a hybrid radio source morphology (Gopal-Krishna and Wiita 2000). The eastern lobe exhibits strong FR-II (Fanaroff and Riley 1974) characteristics, with a hot spot (hereafter, 'HS', RA(J2000) = 01:34:17, Dec(J2000) = -36:30:39) surrounded by an otherwise diffuse lobe. The western lobe more closely matches a FR-I classification with a visible jet. The total radio power of NGC 612 is $P_{4.8GHz} \sim 0.8 \times 10^{25}$ W Hz^{-1} (Morganti et al. 1993), which falls between typical FR-I and FR-II values (Owen and Laing 1989; Owen and White 1991). However, more recent radio images (Morganti et al. 1993), in addition to our study, show a radio classification more typical of a FR II.

The galaxy has been classified as an S0 galaxy at a redshift $z = 0.0297$ (de Vaucouleurs et al. 1991). The optical galaxy has a strong dust lane that is perpendicular to the radio axis (Ekers et al. 1978; Kotanyi and Ekers 1979). X-ray observations of the active galactic nucleus found an inclination angle of the central torus of 87° (Eguchi et al. 2011), implying that each radio lobe is at the same distance from the observer. Tadhunter et al. (1993) observed both strong and narrow absorption features in the optical spectrum, with weak [OII] and [OIII] emission, typical of an early-type galaxy, showing evidence for recent star formation. A young stellar population has been observed throughout the

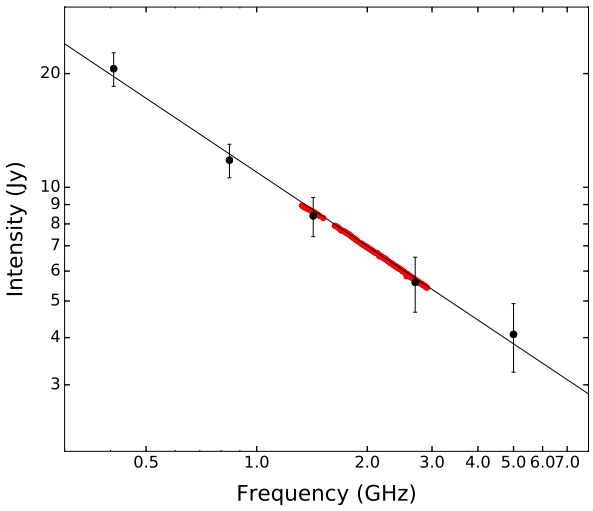

Figure 3.2: Measured flux density of NGC 612 as a function of wavelength. Our observations are shown in red with the displayed marker size of each measured flux being larger than the measured intensity errors. Measurements taken from previous literature are in black. Reference fluxes with corresponding errors are shown at 408 MHz (Schilizzi and McAdam 1975), 843 MHz (Mauch et al. 2003), 1.425 MHz (Fomalont 1968) and 5.0 GHz (Wall and Schilizzi 1979). The figure is truncated and does not show a flux density value of 56 Jy at 85.5 MHz (Mills et al. 1960). Updated flux density values at 408 MHz and 843 GHz were acquired through private communication with Dr. Richard Hunstead. A spectral index of α = -0.65 is measured from our data.

stellar disk by both Raimann et al. (2005) and Holt et al. (2007).

There is diffuse, soft (0.7 - 3 keV) X-ray emission associated with the lobes of NGC 612, with extended emission in the direction of the eastern lobe, described in Tashiro et al. (2000), who argue that the emission is likely due to the cosmic microwave background up-scattering off the synchrotron-emitting electrons in the lobes. Making basic assumptions of the geometry and distribution of matter within the lobes, Tashiro et al. (2000) use the observed quantities of spectral index in both the radio and infrared regimes, as well as the surface brightness of the radio continuum and X-ray emission, to estimate an implied magnetic field strength of the lobes of $1.6 \pm 1.3\,\mu$G.

NGC 612 is a member of a galaxy group containing 7 members (Ramella et al. 2002). The galaxy likely had a previous interaction, as argued by the existence of the dust lane in the optical counterpart in addition to a tenuous HI bridge reaching 400 kpc from the disk of NGC 612 towards its nearest neighbour, NGC 619 (Emonts et al. 2008).

3.3 Observations & Data Reduction

All observations for this project were taken with the ATCA CABB (Wilson et al. 2011), which offers 2 GHz of continuous bandwidth and a spectral resolution of 1 MHz. The wide bandwidths of CABB are ideal for recovering accurate Faraday depths from multiple contributors within the synthesised beam – a wider range of observed wavelengths lead to better the resolving power in Faraday space (Brentjens and de Bruyn 2005).

NGC 612 was observed in multiple array configurations spanning a baseline range of $107 - 2923$ m. Combining multiple array configurations allows for better sampling of the uv-plane leading to improved sampling of the galaxy on all angular scales. Our effective uv-coverage is shown in Figure 3.1 for both the observing bands covering all observing days. A summary of the observations is given in Table 3.1, which lists the array configuration, total time on source and date of observation. The mosaic pointings were Nyquist sampled at the resolution of the highest frequency channel (3100 MHz and 6500 MHz). Each mosaic pointing was observed at 30 second intervals, switching to the phase and leakage calibrator PKS B0153−410 once numerous mosaic cycles completed. The time between observations of the phase calibrator was no more than 20 minutes.

The data were reduced, calibrated and flagged using the MIRIAD software package (Sault et al. 1995). PKS B1934−638 was observed once per day as the absolute flux and bandpass calibrator. The bandpass, gains and polarisation solutions were calculated every 128 MHz in order to avoid any frequency-dependent calibrations. Sault and Cornwell (1999) showed that in order to carry out polarisation calibration using an East-West array, for a source with unknown polarisation levels, observations must be made at ≥ 3 parallactic angles. For observations made for this chapter, leakage calibration was carried out using the phase calibrator source, PKS B0153−410, as observations of this target mostly resulted in sufficient parallactic angle coverage. For short observations, where multiple observations of a point source resulted in inadequate parallactic angle coverage (e.g. 2013Feb24), the bandpass calibrator source PKS B1934−638 has been assumed to have zero polarisation at the 2100 MHz band. This is not absolutely known and polarisation observations for these observations are to within 0.5% accuracy.

During the October 2012 and April 2013 observing semesters, there existed a large ripple running through the middle of the 5500 MHz observing band for all observations involving ATCA antenna CA01. The ripple only affected the Y-polarisation and was highly time variant. Significant effort was made to correct the erroneous data so that we might include all baselines involving CA01; however, the attempts were ultimately unsuccessful and the high-frequency polarisation data was dropped from our analysis. During this process, attempts to correct this ripple were made by forcing the polarisation response as a function of frequency and time across the band. This technique led to the implementation of user-defined polarised calibration flux solutions within the MIRIAD

Table 3.1: Summary of the observing log for NGC 612, which is a subset of ATCA project C2776. Column (1) gives the array configuration; column (2) the central observing frequency in GHz. The total time spent on-source each run is listed in column (3). Column (4) gives the UT date of the commencement of the observations.

Array Config.	Obs. Freq. (MHz)	Time On-Source (hours)	Obs. Date
1.5 C	2100	0.26	2012 Dec 03
1.5 C	5500	0.29	2012 Dec 03
EW 352	5500	0.77	2013 Jan 09
EW 352	5500	1.37	2013 Jan 10
750 C	2100	0.98	2013 Jan 25
750 C	5500	0.49	2013 Jan 26
6A	2100	0.1	2013 Feb 24

software package. Within the gain and polarisation calibration task *'gpcal'*, a user may now specify an I, Q, U and V flux density for each of the frequency bins used for calibration. This method has the potential to improve the polarisation leakage solutions for sources with known polarised flux densities that vary as a function of frequency.

The data were flagged largely with the automated task PGFLAG, with minor manual flagging being carried out with tasks BLFLAG and UVFLAG. In total, 37% and 19% of the data were flagged in the 2100 and 5500 MHz bands due to radio frequency interference (RFI), respectively.

Naturally-weighted Stokes I, Q and U mosaic maps were made every 16 MHz. To avoid any resolution effects between frequencies, the dirty images were convolved to a common resolution of 1 arcmin. We drop the lowest frequency maps due to insufficient uv-coverage after flagging.

Joint maximum entropy deconvolution was performed on the mosaics with the task PMOSMEM. Using previously published values for the total flux density of NGC 612, we find a spectral index value of $\alpha = -0.65$ ($S \propto \nu^{\alpha}$). In the absence of single dish observations for an absolute flux reference, we estimate the expected total source flux extrapolating from this spectral index value and previous measurements (Figure 3.2). To test the validity of this assumption, we additionally cleaned the Stokes I maps with a *multiscale clean* approach with the *Common Astronomy Software Applications (*CASA*)*. We find that corresponding frequency Stokes I maps are nearly identical, with negligible variations in both total flux and on a pixel-by-pixel basis compared to the rms noise.

Cleaned images were generated with the task RESTOR. Our synthesised beam is 1 arcmin across where one pixel corresponds to 10 arcsec in angular size. At the distance to the galaxy of 121.5 Mpc, one beam corresponds to a physical size of ~ 35 kpc for $H_0 = 73.0$ km/sec/Mpc.

Through private communication with the ATCA system scientist, the author was

made aware of a spectral ripple spanning the entirety of the 2100 MHz band with a frequency of 300 MHz. This effect does not have a static central frequency and appears at intermittent times. Furthermore, there is no known means of removing this ripple. Stevens et al. (2017, *in prep.*) will discuss this issue in full detail. As our observations were made over multiple epochs, the manifestations of this ripple become difficult to discern from the polarisation signal, other than the linear λ-dependence of the ripple and the λ^2-dependence of our targeted signal. As we will discuss in §3.6, we restrict our investigation to single-component polarisation models in order to avoid overly complex models that may attempt to fit this instrumental error. However, as the ripple has a linear wavelength dependence and does not dominate the overall polarisation signal, we believe this has not contaminated our resultant best-fit values for single-component models.

3.4 Observational Results

3.4.1 Imaging Results

Our data reduction resulted in 92 independent channel maps in Stokes I, Q and U. Typical maps of total intensity (Stokes I) and both linear polarisations (Stokes Q and U) are shown every 512 MHz in Figure 3.3. We see a signal with clear linearly polarised emission stemming from both lobes. Corresponding frequency maps of polarised intensity ($P = \sqrt{Q^2 + U^2}$) were created from the final Stokes maps. It is immediately evident that the polarisation signal changes as a function of position across NGC 612 (Figure 3.3).

Uncertainties in the intensity values of I, Q, U and P were measured for each frequency interval by taking the rms value (σ) of an area in the final maps near, but not including, the radio emission. Pixels were masked if $> 10\%$ of the channels fell below a threshold of 8σ in Stokes I and 5σ in polarised intensity. We discard all edge pixels from the continuous, accepted pixels that comprise the radio galaxy. This results in 1,277 usable pixels comprised of 45 independent beams for our analysis.

We also make a high-resolution, high-frequency total intensity map at 5500 MHz in order to trace the path of the jet associated with the lobes of NGC 612. The Stokes I imaging results are minimally effected by the hardware issues described in §3.3, leading the deconvolved map of Stokes I to be robust and giving us confidence in the jet position. Contours of the high-frequency position of the jet is marked by the cyan contours in Figure 3.4 and as a grey dashed line in all subsequent parameter maps of the radio lobes.

3.4.2 Fractional Polarisation Spectra

In order to decouple spectral effects from wavelength-dependent polarisation, we adopt fractional polarised notation, as first introduced in §1.2.2, such that $q = Q/I$, $u = U/I$

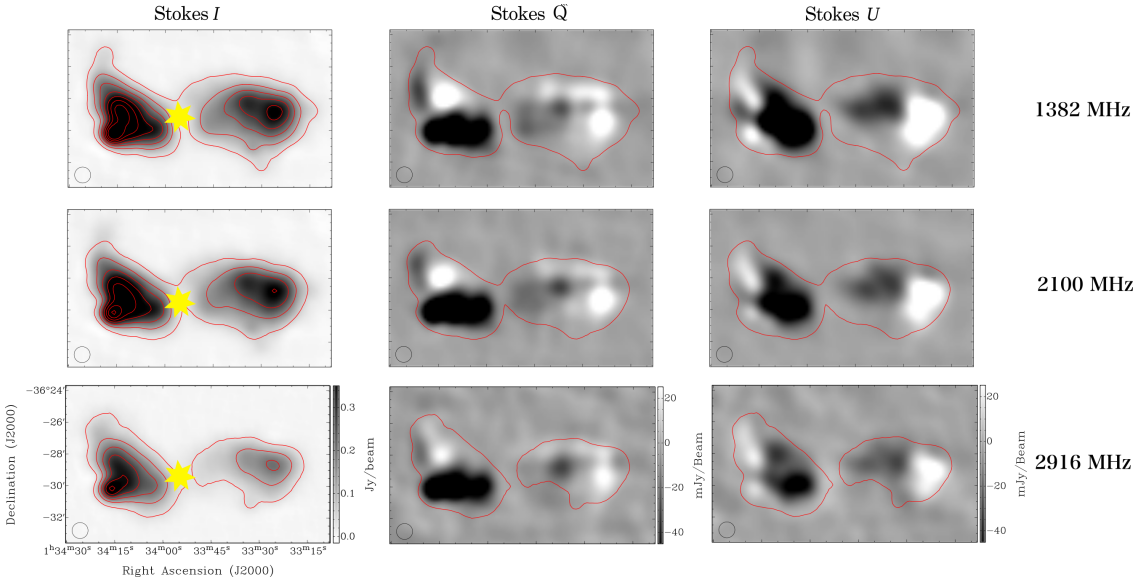

Figure 3.3: Maps of Stokes I, Q and U (left, centre and right respectively) at wavelengths centred at 1332, 2100 and 2916 MHz in ascending order. These frequency channels represent the extremes and middle of the 2100 MHz observing band. Intensity levels are kept constant across the displayed frequency range with the colour bar shown in the bottom panel. The circular beam has a FWHM of 1 arcminute and is shown in the lower left-hand corner of each map. Stokes I contours are shown in red and represent total intensity values of 30 - 480 mJy/beam at intervals of 75 mJy/beam for the total intensity maps and the lowest intensity contour is shown on both the Stokes Q and U maps. The location of the optical galaxy is marked with a yellow star in all total intensity figures.

and $p^2 = q^2 + u^2$. As we have done in Chapter 2, we create fractional polarised spectra, by dividing the observed $Q(\lambda^2)$ and $U(\lambda^2)$ by a second-order polynomial model, bootstrapped to the Stokes I emission. We fit the Stokes I spectrum in linear $S(I)$ versus ν space to avoid over-weighting higher frequency flux density measurements, thus leading to the creation of non-Gaussian noise when propagating the uncertainty as a function of frequency.

Figure 3.4 shows the fractional polarisation spectra of a few representative pixels across the source and also demonstrates the varying levels of polarisation seen in the galaxy. Depolarisation has been defined in §1.4 as a negative change in the observed degree of polarisation as a function of λ^2 ($dp/d\lambda^2 < 0$). We observe this trend most clearly in the region of the hot spot ('HS'), where observed level of polarisation decreases as a function of λ^2.

Assuming the lobes are composed of an optically thin synchrotron radiation source, we calculate the spectral index for each extracted pixel by fitting the Stokes I spectrum to a single, emission component in log-space. In making this assumption we are also

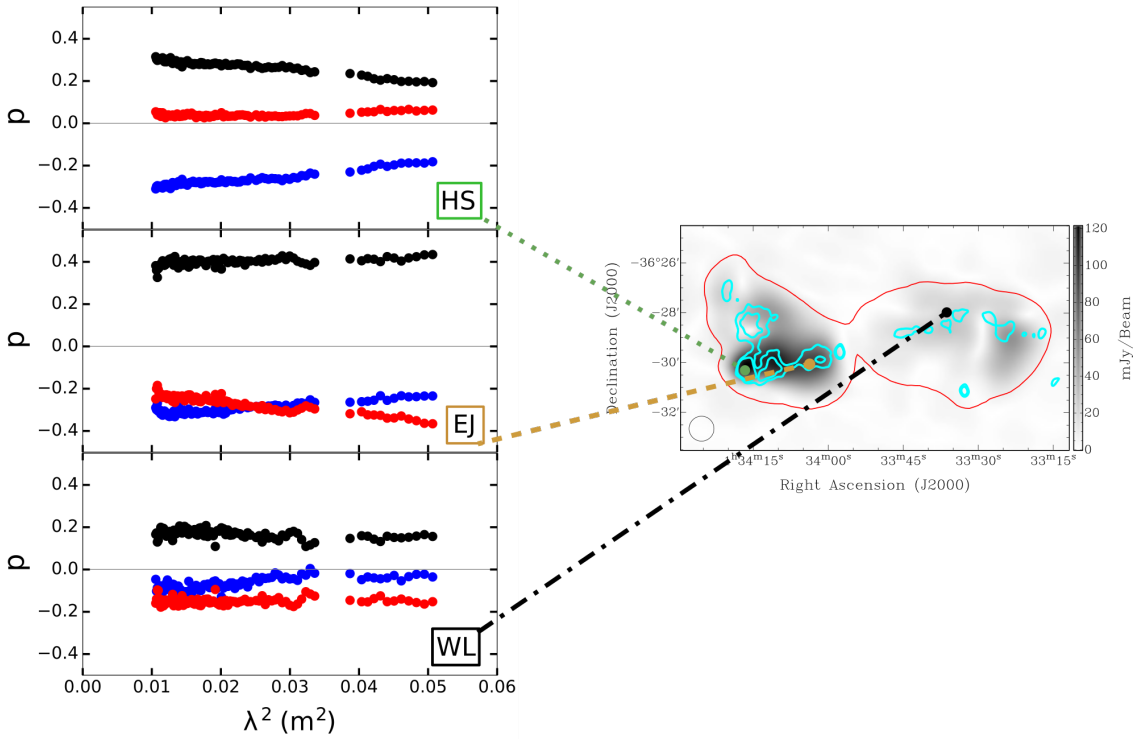

Figure 3.4: Polarised intensity map at 2100 MHz (*right*) with red contours outlining 30 mJy/beam in total intensity (Stokes I). Fractional polarised spectra are shown for the indicated pixel locations. Polarised fraction, p (P/I) is shown in black, q (Q/I) in blue and u (U/I) in red versus λ^2. All data points are displayed on a scale larger than their corresponding errors. Point 'HS' represents the location of the hot spot in total intensity, point 'EJ' (eastern jet) is near the location of the optical counterpart (identified in Figure 3.3) and point 'WL' is a pixel in the western lobe. The path of the jet, as determined from high-frequency imaging, is shown in cyan contours.

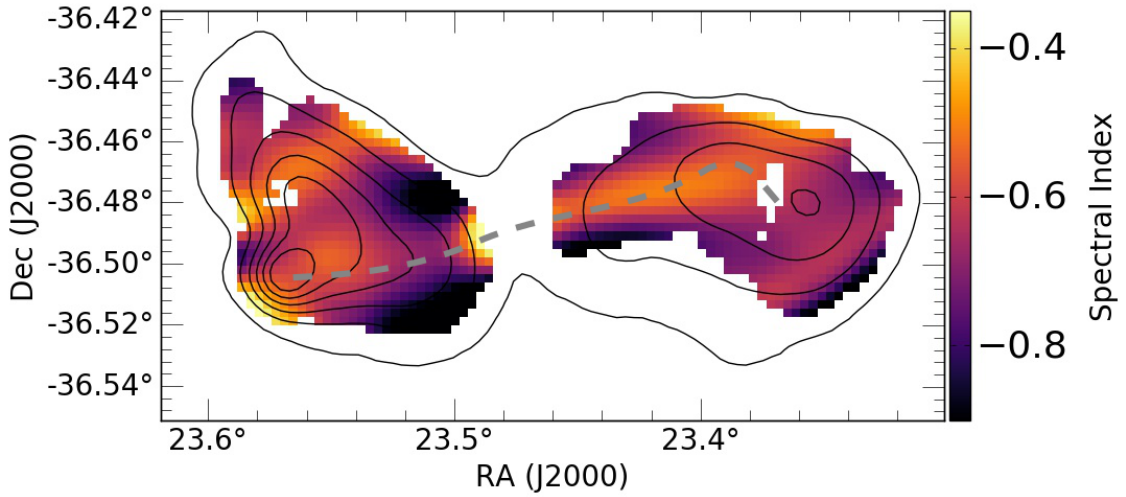

Figure 3.5: Spectral index values for each pixel evaluated as a single-component linear fit to the Stokes I spectrum in log-space. Contours show the total intensity from 25 - 400 mJy/beam in intervals of 75 mJy/beam. The dashed grey line should the path of the jet.

assuming that the dominant polarisation component is also the dominant spectral component, and this may not necessarily be true in the case of the projected area of the jet where it is possible to have two significant spectral components. Figure 3.5 shows a map of spectral index across the lobes of NGC 612. The dashed line traces the projected path of the jet through the lobes.

Our discussion will partially focus on the three representative pixels shown in Figure 3.4. The hot spot, denoted 'HS', represents the area of bright continuum emission at the far east end of the eastern lobe. The eastern jet, denoted 'EJ', is a pixel that is near the optical galaxy and marks the position of peak polarisation. This pixel is located within the jet that can be seen stretching across the eastern lobe. The pixel in the western lobe, denoted 'WL', is a representative pixel for the majority of this lobe, which has on average a lower degree of polarisation than the eastern lobe.

3.5 Model Fitting

Polarised emission in the absence of a Faraday rotating medium can be expressed simply as

$$\mathcal{P} = p_0 e^{2i\Psi_0} \tag{3.1}$$

where p_0 is the intrinsic fractional polarisation and Ψ_0 is the intrinsic polarisation angle of the emission. If the polarised emission passes through a purely foreground magnetised thermal plasma the polarisation angle is rotated from its intrinsic value. This is the simplest scenario of Faraday rotation and the polarised signal that is observed can be

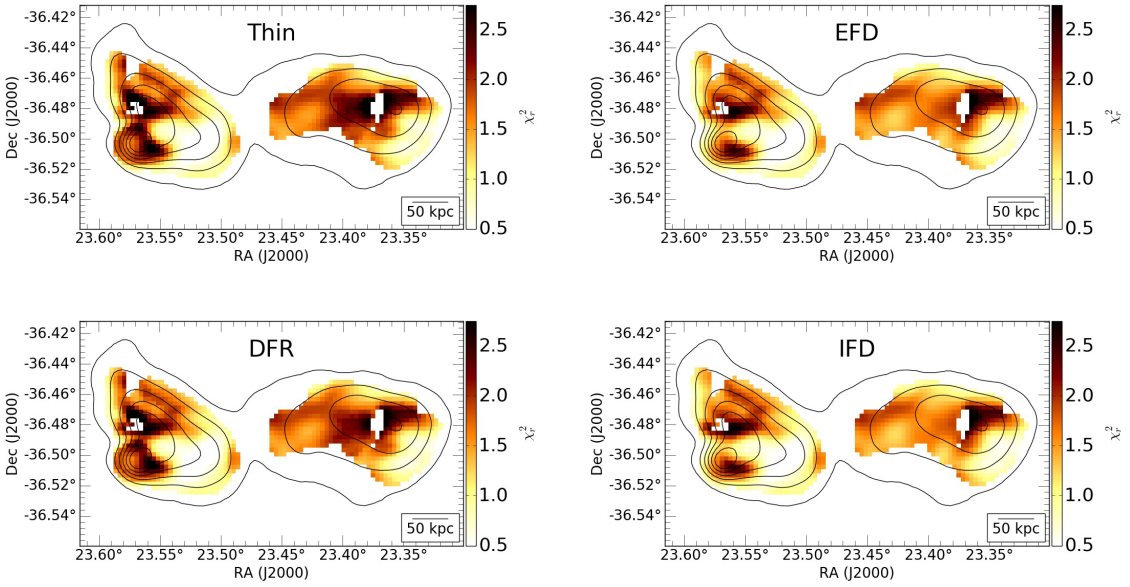

Figure 3.6: χ_r^2 values at each imaged pixel for all polarisation models discussed in this chapter. Black contours outline total intensity levels spanning $25 - 400$ mJy/beam in 75 mJy/beam increments. A scale bar is shown in the bottom righthand corner of each figure. All models have a tendency to have a similar χ_r^2 values.

expressed as

$$\mathcal{P} = p_0 e^{2i(\Psi_0 + \phi\ \lambda^2)}, \tag{3.2}$$

where ϕ is the Faraday depth of the magneto-ionised material.

In highly energetic environments such as radio lobes, complex magnetic field and thermal electron structures will give rise to multiple rotation and/or emitting sources along the line of sight and the observed polarisation signal may experience depolarisation. Depolarisation may be a result of turbulent mixing of gas in the lobes, the emitting and rotating material being co-spatial, or the spatial resolution of the observations. The effects of depolarisation tend to be strongest towards longer wavelengths and the mechanism responsible contains insight on the overall structure of the radio lobes.

The observation of depolarisation in Figure 3.4 at the location of the hot spot makes it immediately evident that it will be necessary to involve some polarisation models that are more complex (i.e. not Faraday thin) in order to accurately describe at least some of the observed polarisation. In order to analyse the nature of the polarisation of NGC 612 and its surrounding area, we test the polarisation models discussed in § 1.4 against the observed polarised signal in NGC 612.

3.5.1 Modelling Procedure

In order to test which mechanisms may be responsible for the observed polarisation, the single-component depolarisation models introduced in §1.4 (i.e. thin, EFD, DFR, IFD) are explored individually. The extracted $q(\lambda^2)$ and $u(\lambda^2)$ data are simultaneously fit to each corresponding depolarisation model using a maximum likelihood method. We employ the same MCMC approach used in Chapter 2, using EMCEE (Foreman-Mackey et al. 2013) to fit the complex polarisation parameters of each depolarisation model. For each pixel in our dataset, we initialise a set of 250 parallel samplers that explore the n-dimensional parameters space (where n is the degrees of freedom). Each of these walkers iteratively calculate the likelihood of a given location in parameter space and in doing so map out a probability distribution for a set of parameters. For any given depolarisation model, the possible parameter solutions were forced to be physical (i.e. $0 \leq p \leq 1$). In order to maximise the effectiveness of initial burn-in phase and have the walkers settle on a parameter space, each iteration of MCMC used the previous pixel's best-fit values as an initial guess.

To assess the goodness-of-fit of each models, the reduced chi-squared value (χ^2_r) was recorded for each pixel. χ^2_r is defined as

$$\chi^2_r = \frac{1}{\nu} \sum_{i=1}^{n} \left(\frac{x_i - \mu_i}{\sigma_i} \right)^2 , \tag{3.3}$$

where x_i is the i^{th} independent data point with Gaussian noise, σ_i; μ_i is the model prediction and ν is the number of free parameters. This statistic penalises according to how many standard deviations lie between the observed point and the model and generally serves as a means of assessing the success of a particular model fit to the observed data. However, it can be misleading to employ χ^2_r when comparing the relative success between models, as it is possible to build, and fit, arbitrarily complex models.

In the case of Gaussian noise, the χ^2_r is equivalent to $-2\log\mathcal{L}$. We note to the reader that χ^2_r is not an ideal statistic with which to evaluate the success of these models as our sampling of λ^2-space is non-linear, which in-turn overweights the importance of low-λ^2 samples and will down-weight samples at high-λ^2. Additionally, for a sufficiently robust dataset of a simple polarised spectrum, a returned $\chi^2_r < 1$ is not uncommon. This is due to the minimum number of model parameters of any physical polarisation model being 3 (p_0, Ψ_0, ϕ) and a model with fewer parameters is deemed unphysical. In these instances, we acknowledge the over-fitted solution, but use the returned best-fit parameters for our analysis.

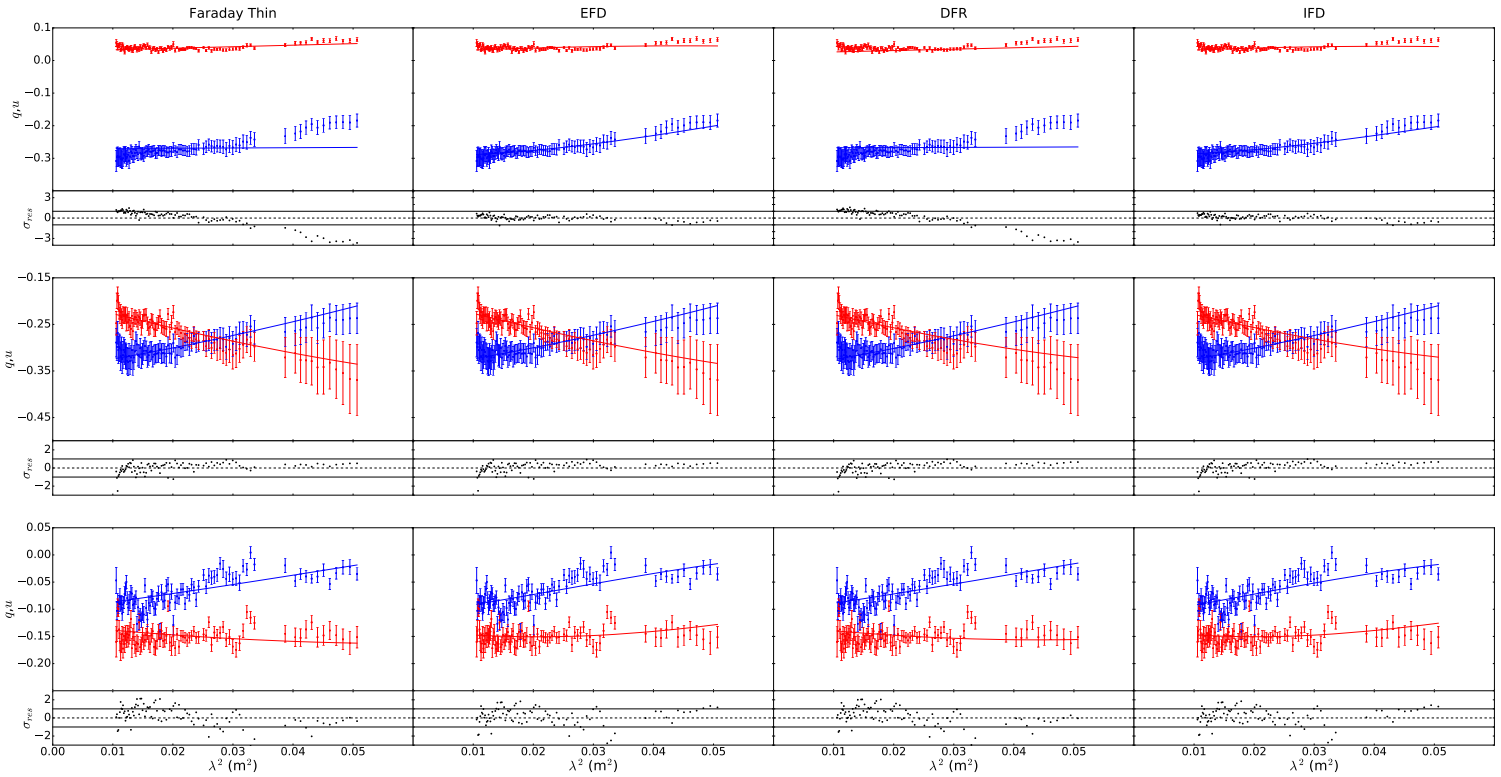

Figure 3.7: Grid of best-fit results from qu-fitting to three distinct pixels in NGC 612. The columns represent the models tested, while each row represents the three pixels tested. Each pixel was chosen from a unique region in the radio lobes – the hot spot (*top*), the eastern jet (*middle*) and western lobe (*bottom*). The blue and red points are the measured q and u data, respectively. The blue and red lines are the resulting joint best-fits from qu-fitting. The bottom panels of each cell show the residual degree of polarisation ($(p_{obs} - p_{mod})/\sigma_p$) for each model, with the solid black lines indicating +1 and -1σ_p deviations from the observations.

3.6 MODELLING RESULTS

Fitting a single polarised component to NGC 612 returns a $\chi^2_r \leq 1.5$ for more than 60% of pixels (Figure 3.6); expanding this to include all pixels with $\chi^2_r \leq 2$ results in the acceptance of more than 90% of pixels across the lobes of NGC 612. We therefore believe that one polarisation component is sufficient to describe the bulk of the polarised signal. Upon inspection, any higher order features of the q and u spectra are likely contaminated by instrumental issues that affected the ATCA at the time of observation (e.g. 300 MHz spectral wiggle, §3.3). Therefore, we limit our investigation to a single polarised component. This minimises the possibility of over-fitting the data and over-interpreting the results. Although this limits the physical interpretation of the polarised morphology, we will demonstrate in the sections that follow that a favourable solution can be found by examining the physics of the implied model. In the following section we explore the relative success of each model with the aim of determining which best represents the polarisation signature associated with the radio galaxy.

Figure 3.7 represents the best-fit solutions to each of the polarisation models for three single-pixel spectra. The pixels are selected to be representative of three independent regions of the radio lobes: the hot spot, the east jet and the western lobe (see Figure 3.4 for specific locations). Below each model fit, the residual polarisation spectrum is shown to demonstrate any latent structure in the spectrum. The similarity between each model's best-fit is immediately evident, with the largest discrepancy between model solutions occurring at the location of the hot spot (*top row*, Figure 3.7). In this region, only polarisation mechanisms with an explicit dispersion term (EFD, IFD § 1.4) are able to fit the spectra at large λ^2.

Global χ^2_r values for each polarisation model are shown in Figure 3.6. The χ^2_r maps allow the reader to assess a model's overall success in fitting the polarisation signal of the entire radio galaxy. Table 3.2 reports the mean reduced chi-squared ($\overline{\chi}^2_r$) for an area equivalent to the synthesised beam in three regions of the radio lobes. Given the relative similarity in model-fitting results, as shown in Figure 3.7, it is unsurprising that each polarisation model also returns a similar global success. In addition to the region of the hot spot, the western lobe has a marginal preference for dispersion models (see Table 3.2).

3.6.1 PARAMETER MAPS

In this section, we present the best-fit parameter maps returned from our qu-fitting routine. The parameter values for each of the polarisation models are similar enough to allow us to present the general signal trends here. Detailed parameter maps and the corresponding uncertainties for each individual polarisation model as given in Appendix B.

Table 3.2: Mean χ^2_r for each depolarisation models discussed in §3.5 for the locations shown in Figure 3.4. The mean is calculated for a number of pixels equivalent to our synthesised beam.

Pixel Location	Thin	EFD	DFR	IFD
Hot Spot	1.9	1.7	1.9	1.7
Eastern Jet	0.40	0.40	0.42	0.43
Western Lobe	2.0	1.6	1.9	1.6

Intrinsic Degree of Polarisation

Figure 3.8 shows the intrinsic polarisation across the lobes of NGC 612. The polarisation signal peaks nearest the location of the optical galaxy (shown as a yellow star in Figure 3.3). There appears to be strong polarisation along the path of the jet in the eastern lobe through to the hot spot whereas the polarisation in the western lobe peaks at the edge of the lobe furthest away from the optical counterpart. The grey dashed line shown in Figure 3.8 traces the jet, as identified from high-frequency observations (Figure 3.4).

Intrinsic Polarisation Angle

Figure 3.9 presents the intrinsic polarisation angle of the electric field vector (Ψ_0). The orientation of the plane-of-the-sky magnetic field ($B_\perp$) is orthogonal to the position angle of the electric vector. The length of each vector in Figure 3.9 is representative of the relative degree of polarisation, with the longest vector equivalent to 40% polarisation. We see coherence in the direction of the intrinsic polarisation angle on scales larger than the scale of our synthesised beam. In both the eastern and western lobe, the direction of the polarisation angle nearest the optical counterpart appears to be nearly parallel to the direction of jet launch, which X-ray observations have found to be nearly perpendicular to our line of sight (Eguchi et al. 2011).

Faraday Depth

Maps of Faraday depth are shown in Figure 3.10. The signal is nearly homogeneous across the source and varies on scales that are generally many times larger than our 1 arcminute beam. The dominant Faraday depth signal across the radio lobes of NGC 612 is positive, implying that the magnetic field along the line-of-sight is oriented predominantly towards the observer. The only considerable exceptions to this orientation is surrounding the location of the hot spot in the eastern lobe, where the Faraday depth sign is predominantly negative.

DFR and IFD models return a similar trend to that seen in Figure 3.10 but ϕ-values are a factor of 2 larger per pixel. As we have discussed in §1.4.2, this is an expected

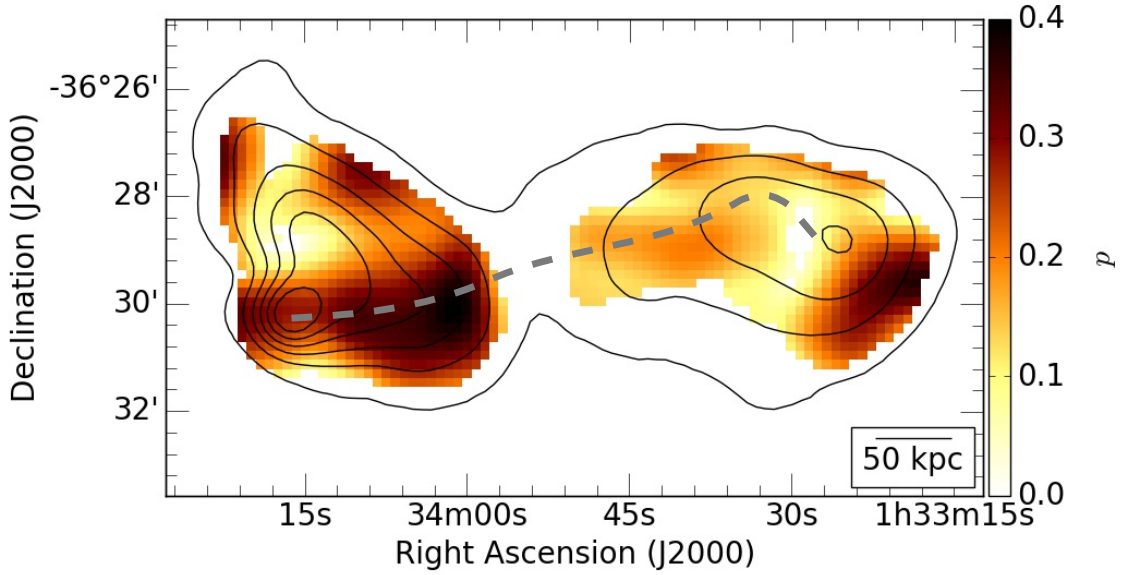

Figure 3.8: Map of the intrinsic polarisation fraction in the radio lobes. All polarisation models yield similar intrinsic polarisation maps. The grey dashed line traces the peak in polarised intensity, which we believe to be representative of the path of the jet. Black contours outline total intensity levels spanning $25 - 400$ mJy/beam in 75 mJy/beam increments.

result. The mean Faraday depth for the Faraday simple components (thin, EFD) are $\overline{\phi}_s = +3.3 \pm 3.5\,\mathrm{rad\,m^{-2}}$. The mean Faraday depth of the complex models (DFR, IFD) is $\overline{\phi}_c = +6.8 \pm 6.7\,\mathrm{rad\,m^{-2}}$. Previous Faraday rotation studies of the lobes of NGC 612 have found a simple Faraday depth that is in agreement with both $\overline{\phi}$ estimates ($+7 \pm 5\,\mathrm{rad\,m^{-2}}$, Haves 1975; $+6 \pm 1\,\mathrm{rad\,m^{-2}}$, Simard-Normandin et al. 1981).

Faraday Dispersion/Depolarisation

Figure 3.11 shows values of external Faraday dispersion (σ_ϕ) for all pixels across the radio lobes. By contrast, the internal Faraday dispersion (ζ) values returned are twice the magnitude of those in Figure 3.11. Assuming that depolarisation scales with dispersion levels, we see varying level of depolarisation as a function of position on the lobes of NGC 612.

Comparing similar χ^2_r values from Figure 3.6, we see that although models with dispersion terms (e.g. EFD and IFD) yield non-trivial dispersion values, there is often minimal improvement to the χ^2_r when compared to models without a depolarisation term (e.g. thin, DFR). This is especially true in the west lobe. We therefore argue that not all regions of NGC 612 require a dispersion model (EFD, IFD). Indeed the strongest dispersion values are located in areas of the lobes that are best fit with a depolarisation term, in that

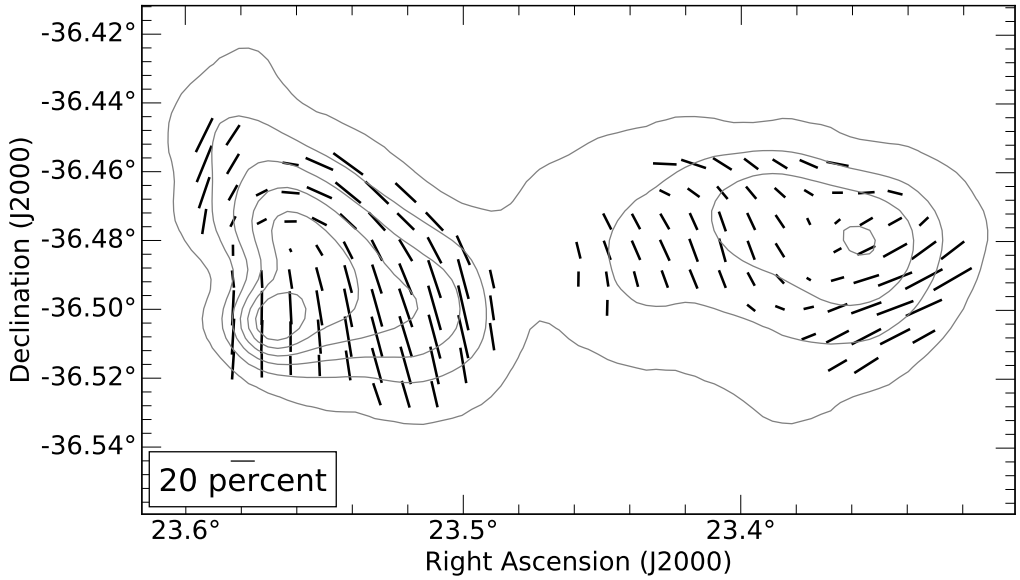

Figure 3.9: Map of the intrinsic polarisation angle vector (ψ_0) orientation towards NGC 612. The length of each vector is proportional to the polarised intensity, with a representative fraction represented in the bottom left corner. Black contours outline total intensity levels spanning $25 - 400$ mJy/beam in 75 mJy/beam increments.

the returned χ^2_r is lower. In the region surrounding the hot spot there are considerable amounts of Faraday dispersion, which increases in magnitude until it peaks at the edge of our pixel sample.

3.7 DISCUSSION

It is not possible to definitively determine which polarisation mechanism is responsible for the observed Faraday rotation towards NGC 612 using the χ^2_r statistic alone. The close χ^2_r values in Table 3.2 and Figure 3.6 show that all single-component models are capable of explaining the observed polarised signal at similar confidence levels. In the following subsections, we consider the physics of the observed Faraday depth signal in conjunction with the relative location of the thermal material along the line-of-sight. We apply any additional information available that may be able to help in distinguishing between models. The key difference in the interpretation of the polarisation models is the location of the Faraday rotating material. The Faraday simple models (thin, EFD) have the rotating material external to the synchrotron radio lobes whereas the Faraday

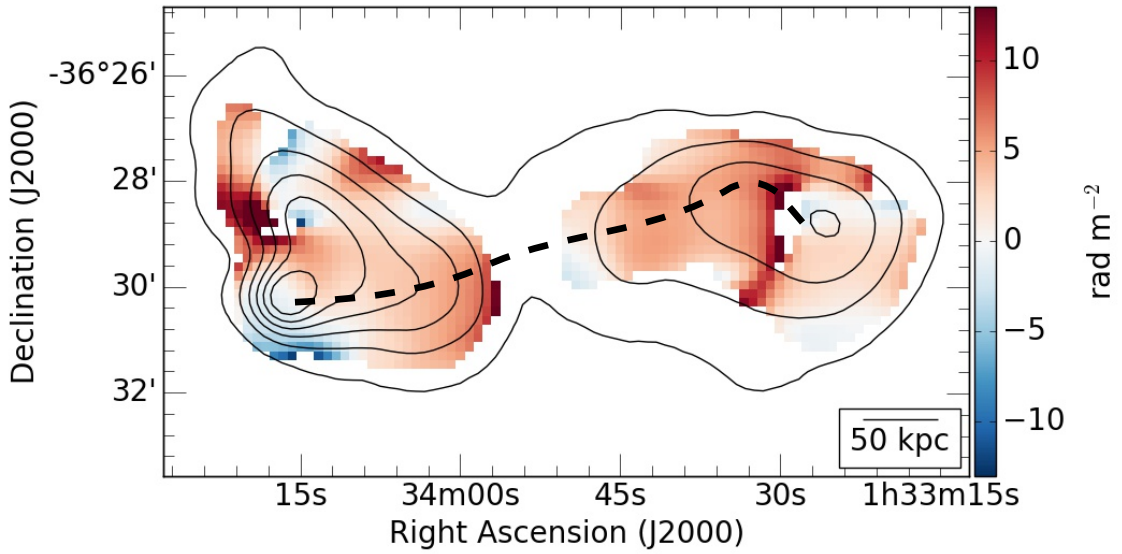

Figure 3.10: Faraday depth across NGC 612, as returned from the EFD model. The grey dashed line traces the path of the jet. DFR and IFD models show a similar trend but return ϕ-values that are a factor of 2 larger in magnitude per pixel. Black contours outline total intensity levels spanning $25 - 400$ mJy/beam in 75 mJy/beam increments.

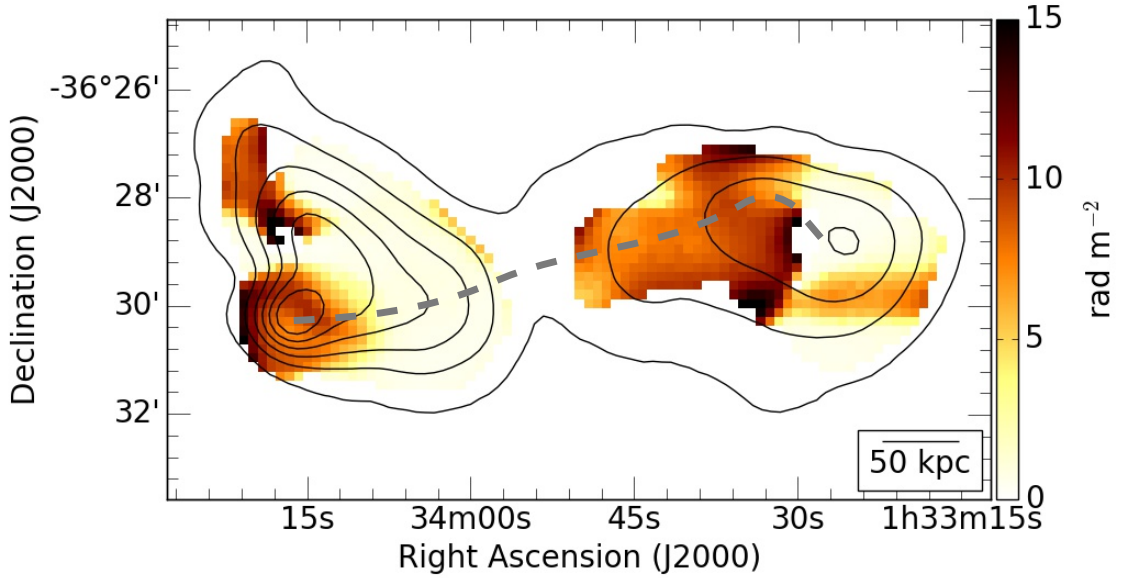

Figure 3.11: Map of Faraday dispersion (σ_ϕ) returned from qu-fitting. Best-fit values of internal Faraday dispersion (ζ) are double that of the external Faraday dispersion. Black contours outline total intensity levels spanning $25 - 400$ mJy in 75 mJy increments. The grey dashed line traces the path of the jet, as identified in higher-frequency observations.

rotation of the complex polarisation models (DFR, IFD) is taking place within the radio lobe. For the remainder of the discussion, we refer to the Faraday simple models as 'Ext' and the complex models as 'Int', symbolising where the Faraday rotation is taking place.

3.7.1 Minimum Energy Estimates

We can estimate the minimum energy magnetic field needed to sustain the lobes of NGC 612 using equation 4 from Beck and Krause (2005). We break the lobes into two symmetric rectangular slabs each with a line-of-sight pathlength of 140 kpc, and spectral index of $\alpha = -0.65$. At 2100 MHz the eastern lobe has a surface brightness of 144 mJy/beam and an average polarised fraction of 23%. The western lobe has a surface brightness of 121 mJy/beam and an average degree of polarisation of 16%. We assume that the polarised emission comes from a regular field with all possible inclinations and that the synchrotron plasma has a filling factor (f) of 0.1 throughout the lobes. We have no information on the proton-to-electron ratio ($\mathbf{K_0}$), therefore we assume unity. With these estimates in mind, we find minimum energy magnetic field strengths of 4.3 and 4.2 μG for the eastern and western lobes respectively. These estimates in turn lead to energy densities of 2.0×10^{-13} and 1.8×10^{-13} erg cm^{-3} for the eastern and western lobes. The field strength is not highly dependent on the inclination of the magnetic field under the assumption that the angle is averaged over the entire synchrotron volume of the lobes. On the other hand, we note that these estimates depend strongly on the filling factor (f) and the $\mathbf{K_0}$-value.

Our average minimum energy estimate of $\overline{B} \sim 4.2\,\mu$G is not within the range provided by Tashiro et al. (2000), who use diffuse X-ray emission and find an implied field strength of $B \simeq 1.6 \pm 1.3\,\mu$G for both lobes. Exploring the possibility that the variation between values could be a result of our estimation of effective pathlength and $\mathbf{K_0}$, we evaluate the minimum-energy magnetic field for decreasing f and increasing $\mathbf{K_0}$. Each iteration results in a larger estimation of the implied magnetic field strength and we are unable to mediate the discrepancies between our estimate of $\overline{B}$ and that reported by Tashiro et al. (2000).

3.7.2 External versus Internal Faraday Rotation

The Milky Way Foreground

One possibility is that the observed Faraday rotation is dominated by a local Galactic component. At a Galactic latitude of $-77°$, the Galactic contribution has been estimated to be on the order of a few rad m^{-2} (Oppermann et al. 2015). The magnitude of this Galactic Faraday depth estimate is of the same order as the observed Faraday depth across the radio lobes ($\overline{\phi}_{ext} = 3.3$ rad m^{-2}; $\overline{\phi}_{int} = 6.5$ rad m^{-2}). Therefore, it is necessary to further investigate and characterise the Faraday contribution from the Milky Way.

Stil et al. (2011) show that the Faraday depth of the Milky Way is coherent on angular scales of a few degrees. NGC 612 has an angular scale of $\sim 18'$ across the two radio lobes, suggesting that there would be minimal variation in the projected Faraday depth on the radio galaxy. However, Figure 3.10 shows multiple regions on NGC 612 where the intensity of the Faraday depth change over scales of a few arcminutes.

Many of the areas where the Faraday depth is seen to change correspond to regions of interest that are local to NGC 612. Figure 3.10 shows that in the East lobe, the magnitude of the Faraday depth decreases as a function of distance from the optical counterpart. In the West lobe, the Faraday depth is seen to increase in magnitude leading up to a ridge of depolarisation, first seen in Figure 3.4. The most convincing trend in the Faraday depth is in the region of the hot spot, where the sign of the Faraday depth is observed to change. We will discuss the specific location of the hot spot in more detail in a subsequent section (§3.7.4), but the morphological correlation between ϕ and Stokes I strongly suggest that the bulk of the observed Faraday rotation is taking place within or near the lobes of NGC 612. It follows that while the Galaxy is responsible for some amount of Faraday depth, it is unlikely that it is responsible for the bulk of the observed Faraday rotation.

The ambient X-ray IGrM

Guidetti et al. (2011, 2012) have argued that the Faraday rotation associated with radio lobes is due to the radio galaxy being embedded in a halo of thermal material. In these instances, the galaxies investigated are members of galaxy clusters and the radio lobes were thought to be embedded in a halo of hot X-ray gas. While not a member of a galaxy cluster, NGC 612 is a member of a loose galaxy group ($N = 7$, Ramella et al. 2002). The galaxy group environment often lacks a diffuse X-ray component; however, Tashiro et al. (2000) observe excess diffuse, soft X-ray emission extending ~ 200 kpc away from NGC 612, and argue the X-rays have been emitted via the IC process, signifying the presence of free electrons in the intragroup medium.

If we assume that the diffuse material in which NGC 612 is embedded is threaded with a coherent magnetic field, then naïvely, any change in the distribution of the X-ray-emitting gas would correlate with a change in the observed Faraday rotation. This assumption of the foreground magnetic field also implies that any regions that are devoid of X-ray emitting gas will correspond with a Faraday depth signal that is consistent with zero. Tashiro et al. (2000) point out a clear anisotropy in the soft X-ray intensity with the majority of emission being associated with the eastern lobe. By contrast, the observed Faraday depth signal is largely isotropic across the two lobes. If the radio galaxy were embedded in a volume of hot gas, the apparent uniformity of the Faraday depth signal becomes difficult to explain given the lopsided nature of the X-ray emission. While this discrepancy does not serve as direct evidence against Faraday rotation due to a magnetised intragroup medium, it does raise some intriguing concerns as to what is responsible

for the observed rotation. Additional high resolution X-ray imaging of the hot gas on the scale of the lobes is needed for further analysis of the potential for external Faraday rotation due to the immediate environment.

A swept up thin skin

It is also possible that the expanding lobes of NGC 612 have swept up and compressed the surrounding intragroup medium, as has been argued to be the case by Rudnick and Blundell (2003). In this scenario, the observed Faraday depth signal is due to the synchrotron lobes being girt by a thin skin of thermal material.

We explore this possibility by assuming such a boundary layer has a depth $dl \sim 20\,\mathrm{kpc}$; which is approximately one-tenth of the scale-height of the lobes. In §3.7.1, we estimate the average total magnetic field in the lobes of NGC 612 to be $\overline{B} \sim 4.2\,\mu\mathrm{G}$. As we have no knowledge of the relative field strengths of the line-of-sight component, we assume a geometrical upper limit of $B_{\parallel} \sim B/\sqrt{3} \sim 2.4\,\mu\mathrm{G}$. Using a mean Faraday depth of $\overline{\phi}_{\mathrm{EFD}} = +3.3\,\mathrm{rad\,m^{-2}}$, we derive an implied electron density for a thin skin of $n_e \simeq 8 \times 10^{-5}\,\mathrm{cm^{-3}}\,(\phi/3.3\,\mathrm{rad\,m^{-2}})\,(B_{\parallel}/2.4\mu\mathrm{G})\,(dl/20\,\mathrm{kpc})$.

By comparison, O'Sullivan et al. (2013) find an implied density of $n_e \sim 1.5 \times 10^{-3}\,\mathrm{cm^{-3}}$ for the lobes of Centaurus A, assuming the same skin-depth ($dl \sim 20\,\mathrm{kpc}$). They argue that the compression of material in the intragroup medium alone is not able to account for such a high density. By contrast, our estimate of the electron density of a thin-skin Faraday screen is a factor of ten less. An intragroup medium equivalent to our required density is typical of many galaxy groups (Mulchaey and Zabludoff 1998; Sun 2012) and accumulating a population of ionised material of this density from the surrounding medium seems plausible, given a moderate ionisation fraction as insinuated by the surrounding X-ray IGrM. Many theoretical models of the evolution of radio lobes assume that the surrounding medium has zero magnetisation (e.g. Gourgouliatos et al. 2010) and typical observed magnetisation levels in an intragroup medium have been quite low at a radius of hundreds of kiloparsec from a galaxy group centre. However, Tashiro et al. (2000) argue that the magnetic energy density of the diffuse, large-scale X-ray plasma is roughly equal to the electron energy density of the lobes of NGC 612. In order to accumulate a density of a thin skin of $n_e \sim 8 \times 10^{-5}\,\mathrm{cm^{-3}}$, little compression of X-ray plasma is required.

We note that our assumed thin-skin pathlength is largely speculative and motivated by similar values used for other radio lobes and the derived n_e used in the previous argument is inversely proportional to the pathlength of the thin skin. To explore how this may change our argument of the thin-skin approximation, changing the pathlength by a factor of 2 (i.e. $10\,\mathrm{kpc} \lesssim dl \lesssim 40\,\mathrm{kpc}$) results in an implied electron density within the range of $2 \times 10^{-4}\,\mathrm{cm^{-3}} \lesssim n_e \lesssim 4 \times 10^{-5}\,\mathrm{cm^{-3}}$. This range of electron densities would still be physically achievable through the compression of the X-ray IGrM.

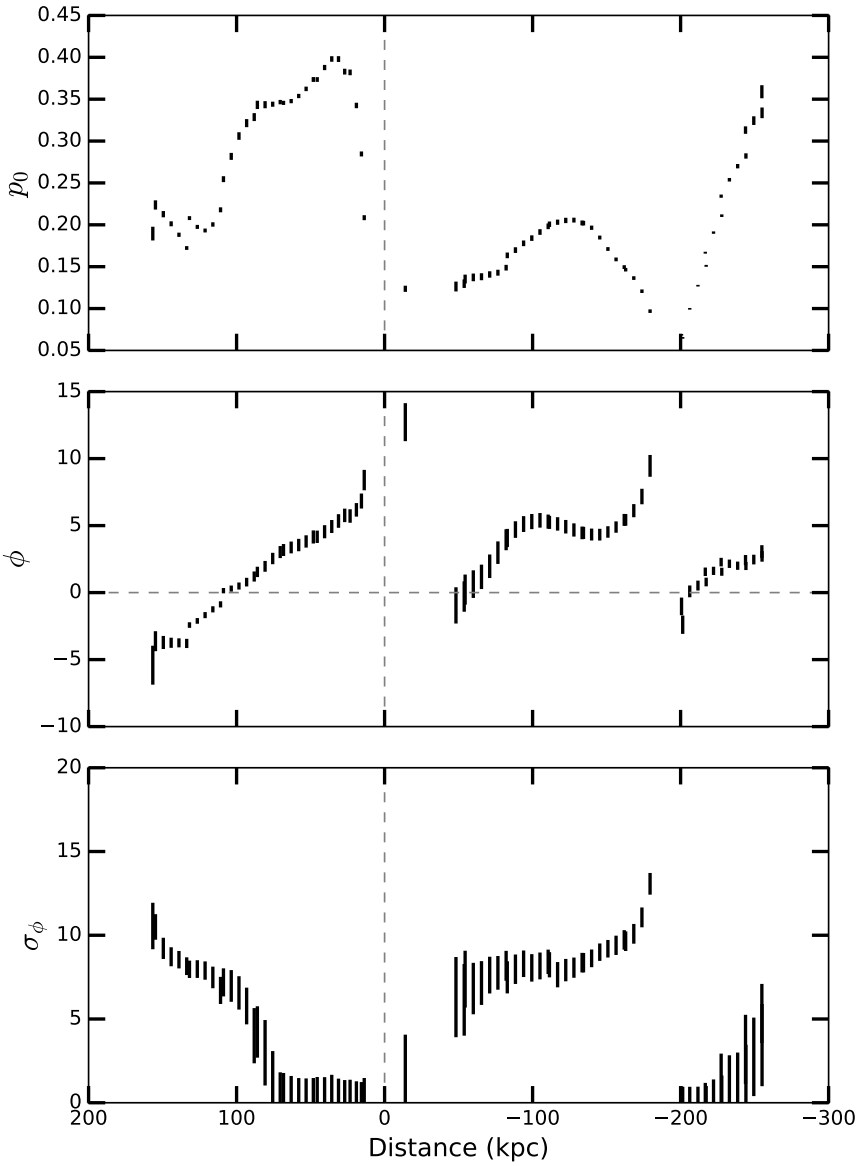

Figure 3.12: Intrinsic polarisation, Faraday depth and Faraday dispersion as a function of position along the lobes of NGC 612, as traced by our assumed jet path (e.g. Figure 3.8. The length of each tick mark represents the corresponding uncertainty at each position. The x-axis is indicative of the distance from the optical galaxy, with negative values indicating positions west of the galaxy. The vertical dashed line therefore marks the position of the host galaxy. The horizontal dashed line in the middle plot indicates $\overline{\phi} = 0$ rad m^{-2}.

Given the lopsided distribution of X-ray plasma, the apparent uniformity of the Faraday depth signal in NGC 612 might be explained if the expanding lobes have swept up the ambient IGrM as they expand outward. Hydrodynamic simulations carried out by Bicknell et al. (1990) show that as lobes expand, it is possible for Kelvin-Helmholtz instabilities to form on the surface of the lobe due to feedback between the synchrotron material and the surrounding medium. In such a case, waves of material would appear on the surface of the radio galaxy, resulting in a unique Faraday depth pattern. Bicknell et al. (1990) also point out that a positive and negative variation in the sign of the Faraday depth should exist on a scale length equivalent to half of the wavelength of the eddy.

Assuming that the jet is the dominant driving force for the expansion of the radio lobes, we choose to evaluate the polarisation properties along the path that the jet traces, as shown in Figure 3.10. The middle panel of Figure 3.12 shows a rough sinusoid in the Faraday depth values as a function of distance from the optical counterpart. The half-wavelength of the surface wave appears to be $(\lambda/2) \sim 1.1\,\mathrm{arcmin} \sim 40\,\mathrm{kpc}$. Although in all instances we do not see the Faraday depth change when the gradient of the Faraday depth changes direction, which is expected from Faraday eddies, we note that we have not corrected for the Faraday rotation contribution from the Milky Way, which may be shifting the observed Faraday depth to more positive values.

If we assume that the depth of the surface wave (d_e) is related to the wavelength of the eddy (λ_e), by a ratio of $d_e/\lambda_e \sim 0.3$ (Bicknell et al. 1990) it is possible to estimate n_e and d_e using Equation 5.2 from Bicknell et al. (1990),

$$\Delta\phi \sim 0.49 \times n_e B_{\parallel} \lambda_e, \tag{3.4}$$

where $\Delta\phi$ is the change in Faraday depth between peaks. From Figure 3.12, we can see that the peak-to-peak difference in Faraday depth is $\Delta\phi \simeq 6\,\mathrm{rad\,m^{-2}}$. Using our previously discussed estimate of $B_{\parallel} \simeq 2.4\,\mu\mathrm{G}$ and an eddy wavelength of $\lambda_e \sim 80\,\mathrm{kpc}$, we find that the necessary electron density in the surface wave would be $n_e \simeq 6 \times 10^{-5}\,\mathrm{cm^{-3}}$ with an implied surface wave depth of $d_e \simeq 20\,\mathrm{kpc}$.

This is in excellent agreement with our thin skin estimate using the mean Faraday depth, although there are large uncertainties in our assumptions. The exercise argues that the observed Faraday signal associated with the bulk of the lobes of NGC 612 can be explained by Faraday eddies formed via an interaction with the X-ray IGrM. This scenario also indicates a preference for the Faraday rotating material to be located external to the synchrotron-emitting plasma.

3.7.3 Internal Faraday Rotation

In contrast to the previous section, we now explore the possibility that the thermal- and synchrotron plasmas are located cospatially within the radio lobes.

NGC 612 contains a young stellar population with on-going large-scale star-formation throughout the disc of the galaxy (Emonts et al. 2008). It is possible that as the lobes of NGC 612 expanded through the disk of the optical galaxy, it advected some material from the stellar disk (Begelman and Cioffi 1989; Churazov et al. 2001).

The advection process may be responsible for the observed Faraday rotation since any thermal material in the lobes would have been entrained from the galactic disk (Laing and Bridle 2002). In this instance, the synchrotron emitting plasma is mixed with the thermal material from the galaxy and the bulk of the observed Faraday rotation takes place internally to the radio lobes. If the Faraday rotation associated with NGC 612 is taking place inside the lobes of the radio galaxy, it would be one of only a few objects (e.g. O'Sullivan et al. 2013) that have been shown to have this distribution of magneto-ionic material. It should be noted that the work carried out by O'Sullivan et al. (2013) was over a more limited frequency range ($1288 - 1480$ MHz) with more sparse sampling across the imaged bandwidth. As polarisation work towards multiple radio sources has yet to be carried out over as large of a band as the work presented here, it is possible that the detection of internal Faraday rotation could become more frequent towards large radio lobes.

Assuming that the lobes are threaded with thermal, magneto-ionic material, it is possible to approximate the amount of thermal material that needs to be diffused in the the lobes of NGC 612 to produce the observed signal. Using our previous assumed values for the pathlength (l), f and $B_{\parallel}$ (§3.7.1), we rearrange Equation 1.13 to solve for the free electron density (n_e) and calculate an implied density of $n_e \sim 1.8 \times 10^{-5}\,\mathrm{cm}^{-3}$. The radio lobes can be roughly resemble two cylinders, each with a radius of 70 kpc and lengths of 160 and 220 kpc, for the eastern and western lobes, respectively. This geometry implies a total volume of the radio emission of $V \sim 2 \times 10^{71}\,\mathrm{cm}^3$. Were this volume to be uniformly filled with the above calculated n_e, it follows that the implied thermal mass within the lobes would be $M_{th} \sim n_e m_H f V \sim 2.5 \times 10^8\,M_\odot$ where m_H is the mass of ionised hydrogen. We note that this estimate depends heavily on the numerous assumptions that we have made.

It is possible that thermal material was entrained from the galaxy as the jet pushed its way through the galactic disk (Laing and Bridle 2002). If we assume an age for the radio lobes of 0.1 Gyr (Blundell and Rawlings 2000; Parma et al. 2002), the lobes of NGC 612 would need to entrain an average amount of $\sim 2.5\,M_\odot\,\mathrm{yr}^{-1}$. This estimate is a few orders of magnitude larger than the amount needed to decelerate relativistic jets (Bicknell 1994; Laing and Bridle 2002) and it is unlikely that entrainment is the sole origin for the bulk of the thermal material. It is more likely that the bulk of the magneto-ionic plasma responsible for the observed Faraday rotation signal has been accumulated by a combination of the mechanisms discussed (e.g. thin skin, Faraday eddies and entrainment).

3.7.4 The Hot Spot

The area surrounding the hot spot in the eastern lobe offers an intriguing polarisation signal. In this region, dispersion levels are strongest (Figure 3.11) and the Faraday depth sign is opposite to that of the majority of the radio galaxy (Figure 3.10). At this particular location, NGC 612 is interacting with its neighbouring galaxy NGC 619 via a tenuous HI bridge (Emonts et al. 2008).

Depolarisation can be caused by change in strength or direction of the coherent magnetic field. It is therefore possible that the observed depolarisation is due to an increase in the turbulence of the magnetic field as the jet of NGC 612 is ploughing into the tidal bridge. However, this increase in random motion would not give rise to a sign change in the coherent magnetic field direction. Furthermore, Figure 3.9 shows that the intrinsic polarisation angle near the hot spot does not have a significant change in orientation, insinuating that the corresponding sign-change in Faraday depth does not come about due to a characteristic change in the geometry of the synchrotron plasma. Explaining the change from positive to negative Faraday depth may require additional factors.

One possibility is that there exists an intervening cloud of magnetised gas along the line of sight associated with the hot spot. Emonts et al. (2008) detect a faint bridge of HI material spanning the distance between NGC 612 and neighbouring galaxy NGC 619. If this bridge, which is believed to be tidal in origin, were to host a coherent line-of-sight magnetic field oriented opposite that of NGC 612, the observed Faraday depth associated with this region would appear opposite to the bulk of NGC 612 if the magnetic field in the HI cloud were sufficiently negative.

There have been numerous detections of magnetised, tidally stripped material associated with continuum bridges (e.g. Condon et al. 1993; Nikiel-Wroczyński et al. 2013a; Basu et al. 2017) as well as neutral HI tidal features (Hill et al. 2009; McClure-Griffiths et al. 2010; Kaczmarek et al. 2017). The existence of a coherent magnetic field in the HI cloud could provide structural support against the intruding AGN jet, resulting in a longer lifetime for the tidal remnant. Higher resolution observations of the polarised signal associated with the HS, in addition to information on the free-electron density in the HI cloud, are needed to explore this region further.

3.8 Conclusions

We have presented a spectropolarimetric study of the radio galaxy NGC 612 using broadband observations covering 1.3 - 3.0 GHz taken with the ATCA. It is immediately evident that the polarisation signal depends upon the position within the lobes. We have demonstrated that majority of the polarisation signal seen associated with the radio lobes can be explained through a single polarisation component, although the exact mechanism re-

mains unclear because of similarity between model fits. Using qu-fitting, we were able to confidently recover the intrinsic polarisation properties associated with the lobes.

We have explored any environmental implications from the observed Faraday depth signal. While we cannot rule out the entrainment of thermal material from the galactic disk, we find evidence of Faraday eddies on the surface of the synchrotron lobes, as seen by a sinusoidal variation in Faraday depth as a function of distance along the lobe. We argue that these surface waves are formed via the expansion of the synchrotron lobes into the surrounding medium, forming a thin skin ($dl \sim 20$ kpc) of thermal material.

We estimate a total minimum magnetic field strength of $B_{min} \sim 4.2\,\mu$G in the lobes of NGC 612. If the thermal material is distributed as a thin skin, we calculate a free-electron density in the skin of order $n_e \sim 10^{-4}\,\mathrm{cm}^{-3}$, assuming equipartition. As NGC 612 is embedded in a halo of hot, X-ray emitting plasma, we believe that achieving this density would require little compression of the ambient IGrM.

We observe intriguing Faraday signal at the location of the hot spot in the east lobe of NGC 612. At this location, a HI cloud, arising from a previous interaction, has been observed. We hypothesise that this signal might be explained if the tidal material is threaded with a coherent magnetic field, oriented in the opposite direction to the bulk of the Faraday rotating material. Future high-resolution polarisation observations, in addition to pathlength estimates, are needed to confirm this hypothesis.

In order to correctly account for any spectral dependencies that may be associated with the two jets or the compact hot spot in the lobes, follow-up, high-resolution radio polarisation observations are required. Furthermore, high-resolution follow-up observations have the potential to break the ambiguity between our modelling results, in that they may resolve smaller surface features, that are predicted by our assumed thin skin model, which have been smoothed by our synthesised beam. Such an observational approach would be advantageous for all future related studies. The early science stages of the Australian Square Kilometre Array Pathfinder will provide additional λ^2 coverage allowing for the resolution of all Faraday components along the line-of-sight, making it easier to deduce the true polarisation mechanisms responsible for the observed signal. Better electron density estimates of the intragroup medium and magnetic field estimates will strengthen further analysis of the NGC 612 system and should be possible with sensitive X-ray observations, such as those offered with the XMM-Newton telescope.

4

FARADAY STRUCTURES ON THE LOBES OF MSH 05−3*13*

4.1 INTRODUCTION

The large synchrotron lobes typically associated with FR I radio galaxies serve as polarised backdrops towards which one can investigate the foreground magnetic field. The vast majority of investigations into the nature of kiloparsec-scale Faraday depths associated with the lobes of FR Is have found distributions that appear nonhomogeneous (e.g. Bonafede et al. 2010; Govoni et al. 2010). The irregular distributions of Faraday depth structures have been largely attributed to the superposition of intervening material along the line of sight. For example, Bonafede et al. (2010) observed seven individual FR I radio galaxies and concluded that in all cases, the physical location of the observed Faraday structures were not immediately coincident with the source of polarised emission. However, there have been noted exceptions. Feain et al. (2009) argue that the rotation measure and depolarisation structures seen on the surface of Centaurus A were intrinsic to the lobes themselves. And as we have argued in Chapter 3, the lobes of NGC 612 also show a strong correlation between the Faraday depth distribution and total intensity surface features.

There is still no clear consensus on what aspect of their cosmic environment causes the observed Faraday depth distributions on the lobes of radio galaxies. This chapter aims to address this with a detailed analysis of the polarised signal associated with the radio galaxy, MSH 05−3*13* (Mills et al. 1960). With an angular extent of 9 arcminutes and a total flux of 1.85 Jy at 843 MHz (Jones and McAdam 1992), MSH 05−3*13* is one of the brightest, large angular-scale radio galaxies in the Southern hemisphere sky.

MSH 05−3*13* hosts two extended lobes that stretch over an angular scale of $\sim 9'$. At a redshift of $z = 0.03719$ (Wegner et al. 2003; Jones et al. 2009), this translates to a physical scale of 420 kpc. There exists a narrow jet emanating from a compact central core. The lobes are limb-brightened but have no clear hot spots, though this

Table 4.1: Summary of the observing log for MSH 05−3*13*, which is a subset of ATCA project C2776. Column 1 gives the array configuration. The total time spent on-source each run is listed in column 2. Column 3 gives the UT date of the commencement of the observations.

Array Config.	Time On-Source (hours)	Obs. Date
1.5 C	0.39	2012 Dec 03
750 C	0.73	2013 Jan 25
6A	0.44	2013 Feb 24

is not surprising as the radio galaxy is not particularly powerful, and Ekers et al. (1989) classify MSH 05−3*13* as an FR I. The optical counterpart is the elliptical galaxy, ESO363 G-027, (R.A. 05h48m27.60s, Dec. -32d58m38.0s J2000, $\ell = 238.172°$, $b = -26.794°$, Lauberts 1982).

Both lobes of MSH 05−3*13* are deflected towards the east. While the galaxy exists as the dominant member of a sparse group (N=6, Tully 2015), the group members all lie eastward of the radio source. The relatively low density environment of MSH 05−3*13* makes it a good candidate with which to study Faraday rotation within and amongst radio jets and lobes.

This chapter is laid out as follows. We detail the observing and imaging strategy carried out in §4.2. §4.3 presents a brief recap of our analysis procedure, which has been described in-depth in Chapters 2 and 3. We present our results in §4.4, which is followed by a detailed analysis of the polarisation signal in §4.5. In §4.6, we discuss the observed Faraday gradients and possible interpretations.

4.2 Observations & Imaging

The radio galaxy was observed with the Australia Telescope Compact Array using the Compact Array Broadband Backend (CABB, Wilson et al. 2011) covering $1300 - 3000$ MHz with a spectral resolution of 1 MHz. Observations were taken in snapshot mode in multiple array configurations in order to be sensitive to a range of angular scales. Our observations are summarised in Table 4.1 with our final uv-coverage, shown in Figure 4.1. The galaxy and surrounding environment were observed as a mosaic of six pointings which were Nyquist sampled for 3100 MHz. Pointings were observed in 30 second intervals and the phase calibrator PKS B0537−286 was observed at the completion of $3 - 4$ mosaic cycles, at typical intervals of $\lesssim$ 30 minutes. PKS B1934−638 was used as the bandpass and flux calibrator for each set of observations.

Our data were calibrated, reduced and flagged using the MIRIAD software package (Sault et al. 1995). Bandpass and polarisation leakage solutions were calculated every 512 MHz. The majority of the data were flagged via the automated task '*pgflag*' with

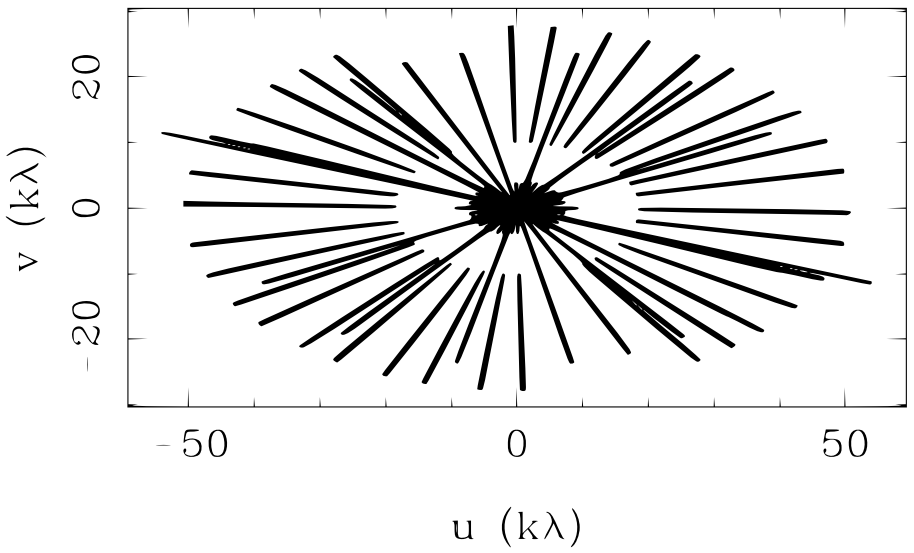

Figure 4.1: The final uv-coverage for our observations of MSH 05−3*13*.

minimal manual flagging being carried out with tasks '*blflag*' and '*uvflag*'. In total, 38% of the original dataset was flagged due to radio frequency interference (RFI).

Naturally weighted Stokes I, Q, U and V images were made averaging every 32 MHz. Joint maximum entropy deconvolution was carried out with the task '*pmosmem*' and allowed to converge to an rms level that was 1.2 times the theoretical noise of the input dirty maps. Cleaned images were restored with a $15''$ synthesised beam with $3''$ pixels. One beam represents a physical scale of ~ 10.5 kpc at the distance of MSH 05−3*13* for $H_0 = 73.0\,\mathrm{km\,s^{-1}\,Mpc^{-1}}$. We compare the measured integrated flux from our data to previously published flux levels (Figure 4.2) and find cohesion between our measured spectral index ($S \propto \nu^{\alpha}$) of $\alpha = -0.73$ and that implied from previous studies.

As noted by Ekers et al. (1989), the diffuse outer lobes of MSH 05−3*13* are lacking any clear, compact hot spots. The total intensity images shown in Figure 4.3 show the existence of warm spots near the ends of the lobes. Furthermore, contours bounding the lobe ends appear sharp, especially in the South Lobe, which suggests that the synchrotron plasma is confined by the external medium.

The reduction described above results in 40 independent channel maps in Stokes I, Q, U and V. Representative Stokes I, Q and U maps of the lowest, middle and highest frequency observations are given in Figure 4.3. The right column of Figure 4.5 shows the Stokes I spectra in log-space for three representative pixels in the radio lobe. The level of linearly polarised emission, as traced by Stokes Q and U, is clearly shown to have a strong frequency dependence across the lobes of MSH 05−3*13*. There is also a polarised background radio source near RA = 05h 49m 26.37s; Dec = −32° 47m 48.67s (J2000).

Uncertainty in Stokes I, Q and U maps were measured at each frequency interval as

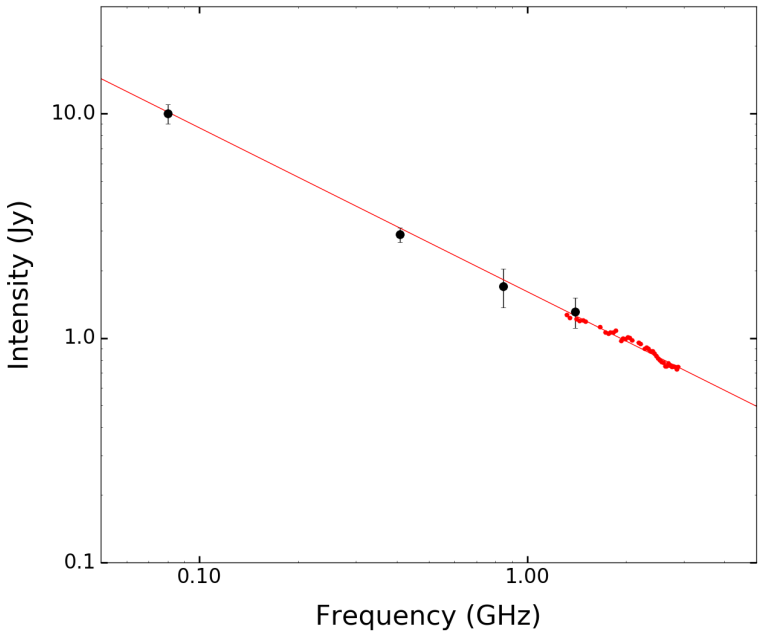

Figure 4.2: MSH 05−3*13* flux density as a function of wavelength. Our measurements are shown in red with the marker size larger than the measured uncertainty. Flux levels from the literature are shown in black with displayed values from Slee (1995) (80 MHz) Ekers et al. (1989) (408 MHz) and Jones and McAdam (1992) (843 MHz) and van Velzen et al. (2012) (1400 MHz). Our observations return a source spectral index of $\alpha = -0.73$.

the rms value (σ) of an area devoid of emission. We measured typical rms flux densities of $0.68, 0.53$ and 0.53 mJy/beam for Stokes I, Q, and U, respectively. In order to estimate the uncertainty in linear polarisation, we assume $\sigma_Q \simeq \sigma_U \simeq \sigma_P/\sqrt{2}$. A spectral index map of the entire radio galaxy was created by fitting the total intensity spectrum at each pixel location assuming a simple power law for pixels with a surface brightness $S(\nu) \geq 3\sigma_I$ for more than 80% of our observed frequency range (Figure 4.4). This image includes more pixels than were accepted for our analysis, as there was no polarisation emission criteria in place for pixel selection. Spectral index fits are shown for a few representative pixels in Figure 4.5 on the right-hand side.

We note that the intriguing spectral index signature associated with the jet, which displays a varying spectral index pattern with values typical of $-0.4 \leq \alpha \leq 0$. These flat α values are atypical for large-scale radio jets and are considered unusually flat, in contrast to compact cores which may exhibit flat spectra (e.g. Saripalli et al. 2002; Subrahmanyan et al. 2006). Previous investigations into the core of the radio galaxy have shown the source to have a positive spectral index ($\alpha = +0.34$ Slee et al. 1994), which is in agreement with our work. Furthermore, the measured total flux (Figure 4.2) suggests

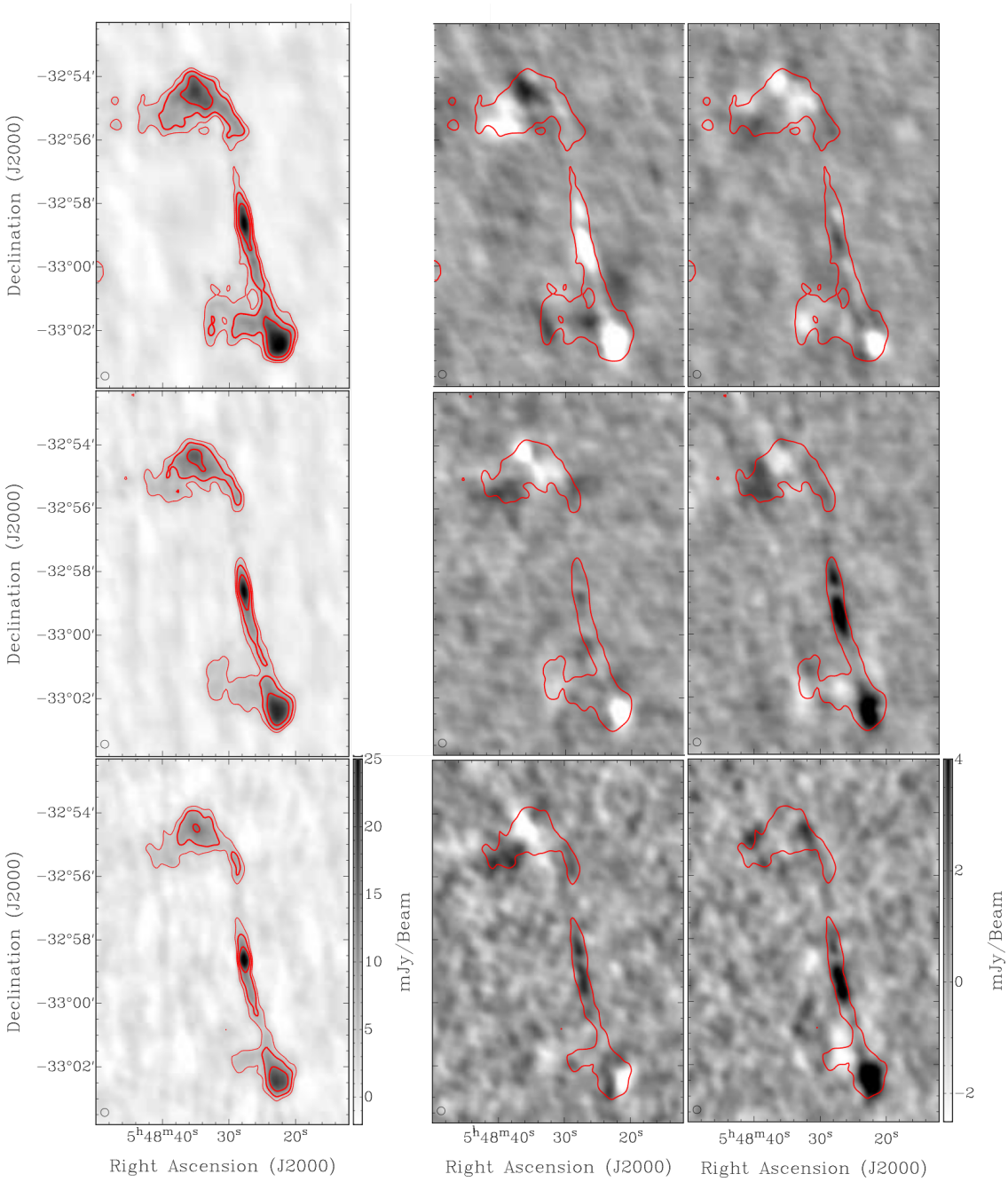

Figure 4.3: Images of MSH 05−3*13* in Stokes I, Q and U (from left to right) at frequencies of $1332, 2100$ and 3000 MHz (from top to bottom). The flux scales have been keep identical for each Stokes parameter and is displayed for the highest frequency images. The Stokes I maps have red contours of total intensity representing $3, 6,$ and 12 mJy/beam for each corresponding frequency. For the linear polarisation maps (Q, U), only the lowest total intensity contour is shown. All images have the synthesised beam represented in the lower lefthand corner.

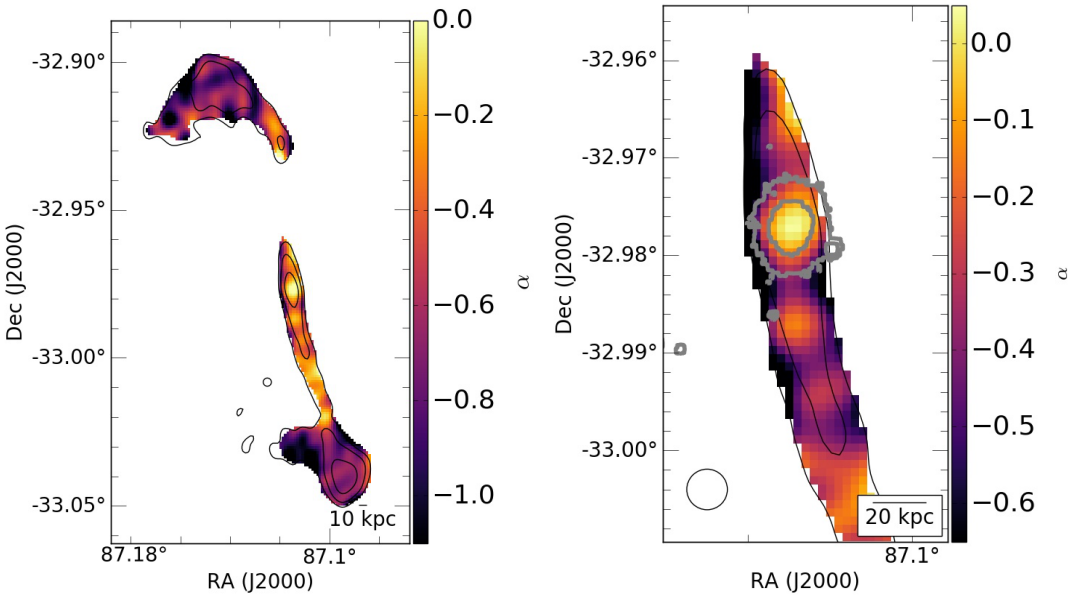

Figure 4.4: (*Left*) Spectral index map for all pixels with a $S(\nu) \geq 10\sigma$ in total intensity. (*Right*) Spectral index values for the region associated with the jet and core. In both images, black contours trace total intensity (Stokes I) levels spanning $4, 8,$ and 16 mJy/beam.

that we are not missing any flux. Attempts to recalibrate the data were made, with a similar outcome. We therefore are unable to comment further on the spectral index in this region and will be made the focus of a future, high-resolution investigation.

To create our polarised dataset, a pixel spectra was accepted if the total intensity and linearly polarised intensity ($P^2 = Q^2 + U^2$) were greater than $5\sigma_I$ and $3\sigma_P$ for 80% of the observed frequency range. This results in 984 pixel spectra associated with MSH 05−3*13* and the polarised radio background source near our primary target. This is equivalent to roughly 50 independent beams over the area of the radio galaxy.

4.3 ANALYSIS

It now becomes convenient to work in terms of fractional polarisation, such that $q = Q/I$, $u = U/I$ and $p^2 = q^2 + u^2$. As we have done with Chapters 2 and 3, we create fractional polarised spectra, by dividing the observed $Q(\lambda^2)$ and $U(\lambda^2)$ by a second order polynomial fit to the Stokes I emission. This is done with the same technique described in previous chapters for similar motivations. Figure 4.5 gives an example of typical fractional polarisation spectra across the radio galaxy.

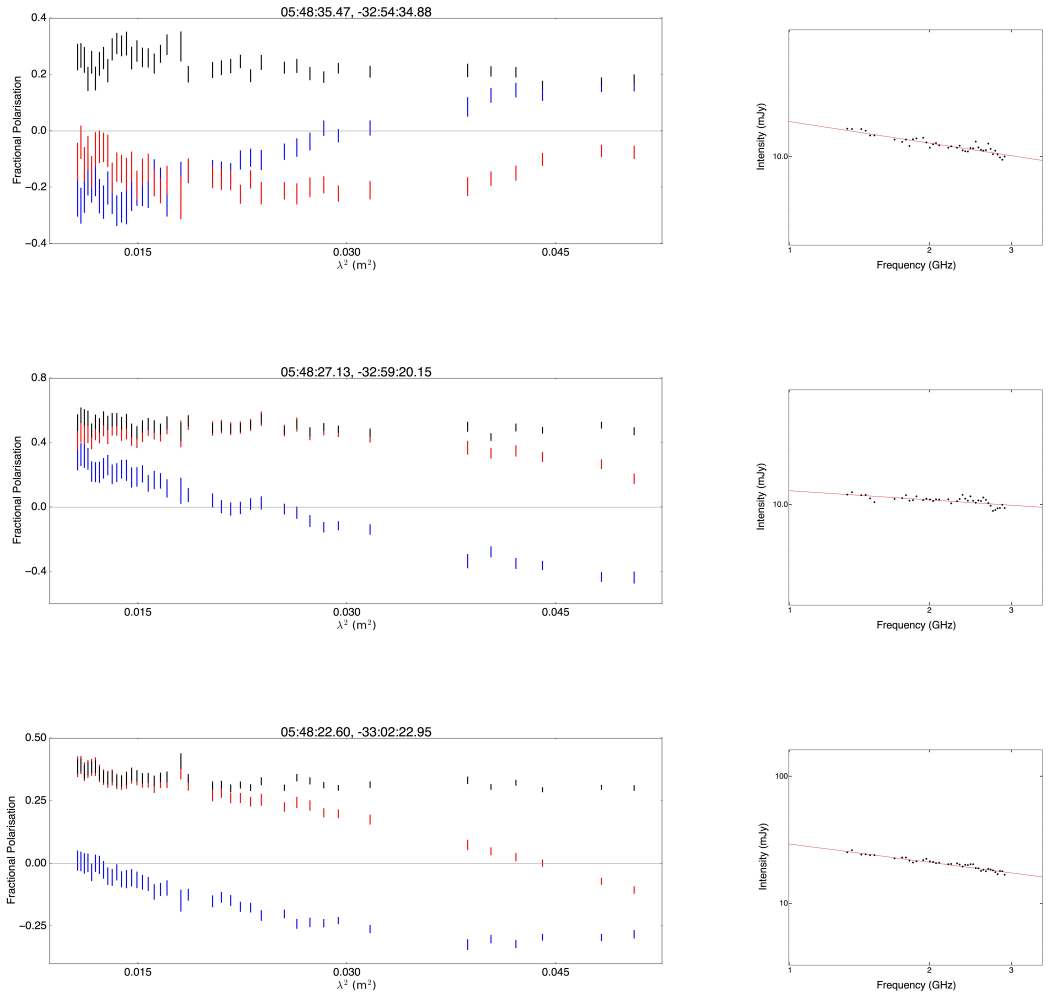

Figure 4.5: (Left column): Polarised spectra extracted from 3 sample pixels in MSH 05−3*13*. Blue and red markers are representative of the q and u intensity, respectively. The length of each marker is equivalent to the flux uncertainty. Black markers represent the fractional polarisation. The coordinate of each pixel in J2000 (R.A., Dec) is given at the top of each plot. (Right column): Corresponding total intensity spectra in log-space. The red line represents the fit to the spectral index value of the pixel.

4.3.1 POLARISATION MODEL FITTING

Based on a thorough examination of the polarised spectra (e.g. Figure 4.5, we chose to fit the external Faraday dispersion model (EFD, § 1.4.1) to the entirety of the polarised emission. In order to obtain the intrinsic polarisation properties along the line of sight, we employ the qu-fitting technique, as previously described in Chapters 2 and 3. Given the tendency for the EFD model to return a $\chi^2_r \leq 1$, we discounted fitting other, more complicated polarisation models, as this low χ^2_r value already suggests our model may be over-fitting the data. As we have discussed § 3.6, this is not unexpected for a seemingly simple polarisation spectrum and the low χ^2_r is reflective of the minimum number of free-parameters of any polarisation model.

4.4 RESULTS

4.4.1 INTRINSIC POLARISATION FRACTION

The map of intrinsic fractional polarisation (p_0) is presented in Figure 4.6. Also shown in Figure 4.6, we delineate three individual regions which we will address in our analysis and discussion. Maps of uncertainty are given in Appendix C, with general confidence levels introduced in the text.

Figure 4.6 shows that p_0 is strongly dependent upon relative position along the radio lobes of MSH 05−3*13*. The overall polarisation of the lobes is surprisingly high, with a mean $\overline{p}_0 = 0.30 \pm 0.12$ and peak intensities of $p_0 \simeq 0.6$ existing at the termination points of the North and South lobes. The inner jet region shows an asymmetric spatial distribution of fractional polarisation, with the mean values in the North jet of $\overline{p}_0 = 0.27 \pm 0.08$ compared with $\overline{p}_0 = 0.40 \pm 0.14$ in the South jet.

We are confident in our fit to Stokes I and total flux measurements for MSH 05−3*13* (Figure 4.2). Therefore, we believe the returned levels of polarisation are correct. The mean uncertainty returned from qu-fitting is $\overline{\sigma}(p_0) = \pm 0.018$ (Figure C.1(a)).

Contrary to other radio lobes studied at similar frequency ranges in the literature (e.g. NGC 612, Chapter 3; Cygnus A, Bicknell et al. 1990; Fornax A, Anderson et al. 2017 *submitted.*), we do not observe any strong depolarisation regions distributed on the surface of the lobes themselves. If depolarisation were due to the development of instabilities within the lobes, one would expect the oldest material, in this case the diffuse backflow, to exhibit the strongest depolarisation. One explanation could be our relatively high total intensity and polarisation thresholds; depolarisation regions may be present at lower signal-to-noise levels. For example, although we see polarised emission associated with the diffuse, back-flow regions of the north and south lobes (Figure 4.3) no pixels from this region are accepted for our analysis due to insufficient Stokes I intensity.

Furthermore, future high-resolution polarisation studies of this source may resolve small-scale depolarisation which our current imaging beam is smoothing over.

4.4.2 Intrinsic polarisation angle

The de-rotated intrinsic polarisation angle (Ψ_0) across MSH 05−*313* is shown in Figure 4.7, where the length of each vector has been weighted to represent the fractional polarisation at each position. Ψ_0 is directly indicative of the position angle of the electric field vector with $B_\perp$ being oriented orthogonal to Ψ_0. The red contours in Figure 4.7 trace the red optical light from the host galaxy, as observed by the Digitized Sky Survey*. The polarisation angle across the inner jet region and outer lobes has an orientation largely aligned along the jet. This behaviour is typical for radio jets (Laing 1981). Typical uncertainties in position angle are $\overline{\sigma}(\Psi_0) = \pm\, 3.3°$.

4.4.3 Observed Faraday depth and the Galactic Plane

A map of the observed Faraday depth (ϕ_{obs}) for the entire imaged region is given in Figure 4.8. The ϕ_{obs} values for the entire image are positive with a mean magnitude of $\overline{\phi}_{obs} \simeq +26.7$ rad m^{-2} and a standard deviation $\sigma = 4.5$ rad m^{-2}. The structure of ϕ_{obs} appears to vary smoothly with right ascension and declination, with the lowest value at the southern end of the South lobe and peaking at the location of the background polarised source.

The observed gradient in ϕ_{obs} is consistent with the gradient expected if the Faraday rotation was due to the Milky Way foreground. Our mean $\overline{\phi}_{obs}$ agrees well with regional estimates from Oppermann et al. (2015). The black arrow in Figure 4.8 represents the direction vector towards the Galactic plane, which is oriented $\sim 80°$ clockwise with respect to the radio lobes as they appear in our images. This direction is consistent with the apparent direction of the gradient in Faraday depth across our field of view. Motivated by the relatively low Galactic latitude of the radio galaxy, ($b \simeq -26.8°$), we treat the total observed Faraday depth as the summation of components due to the Milky Way and source(s) located at further distances. In doing this, we assume the contributions from MSH 05−*313* dominate the residual line-of-sight Faraday rotation, which we denote by ϕ_{RL}. By assuming now that $\phi_{obs} = \phi_{MW} + \phi_{RL}$, the dominant Milky Way foreground, which acts as an external Faraday screen, can be fit and subtracted.

If we assume that the Galactic plane acts as a Faraday screen for the polarised emission from MSH 05−*313*, we can fit and subtract the additional Faraday rotation that is

*The Digitized Sky Surveys were produced at the Space Telescope Science Institute under U.S. Government grant NAG W-2166. The images of these surveys are based on photographic data obtained using the Oschin Schmidt Telescope on Palomar Mountain and the UK Schmidt Telescope. The plates were processed into the present compressed digital form with the permission of these institutions.

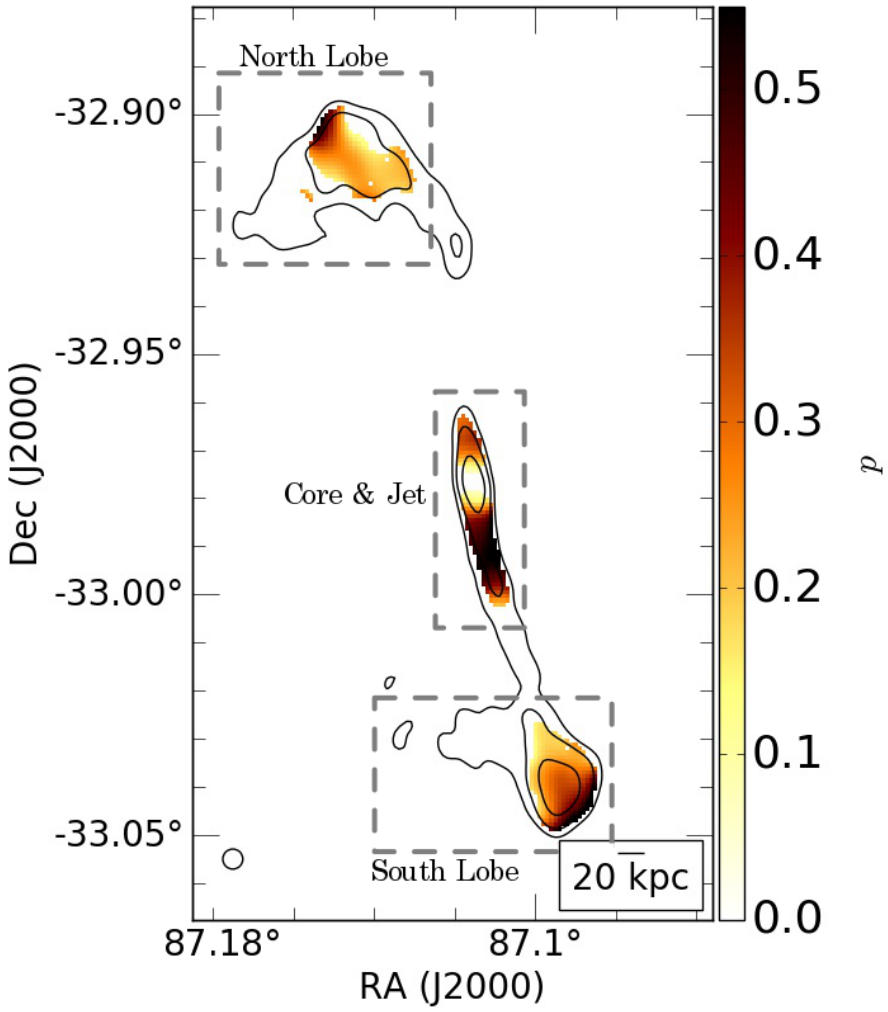

Figure 4.6: Map of the intrinsic polarisation fraction (p_0) across MSH 05−3*13*. Surface brightness contours are shown as solid black lines for $4, 8,$ and 16 mJy/beam at 2100 MHz. Areas designated by dashed grey lines identify regions that will be discussed individually in our analysis and discussion. Our 15″ synthesised beam is shown in the lower left corner, with a scale bar shown in the lower right.

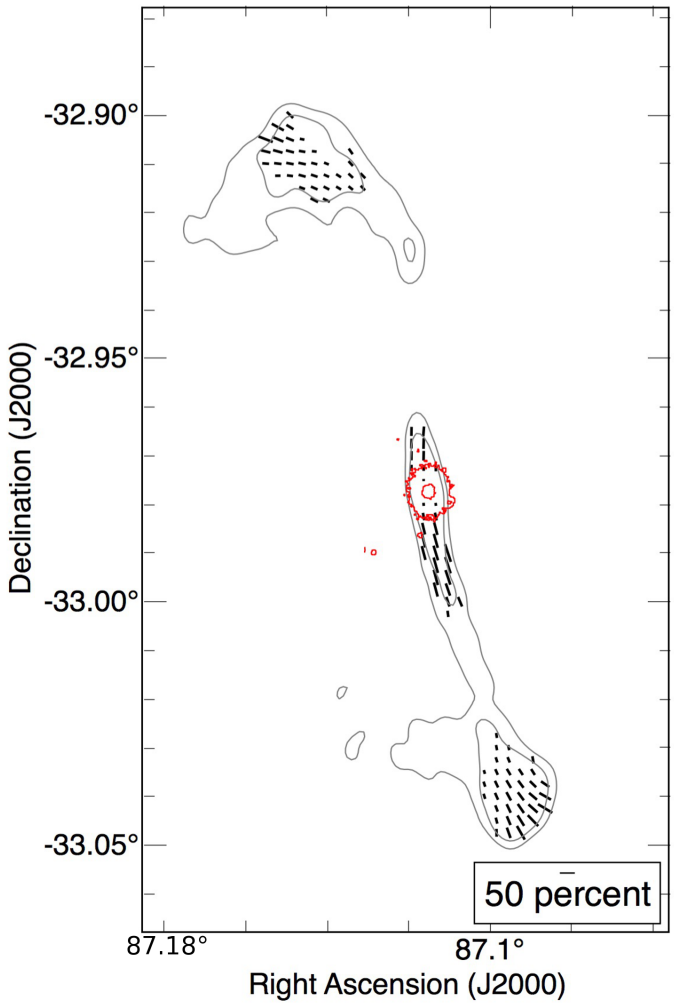

Figure 4.7: Intrinsic polarisation angle (Ψ_0) across the lobes of MSH 05−*3*13. The length of each vector is proportional to the intrinsic polarisation level at that position. A fractional-polarisation scale bar is given in the lower righthand corner. Total intensity contours are shown at 4 and 8 mJy/beam at 2100 MHz. The red contours traces the optical emission associated with the galaxy (Digitalized Sky Survey). Typical uncertainties in Ψ_0 are $\overline{\sigma}(\Psi_0) = \pm 3.3°$.

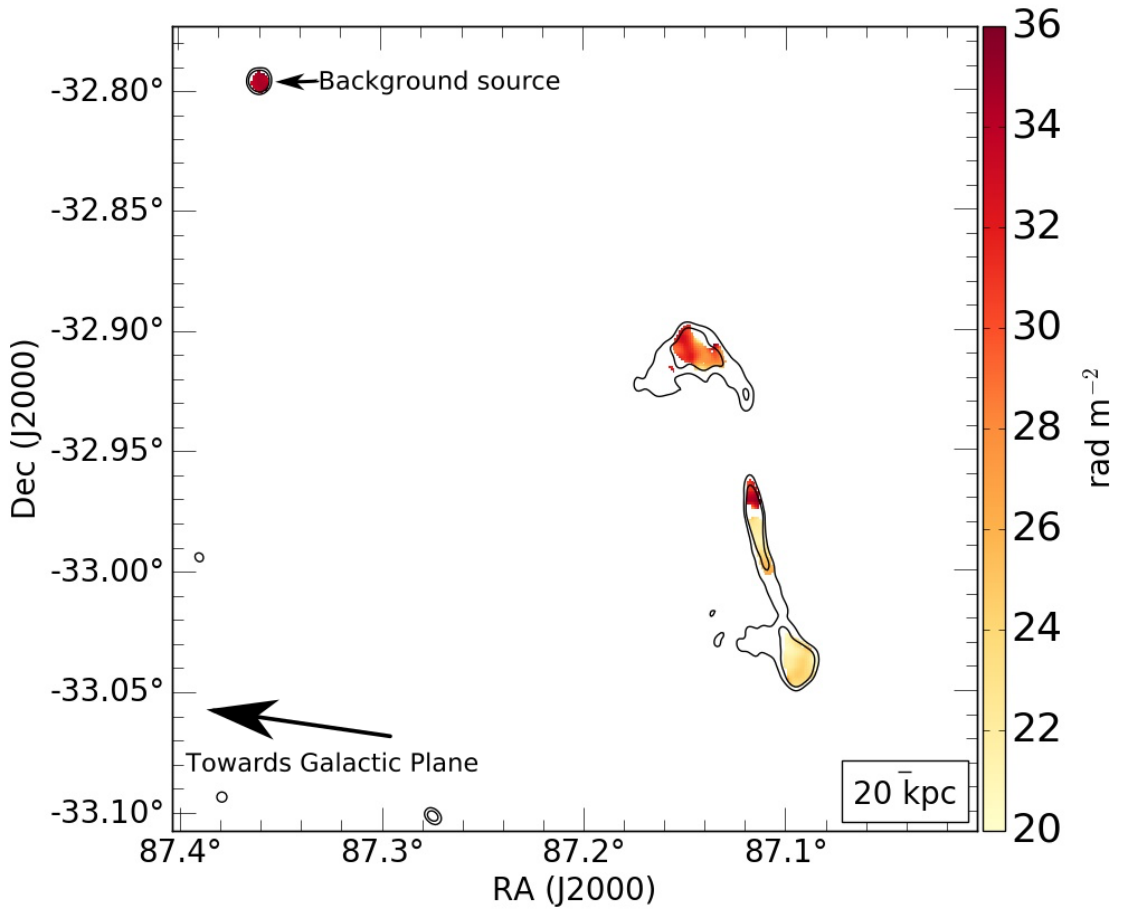

Figure 4.8: Map of observed Faraday depth (ϕ_{obs}) across the entire imaged region, including the polarised background source (§4.2). Surface brightness contours are shown in black for $4, 8,$ and 16 mJy/beam. The $15''$ synthesised beam is shown in the lower lefthand corner.

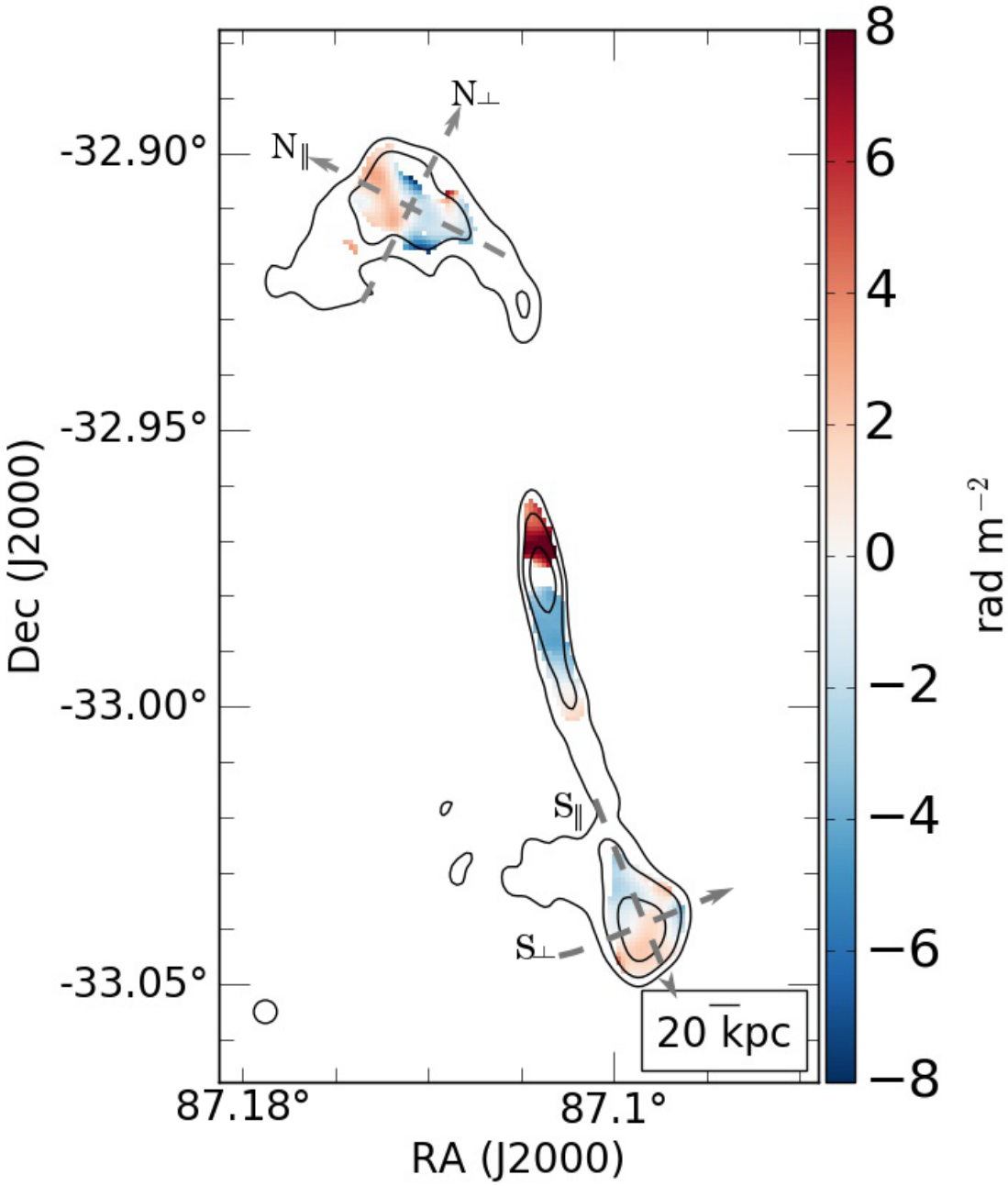

Figure 4.9: Map of the MW-corrected Faraday depth across MSH 05−3*13*. Total intensity contours are overlaid at $4, 8,$ and 16 mJy/beam. Dashed lines are shown in both the North and South lobe, taken to represent the profiles that run parallel (subscript '$\parallel$') and perpendicular (subscript '$\perp$') to the bulk movement of material.

induced by the Galaxy. We choose to fit a tilted-plane model of the Milky Way Faraday depth, $\phi_{MW}(\alpha, \delta)$, to the ϕ_{obs} associated only with the lobes of MSH 05−3*13*. In doing so, we allow the background source to act as a means with which we can justify our fit to the Milky Way. If the background polarised point source is effected by a similar Faraday screen due to the Milky Way, expanding our model to the background source should result in $\phi_{corr} \simeq 0$ rad m^{-2} if our previous assumptions are valid.

After fitting and subtracting the model value for $\phi_{\rm MW}(\alpha, \delta)$ from the location of background source, we find the mean, corrected $\overline{\phi}_{corr}$ to be consistent with zero. This value is expected if we assume that the Galaxy is responsible for the majority of the observed Faraday rotation at this latitude.

Figure 4.9 shows the resultant ϕ_{RL} distribution once our approximation to the MW foreground has been removed. This figure reveals a complex Faraday structure where the sign and magnitude of ϕ_{RL} is highly dependent upon its relative position. The jets immediately north and south of the optical galaxy (see Figure 4.6) show oppositely-signed ϕ for the majority of the polarised emission. The North and South lobes both display Faraday depth values that change as function of position. Each lobe exhibits ridges of Faraday depth consistent with 0 rad m^{-2} and oppositely-signed Faraday depths on either side of the ridge defined by $\phi_{corr} = 0$ rad m^{-2}.

4.4.4 FARADAY DISPERSION IN THE JET AND LOBES

Our qu-fitting routine also return estimates of the rms fluctuations in Faraday depth on scales smaller than our synthesised beam (σ^2_ϕ). Any small fluctuations in Faraday depth will be smoothed over a beam, resulting in an overall lower polarisation level. Therefore, regions of high σ_ϕ are coincident with sightlines that exhibit the highest amounts of frequency-dependent depolarisation ($dp/d\lambda^2 < 0$). We will use this correlation between σ_ϕ and depolarisation in our discussion.

Figure 4.10 shows values of σ_ϕ across MSH 05−3*13*. Across the entire radio galaxy, we observe varying levels of Faraday dispersion, which indicate that the bulk of the frequency-dependent polarisation signal is not the consequence of a single, smooth, turbulent depolarising foreground screen (Burn 1966). We note that although ϕ_{RL} values are low compared to σ_ϕ, both parameters are well constrained and we believe them to be representative of the true polarisation behaviour along individual sightlines.

The area of the highest σ_ϕ, and thus depolarisation, is seen in the North lobe, which has a mean $\overline{\sigma}_\phi = 7.7 \pm 2.8$ rad m^{-2}. Intriguingly, the intensity of σ_ϕ across the North lobe appears to have an episodic pattern across the diffuse material and in all regions of MSH 05−3*13*. In contrast, the South lobe exhibits lower dispersion, with $\overline{\sigma}_\phi = 5.3 \pm 1.7$ rad m^{-2} and appears to lack any strong trend with respect to position.

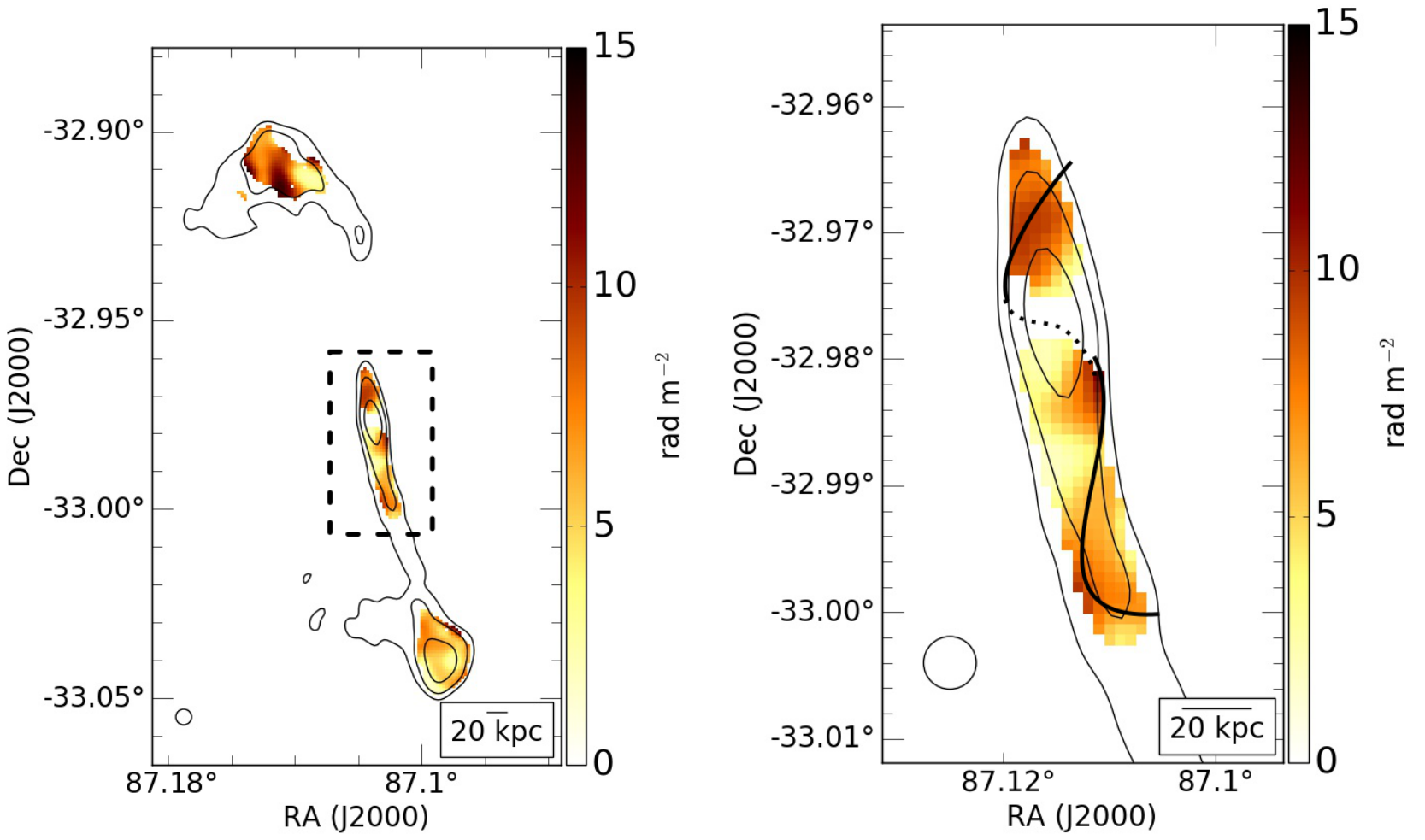

(a) (b)

Figure 4.10: Map of Faraday dispersion (σ_ϕ) across MSH 05−3*13* for the entire radio galaxy (a) and the inner core and jet region (b). Surface brightness contours are shown in black for $4, 8$, and 16 mJy/beam at 2100 MHz. The synthesised beam is given in the lower left-hand corner and a scale bar in the lower right. The twisted black line shown in (b) traces the ridge of highest Faraday dispersion with the dotted line representing one possible geometry between the north and south jet.

Perhaps the most interesting polarisation feature of MSH 05−3*13* is the Faraday dispersion signal exhibited in the region of the jet, where we see the magnitude of σ_ϕ strongly dependent upon position along the inner jet (Figure 4.10(b)) and distance from the optical galaxy. With an average uncertainty in σ_ϕ in this region of ~ 2.3 rad m^{-2}, roughly one-third of the pixels exhibit Faraday dispersion consistent with zero, whereas the other two-thirds exhibit polarisation that is λ^2-dependent. Tracing the peak pixels in σ_ϕ, we see a clumping pattern with peak in σ_ϕ appearing at the alternating edges of the polarised jet emission. As a result of our total intensity and polarisation thresholds, the width of the analysed region is approximately ~ 1.2 synthesised beam across, indicating that we are probably not resolving the full structure of the polarised emission. Nonetheless, the pattern is also repeated vertically over 9.4 independent synthesised beam widths. This region is almost undoubtedly complex and is the focus of future work.

4.5 DISCUSSION

4.5.1 MINIMUM MAGNETIC FIELD STRENGTH

As discussed in Chapter 1.2, spectral indices associated with synchrotron emission act as a probe of magnetic field strength. Therefore, in order to estimate the magnetic field strength in the combined diffuse radio lobes, we first measure the mean spectral index of the north and south lobes. Figure 4.4 shows the spectral index map across each of the lobes for all pixels with a total intensity surface brightness $I(\nu) \geq 10\sigma$. There is a distinct difference between the mean spectral index seen between the jet and the outer lobes. The North and South lobes exhibits a total mean spectral index of $\overline{\alpha} = -0.79$.

Using the mean spectral index of the north and south lobes, we are able to estimate the equipartition energy magnetic field of the diffuse lobes, as per Equation 3 in Beck and Krause (2005). We approximate the lobes as two slabs of pathlength of $l \sim (80 \times f)$ kpc, where f is the filling factor. Little is known of the true value of f in radio lobes and estimates of f vary wildly between astrophysical sources. It is widely held that values of $f \ll 1$ are normal for the volume of FR I radio lobes. Perley et al. (1984) and Carilli et al. (1989) both argue for values of $f \lesssim 0.1$ for the lobes of Cygnus A, assuming pressure equilibrium. As a lower limit, Seta et al. (2013) are only able to constrain the filling factor to $f > 1 \times 10^{-6}$ for the radio galaxy Centaurus A, assuming that the emitting material was distributed in dense clumps. For our analysis of MSH 05−3*13*, we assume an arbitrary value of $f = 0.01$. The two lobes have a combined synchrotron intensity of 1.1 Jy at 1700 MHz and an average intrinsic polarisation fraction of $\overline{p}_0 = 0.20$.

We have no measurement of the inclination of the lobes with respect to the line of sight. However, the similar linear scales of the North and South lobes indicates that we

are observing the radio galaxy nearly in the plane of the sky. Yet, as we pointed out in §4.4.3, the jets immediately north and south of the core are oppositely signed, suggesting that the jet is being viewed at some inclination relative to the observer. Therefore, it is likely that the radio galaxy is inclined at some small angle on the sky, and we assume some arbitrary inclination angle of $i \sim 10°$.

Using the above values, we estimate a total equipartition field to be $B_{eq} \sim 5.4\,(0.01/f)$ μG. We stress that many of the values used in this calculation are largely dependent on our assumptions; in the case of a larger filling factor ($f \sim 0.1$), the implied field estimate becomes $B_{eq} \sim 2.9\,(0.1/f)\mu$G.

We are unable to extend the same analysis to the inner jets and core region, as Beck and Krause (2005) stress, their models only work for spectral indices steeper than $\alpha \leq -0.5$. The jets exhibit a large range of spectral indices with regions of relatively flat spectral indices, indicating possible reacceleration. Combined with the intriguing σ_ϕ associated with the jets, a thorough investigation into this region is the focus of a future study.

4.5.2 Timescales for the Outer Lobes

In order to carry out analysis of the observed polarisation signal, it would be advantageous to have an estimate of the age of the radio plasma of MSH 05−3*13*. Given the relaxed morphology of the outer lobes, the relative distribution of surface brightnesses, and the difference in spectral indices between the inner core and the diffuse outer lobes, we postulate that the evolution of MSH 05−3*13* took place over two active phases. During the first active period, material was expelled leading to the extended lobe emission once the jets turned off and the second burst of activity is just now being witnessed in the jet/core region.

As we have previously noted in §4.2, there is a marked difference between the measured spectral indices in the jet region ($\overline{\alpha} \simeq -0.37$) and the outer lobes ($\overline{\alpha} \simeq -0.79$) (Figure 4.4). The flat spectral index in the core is typically indicative of renewed jet activity and indicates that the material is recently accelerated. Furthermore, the lack of a spectral index gradient along the jet, from a flat at the point of injection and steepening as a function of distance, may indicate that the jet material may be advancing within relic cocoons at speeds of $(0.2 - 0.3)c$ (Schoenmakers et al. 2000). This scenario could also explain why the jet appears to span the space between the two outer lobes. Clarke et al. (1992) argue that restarted jet activity should result in a bow shock within the older cocoon. We do not see this feature in our observations, nor has it been found in other double-double radio galaxies (Saripalli et al. 2002; Kaiser et al. 2000). Similar spectral ageing and morphology arguments are made for the giant radio galaxy PKS J0116−473 (Saripalli et al. 2002) in order to argue for renewed jet activity and give age estimates of the outer lobes.

Given the expected energy losses of the synchrotron electron population over time, a'break' in the power-law spectrum will appear at some characteristic frequency (ν_b) at which the observed spectral index steepens from its initial injected value. If we assume that during the active phase that led to the creation of the outer radio lobes the synchrotron plasma was injected at a similar spectral index value as we see associated with the jet now, we then might expect to observe the break frequency from our total intensity spectra. Upon investigating the total intensity spectra (e.g. right column of Figure 4.5), we find no positions with a significant turnover in spectral index in our observed frequency range over the entire source. We therefore set an upper limit of $\nu_b < 1.3\,\mathrm{GHz}$ in the outer lobes.

Now armed with approximations for the magnetic field strength and an upper limit to the break frequency, we estimate the minimum spectral age of the outer lobes of MSH 05−3*13* using Equation (1) from Liu et al. (1992):

$$\tau \simeq 5.02 \frac{(B/\mathrm{nT})^{0.5}}{(B/\mathrm{nT})^2 + (\mathrm{B_{CMB}}/\mathrm{nT})^2} (\nu_b/\mathrm{GHz})^{-0.5}\, 10^7\,\mathrm{yr}, \tag{4.1}$$

where B_{CMB} is the equivalent magnetic field strength of the cosmic microwave background at redshift z, such that $B_{\mathrm{CMB}} = 0.32(1+z)^2$ nT. Including B_{CMB} in our timescale estimates corrects of inverse-Compton losses. Using Equation 4.1 in conjunction with B_T and ν_b, we find an approximate age for the outer lobes of $\tau \simeq 80$ Myr. A lower magnetic field estimate (returned from a higher assumed f) indicates an older electron population: $\tau(f = 0.1) \simeq 120$ Myr.

Our upper limit of ν_b reflects a lower limit to our age estimates. we explore the timescales implied from a lower break frequency. We find that for $\upsilon_b \sim 408\,MHz$, the age estimates of the lobes are $\tau(\nu_b = 0.408, f = 0.01) \simeq 2 \times 10^8$ and $\tau(\nu_b = 0.408, f = 0.01) \simeq 1.4 \times 10^8$ yr. As our upper limit ν_b and range of possible filling factors return similar age estimates, we conclude that the timescale for the outer synchrotron lobes is $\tau \gtrsim 100$ Myr. This value is in agreement with the average timescale of $\tau \sim 10^8$ yr, over which the emission from radio galaxies is detectable (Komissarov and Gubanov 1994).

4.5.3 FARADAY DEPTH GRADIENTS IN THE OUTER LOBES

The scale of the varying foreground-corrected Faraday depth signature in MSH 05−3*13* (Figure 4.9) implies the existence of thermal material within, or in the immediate vicinity of, the radio galaxy. The small change in the residual Faraday depth indicates that the surrounding galaxy group medium is likely to have a low thermal density (n_e). We observe ridges in the north and south lobes where $\phi_{RL} = 0$ rad m^{-2}, which implies that either n_e or $B_{\parallel}$ are zero. As it is unlikely that the n_e of the intervening medium is zero at these locations, we assume that these positions indicate a line-of-sight field reversal.

The observed change in ϕ_{RL} across the lobes could be due to under-resolving the changes in the regular $B_{\parallel}$ component of the intervening magnetic field. However, this is unlikely, as the Faraday depth values only vary by ± 2 rad m^{-2} in both the North and South lobes; whereas the dispersion takes on values up to $\sigma_{\phi} = 12$ rad m^{-2}. The relatively high values of σ_{ϕ} compared to ϕ_{RL} may be indicating that the changes to the turbulent component of the field is coupled with changes in the regular field component. Below, we explore whether the evolution of lobes and the corresponding magnetic field have testable predictions on the resultant Faraday depth. For the following discussion, we assume that we have subtracted the Milky Way's Faraday contribution completely.

Primordial toroidal field

Parsec-scale gradients in Faraday rotation have been reported across numerous AGN (e.g. Gómez et al. 2008; Kharb et al. 2009; Hovatta et al. 2012; Mahmud et al. 2013; Gabuzda et al. 2014b). Often, these systematic changes in Faraday depth value have been attributed to a changing magnitude of the line-of-sight component of a magnetic field due to a toroidal or helical jet. Ordered magnetic field structure persisting to larger physical scales remains an intriguing possibility. However, the tendency for feedback between the collimated jet and the surrounding environment leads to an altered magnetic field orientation, and the magnetic field that was once characteristic to the jet and its launch history becomes mixed with the random distributions of field orientations and electron densities of the surrounding medium. Interestingly, there have been a few instances of such an observation; on the hundred-parsecs scale, Gabuzda et al. (2014a) observed gradients in Faraday rotation measure across the jets of 3C 380 and, on the kiloparsec scale, Kronberg et al. (2011) observed gradients across knots in the jet spine of 3C303 out to 50 kpc. If such a magnetic field structure can remain imprinted out to kpc-scales, the clearly collimated and apparently unperturbed jets of MSH 05−3*13* make the radio galaxy an ideal candidate to search for such signatures

However, with our present data, we are unable to resolve the jet to better than 1.2 synthesised beams, making it unlikely to find any such gradients. We instead expand our search for transverse gradients in Faraday depth to the outer lobes of MSH 05−3*13*. One might anticipate any Faraday depth structure associated with jet launch to become disrupted as the material propagates away from the galaxy nucleus and the influence of the surrounding environment comes to dominate. However, we have argued that the ambient medium into which the lobes of MSH 05−3*13* are expanding is likely sparsely populated and may not be contributing to the observed Faraday depth. Therefore, there may still be some signature of the jet launch conditions imprinted on the surface of the lobes.

To investigate the possibility of transverse Faraday depth gradients in the outer lobes of MSH 05−3*13*, we evaluate the ϕ_{corr} values along large cross sections of the northern

and southern lobe (marked '$N_\perp$' and '$S_\perp$' in Figure 4.6, respectively). These slices are taken to represent the axis perpendicular to the jet axis. The length of each analysed slice is equivalent to $\geq$ 2 synthesised beams. In contrast to the inner jet, we believe that the outer lobes are well-resolved and the observation of a gradient in Faraday depth would indicate a reliable detection (e.g. Mahmud et al. 2013).

Figure 4.11 shows the p_0, ϕ_{RL} and σ_ϕ parameter values associated with slices '$N_\perp$' and '$S_\perp$'. A systematic change is observed across all parameters and there are clear changes in ϕ_{RL} along both slices. We note that this is a general trend – the values in Figure 4.11 are of the same order as their corresponding uncertainties.

We explore the possibility that our foreground ϕ_{MW} correction has introduced the observed signature in Faraday depth and find that along the same paths, the raw Faraday depth (i.e. ϕ_{obs}) shows similar gradients. Without the foreground correction, the confidence Faraday depth gradient also increases since the uncertainty in the Faraday depth is a factor of ten less than the measured ϕ_{obs}. We therefore conclude that the observed pattern in Faraday depth across the north and south lobes of MSH 05−3*13* are not induced by our foreground MW correction and are indeed robust.

In helical magnetic fields, the net line-of-sight magnetic field should change across the jet/lobe structure with increasing values tending towards the boundaries (e.g. Blandford 1993). The consequence of this geometry would be observable as a single gradient in Faraday rotation, with the slope indicative of the handedness of the magnetic field. Transverse Faraday depth gradients are expected to be monotonic, which can be argued as observed in the North lobe, but this is not observed in the South lobe, where we see a sinusoidal pattern beginning to develop. The ϕ-pattern in the southern lobe argues against a torus-like magnetic field structure.

It is possible that we are probing an intervening cloud of thermal material which is altering observed Faraday depth; however, the apparent smoothness of the change in Faraday depth in conjunction with the seemingly static level of Faraday dispersion (Figure 4.11) argues against this. While we do not go so far as to say that the Faraday depth structure in the outer lobes is not repercussion of the jet-launch morphology, we argue that it is not the dominant observed signal.

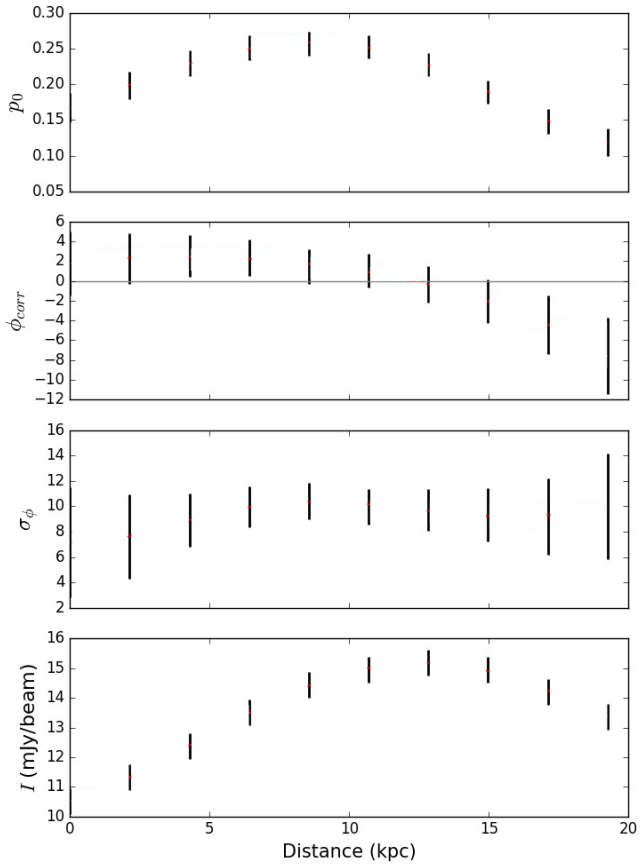

(a) North lobe transverse slice

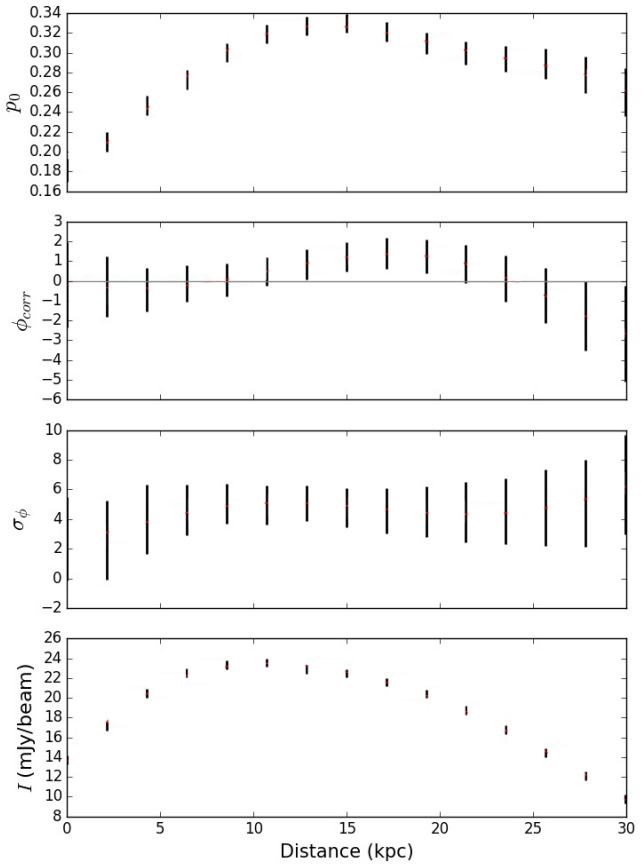

(b) South lobe transverse slice

Figure 4.11: Profiles of p_0 (top), ϕ_{RL} (top middle), σ_ϕ (bottom middle) and total intensity (bottom) for the North lobe (a) and South lobe (b) taken along the slices 'N$_\perp$' and 'S$_\perp$' identified in Figure 4.9. The length of each line is equivalent to the uncertainty in each parameter value, as calculated from qu-fitting. The x-axis measures distance along the slice in kpc, assuming a redshift of $z = 0.037$. The zero position represents the eastern-most edge of the polarised lobe with an increase in distance moving east.

Faraday surface eddies

As reported in §4.4.3, we observe smoothly varying polarised surface features on the lobes of MSH 05−3*13*. Bicknell et al. (1990) invoked Kelvin-Helmholtz (K-H) instabilities existing on the surface of the lobes of Cygnus A and PKS B2104 − 25N to explain the observation of substantial variations in Faraday depth across the radio galaxies. Bicknell et al. (1990) argue that for a radio lobe roughly in pressure equilibrium with its surrounding environment, numerous small-scale waves may build up on the surface of the lobe/IGM interface. The eventual merging of the waves results in the appearance of large-scale instabilities at the boundary of the synchrotron lobe and surrounding medium.

Motivated by the apparent repetition of the observed features in Faraday depth on the lobes of MSH 05−3*13*, we explore whether this signature can be explained by K-H instabilities at the interface of the lobe and the surrounding medium. This section follows similar logical arguments made in Anderson et al. (2017 *in prep.*), which seeks to explain depolarisation filaments associated with Fornax A. Their work ultimately concludes that K-H instabilities are not the likely driving mechanism for the depolarisation features. As the lobes of MSH 05−3*13* are generally lacking regions of strong depolarisation (Figure 4.10) and our analysis is motivated by patterns seen in Faraday depth, we seek to explain a different physical phenomenon.

As robust K-H instabilities are expected to manifest along this axis consistent with the bulk movement of material, we investigate the polarisation signal along the lobes of MSH 05−3*13*, which is represented as '$N_{\parallel}$' and '$S_{\parallel}$' in Figure 4.9. K-H instabilities are predicted to result in the manifestation of numerous observable characteristics in the polarised signal. Below, we detail some of the main predictions from Bicknell et al. (1990) compared to what is observed in Figure 4.12:

- There is a predicted Faraday-depth sign change on a scale length equal to half of the wavelength of the eddy (λ_e). Figure 4.12, in particular Figure 4.12(a), shows that the Faraday depth values exhibit such behaviour with a wavelength of $\lambda_e \sim 30$ kpc.
- The trough behind an eddy will host a turbulent wash of material from the lobe and surrounding environment. This will lead to an increase in Faraday dispersion / depolarisation that is spatially coupled with the advancing wave. This is consistent with what is seen in Figure 4.12, where the peaks in σ_ϕ trail the position of the Faraday sign change.
- Bicknell et al. (1990) also argue that surface waves should form on the edges of the radio lobes, but as the vast majority of pixels in these locations do not meet our polarisation selection criteria, we are left to consider only the broader lobe surface. For our analysis, we consider that the lobe surface is plane and oriented perpendicular to our line of sight.

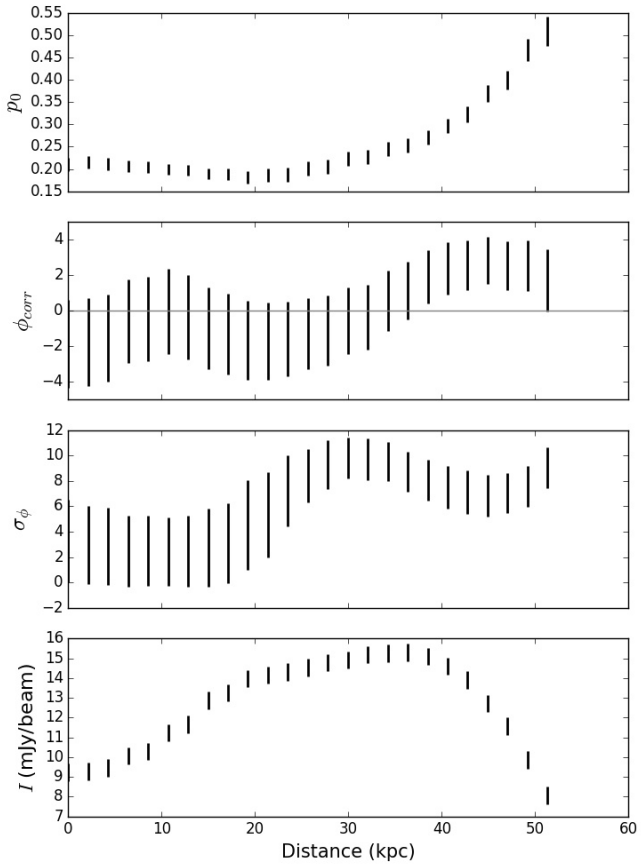

(a) North lobe

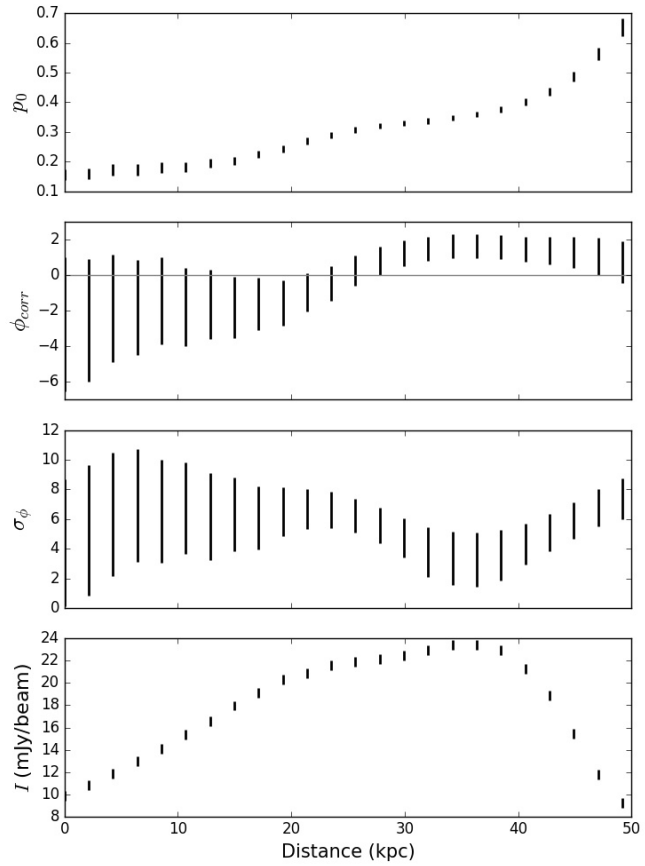

(b) South lobe

Figure 4.12: Profiles of p_0 (top), ϕ_{RL} (top middle), σ_ϕ (bottom middle) and total intensity (bottom) for the North lobe (a) and South lobe (b) taken along the slices '$N_\parallel$' and '$S_\parallel$' identified in Figure 4.9. The length of each line is equivalent to the uncertainty in each parameter value, as calculated from qu-fitting. The x-axis measures the distance along the profiles in kpc, assuming a redshift of $z = 0.037$. The zero position is consistent with the edge of the polarised lobe nearest the optical counterpart with an increase in x signifying distances north and south of this position for subfigures 4.12(a) and 4.12(b), respectively.

We argue that K-H instabilities have the potential to explain some of the key observations seen across the outer lobes. However, it would be prudent to verify that the age of the lobes are able to support K-H instabilities, as a significant amount of time is required for their development. From Chandrasekhar (1961), the timescale needed for a K-H instability to develop can be approximated as

$$\tau_{\mathrm{K-H}} = \left[\frac{(\rho_l + \rho_{IGM})^2}{k^2 \rho_l \rho_{IGM} \Delta v^2}\right]^{1/2}, \tag{4.2}$$

where $\tau_{\mathrm{K-H}}$ is the time required for the instability to develop in seconds, and ρ_l and ρ_{IGM} are the densities of the lobe and surrounding medium, respectively. The wavenumber, k, is inversely related to the mean eddy wavelength as, $k = (2\pi)/\lambda_e$ and Δv is the shear velocity between the two layers.

We know very little about the multi-phase environment surrounding MSH 05−3*13*. However, as stated earlier, K-H instabilities require that the lobe and the IGM be near pressure equilibrium. For simplicity, we assume $\rho_l \simeq \rho_{IGM}$. Following this, the above equation simplifies to

$$\tau_{\mathrm{K-H}} \simeq \left[\frac{4}{k^2 \Delta v^2}\right]^{1/2}, \tag{4.3}$$

where no estimates of the relative densities need to be made. As there are no clear driving forces acting upon the oldest lobe material, we assign the shear velocity to be equivalent to the buoyant velocity of the lobes in the group environment. The buoyant velocity (v_b) can be calculated in cm/s from

$$v_b = \sqrt{\frac{2gV}{SC_D}}, \tag{4.4}$$

where V is the estimated volume of the lobe, S is the cross-sectional area, C_D is the drag coefficient and g is the gravitational acceleration, assuming the surrounding environment is in hydrostatic equilibrium. We approximate the lobes as two spheroids with radii of 25 kpc. We assign the same C_D as derived from the simulations of Churazov et al. (2001), which find the drag coefficient of a buoyant bubble in a stratified medium to be $C_D \simeq 0.75$. We estimate the gravitational acceleration by approximating the enclosed mass of the galaxy group to the extent of the position of MSH 05−3*13*. Using the galaxy group viral mass from Tully (2015), there is an implied enclosed mass of $M(< R_{400}) \sim 6.7 \times 10^{46}$ g at the position of MSH 05−3*13* within the galaxy group ($R \sim 400$ kpc). Using these values in conjunction with Equation 4.4 returns a buoyant velocity estimate of $v_b \sim 3.6 \times 10^7$ cm/s. For comparison, Wykes et al. (2013) estimate a buoyant velocity of $v_b \sim 4.9 \times 10^7$ cm/s for the lobes of Centaurus A, another FR I radio galaxy in a loose group of galaxies.

Returning to Equation 4.3, now armed with estimates of the shear velocity (assumed

equivalent to v_b) and a measurement of the eddy wavelength ($\lambda_e \simeq 30$ kpc), we derive an estimated eddy timescale of $\tau_{K-H} \sim 20$ Myr. Given that τ_{K-H} is equivalent to a single e-folding timescale, the development of well-structured K-H instabilities would require time passage equivalent to multiples of τ_{K-H}. This timescale is supported by our lobe age estimate ($\tau \sim 100$ Myr), which may allow more than ~ 5 e-folding times to have passed. We also point out that the back-flow regions in North and South lobes both exhibit a lack of robust polarised emission spanning our observing band. This observation may be consistent with the scenario presented above, in which the material in the outer lobes have developed more turbulent structures, thus leading to a depolarised signal.

However, multiple e-foldings may not be necessary to explain our observations, as the surface waves we observe are of eddies that are roughly consistent with the size of the lobes. Furthermore, we do not observe strong depolarisation associated with the surfaces of the lobes (i.e. Figure 4.10), which is expected to increasing with the passing of every τ_{K-H}. This would imply that even if the age estimate of the lobes is erroneous by a factor of 5, a single, large-scale eddy could still develop on the timescale of the age of MSH 05−3*13*.

The Surrounding Thermal Environment

We have demonstrated that K-H instabilities are able to explain some of our key polarisation observations and argue that they are able to develop on timescales that are in agreement with our derived age of MSH 05−3*13*. We now explore the physical conditions of the environment implied by the observed change in ϕ_{RL}.

Bicknell et al. (1990) show that the ratio of eddy depth (L_e) to eddy wavelength is approximately $L_e \sim 0.3\lambda_e$. By rearranging Equation 5.2 from Bicknell et al. (1990), we are able to estimate the required free electron density at the boundary layer of the Faraday eddies as

$$n_e = \frac{\Delta\phi}{0.49\, B_{\parallel}\, \lambda_e} \ \mathrm{cm}^{-3}, \tag{4.5}$$

where $\Delta\phi$ is the change in ϕ_{RL} over one eddy wavelength and all other variables have their previous definitions. Figure 4.12 allows us to directly measure both $\Delta\phi$ and λ_e. We find an implied $\lambda_e \simeq 30$ kpc for both the North and South lobes and estimate $\Delta\phi$ to be ~ 4 rad m^{-2} for both of the lobes. In §4.5.2, we measure the minimum total magnetic field strength in the outer lobes to be $B_T = 5.4\,\mu$G. From this measurement, we are able to place a geometrical upper limit for the line-of-sight magnetic field of $B_{\parallel} \sim B_T/\sqrt{3} \sim 3.1\,\mu$G. Using the parameter values from the previous paragraph, we calculate $n_e \simeq 9\times 10^{-5}$ cm^{-3} for the North and South lobes. We note here that we do not use the density implied from our earlier calculation of the enclosed mass since the majority of the mass in this estimate will be associated with individual galaxies, rather than the ambient medium – which we are trying to approximate through this exercise.

As lobes expand, they are expected to sweep up and compress the ambient medium on the surface of the lobes. We test the plausibility of our density estimate of the eddy by comparing the density of the skin to that of the ambient medium. We assume that MSH 05−3*13* is embedded within group boasting a standard profile $n_{IGM}(R) \sim n_0(R/a_0)^{-b}$ (e.g. Jones and Forman 1984). Applying typical values of $n_0 \sim 10^{-2}\,\mathrm{cm}^{-3}$, $a_0 \sim 10\,\mathrm{kpc}$ and $b \sim 1.5$ (Mulchaey and Zabludoff 1998; Sun 2012) returns a value of $n_{IGM}(400\,\mathrm{kpc}) \sim 4 \times 10^{-5}\,\mathrm{cm}^{-3}$. It should be noted that the typical profile values stated above have large scatter in their uncertainties. Given the lack of hot spots in MSH 05−3*13* (Ekers et al. 1989), we do not expect there to be strong shock at the contact between the lobe and the intragroup medium, thus implying that the maximum compression of the surrounding medium will be less than 4. Comparing our estimate of $n_{IGM}(400\,\mathrm{kpc})$ to the eddy densities implies a compression factor of 2 on the lobe surface.

We believe that the arguments made in this chapter, namely τ, v_b, λ_e and n_e, support the existence of K-H instabilities on the lobe surfaces of MSH 05−3*13* and that these instabilities offer a favourable explanation for the observed polarisation signatures on the outer lobes. Given that we are confident that only a fraction of the synchrotron lobes is significantly polarised across our observing band, one might predict that higher sensitivity observations of MSH 05−3*13* will expose more polarised surface eddies, further strengthening our conclusion.

4.6 CONCLUSIONS

We have presented a $1300 - 3000\,\mathrm{MHz}$ analysis of the radio galaxy MSH 05−3*13* and identified large-scale polarisation structures that stretch across the outer synchrotron lobes. We sought to identify the mechanisms responsible for the Faraday structures we observe. In order to carry out an analysis of these mechanisms, we have made numerous arguments toward the overall structure and evolution of the radio lobes, namely:

- We estimate an equipartition magnetic field strength of $B_{eq} \simeq 5.4\,\mu\mathrm{G}$ associated with the outer lobes of MSH 05−3*13*. We are unable to extend the same analysis to the jets, since they have regions associated with relatively flat spectral indices and an assumption of equipartition would be erroneous in this dynamic region.

- Motivated by the clear discrepancy between average spectral indices associated with the jet and the outer lobes, we argue that the outer lobes are approximately 100 Myr old.

- We argue that the bulk of the observed Faraday rotation towards MSH 05−3*13* is due to the Milky Way foreground. After correcting for the Galaxy's contribution,

we observe a changing Faraday depth as a function of position across the radio lobes, where each lobe has ridges associated with $B_{\parallel}$ field reversals. By examining the polarisation profiles along slices that run parallel to the orientation of the lobes, we see a wave-like pattern in both Faraday depth and Faraday dispersion in both the North and South lobes.

- We observe gradients in Faraday depth and explore whether this phenomenon could be due to feedback between the synchrotron lobes and their surrounding medium in the form of Kelvin-Helmholtz instabilities. Comparing the predicted changes in observable Faraday depth due to each of these mechanisms, we find that K-H instabilities may be able to explain the polarisation signature associated with the lobes of MSH 05−3*13*.

5

Faraday Rotation through the Intragroup Medium of Galaxy Groups

5.1 Background & Motivation

The existence of magnetic fields in clusters has been confirmed using a number of different approaches including investigation of inverse Compton X-ray emissions from cluster centres (Jaffe 1977; Bonafede et al. 2009), extended synchrotron emission and radio halos and relics(Govoni et al. 2011; Bonafede et al. 2013), and analysis of background and embedded Faraday rotation measures (Clarke et al. 2001; Johnston-Hollitt et al. 2004). Magnetic field strengths of a few μG are likely to play a significant part in the evolution of the (ICM), but the question of how magnetic fields became as pervasive as they are in the ICM is still largely unanswered (Subramanian 2008). Some evidence suggests that large-scale magnetic fields in the ICM was formed through galaxy interactions (Menon 1995; Chyży and Beck 2004) and galaxy ejecta (Rees 1987; Goldshmidt and Rephaeli 1993; Kronberg 1996; Bertone et al. 2006) while other studies argue that cluster-wide magnetic fields were created via shocks during structure formation (Zweibel 1988; Kulsrud et al. 1997; Waxman and Loeb 2000).

Donnert et al. (2009) suggest that in order to understand the origin of large-scale magnetism, measuring magnetic fields in environments with lower densities than galaxy clusters may prove a more useful approach towards understanding the evolution of cosmic magnetism. Assuming hierarchical structure growth, galaxy clusters are built up through the merger and accretion of galaxy groups (Springel et al. 2006; McGee et al. 2009). If the intragroup medium (IGrM) were to already have a magnetic field associated with it, the field lines might be compressed and amplified upon infall into the denser environment. Consequently, any observed cluster-wide magnetic field would be an amal-

gamation of the fields that were once intrinsic to galaxy groups. Therefore, observations and analysis of magnetic fields in galaxy groups may hold key insight into distinguishing between theories of the origin and evolution of large-scale magnetism.

A systematic investigation into the origins of large scale magnetic fields is a crucial step in answering the question how the universe became magnetised. Therefore, this chapter will study magnetic fields in the intragroup medium of galaxy groups using Faraday rotation of background polarised radio sources by matching the positions of well-defined galaxy groups in the GAMA galaxy group catalogue (Robotham et al. 2011) with a catalogue of rotation measures toward background polarised radio sources (Taylor et al. 2009). This is the first statistical study of Faraday rotation associated with the galaxy group environment.

Observations of the in-falling galaxy group, NGC 4829, onto the Coma cluster have suggested that NGC 4829 may have created shocks in the region of the Coma radio relic (Akamatsu and Kawahara 2013) and boosted the magnetic fields in an area of the cluster by a factor 3 (Bonafede et al. 2013). A shock can only compress a magnetic field in the plane of motion, keeping the orientation of any field lines that are leading the shock. Therefore, information from any frozen-in magnetic field from a galaxy group could be preserved as it falls into a cluster and will begin to be integrated with the cluster once the infall shock dissipates.

Compared to galaxy clusters, galaxy groups have a higher frequency of disruptive interactions due to their shallower potential well and consequently slower infall velocities of group members (Sparke and Gallagher 2007). Tidal disruptions and ram pressure stripping have the potential to not only drag out gas into the surrounding medium but also a galaxy's coherent magnetic fields. This is most classically seen in the Taffy galaxies (Condon et al. 1993, 2002). However, studies of magnetic fields in galaxy groups have largely been limited to the investigation of continuum emission and polarisation associated with specific group features and galaxy-merger remnants such as those caused by tidal and ram pressure stripping (Condon et al. 1993; Xu et al. 2003; Kantharia et al. 2005; Drzazga et al. 2011; Nikiel-Wroczyński et al. 2013b). These approaches have been able to measure field strengths of the IGrM ranging from $\leq 1\,\mu$G to a few μG. Synchrotron emission is a useful tracer of polarisation and magnetic fields; however, there is a detection bias toward regions with high density or strong magnetic fields. Since we do not expect the IGrM to necessarily have either of these two characteristics, a thorough investigation of magnetic fields in the diffuse intragroup medium has not been feasible with the sensitivity limits of most radio telescopes.

In order to trace the history of magnetic fields in a galaxy group, one must also consider magnetic fields from AGN. Furlanetto and Loeb (2001) find that as much as 20% of the IGM can be filled with magnetic fields from QSOs. There has been some evidence of diffuse synchrotron emission originating in the IGrM of poor clusters (Brown and Rud-

nick 2009; Giovannini et al. 2011). Yet detailed investigations have been hindered due to the relatively low thermal electron density comprising the diffuse IGrM, making it difficult for past telescopes to confidently detect any existing field. Therefore, the magnetic field contributions from radio lobes has not been ruled out as a means of magnetising large volumes of space, as predicted by Furlanetto and Loeb (2001). The knowledge of magnetic fields in the diffuse IGrM, and their classification as either coherent or turbulent, is the key to understanding the origin and evolution of large-scale cosmic magnetism by allowing us to rule out different mechanisms for propagation of fields to larger and larger scales.

Faraday rotation is a powerful approach for measuring magnetic fields in diffuse gas. The observed rotation measure (RM) and Faraday depth (ϕ) depend upon the source redshift (z_s), line-of-sight magnetic field strength ($B_\parallel$ in μG) and thermal gas density (n_e, in units of cm^{-3}) along the line-of-sight (dl, measured in parsecs) by:

$$\mathrm{RM}(z_s) = 0.812 \int_{z_s}^{0} \frac{n_e B_\parallel(z)}{(1+z)^2} \frac{dl}{dz} dz \ \ \mathrm{rad\,m^{-2}}. \tag{5.1}$$

Measuring a RM does not directly yield a magnetic field strength, rather it is indicative of a non-zero coherent component of the magnetic field and provides information on the orientation of the field lines. Therefore, the detection of Faraday rotation in galaxy clusters shows that intracluster magnetic fields cannot be comprised of completely tangled and turbulent magnetic field lines and there exists a preserved coherent field present with a minimum number of reversals through the ICM. If such a coherent field were to exist in the IGrM, we would expect to see a similar enhancement of RM values towards sightlines that intersect galaxy groups. If such a signal were to be observed, it would be a direct detection of thermal plasma in IGrM, regardless of any electron density estimates.

We present a brief overview of both the GAMA Galaxy Group and Taylor catalogues in sections §2.1 and §2.2, respectively. The cross-matching methods are described in §3, followed by the results in §4. The two different samples created by two different crossmatching techniques are addressed separately. §5 begins our discussion into the possible forms that a signal may take and compares our results with previous work. Our conclusions are presented in §6. Throughout this study, we adopt the same cosmology used by Robotham et al. (2011): Ω_m = 0.25, and Ω_Λ = 0.75. In order to turn measured physical distances into angles, we adopt the recent Planck result of H_0 = 67.1 km/s/Mpc*.

*Based on observations obtained with Planck (http://www.esa.int/Planck), an ESA science mission with instruments and contributions directly funded by ESA Member States, NASA, and Canada.

5.2 CATALOGUES

5.2.1 THE GALAXY AND MASS ASSEMBLY (GAMA) GALAXY GROUP CATALOGUE

The GAMA Galaxy Group Catalogue described by Robotham et al. (2011) (referred to hereafter as G3C) was a major science goal of the larger Galaxy and Mass Assembly (GAMA) project (Driver et al. 2011). GAMA is a spectroscopic galaxy survey conducted with the Anglo-Australian Telescope (AAT) that covers three equatorial regions centred at 9h, 12h and 14.5h each of size $12 \times 4\,\mathrm{deg}^2$. The final survey aims to take ∼400,000 redshift measurements over 142 deg^2 down to a sensitivity limit of $r_{AB} = 19.4$. The velocity errors on GAMA redshifts are typically $1\sigma \simeq 50\mathrm{km\,s^{-1}}$ (compared to $\sim 35\,\mathrm{km\,s^{-1}}$ in the Sloan Digital Sky Survey).

Of the 110,912 galaxies in the GAMA-I catalogue, G3C has identified 14,388 galaxy groups (with multiplicity ≥2), containing 44,186 galaxies out to a maximum redshift $z = 0.496$. G3C was built through a friends-of-friends (FoF) grouping algorithm, which builds links between galaxies if they are separated by less than the nominal linking condition, which is a function of the local density, angular separation and peculiar velocity (see Robotham et al. 2011 for a full justification of the methods used). Survey incompleteness has little effect on the final catalogue because the original GAMA survey has a completeness level of ∼98%

Galaxy group centres are given in terms of the iterative centre, as calculated in G3C. The iterative centre is found by calculating the r_{AB} centroid of light, and with each iteration, the furthest galaxy from the centre is rejected. When only two galaxies are left, the brighter galaxy is considered the group centre (see §4.2.1 of Robotham et al. 2011 for further information). From this centre point, three different radii are defined: R_{50}, R_σ and R_{100}, representing the radii that contain 50%, 68% and 100% of the group members, respectively. We consider R_{50} and R_σ to be the radii that contain a significant IGrM; R_{100} and our search radius ($1.25\times R_{100}$) are used as minimum match conditions. We find a mean angular diameter of groups defined by R_{100} of 8 arcminutes.

In addition to the iterative centre and radii, we utilise the G3C-calculated values for galaxy-specific redshifts, group redshift, multiplicity, and corrected velocity dispersion in our analysis.

5.2.2 TAYLOR ET AL. (2009) RM CATALOGUE

The catalogue of rotation measures of NVSS radio sources by Taylor et al. (2009) is comprised of 37,543 sources that are part of the much larger NRAO VLA Sky Survey (NVSS; Condon et al. 1998). The original NVSS data were reanalysed by Taylor et al. (2009) to derive rotation measures of the polarised NVSS sources at the observed frequencies of

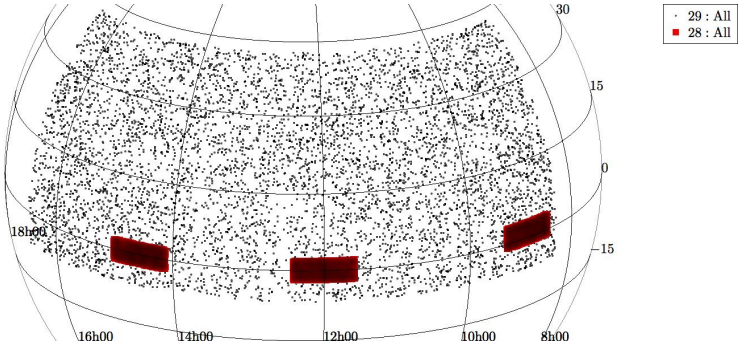

Figure 5.1: Sinusoid projection of the equatorial positions of all GAMA groups (red) and polarised sources from Taylor et al. (2009) (black) that were used in our investigation.

1364.9 MHz and 1435.1 MHz. The RM catalogue covers the sky above declination $-40°$ and has an average density of $\sim$1 source per deg^2 with 45" resolution.

Taylor et al. (2009) report uncertainties of $1 - 2$ rad m^{-2} for $|\mathrm{RM}| \leq 650$ rad m^{-2}, which contradict the typical uncertainty of our sample of ~ 10 rad m^{-2}. Larger RMs are subject to a wrapping ambiguity. However, none of the sources that are positively matched to galaxy groups have a large enough RM value to incur this uncertainty.

The RM map that is constructed from the Taylor catalogue clearly shows large-scale structure that is a consequence of the Milky Way's magnetic field. The GAMA survey is situated such that it is sufficiently above the disk of the Milky Way, to avoid any major foreground contamination (Schnitzeler 2010). For this reason, we create our control samples by increasing the declination of the GAMA survey so that we may minimise the contributions from the Galaxy. Due to the location of the GAMA fields, an increase in declination is equivalent to an increase in the Galactic latitude away from the plane of the Milky Way.

We note that Taylor et al. (2009) use the classical definition of RM such that

$$\mathrm{RM} = \frac{d\psi}{d\lambda^2}, \tag{5.2}$$

where $d\psi$ is the change in polarisation angle as a function of the square of the observed wavelength (λ). For the purpose of our research, we must expand this definition and assume that the RM is equivalent to the Faraday depth (Equation 1.13) so that we may extend our analysis to include and separate Faraday rotation contributions from multiple sources along the line of sight.

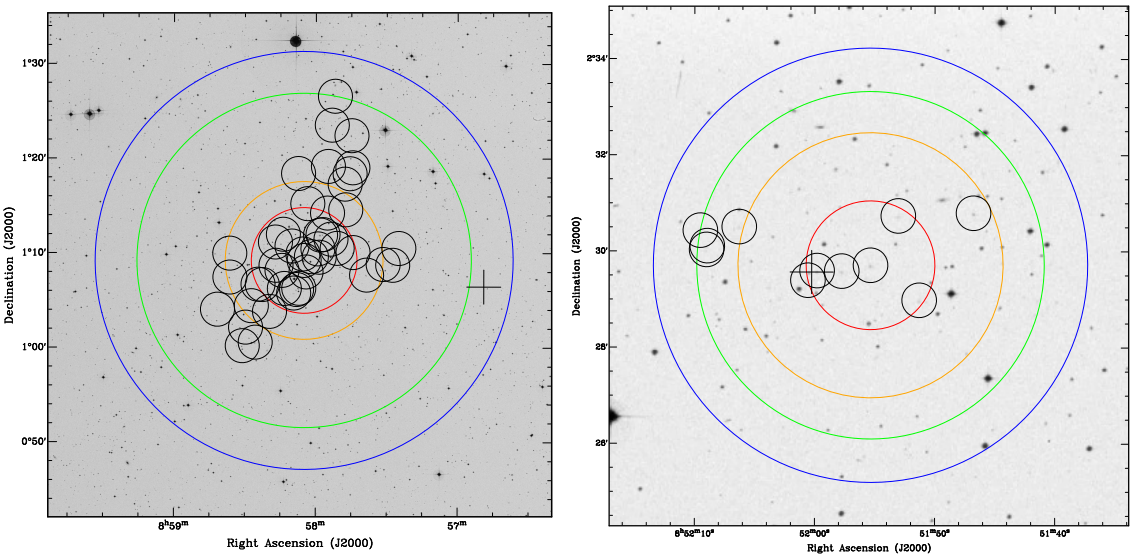

Figure 5.2: SDSS DR9 images of GAMA groups 100004 (*left*) and 100201 (*right*). The concentric rings represent the R_{50} (*red*), R_{σ} (*orange*), R_{100} (*green*) and our effective search radius out to which the crossmatch was carried ($1.25\times$ R_{100}) (*blue*). The smaller, black circles circumscribe each group member's position as given in the catalogue of GAMA galaxies. The individual galaxies are difficult to see and the black circles are used as a representation for the group geometry. The black cross marks the position of the polarised radio source. 100004 is the largest multiplicity group that was matched with a polarised radio source (N = 45) and 100201 represents a scenario where the projection of the polarised radio source is close to the galaxy group centre, but is not a group member.

5.3 METHOD

5.3.1 GALAXY GROUP CROSSMATCH

We create the main crossmatch catalogue by iterating through each GAMA galaxy group's angular projection on the sky and identifying all possible polarised radio sources that pass through the on-sky area defined by the group. The centre of each group is defined by the iterative centre and the radius, given as a comoving separation, is converted into an angular projection using the group median redshift. We extend our crossmatch to 1.25 times the maximum radius of the group with the intention of observing the radial dependence on observed RM drop to zero past the extent of the group.

The algorithm allows for multiple matches per galaxy group. Once a background source had been matched to a group, we identify the group member to which the polarised source has the lowest impact parameter, or least angular diameter distance, using the galaxy-specific redshift from the GAMA catalogue. The now matched polarised radio source and optical galaxy are checked to ensure that the radio-optical match are not the

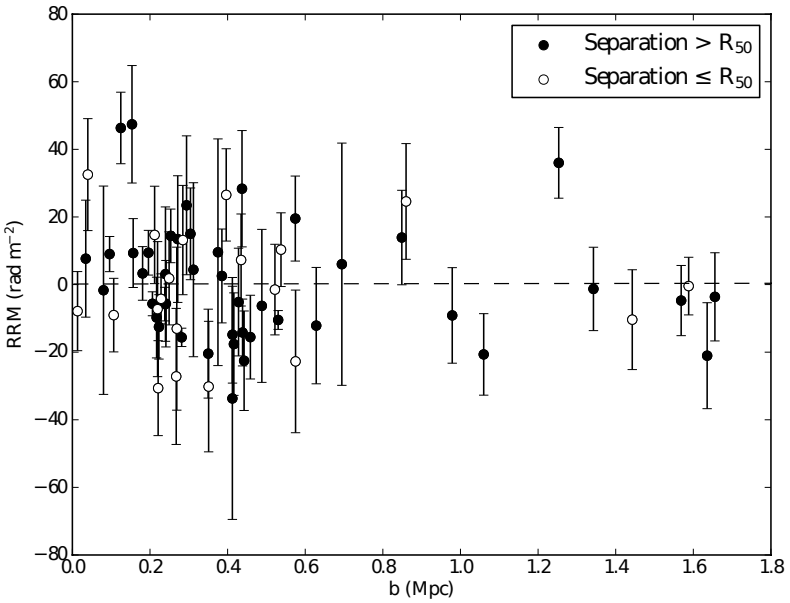

Figure 5.3: RRM plotted as a function of galaxy group impact parameter (b) . Open circles represent the 20 instances where $b \leq R_{50}$ and closed circles represent the cases where $b > R_{50}$.

same source. We additionally throw away any instances where the sightline towards the radio source is intersected by the optical disk of the galaxy.

A control sample was created by shifting the declination centre of each field up by 4°, 8° and 12° relative to the Taylor catalogue, then re-running the same crossmatch algorithm to the entire RM catalogue. As the GAMA fields each span 4° of declination, we choose these declination-increments so that each iteration covers a completely new area of the sky from the GAMA survey. Furthermore, the control sample declination is only increased in order to avoid any overwhelming Galactic contributions to RM that are likely to stem from the Milky Way disk, which come to dominate at lower declinations.

5.3.2 GAMA Catalogue Crossmatch

A second crossmatch is carried out by calculating the projected angular diameter distance from each galaxy in GAMA-I to its nearest polarised radio source. In this instance, the least separation distance is considered to be the matching condition. The algorithm only allows for one polarised source to be matched to one optical galaxy and a previous closest-radio-optical match is excluded if a different galaxy is found to have a smaller angular separation. By running the crossmatch on the entire GAMA galaxy sample, we create an environmentally unbiased measure of RM as a function of impact parameter to

the nearest galaxy, as we are not preferencing galactic environment.

5.4 RESULTS

The method described in §5.3.1 results in 129 occasions of a galaxy group (at R_{125}) being matched with the RM of a polarised radio source. Of these matches, there are 59 instances of a polarised source being matched to more than one group. Due to the inability to separate out each galaxy group's influence on the observed RM, we chose to exclude these matches from the final dataset. In order to exclude embedded sources, we compare the redshift of the galaxy group members to the redshift of the polarised radio source (Hammond et al. 2012) and identify 5 instances of the polarised source and group member being the same source. Once each of the aforementioned exclusions have been accounted for, the final crossmatch consists of 64 polarised sources with lines-of-sight that intersect a galaxy group. In the catalogue, there are five galaxy groups that have been matched with two polarised radio sources each. FIRST reveals that in each of these instances, the polarised sources are the two lobes of a single background radio galaxy.

Figure 5.2 gives an example of two positive radio-optical pairs to G3C groups 100004 (*left*) and 100201 (*right*). The black circles represent the location of each group member and the cross marks the position of the polarised radio source. From smallest to largest, the coloured concentric circles represent the R_{50}, R_{σ}, R_{100} and the adopted search radius ($1.25 \times R_{100}$). Group 100004 is the largest multiplicity group in our sample (N = 45) that was matched with a polarised radio source and has a radius (R_{100}) of 1610 kpc. As shown in Figure 5.2, the polarised radio source is clearly separated from the majority of the group members and the nearest galaxy to the polarised radio source has a projected separation of 830 kpc. In contrast to group 100004, group 100201 (Figure 5.2, right) is a radio-optical pair that exhibits a small angular separation between the location of the polarised source, group members and the group centre. The galaxy group is known to be at a redshift $z = 0.212$ while the radio source has a redshift $z = 1.177 \pm 0.0022$, which definitively establishes the polarised source as being background to the galaxy group.

Table 5.2 lists all the radio and optical data from the G3C and NVSS catalogues used to derive the 64 robust radio-optical pairs. Column (1) lists the galaxy group ID number as listed in G3C. The corresponding α and δ follow in column (2) and represent the coordinates of the iterative centre galaxy, as described in §2.1 and §2 of Robotham et al. (2011). The mean redshift of all the galaxy group members is listed in column (3). All redshifts are accurate to $\Delta z \simeq 0.000167(50\,\mathrm{km\,s^{-1}})$. Column (4) gives the radius (in kpc) of the galaxy group that contain 100%, 68% and 50% of the group members, respectively. The α and δ of the polarised radio source is listed in column (5), the average uncertainty is $< \sigma_{\alpha} > \simeq 0.71''$ and $< \sigma_{\delta} > \simeq 0.64''$. The location uncertainty for an individual source can be found in the catalogue of Taylor et al. (2009). Column (6) gives

the projected distance separating the polarised radio source and the centre of a galaxy group, in kpc. The distance has been translated from the angle on a curved surface created by the positions of the radio and optical source using the mean redshift of the galaxy group. The matching condition required the separation to be less than or equal to $1.25\times R_{100}$ from a group iterative centre. Column (6) lists the impact parameter (b) of a polarised radio source on a galaxy group. The G3C galaxy ID of the nearest group member to the projected position of the polarised radio source is listed in column (7) with the respective coordinates of the galaxy given in column (8).

An unbiased-environment crossmatch was carried out according to the technique described in §5.3.2, which results in 212 polarised sources that are matched to GAMA galaxies. Noting that the density of polarised radio sources is $\sim$1 deg^{-2} and that the nearest polarised radio source to a galaxy may be outside the GAMA fields, the number of polarised sources matched to galaxies is consistent with the total 142 deg^2 size of GAMA. Of the 212 total matches, 153 are associated with field galaxies and 48 are associated with galaxy group members. Cross referencing the polarised sources with the known redshifts of Hammond et al. (2012) shows there to be 9 instances where the polarised source and GAMA galaxy are at the same redshift and an additional 3 matches show the background polarised source passing through the disk of the GAMA galaxy. We have excluded these radio-optical pairs from our final sample, just as we have done in the crossmatch described in the previous paragraph.

5.5 Analysis & Discussion

5.5.1 Milky Way Foreground Correction

In order to investigate the amount of Faraday rotation due to the group environment and thus the magnetic field of the IGrM, the Faraday contributions due to the foreground Milky Way must first be taken into account. The magnetic field in the Milky Way has been shown to be coherent on scales of a few degrees (Stil et al. 2011); therefore, polarised radio sources with a small angular separation from one another will experience a similar amount of Faraday rotation due to the Galactic magnetic field. To carry out the foreground correction, a subset of RM values is created for each radio-optical pair consisting of all non-matched polarised radio sources within a 3.0° radius of a matched radio source. We consider the mean RM of each subset to represent the amount of Faraday rotation induced by the Galactic foreground. In order to avoid any polarised sources with intrinsically high RM skewing the foreground fit, a 4.4 median average deviation from the median (MADfM) clip is applied to each subset. This MADfM clipping is repeated until all members of the foreground subset fall within 4.4 MADfM (approximately equivalent to 3σ) of one another. By subtracting the mean RM of the subset from the matched

RM, we assume that the Galactic RM has been corrected for and the residual RM (RRM) represents the Faraday rotation that may be due to the intragroup medium. We account for the uncertainty in the foreground fit by summing the uncertainty in the RM of the polarised radio source (Taylor et al. 2009) in quadrature with the standard deviation of the mean foreground RM. The RRM and associated uncertainty are listed in column (5) in Table 5.2. The mean RRM for the entire catalogue is $\overline{\mathrm{RRM}} = 0.0 \pm 18\,\mathrm{rad\,m^{-2}}$.

5.5.2 IMPACT OF GROUP-SPECIFIC PARAMETERS ON RRM

Angular extent of galaxy groups

Clarke et al. (2001) show that for galaxy clusters, the magnitude of a RM is inversely related to the angular distance between the cluster centre and the polarised source. They argue that the correlation is due to the relative electron density and pathlength through the intervening magnetised intracluster medium. If galaxy groups were to host diffuse magnetic fields, then one might expect to see a similar relationship between RRM and impact parameter (b). In order explore this possibility, Figure 5.3 shows the calculated RRM as a function of projected separation from the group centre for polarised sources with a projected position less than, and greater than R_{50}. We take R_{50} to be the defining radius within which the most significant Faraday rotation contribution from the IGrM is expected. If the group environment was creating an excess in the observed RM, the largest RRM would be associated with sources with a separation less than R_{50} and small b. The mean RRM for the radio-optical pairs within R_{50} is $\overline{\mathrm{RRM}} = -1.7 \pm 18\,\mathrm{rad\,m^{-2}}$ and $\overline{\mathrm{RRM}} = 0.7 \pm 18\,\mathrm{rad\,m^{-2}}$ for polarised sources outside of R_{50}.

Figure 5.4 is similar to Figure 5.3, but in this case we plot the foreground-corrected RRM as a function of fractional position within the group. We calculate this by dividing the separation of the polarised radio source from the group centre by R_{100}. This serves as a simple way of normalising the varying size of galaxy groups. Values larger than 1.0 are allowed due to our initial crossmatch running to a radius that was 1.25 times the maximum radius of the group. The paucity of radio sources in the inner regions of galaxy groups is largely due to the fact that many of radio-optical matches that exhibited a small fractional separation were excluded due to the polarised source and galaxy existing as the same source, as identified by identical redshift values for the optical and radio source. Similar to Figure 5.3, if there was significant Faraday rotation caused by the IGrM, one would expect Figure 5.4 to exhibit an increase in the magnitude of the RRM at small separation if there was significant Faraday rotation due to the IGrM.

While considering the RMs of polarised sources behind and embedded within galaxy clusters, Clarke et al. (2001) investigate the magnitude of magnetic fields in 16 Abell clusters. They found a negative correlation between measured RM and b and find that the excess RM is indicative of an intracluster magnetic field strengths of $5 - 10$s of μG.

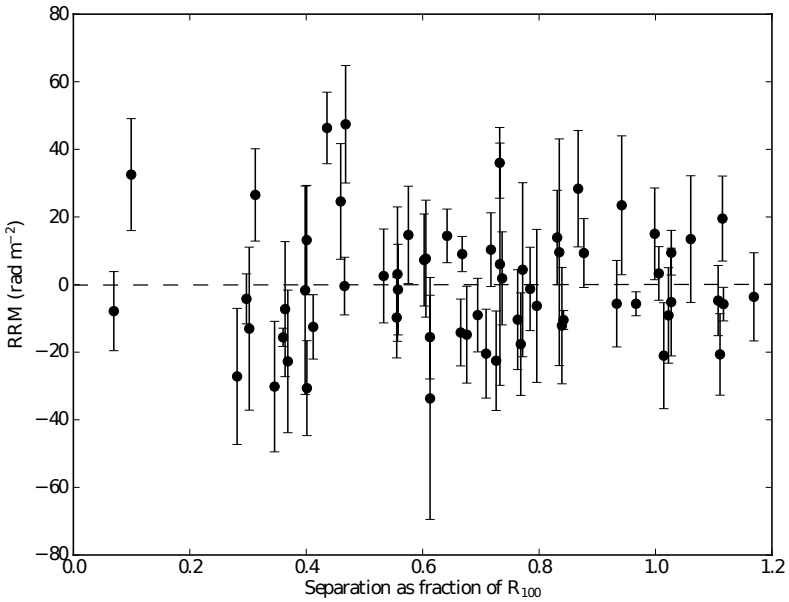

Figure 5.4: RRM as a function of impact parameter normalised to the R_{100} of each galaxy group. A value of 1 means that the polarised background source is at an angular separation from the group centre equal to that of the furthest group member. Values greater than one are possible because our initial crossmatch was run to a maximum distance of 1.25 times the galaxy group's maximum radius.

In contrast, neither Figure 5.3 nor Figure 5.4 shows an apparent RRM signal as a function of position within a galaxy group. This is partially due to our large uncertainty in RRM values. The cases in which the position of the polarised source is within R_{50} are crudely representative of the instances where we would expect the highest density of free electrons and largest values for RRM. The median RRM in these instances (seen in Figure 5.3) is consistent with zero (RRM = $-1.23 \pm 17.9\,\mathrm{rad\,m^{-2}}$). In order to definitively say whether or not we are observing coherent magnetic fields, one would ideally have multiple background radio sources through each galaxy group, and probe polarisation and RRM as a function of impact parameter.

Group Multiplicity

Investigations into the composition and density of the IGrM of galaxy groups have shown that the IGrM may contain dynamically significant amounts of mass (Trinchieri et al. 2005; Freeland and Wilcots 2011). This gas is subject to continuous tidal disruptions and shocks as group members interact with it and other near-by galaxies (Hickson 1982). If the IGrM is a significant dynamical component of a galaxy group one might expect the

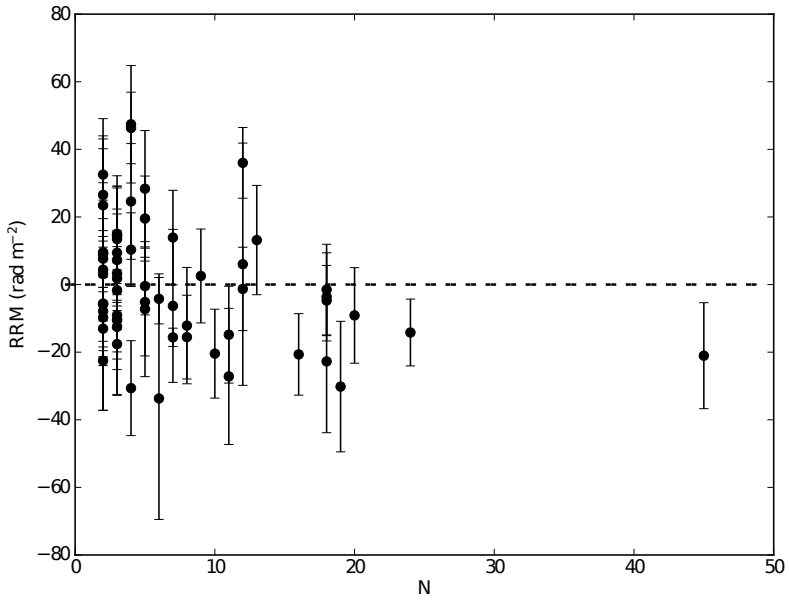

Figure 5.5: RRM value versus galaxy group multiplicity.

density of free electrons in the IGrM to increase with group membership (N), as this would indicate a larger number of galaxy-galaxy interactions. As a consequence, both group impact parameter and multiplicity (N) should display some type of correlation with RRM.

Column (2) of Table 5.2 lists the multiplicity for each galaxy group as reported in G3C. We explore this proposed correlation in Figure 5.5, where the RRM is plotted as a function of N. One-quarter of our crossmatches represent groups with only N = 2 members and the sole radio source at $N = 45$ is group 100004, which is shown in Figure 5.2. Binning the groups by multiplicity shows no apparent trend in RRM value.

Group Velocity Dispersion

Slow galaxy-galaxy interactions tend to have a greater impact on tidal stripping (Sparke and Gallagher 2007). Streamers and tidal bridges created as a consequence of galaxy interactions have been shown to retain some of the ordered magnetic field components of their parent galaxy, as shown in the Leo Triplet (Nikiel-Wroczyński et al. 2013b) as well as in the Magellanic Bridge (Chapter 2). If a polarised radio signal were to pass through such a feature, one might anticipate observing an amplified RM towards the background emitting source due to the non-random nature of the foreground magnetic field.

Figure 5.6 plots velocity dispersion versus RRM and has been truncated to omit 2 points with very high velocity dispersion. Figure 5.6 shows no correlation between group

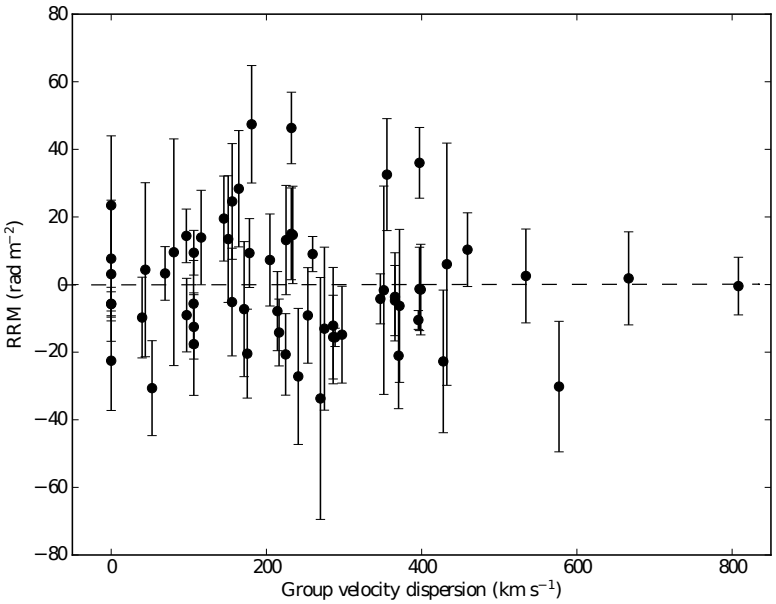

Figure 5.6: RRM as a function of GAMA group velocity dispersion, corrected for the total group velocity dispersion. All matched galaxy groups with $\sigma \leq 800\,\mathrm{km\,s^{-1}}$ are shown, and two points with $\sigma > 1600\,\mathrm{km\,s^{-1}}$ are not shown.

velocity dispersion and RRM. This is likely due to the fact that we are not probing any streamers or tidal remnants, which would have been improbable since tidal streams take up a relatively small fraction of the total volume of a galaxy group. The lack of excess RRM does not mean that there is not a significant medium in those groups with slow velocity dispersions, but rather that the line-of-sight magnetic field is not significant in these instances.

5.5.3 UNBIASED ENVIRONMENTAL APPROACH

The cumulative histogram of the absolute residual rotation measures $|\overline{\mathrm{RRM}}|$ of field galaxies and group members is shown in Figure 5.7, which uses the catalogue created by running the environment-independent crossmatch catalogue (§5.3.2). The motivation for this approach was to create an environmentally unbiased sample in order to remove any role that environment might play on measured RRM. Comparing the RRM populations for field and group radio-optical pairs shows the two samples to be nearly identical. Running a K-S test on the two samples returned a p-value of 0.415.

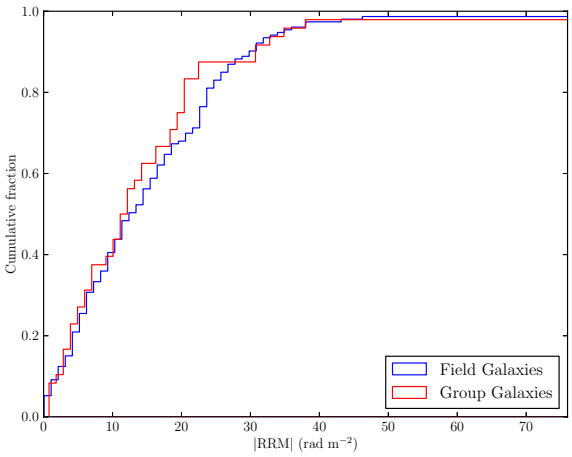

Figure 5.7: A cumulative histogram of |RRM| for all polarised radio sources matched to GAMA galaxies. A radio source is only matched to one galaxy. Whether that galaxy belongs to a group or was considered a field galaxy is shown in red and blue, respectively.

5.6 DISCUSSION

We find no significant amplification in RRM for polarised radio sources for which Faraday rotation is measured through a galaxy group's intragroup medium. In order to calculate our detection limit, we now consider whether any significant contribution to RM occurred only in instances where the polarised source sits in projection within R_{50} of a group – where the local over-density is highest, interactions are most frequent and tidally-stripped material is most abundant. With this constraint, we consider the upper limit imposed from the subset of radio-optical pairs in which the polarised radio source is separated from the group centre by less than R_{50}. Applying this separation criterion limits our sample to 20 radio-optical matches from the possible 64 pairs.

In order to calculate the upper limit to the line-of-sight magnetic field ($B_{\parallel}$) towards each sightline using Equation 5.1, values for the line-of-sight pathlength and free electron density (n_e) must be estimated. The redshift of each sightline (z_s) is assumed to be the median galaxy redshift of the group, and is given in Column (3) in Table 5.1. We designate the pathlength (dl) to be the distance that the polarised radio signal travels through the inner R_{50}, calculated using the impact parameter, b, such that:

$$dl = 2\sqrt{R_{50}^2 - b^2}. \tag{5.3}$$

Column (6) in Table 5.2 lists the calculated dl for each group in kpc. We have no specific information on the thermal electron density (n_e) of individual groups. However, using

bent-double radio sources, Freeland and Wilcots (2011) find IGrM gas densities from 10^{-3} – 10^{-4} cm^{-3} within the inner 700 kpc of groups. With the exception of one G3C group (301416), each group in this subset has an impact parameter less than 700 kpc. Since groups are not virialised, it would not be easy to justify any radial dependence in electron density. For simplicity of calculations, we assign a flat density profile of $n_e = 10^{-4}$ cm^{-3} for each IGrM. Column (7) in Table 5.2 gives the calculated upper limit to $B_\parallel$ in μG.

To get a representative measure of the magnetic field for the subset of twenty optical-radio pairs with a separation less than or equal to R_{50}, we take the mean of the absolute value of the implied line-of-sight magnetic field ($\overline{B}_\parallel$). The resulting magnetic field value is $\overline{B}_\parallel \leq 0.53\,(n_e/10^{-4}\,\mathrm{cm}^{-3})\,\mu$G with a standard deviation of $\sigma = 0.65\,(n_e/10^{-4}\,\mathrm{cm}^{-3})$ μG. The $3\,\sigma$ upper limit is therefore $\overline{B}_\parallel \leq 2.5\,(n_e/10^{-4}\,\mathrm{cm}^{-3})\,\mu$G.

Faraday rotation only probes the magnetic field along the line-of-sight; assuming equipartition between the magnetic field and cosmic rays allow for the total magnetic field (B_0) to be approximated as $B_0 \sim \sqrt{3\mathcal{N}}B_\parallel$, where $\mathcal{N}$ represents the number of field reversals in the group medium. We find an upper limit on the total magnetic field of $B_0 \lesssim 3.4\,(n_e/10^{-4}\,\mathrm{cm}^{-3})\,\sqrt{\mathcal{N}}\,\mu$G. The scale-length of the reversals (ℓ) does not depend on the structure or magnitude of the initial magnetic field (Dolag et al. 2002), but as a field becomes more turbulent (due to shocks, interactions, outflows, etc.), more field reversals are expected over smaller physical scales.

Using only the eight radio-optical pairs where RRM > dRRM, we estimate the average line-of-sight magnetic field through the IGrM as $\overline{B}_\parallel \leq 0.76(n_e/10^{-4}\,\mathrm{cm}^{-3})\,\mu$G, with a 3σ upper limit to the line-of-sight field strength of $1.1\,(n_e/10^{-4}\,\mathrm{cm}^{-3})\,\mu$G. The upper limit to the total magnetic field is $B_0 \leq 1.9\,(n_e/10^{-4}\,\mathrm{cm}^{-3})\,\mu$G. It is clear at this point that small number statistics are a large factor and any assertion should be approached with caution.

Comparing with published literature, Nikiel-Wroczyński et al. (2013b) report an upper limit of $B_0 \leq 2.8\,\mu$G for the Leo Triplet and Bonafede et al. (2013) argue that the galaxy group NGC 4839 has a core total magnetic field strength on the order of $B_0 \simeq 3.6\,\mu$G. Stephan's Quintet has an estimated total magnetic field of $B_0 \simeq 6.4 \pm 1.1\,\mu$G (Nikiel-Wroczyński et al. 2013a) using revised equations for synchrotron equipartition according to Beck and Krause (2005). Stephan's Quintet is an interesting case in that the compact group members are surrounded by a large envelope of radio emission which further indicates a large fraction of intragroup matter (Nikiel-Wroczyński et al. 2013a). Additionally, the infall of members into the core of the compact group has produced polarised ridges on scales spanning the local topology. In the case of Stephan's Quintet, the magnetic field estimate is of the same order of magnitude as the star-forming regions found within the group members.

5.6.1 POSSIBLE ORIGINS FOR IGRM MAGNETIC FIELDS

Typically two scenarios are discussed for the origins of magnetic fields in the intergalactic medium (IGM) – either magnetic fields blown out from dwarf irregular galaxies into the IGM via strong winds (Kronberg et al. 1999) or magnetic fields lines are dragged out into the IGM by interactions between spiral galaxies (Chyży and Beck 2004).

As to the question of where magnetic fields in galaxy-groups may originate, we can crudely hypothesise that fields are generated from the kinetic and potential energies of galaxy groups. Radio-loud galaxies are most likely found in galaxy groups or poor clusters (Best 2004), and Shen et al. (2007) show that as many as 4% of galaxy group members host an AGN, down to an absolute magnitude of $M = -18$. Feedback from radio jets and their outflows have been observed to strongly affect the physics of the IGrM (Furlanetto and Loeb 2001; Kronberg et al. 2001) and AGN are promising candidates for the propagation of magnetic fields on large scales. AGN are able to distribute material on relatively short time scales and have the potential to expel material out to scales of Mpc (e.g. Kronberg et al. 2001). A typical giant radio galaxy has a radiative life time of $\sim 10^7$ years and can have a total energy of $\sim 10^{60}$ ergs. Assuming equipartition of the lobes, half of this energy takes the form of magnetic fields. Distributing the magnetic energy over an average group volume V_{gr}, as calculated from the average R_{50} of our sample, results in a magnetic field of order $0.4\,\mu$G. This estimate for magnetic field distribution is still much lower than our upper-limit and we cannot rule out pure AGN seed-fields as the propagators of large-scale magnetic fields.

Perhaps the frequent interactions in galaxy groups increases the magnetic field in the surrounding group medium. Stephan's Quintet has been observed to have an envelope of radio emission encompassing all of the group members and the field in the IGrM has been estimated to have a total magnetic field strength of $B_0 = 6.4\,\mu$G with magnetic energy density of $E_B = 1.8 \pm 0.5 \times 10^{-12}\,\mathrm{erg\,cm^{-3}}$ (Nikiel-Wroczyński et al. 2013a). This magnetic field estimate is approximately equal to the field strengths measured in star forming regions within Stephan's Quintet. Dissipating these fields over the larger volume representative of our average group, the magnetic field drops as $R^{-3/2}$ and the magnetic energy in the IGrM in Stephan's Quintet would result in a magnetic field of only $B_0 = 0.14\,\mu$G. Although this estimate is much lower than our upper limit, it does not take into account the magnetic fields deposited by the starburst regions, nor the effects of any infall onto the group.

Our upper limit to the IGrM magnetic field, $B_0 \lesssim 3.4\,(n_e/10^{-4}\,\mathrm{cm^{-3}})\,\mu$G, is higher than our estimates of magnetic field strength due to various forms of feedback and neither AGN-seed fields, nor structure formation can be ruled out as the sole origin for magnetic fields in galaxy groups. However, in all likelihood, magnetic fields on large scales will have been built up out of multiple episodes of group feedback, whether it be AGN activity, increased star formation, tidal stripping, shocked gas from galactic infall, etc. Future

work into how each of these phenomena affect large-scale magnetic fields and build upon already existent fields will be useful in determining whether or not galaxy groups have magnetic fields in the diffuse gas and of what strength.

5.7 SUMMARY

We have searched for the effect of the intragroup medium of galaxy groups on the rotation measures of background polarised radio sources. By crossmatching well-defined catalogues of galaxy groups (Robotham et al. 2011) and polarised radio sources with known rotation measures (Taylor et al. 2009), we built a sample of 64 RMs with intervening galaxy groups. After correcting for any contribution due to the Galactic foreground, we investigated residual rotation measures as a function of several different defining group characteristics – including distance from group centre, impact parameter, multiplicity and velocity dispersion – and see no RRM enhancement along sightlines through galaxy groups. Using only radio-optical matches with radio sources with sightlines that exist at a projected distance less than R_{50} from the group centre, we were able to estimate the upper limits of $B_{\parallel} \lesssim 2\,\mu$G and $B_0 \lesssim 3.4\,\mu$G.

An environmentally-unbiased sample was also created by running an algorithm that matches every GAMA galaxy with its nearest polarised radio source. Separations were calculated as an angular diameter distance, assuming the radio source to be at the same redshift as the galaxy. Of the 201 galaxy-radio source matches, 48 galaxies are considered to be group members and 153 are field galaxies. There is no apparent dependence between RRM and group environment.

Estimates of n_e for each galaxy group are needed in order to measure the magnetic field strength in galaxy groups. Since RM is directly proportional to the electron density, one would expect to see an anti-correlation between RRM and separation from a galaxy group centre. Assuming a density profile to each group would allow for one to measure magnetic field strength as a function of radius, rather than having a two-variable fit with RRM.

We note that significant effort has been dedicated to the study of X-ray emission in galaxy groups (e.g. Mulchaey et al. 1996; Helsdon and Ponman 2000; Mulchaey et al. 2003; Finoguenov et al. 2006; Sun et al. 2009), with more recent, extremely-sensitive surveys having been carried out on groups at moderately high redshifts (Connelly et al. 2012; Erfanianfar et al. 2013; Finoguenov et al. 2015). The majority of these studies were carried out on galaxy groups that are too small in angular scale to apply the same analysis procedure carried out in this chapter. However, future research into the magnetised nature of in the IGrM will be able to target groups with known X-ray emission and build upon these previous studies.

All galaxy groups are not alike. In this analysis, we have attempted to normalise the

GAMA galaxy groups in order to find an overall trend in RRM as a function of a number of galaxy group parameters. An ideal approach using Faraday rotation would include a number of radio sources at different radii from the group centre. Multiple RM radio sources will give insight into not only the density profile of the IGrM, but will also trace the radial dependence of magnetic fields on a case-by-case basis. This would waive any currently necessary normalisation and be more sensitive to an individual galaxy group's dynamics and kinematics. Telescopes such as the Square Kilometre Array (SKA) and the Australia Square Kilometre Array Pathfinder (ASKAP) will increase the number of known polarised radio sources one-hundredfold (Beck and Gaensler 2004) and make this a more viable technique for detecting the magnetic fields in diffuse IGrM.

Table 5.1: Table of all intrinsic values for each radio-optical pair. A full description of table content is given in §5.4

(1)	(2)		(3)	(4)			(5)		(6)	(7)	(8)	
Group ID	α_{Gr}	δ_{Gr}	Z_{Gr}	R_{100}	R_{σ}	R_{50}	α_{NVSS}	δ_{NVSS}	b	Galaxy ID	α_{gal}	δ_{gal}
	(deg)			(kpc)			(deg)		(kpc)		(deg)	
100004	134.5206	1.1537	0.0712	1612.70	761.00	509.80	134.204	1.107	1635.60	372105	134.3645	1.1455
100017	129.9227	1.0743	0.1578	1015.80	624.70	502.90	129.957	1.074	351.10	300552	129.9631	1.0689
100027	138.6104	2.9220	0.1609	957.50	794.80	569.40	138.695	2.882	978.80	519000	138.6842	2.9035
100045	130.9266	2.6012	0.2193	947.60	305.80	274.00	130.975	2.620	694.40	422462	130.9302	2.6163
100107	137.3084	1.3473	0.2268	781.80	197.80	113.80	137.292	1.360	281.60	302354	137.3054	1.3516
100115	134.2929	1.4138	0.0702	493.80	350.90	335.70	134.277	1.481	350.10	376584	134.2580	1.4451
100124	135.0539	2.8187	0.2015	722.80	502.40	202.90	135.058	2.788	385.30	423367	135.0572	2.8182
100125	135.3058	2.9706	0.1927	1561.10	904.70	587.60	135.351	2.985	575.10	423491	135.3157	2.9828
100201	132.9806	2.4952	0.2115	951.30	725.80	352.40	133.001	2.493	267.60	517586	132.9992	2.4933
100215	129.7053	-0.6206	0.1690	768.40	538.50	488.80	129.723	-0.631	228.40	548952	129.7053	-0.6206
100330	130.0002	2.8378	0.2104	672.80	364.90	299.50	129.981	2.863	412.30	521610	129.9842	2.8421
100531	138.4296	2.4954	0.1541	504.10	350.60	261.90	138.405	2.531	437.10	388015	138.4276	2.5178
100588	134.5650	-0.4883	0.0709	515.20	306.70	253.40	134.675	-0.463	574.50	550248	134.5827	-0.4309
100637	129.1060	-0.6748	0.0518	368.20	296.30	255.80	129.085	-0.623	211.90	196057	129.1060	-0.6748
100643	131.7834	-0.7577	0.2467	721.50	701.80	690.80	131.792	-0.786	434.70	196610	131.7959	-0.7933
100769	140.8790	0.5225	0.1390	603.60	531.00	401.50	140.901	0.513	219.50	217020	140.9043	0.4940
100882	131.6990	2.0183	0.0600	201.50	88.60	25.10	131.681	2.014	80.20	345927	131.6990	2.0183
101352	138.3127	0.7187	0.1697	304.70	229.10	186.60	138.317	0.746	304.30	623336	138.2999	0.7258
101890	140.2077	0.5590	0.1702	430.80	292.90	215.40	140.216	0.539	239.80	216851	140.2077	0.5590
102026	131.2674	1.1770	0.1532	404.20	274.80	202.10	131.296	1.165	311.90	300891	131.2779	1.1437
102142	130.0448	1.6458	0.3590	890.50	605.50	445.20	130.059	1.648	269.00	323043	130.0448	1.6458
102622	140.3529	1.6471	0.1021	56.90	38.70	28.50	140.351	1.643	34.50	378037	140.3529	1.6471
103072	130.2963	2.9703	0.1940	449.40	305.60	224.70	130.268	2.982	375.10	425842	130.2963	2.9703
103180	138.8518	2.9636	0.1753	390.70	265.70	195.30	138.868	2.974	217.00	519023	138.8518	2.9636
103367	132.1667	-0.5822	0.1893	400.80	272.50	200.40	132.168	-0.579	39.80	549638	132.1667	-0.5822
200056	181.9302	-1.0655	0.1804	936.00	752.90	671.20	181.924	-1.110	521.90	31820	181.9068	-1.1163
200068	176.2745	-0.5932	0.2571	1711.30	914.70	807.50	176.211	-0.532	1342.70	559240	176.2519	-0.5660
200068	176.2745	-0.5932	0.2571	1711.30	914.70	807.50	176.225	-0.527	1253.20	559240	176.2519	-0.5660
200083	178.1093	-0.1100	0.1284	710.20	422.10	384.40	178.085	-0.088	284.60	584113	178.0797	-0.0831
200109	175.1319	0.8532	0.0753	610.60	400.70	221.80	175.069	0.898	412.60	97883	175.0775	0.9008
200245	184.0461	-0.8963	0.1981	613.30	448.20	299.80	184.057	-0.934	488.20	537089	184.0475	-0.9164
200525	180.3111	0.4743	0.2545	749.40	595.10	575.90	180.347	0.475	537.60	84951	180.3111	0.4743
200663	175.7447	1.9062	0.1323	286.40	132.90	100.10	175.752	1.918	124.80	402536	175.7447	1.9062
200687	175.9213	-0.6235	0.2175	328.50	227.90	151.50	175.918	-0.635	153.60	559151	175.9213	-0.6235
200855	184.6717	-1.3029	0.0804	550.90	443.90	363.90	184.645	-1.331	221.00	145461	184.6717	-1.3029
201014	182.3694	0.5333	0.0197	416.90	260.10	166.80	182.630	0.418	428.10	85464	182.5308	0.4262
201105	185.2388	-1.7699	0.1756	541.50	301.00	165.70	185.202	-1.772	416.10	139015	185.2351	-1.7819
201105	185.2388	-1.7699	0.1756	541.50	301.00	165.70	185.219	-1.772	223.10	139015	185.2351	-1.7819
201302	174.9768	1.7976	0.1338	394.90	244.00	159.10	174.950	1.808	253.50	287764	174.9768	1.7976
201470	176.6668	-0.1101	0.2598	338.50	311.70	296.70	176.671	-0.126	249.30	583789	176.6668	-0.1101
201501	183.5165	-0.0697	0.0210	256.00	184.80	144.80	183.495	0.099	271.50	585601	183.4294	-0.0525
201779	179.9081	1.1984	0.2585	609.30	414.30	304.70	179.937	1.202	442.50	23010	179.9081	1.1984
202248	181.5832	-0.4300	0.0632	312.30	212.40	156.20	181.535	-0.387	294.20	55307	181.5201	-0.4186
203940	184.4517	-0.4940	0.0796	258.20	175.60	129.10	184.494	-0.496	241.00	561649	184.4517	-0.4940
300028	222.7488	-0.0375	0.0431	659.10	450.70	409.10	222.634	-0.112	438.50	594946	222.6292	-0.1290
300062	213.5410	-0.1409	0.1240	954.10	533.00	472.20	213.596	-0.027	1059.90	592612	213.5774	-0.1094
300169	220.0161	0.6924	0.1161	1021.40	634.90	299.40	219.915	0.726	848.90	16751	220.0161	0.6924
300210	214.3023	1.9919	0.0550	1416.30	632.70	451.80	214.057	2.323	1655.60	250192	214.3023	1.9919
300210	214.3023	1.9919	0.0550	1416.30	632.70	451.80	214.067	2.303	1568.70	250192	214.3023	1.9919
300415	215.8506	-0.7645	0.1370	748.80	550.60	447.60	215.861	-0.832	628.40	48102	215.8422	-0.7843
300415	215.8506	-0.7645	0.1370	748.80	550.60	447.60	215.865	-0.813	458.60	48102	215.8422	-0.7843
301104	211.8540	1.5554	0.4447	1890.20	1640.50	1500.00	211.788	1.553	1442.70	296456	211.8048	1.5897

Table 5.1 *continued.*

(1)	(2)		(3)	(4)			(5)		(6)	(7)	(8)	
Group ID	α_{Gr}	δ_{Gr}	Z_{Gr}	R_{100}	R_{σ}	R_{50}	α_{NVSS}	δ_{NVSS}	b	Galaxy ID	α_{gal}	δ_{gal}
	(deg)			(kpc)			(deg)		(kpc)		(deg)	
301108	214.5842	1.4834	0.0724	190.80	87.70	29.70	214.617	1.465	196.00	297090	214.5842	1.4834
301195	213.3110	-1.7890	0.3073	1872.30	1149.80	935.60	213.360	-1.780	859.80	460687	213.3444	-1.7521
301293	221.5568	-1.3497	0.1323	179.90	120.90	87.70	221.546	-1.367	180.90	493576	221.5605	-1.3576
301416	217.8383	-0.8956	0.4019	3409.40	2483.20	2073.80	217.909	-0.926	1588.00	544991	217.8499	-0.9002
301530	219.6981	-0.1348	0.1053	629.80	426.30	311.90	219.640	-0.091	530.30	594270	219.6342	-0.0895
301569	222.1764	0.2904	0.0858	153.40	125.00	109.10	222.167	0.305	106.50	619905	222.1697	0.3056
301902	222.3898	-0.7842	0.0271	178.70	121.50	89.30	222.319	-0.755	156.70	49732	222.3053	-0.7915
302027	218.2537	-0.4874	0.0251	192.20	130.70	96.10	218.256	-0.481	13.40	569203	218.2537	-0.4874
302286	216.9649	0.4849	0.3786	1268.60	862.60	634.30	216.946	0.480	396.40	92606	216.9649	0.4849
303401	220.8274	-1.2535	0.0498	213.50	145.20	106.70	220.784	-1.302	238.40	493397	220.7742	-1.2695
303401	220.8274	-1.2535	0.0498	213.50	145.20	106.70	220.785	-1.290	206.30	493397	220.7742	-1.2695
304176	216.0772	0.4171	0.1372	143.60	97.60	71.80	216.083	0.426	95.90	618556	216.0772	0.4171

Table 5.2: Column (1) lists the G3C group ID with group multiplicity shown in column (2). The group velocity dispersion is listed in column (3). This was calculated by Robotham et al. (2011) and is blanked if the reported error in the velocity dispersion was greater than the raw velocity dispersion of the group (see eq. 17 in Robotham et al. (2011)). Column (4) represents the raw measured RM and RM uncertainty for each polarised radio source, as given in Taylor et al. (2009). We correct for any foreground Galactic contribution and list the residual rotation measure (RRM) and the corresponding uncertainty in column (5). Columns (6) & (7) relate to the calculated upper limits to IGrM magnetic fields – only radio-optical matches that satisfied $b \leq R_{50}$ were considered as having significant magnetic fields in the IGrM and all other pairs were blanked. Column (6) reports the pathlength (dl) of a background radio source through the IGrM in kpc and the resultant upper limit to $B_{||}$ is listed in column (7). The G3C ID and redshift of the nearest group member to the polarised radio source is given in columns (8) and (9). The projected separation (10) is calculated as the angular diameter distance between the two sources at the given redshift of the group member.

(1)	(2)	(3)	(4)		(5)		(6)	(7)	(8)	(9)	(10)
Group ID	N	σ	RM	dRM	RRM	dRRM	$dl(R_{50})$	$B_{\|\|}(R_{50})$	Gal. ID	Gal. Z	Gal. Sep.
		(km s^{-1})	(rad m^{-2})		(rad m^{-2})		(kpc)	(μG)			(kpc)
100004	45	370.27	-10	11	-21	15	–	–	372105	0.0699	829.9
100017	19	576.97	-13	9	-30	19	720.1	0.7	300552	0.1578	85.2
100027	20	253.38	-1	11	-9	14	–	–	519000	0.1610	254.1
100045	12	432.44	41	7	6	35	–	–	422462	0.2186	597.8
100107	7	288.44	-18	1	-15	2	–	–	302354	0.2258	213.1
100115	10	175.33	-9	7	-20	13	–	–	376584	0.0705	206.3
100124	9	534.28	15	5	2	13	–	–	423367	0.2024	376.0
100125	18	427.87	-10	17	-22	21	241.7	1.6	423491	0.1918	426.5
100201	11	241.02	-8	6	-27	20	458.7	1.1	517586	0.2122	25.3
100215	6	346.78	2	2	-4	7	864.2	0.1	548952	0.1682	227.6
100330	6	269.59	-3	18	-33	35	–	–	521610	0.2106	273.4
100531	5	164.40	36	15	28	17	–	–	388015	0.1540	267.3
100588	5	145.19	20	12	19	12	–	–	550248	0.0717	502.5
100637	3	233.97	21	12	14	14	286.5	0.7	196057	0.0524	214.3
100643	3	204.53	13	12	7	13	1073.7	0.1	196610	0.2458	122.4
100769	5	171.29	-16	17	-7	19	672.4	0.2	217020	0.1391	179.4
100882	3	351.24	24	16	-1	30	–	–	345927	0.0600	80.2
101352	3	232.05	7	11	15	13	–	–	623336	0.1704	293.8
101890	2	–	-6	17	3	19	–	–	216851	0.1702	239.8
102026	2	43.97	27	12	4	25	–	–	300891	0.1533	284.7
102142	2	274.74	9	8	-13	24	709.6	0.4	323043	0.3585	268.8
102622	2	–	-1	14	7	17	–	–	378037	0.1021	34.5

Table 5.2 *continued.*

(1)	(2)	(3)	(4)		(5)		(6)	(7)	(8)	(9)	(10)
Group ID	N	σ	RM	dRM	RRM	dRRM	$dl(R_{50})$	$B_{\parallel}(R_{50})$	Gal. ID	Gal. Z	Gal. Sep.
		(km s^{-1})	(rad m^{-2})		(rad m^{-2})		(kpc)	(μG)			(kpc)
103072	2	80.71	41	11	9	33	–	–	425842	0.1941	375.3
103180	2	39.85	-1	8	-9	11	–	–	519023	0.1752	216.9
103367	2	355.25	40	14	32	16	392.8	1.4	549638	0.1898	39.9
200056	18	398.82	10	6	-1	13	844.2	0.0	31820	0.1808	204.6
200068	12	397.21	9	6	-1	12	–	–	559240	0.2594	818.4
200068	12	397.21	46	1	36	10	–	–	559240	0.2594	724.3
200083	13	225.27	26	9	13	16	516.8	0.4	584113	0.1288	61.1
200109	11	297.38	-8	12	-14	14	–	–	97883	0.0775	48.3
200245	7	371.45	9	15	-6	22	–	–	537089	0.1985	250.2
200525	4	459.07	20	4	10	10	413.5	0.5	84951	0.2548	538.0
200663	4	232.20	54	6	46	10	–	–	402536	0.1323	124.8
200687	4	180.95	53	16	47	17	–	–	559151	0.2168	153.2
200855	4	52.65	-18	6	-30	14	578.1	0.8	145461	0.0804	221.0
201014	5	155.68	4	12	-5	15	–	–	85464	0.0199	151.5
201105	3	106.46	-12	14	-17	15	–	–	139015	0.1754	388.7
201105	3	106.46	-7	7	-12	9	–	–	139015	0.1754	211.4
201302	3	96.84	20	5	14	7	–	–	287764	0.1338	253.5
201470	3	666.65	11	9	1	13	321.7	0.1	583789	0.2598	249.3
201501	3	150.76	19	17	13	18	–	–	585601	0.0203	254.6
201779	2	–	-8	4	-22	14	–	–	23010	0.2585	442.5
202248	2	–	36	15	23	20	–	–	55307	0.0633	158.3
203940	2	106.15	4	7	-5	12	–	–	561649	0.0798	241.4
300028	24	216.30	-6	6	-14	9	–	–	594946	0.0439	56.3
300062	16	224.74	-19	12	-20	12	–	–	592612	0.1238	706.3
300169	7	115.89	21	11	13	13	–	–	16751	0.1162	849.5
300210	18	365.63	-1	12	-3	13	–	–	250192	0.0560	1683.3
300210	18	365.63	-2	10	-4	10	–	–	250192	0.0560	1594.9
300415	8	285.97	-1	13	-12	17	–	–	48102	0.1385	477.5
300415	8	285.97	-4	5	-15	12	–	–	48102	0.1385	334.9
301104	3	1675.14	-9	14	-10	14	821.8	0.3	296456	0.4483	885.4
301108	3	106.43	9	6	9	6	–	–	297090	0.0724	196.0
301195	4	155.88	25	17	24	17	737.6	0.7	460687	0.3066	545.1
301293	3	69.43	5	7	3	7	–	–	493576	0.1323	155.2
301416	5	808.10	0	8	0	8	2667.3	0.0	544991	0.3970	1322.5
301530	3	395.76	-9	2	-10	2	–	–	594270	0.1060	43.9
301569	3	97.23	1	3	-9	10	47.5	2.8	619905	0.0858	19.4
301902	2	178.14	13	9	9	10	–	–	49732	0.0269	79.2
302027	2	214.15	-9	11	-7	11	190.3	0.5	569203	0.0254	13.5
302286	2	1783.55	25	13	26	13	990.3	0.6	92606	0.3819	398.6
303401	2	–	-3	4	-5	4	–	–	493397	0.0498	122.6
303401	2	–	-3	3	-5	3	–	–	493397	0.0498	86.4
304176	2	259.54	8	5	9	5	–	–	618556	0.1376	96.1

Who are you who are so wise in the ways of science?

Sir Bedevere

6 Conclusions and Future Work

In this chapter, I conclude the thesis with a restatement of the main results, framed around the questions I originally set out to answer in §1.7. I also outline prospects for future work.

6.1 Summary of main results

This thesis was aimed at addressing some of the long-standing questions concerning the evolutionary traits and mechanisms of cosmic magnetic fields. In order to do so, I carried out four separate investigations directed at answering three fundamental questions. I summarise the main results below and relate how they have addressed the original thesis goals.

6.1.1 Remnants of coherent magnetic fields in tidal features

In Chapter 2, I show unequivocally the presence of a coherent magnetic field that spans the entirety of the Magellanic Bridge. Speculations towards the existence of such a field had been made almost half a century ago – though there were no indications that the magnetic field would remain coherent across the tidal bridge. Even with the onset of star-formation in the Magellanic Bridge, we find that the line-of-sight magnetic field structure is almost uniformly pointing away from the observer. Intriguingly, we note that only in the most diffuse regions of the Magellanic Bridge, the ordered magnetic field may come to dominate. This observation suggests that turbulence induced by the interacting galaxies does not destroy the coherent field structure.

6.1.2 Magneto-ionic properties associated with radio galaxies

This thesis set out to identify the polarimetric properties associated with radio galaxies. Using spectropolarimetric observations of the polarisation signal stemming from

the lobes of NGC 612, I endeavoured to identify which polarisation mechanism was responsible for the observed Faraday rotation; however, the model degeneracies between differing polarisation mechanisms made this a non-trivial task. Through detailed analysis of the implied geometries and thermal gas environments, I argued that the Faraday rotation towards the radio galaxy is taking place at the location of the radio galaxy, rather than a consequence of the magneto-ionic structures elsewhere along the line of sight. I went on to state that the observed Faraday rotation is likely not the consequence of internal Faraday rotation, as the amount of thermal material needed to have been entrained from the disk of the optical galaxy would be a factor of ten higher than predicted rates.

In Chapter 4, I carried out a detailed spectropolarimetric analysis of the radio galaxy MSH 05−3*13*. After removing the Faraday rotation due to the Milky Way foreground, I revealed a sinusoidal Faraday-depth pattern implanted on the radio lobes. I used the physical scales of the changing Faraday depth to argue that the observed Faraday rotation must be taking place in the immediate vicinity of the radio galaxy. I highlighted the unique depolarisation signature associated with the jets of the galaxy and target this region as an area for future research.

6.1.3 MAGNETIC FIELDS IN THE DIFFUSE INTRAGROUP MEDIUM

In Chapters 3 and 4, I studied two radio galaxies, NGC 612 and MSH 05−3*13*, that are each members of galaxy groups. Although embedded in a relatively low-density environment, in both cases I found potential evidence of feedback at the interface between the synchrotron lobes and the surrounding intragroup medium. I argued that the observation of varying Faraday depth structures spanning the large radio lobes may be indicative of a thin skin of thermal material having been swept up from the surrounding medium resulting in Faraday eddies on the surface of the lobes. Feedback of this sort has been invoked previously by Bicknell et al. (1990) to explain the Faraday gradients observed towards the lobes of Cygnus A. I showed that observed variations in Faraday depth are consistent with what is predicted for surface eddies of the observed scale and argue that minimal compression of the IGrM would be required to result in the observed signal.

Finally, in Chapter 5, while observing sight lines that probed optically-defined galaxy groups, I was unable to identify any change to the observed polarised signal towards a background radio galaxy that may have been caused by the passage through the group environment. While I was limited in my discussion of the impact of the galaxy group environment on the evolution of large-scale magnetic fields, I laid out some necessary requirements for future work.

6.2 LOOKING FORWARD

I began this thesis stating that astronomers were in the middle of a revolution in understanding cosmic magnetism. While I have used some of the best technologies and techniques available at the present date to advance our understanding of the evolution of magnetic fields on cosmic scales, it has become clear that more work is needed to answer many remaining questions into the origin and evolution of large-scale magnetic fields.

As introduced in Chapter 5, any future success of an investigation into the diffuse medium of galaxy groups will rely partially on density measurements of the intervening thermal material, and I proposed targeting galaxy groups with diffuse X-ray emission. By choosing to target only galaxy groups with X-ray emission, it guarantees the existence of a magnetic field in the intervening medium between the group member galaxies if we assume that the hot, ionised material responsible for the X-ray emission is moving, thus creating a magnetic field. Furthermore, the X-ray data will provide a thermal electron density for each group. By observing polarised background sources that shine through the intervening intragroup medium, we will definitively answer the question: *'are magnetic fields in the intragroup medium coherent or random'*.

Furthermore, with the advent of wide-field radio survey telescopes, such as the Australia Square Kilometre Array Pathfinder (ASKAP, DeBoer et al. 2009), large-area surveys of the polarised Universe will be carried out with unprecedented speed and sensitivity. Upcoming continuum observations with ASKAP are anticipated to produce ~ 50 polarised sources per square degree. This will vastly improve previous work towards expanding a RM grid that has currently found ~ 1 polarised source per square degree (i.e. Taylor et al. 2009). Creating such a grid is a major focus of the POlarisation Sky Survey of the Universe's Magnetism (POSSUM, Gaensler 2009) survey, which aims to measure hundreds of thousands of polarised sources spanning the frequency range of $1100 - 1400$ GHz. The analysis of such a grid will undoubtedly reveal Faraday structure of the Milky Way, but also of any intervening structures on large angular scales, such as nearby galaxy clusters.

In the high signal-to-noise regime, such as was the case of NGC 612 and MSH 05−3*13*, I have shown that additional information was required in order to carry out a full analysis of a each radio galaxy. Such an approach will undoubtedly be necessary for future investigations using next-generation telescopes. In the era of ASKAP, building automatic analysis techniques will be difficult, as every polarised source will need to be treated as a unique case. The way forward will likely require multi-wavelength analysis in order to build a complete picture of the polarisation of radio galaxies and other resolved sources.

By employing new powerful survey telescopes in conjunction with evolving polarisation analysis techniques, astronomers will be soon have the ability to carry out unique polarisation observations that were once thought unfeasible. The majority of these ex-

periments will be carried out in the next decade and are likely to yield unprecedented and unanticipated results. During this time, the study of cosmic magnetism will undoubtedly enter its prime, in which many of the fundamental questions pertaining to the magnetic Universe will finally be answered.

Bibliography

A. Aguirre, L. Hernquist, J. Schaye, N. Katz, D. H. Weinberg, and J. Gardner. Metal Enrichment of the Intergalactic Medium in Cosmological Simulations. *ApJ*, 561:521–549, November 2001. doi: 10.1086/323370.

T. Akahori and D. Ryu. Faraday Rotation Measure Due to the Intergalactic Magnetic Field. *ApJ*, 723:476–481, November 2010. doi: 10.1088/0004-637X/723/1/476.

T. Akahori and D. Ryu. Faraday Rotation Measure due to the Intergalactic Magnetic Field. II. The Cosmological Contribution. *ApJ*, 738:134, September 2011. doi: 10.1088/0004-637X/738/2/134.

H. Akamatsu and H. Kawahara. Systematic X-Ray Analysis of Radio Relic Clusters with Suzaku. *PASJ*, 65:16, February 2013.

C. S. Anderson, B. M. Gaensler, and I. J. Feain. A Study of Broadband Faraday Rotation and Polarization Behavior over 1.3–10 GHz in 36 Discrete Radio Sources. *ApJ*, 825:59, July 2016. doi: 10.3847/0004-637X/825/1/59.

K. A. Barger, L. M. Haffner, and J. Bland-Hawthorn. Warm Ionized Gas Revealed in the Magellanic Bridge Tidal Remnant: Constraining the Baryon Content and the Escaping Ionizing Photons around Dwarf Galaxies. *ApJ*, 771:132, July 2013. doi: 10.1088/0004-637X/771/2/132.

A. Basu, S. A. Mao, A. A. Kepley, T. Robishaw, E. G. Zweibel, and J. S. Gallagher, III. Detection of an $\sim$20 kpc coherent magnetic field in the outskirt of merging spirals: the Antennae galaxies. *MNRAS*, 464:1003–1017, January 2017. doi: 10.1093/mnras/stw2369.

R. Beck. Magnetic fields in normal galaxies. *Philosophical Transactions of the Royal Society of London Series A*, 358:777, February 2000. doi: 10.1098/rsta.2000.0558.

R. Beck and B. M. Gaensler. Observations of magnetic fields in the Milky Way and in nearby galaxies with a Square Kilometre Array. *New AR*, 48:1289–1304, December 2004. doi: 10.1016/j.newar.2004.09.013.

R. Beck and M. Krause. Revised equipartition and minimum energy formula for magnetic field strength estimates from radio synchrotron observations. *Astronomische Nachrichten*, 326:414–427, July 2005. doi: 10.1002/asna.200510366.

M. C. Begelman and D. F. Cioffi. Overpressured cocoons in extragalactic radio sources. *ApJ*, 345:L21–L24, October 1989. doi: 10.1086/185542.

M. C. Begelman, R. D. Blandford, and M. J. Rees. Theory of extragalactic radio sources. *Reviews of Modern Physics*, 56:255–351, April 1984. doi: 10.1103/RevModPhys.56.255.

S. Bertone, C. Vogt, and T. Enßlin. Magnetic field seeding by galactic winds. *MNRAS*, 370:319–330, July 2006. doi: 10.1111/j.1365-2966.2006.10474.x.

G. Besla, N. Kallivayalil, L. Hernquist, R. P. van der Marel, T. J. Cox, and D. Kereš. Simulations of the Magellanic Stream in a First Infall Scenario. *ApJ*, 721:L97–L101, October 2010. doi: 10.1088/2041-8205/721/2/L97.

G. Besla, N. Kallivayalil, L. Hernquist, R. P. van der Marel, T. J. Cox, and D. Kereš. The role of dwarf galaxy interactions in shaping the Magellanic System and implications for Magellanic Irregulars. *MNRAS*, 421:2109–2138, April 2012. doi: 10.1111/j.1365-2966.2012.20466.x.

P. N. Best. The environmental dependence of radio-loud AGN activity and star formation in the 2dFGRS. *MNRAS*, 351:70–82, June 2004. doi: 10.1111/j.1365-2966.2004.07752.x.

E. Bica, C. Bonatto, C. M. Dutra, and J. F. C. Santos. A general catalogue of extended objects in the Magellanic System. *MNRAS*, 389:678–690, September 2008. doi: 10.1111/j.1365-2966.2008.13612.x.

G. V. Bicknell. Extragalactic radio sources and the role of relativistic jets. *Australian Journal of Physics*, 47:669–680, 1994.

G. V. Bicknell, R. A. Cameron, and R. A. Gingold. Rotation measure variations across the lobes of extragalactic radio sources. *ApJ*, 357:373–387, July 1990. doi: 10.1086/168928.

R. D. Blandford. Astrophysical jets : proceedings of the Astrophysical Jets Meeting, Baltimore, 1992 May 12-14. 1993.

K. M. Blundell and S. Rawlings. The Spectra and Energies of Classical Double Radio Lobes. *AJ*, 119:1111–1122, March 2000. doi: 10.1086/301254.

A. Bonafede, L. Feretti, G. Giovannini, F. Govoni, M. Murgia, G. B. Taylor, H. Ebeling, S. Allen, G. Gentile, and Y. Pihlström. Revealing the magnetic field in a distant galaxy cluster: discovery of the complex radio emission from MACS J0717.5 +3745. *A&A*, 503:707–720, September 2009. doi: 10.1051/0004-6361/200912520.

A. Bonafede, L. Feretti, M. Murgia, F. Govoni, G. Giovannini, D. Dallacasa, K. Dolag, and G. B. Taylor. The Coma cluster magnetic field from Faraday rotation measures. *A&A*, 513:A30, April 2010. doi: 10.1051/0004-6361/200913696.

A. Bonafede, F. Vazza, M. Brüggen, M. Murgia, F. Govoni, L. Feretti, G. Giovannini, and G. Ogrean. Measurements and simulation of Faraday rotation across the Coma radio relic. *MNRAS*, 433:3208–3226, August 2013. doi: 10.1093/mnras/stt960.

J. N. Bregman. A wind in the Galaxy. *ApJ*, 237:280–284, April 1980. doi: 10.1086/157867.

M. A. Brentjens and A. G. de Bruyn. Faraday rotation measure synthesis. *A&A*, 441: 1217–1228, October 2005. doi: 10.1051/0004-6361:20052990.

A. H. Bridle and R. A. Perley. Extragalactic Radio Jets. *ARA&A*, 22:319–358, 1984. doi: 10.1146/annurev.aa.22.090184.001535.

S. Brown and L. Rudnick. Diffuse Cluster-Like Radio Emission in Poor Environments. *AJ*, 137:3158–3171, February 2009. doi: 10.1088/0004-6256/137/2/3158.

C. Brüns, J. Kerp, L. Staveley-Smith, U. Mebold, M. E. Putman, R. F. Haynes, P. M. W. Kalberla, E. Muller, and M. D. Filipovic. The Parkes H I Survey of the Magellanic System. *A&A*, 432:45–67, March 2005. doi: 10.1051/0004-6361:20040321.

B. J. Burn. On the depolarization of discrete radio sources by Faraday dispersion. *MNRAS*, 133:67, 1966.

C. L. Carilli, J. W. Dreher, S. Conner, and R. A. Perley. Broad- and narrow-band imaging of the giant radio galaxy Cygnus A. *AJ*, 98:513–523, August 1989. doi: 10.1086/115155.

R. Cen and J. P. Ostriker. Where Are the Baryons? *ApJ*, 514:1–6, March 1999. doi: 10.1086/306949.

C. J. Cesarsky. Cosmic-ray confinement in the galaxy. *ARA&A*, 18:289–319, 1980. doi: 10.1146/annurev.aa.18.090180.001445.

S. Chandrasekhar. On the Radiative Equilibrium of a Stellar Atmosphere. XV. *ApJ*, 105: 424, May 1947. doi: 10.1086/144917.

S. Chandrasekhar. *Hydrodynamic and hydromagnetic stability*. 1961.

C.-H. R. Chen, R. Indebetouw, E. Muller, A. Kawamura, K. D. Gordon, M. Sewiło, B. A. Whitney, Y. Fukui, S. C. Madden, M. R. Meade, M. Meixner, J. M. Oliveira, T. P. Robitaille, J. P. Seale, B. Shiao, and J. T. van Loon. Spitzer View of Massive Star Formation in the Tidally Stripped Magellanic Bridge. *ApJ*, 785:162, April 2014. doi: 10.1088/0004-637X/785/2/162.

E. Churazov, M. Brüggen, C. R. Kaiser, H. Böhringer, and W. Forman. Evolution of Buoyant Bubbles in M87. *ApJ*, 554:261–273, June 2001. doi: 10.1086/321357.

K. T. Chyży and R. Beck. Magnetic fields in merging spirals - the Antennae. *A&A*, 417: 541–555, April 2004. doi: 10.1051/0004-6361:20031778.

D. A. Clarke, A. H. Bridle, J. O. Burns, R. A. Perley, and M. L. Norman. Origin of the structures and polarization in the classical double 3C 219. *ApJ*, 385:173–187, January 1992. doi: 10.1086/170925.

T. E. Clarke, P. P. Kronberg, and H. Böhringer. A New Radio-X-Ray Probe of Galaxy Cluster Magnetic Fields. *ApJ*, 547:L111–L114, February 2001. doi: 10.1086/318896.

J. J. Condon, G. Helou, D. B. Sanders, and B. T. Soifer. The 'Taffy' galaxies UGC 12914/5. *AJ*, 105:1730–1736, May 1993. doi: 10.1086/116549.

J. J. Condon, W. D. Cotton, E. W. Greisen, Q. F. Yin, R. A. Perley, G. B. Taylor, and J. J. Broderick. The NRAO VLA Sky Survey. *AJ*, 115:1693–1716, May 1998. doi: 10.1086/300337.

J. J. Condon, G. Helou, and T. H. Jarrett. A Second "Taffy" Galaxy Pair. *AJ*, 123: 1881–1891, April 2002. doi: 10.1086/339558.

J. L. Connelly, D. J. Wilman, A. Finoguenov, A. Hou, J. S. Mulchaey, S. L. McGee, M. L. Balogh, L. C. Parker, R. Saglia, R. D. E. Henderson, and R. G. Bower. Exploring the Diversity of Groups at 0.1 ¡ z ¡ 0.8 with X-Ray and Optically Selected Samples. *ApJ*, 756:139, September 2012. doi: 10.1088/0004-637X/756/2/139.

B. F. C. Cooper and R. M. Price. Faraday Rotation Effects associated with the Radio Source Centaurus A. *Nature*, 196:761, November 1962. doi: 10.1038/196761a0.

W. D. Cotton. Calibration and imaging of polarization sensitive Very Long Baseline Interferometer observations. *AJ*, 106:1241–1248, September 1993. doi: 10.1086/116723.

W. D. Cotton, D. Dallacasa, C. Fanti, R. Fanti, A. R. Foley, R. T. Schilizzi, R. Spencer, D. J. Saikia, and S. Garrington. Polarimetry of GPS and CSS Sources. *PASA*, 20: 12–15, 2003. doi: 10.1071/AS02031.

R. Crutcher, C. Heiles, and T. Troland. . In E. Falgarone and T. Passot, editors, *Turbulence and Magnetic Fields in Astrophysics*, volume 614 of *Lecture Notes in Physics, Berlin Springer Verlag*, pages 155–181, 2003.

S. Das, H. Kang, D. Ryu, and J. Cho. Propagation of Ultra-High-Energy Protons through the Magnetized Cosmic Web. *ApJ*, 682:29-38, July 2008. doi: 10.1086/588278.

G. de Vaucouleurs, A. de Vaucouleurs, H. G. Corwin, Jr., R. J. Buta, G. Paturel, and P. Fouqué. *Third Reference Catalogue of Bright Galaxies. Volume I: Explanations and references. Volume II: Data for galaxies between 0^h and 12^h. Volume III: Data for galaxies between 12^h and 24^h.* 1991.

D. R. DeBoer, R. G. Gough, J. D. Bunton, T. J. Cornwell, R. J. Beresford, S. Johnston, I. J. Feain, A. E. Schinckel, C. A. Jackson, M. J. Kesteven, A. Chippendale, G. A. Hampson, J. D. O'Sullivan, S. G. Hay, C. E. Jacka, T. W. Sweetnam, M. C. Storey, L. Ball, and B. J. Boyle. Australian SKA Pathfinder: A High-Dynamic Range Wide-Field of View Survey Telescope. *IEEE Proceedings*, 97:1507–1521, August 2009. doi: 10.1109/JPROC.2009.2016516.

K. Dolag, M. Bartelmann, and H. Lesch. Evolution and structure of magnetic fields in simulated galaxy clusters. *A&A*, 387:383–395, May 2002. doi: 10.1051/0004-6361:20020241.

M. Donahue, G. Aldering, and J. T. Stocke. Low Surface Brightness H alpha Observations of Local Intergalactic Hydrogen Clouds. *ApJ*, 450:L45, September 1995. doi: 10.1086/316771.

E. D'Onghia and A. J. Fox. The Magellanic Stream: Circumnavigating the Galaxy. *ARA&A*, 54:363–400, September 2016. doi: 10.1146/annurev-astro-081915-023251.

J. Donnert, K. Dolag, H. Lesch, and E. Müller. Cluster magnetic fields from galactic outflows. *MNRAS*, 392:1008–1021, January 2009. doi: 10.1111/j.1365-2966.2008.14132.x.

J. B. Dove, J. M. Shull, and A. Ferrara. The Escape of Ionizing Photons from OB Associations in Disk Galaxies: Radiation Transfer through Superbubbles. *ApJ*, 531:846–860, March 2000. doi: 10.1086/308481.

S. P. Driver, D. T. Hill, L. S. Kelvin, A. S. G. Robotham, J. Liske, P. Norberg, I. K. Baldry, S. P. Bamford, A. M. Hopkins, J. Loveday, J. A. Peacock, E. Andrae, J. Bland-Hawthorn, S. Brough, M. J. I. Brown, E. Cameron, J. H. Y. Ching, M. Colless, C. J. Conselice, S. M. Croom, N. J. G. Cross, R. de Propris, S. Dye, M. J. Drinkwater, S. Ellis, A. W. Graham, M. W. Grootes, M. Gunawardhana, D. H. Jones, E. van Kampen,

C. Maraston, R. C. Nichol, H. R. Parkinson, S. Phillipps, K. Pimbblet, C. C. Popescu, M. Prescott, I. G. Roseboom, E. M. Sadler, A. E. Sansom, R. G. Sharp, D. J. B. Smith, E. Taylor, D. Thomas, R. J. Tuffs, D. Wijesinghe, L. Dunne, C. S. Frenk, M. J. Jarvis, B. F. Madore, M. J. Meyer, M. Seibert, L. Staveley-Smith, W. J. Sutherland, and S. J. Warren. Galaxy and Mass Assembly (GAMA): survey diagnostics and core data release. *MNRAS*, 413:971–995, May 2011. doi: 10.1111/j.1365-2966.2010.18188.x.

R. T. Drzazga, K. T. Chyży, W. Jurusik, and K. Wiórkiewicz. Magnetic field evolution in interacting galaxies. *A&A*, 533:A22, September 2011. doi: 10.1051/0004-6361/201016092.

S. Eguchi, Y. Ueda, H. Awaki, J. Aird, Y. Terashima, and R. Mushotzky. Suzaku View of the Swift/BAT Active Galactic Nuclei. III. Application of Numerical Torus Models to Two Nearly Compton Thick Active Galactic Nuclei (NGC 612 and NGC 3081). *ApJ*, 729:31, March 2011. doi: 10.1088/0004-637X/729/1/31.

R. D. Ekers, W. M. Goss, C. G. Kotanyi, and D. J. Skellern. NGC 612-A Radio Galaxy with a Disk. *A&A*, 69:L21, October 1978.

R. D. Ekers, J. V. Wall, P. A. Shaver, W. M. Goss, R. A. E. Fosbury, I. J. Danziger, A. F. M. Moorwood, D. F. Malin, A. S. Monk, and J. A. Ekers. A complete sample of radio galaxies. I - The radio data. *MNRAS*, 236:737–777, February 1989. doi: 10.1093/mnras/236.4.737.

B. H. C. Emonts, R. Morganti, T. A. Oosterloo, J. Holt, C. N. Tadhunter, J. M. van der Hulst, R. Ojha, and E. M. Sadler. Enormous disc of cool gas surrounding the nearby powerful radio galaxy NGC612 (PKS0131-36). *MNRAS*, 387:197–208, June 2008. doi: 10.1111/j.1365-2966.2008.13142.x.

G. Erfanianfar, A. Finoguenov, M. Tanaka, M. Lerchster, K. Nandra, E. Laird, J. L. Connelly, R. Bielby, M. Mirkazemi, S. M. Faber, D. Kocevski, M. Cooper, J. A. Newman, T. Jeltema, A. L. Coil, F. Brimioulle, M. Davis, H. J. McCracken, C. Willmer, B. Gerke, N. Cappelluti, and S. Gwyn. X-Ray Groups of Galaxies in the AEGIS Deep and Wide Fields. *ApJ*, 765:117, March 2013. doi: 10.1088/0004-637X/765/2/117.

B. L. Fanaroff and J. M. Riley. The morphology of extragalactic radio sources of high and low luminosity. *MNRAS*, 167:31P–36P, May 1974.

J. S. Farnes, B. M. Gaensler, and E. Carretti. A Broadband Polarization Catalog of Extragalactic Radio Sources. *ApJS*, 212:15, May 2014. doi: 10.1088/0067-0049/212/1/15.

D. Farnsworth, L. Rudnick, and S. Brown. Integrated Polarization of Sources at λ ˜ 1 m and New Rotation Measure Ambiguities. *AJ*, 141:191, June 2011. doi: 10.1088/0004-6256/141/6/191.

I. J. Feain, R. D. Ekers, T. Murphy, B. M. Gaensler, J.-P. Macquart, R. P. Norris, T. J. Cornwell, M. Johnston-Hollitt, J. Ott, and E. Middelberg. Faraday Rotation Structure on Kiloparsec Scales in the Radio Lobes of Centaurus A. *ApJ*, 707:114–125, December 2009. doi: 10.1088/0004-637X/707/1/114.

L. Feretti, G. Giovannini, F. Govoni, and M. Murgia. Clusters of galaxies: observational properties of the diffuse radio emission. *A&A Rev.*, 20:54, May 2012. doi: 10.1007/s00159-012-0054-z.

A. Finoguenov, D. S. Davis, M. Zimer, and J. S. Mulchaey. The Two-dimensional XMM-Newton Group Survey: z ¡ 0.012 Groups. *ApJ*, 646:143–160, July 2006. doi: 10.1086/504697.

A. Finoguenov, M. Tanaka, M. Cooper, V. Allevato, N. Cappelluti, A. Choi, C. Heymans, F. E. Bauer, F. Ziparo, P. Ranalli, J. Silverman, W. N. Brandt, Y. Q. Xue, J. Mulchaey, L. Howes, C. Schmid, D. Wilman, A. Comastri, G. Hasinger, V. Mainieri, B. Luo, P. Tozzi, P. Rosati, P. Capak, and P. Popesso. Ultra-deep catalog of X-ray groups in the Extended Chandra Deep Field South. *A&A*, 576:A130, April 2015. doi: 10.1051/0004-6361/201323053.

E. B. Fomalont. The East-West Structure of Radio Sources at 1425 MHz. *ApJS*, 15:203, January 1968. doi: 10.1086/190166.

E. B. Fomalont, K. A. Ebneter, W. J. M. van Breugel, and R. D. Ekers. Depolarization silhouettes and the filamentary structure in the radio source Fornax A. *ApJ*, 346:L17–L20, November 1989. doi: 10.1086/185568.

D. Foreman-Mackey, D. W. Hogg, D. Lang, and J. Goodman. emcee: The MCMC Hammer. *PASP*, 125:306–312, March 2013. doi: 10.1086/670067.

A. J. Fox, B. P. Wakker, B. D. Savage, T. M. Tripp, K. R. Sembach, and J. Bland-Hawthorn. Multiphase High-Velocity Clouds toward HE 0226-4110 and PG 0953+414. *ApJ*, 630:332–354, September 2005. doi: 10.1086/431915.

E. Freeland and E. Wilcots. Intergalactic Gas in Groups of Galaxies: Implications for Dwarf Spheroidal Formation and the Missing Baryons Problem. *ApJ*, 738:145, September 2011. doi: 10.1088/0004-637X/738/2/145.

S. R. Furlanetto and A. Loeb. Intergalactic Magnetic Fields from Quasar Outflows. *ApJ*, 556:619–634, August 2001. doi: 10.1086/321630.

D. C. Gabuzda, T. M. Cantwell, and T. V. Cawthorne. Magnetic field structure of the extended 3C 380 jet. *MNRAS*, 438:L1–L5, February 2014a. doi: 10.1093/mnrasl/slt129.

D. C. Gabuzda, A. R. Reichstein, and E. L. O'Neill. Are spine-sheath polarization structures in the jets of active galactic nuclei associated with helical magnetic fields? *MNRAS*, 444:172–184, October 2014b. doi: 10.1093/mnras/stu1381.

B. M. Gaensler. Cosmic magnetism with the Square Kilometre Array and its pathfinders. In K. G. Strassmeier, A. G. Kosovichev, and J. E. Beckman, editors, *Cosmic Magnetic Fields: From Planets, to Stars and Galaxies*, volume 259 of *IAU Symposium*, pages 645–652, April 2009. doi: 10.1017/S1743921309031470.

B. M. Gaensler, M. Haverkorn, L. Staveley-Smith, J. M. Dickey, N. M. McClure-Griffiths, J. R. Dickel, and M. Wolleben. The Magnetic Field of the Large Magellanic Cloud Revealed Through Faraday Rotation. *Science*, 307:1610–1612, March 2005. doi: 10.1126/science.1108832.

L. T. Gardiner and M. Noguchi. N-body simulations of the Small Magellanic Cloud and the Magellanic Stream. *MNRAS*, 278:191–208, January 1996. doi: 10.1093/mnras/278.1.191.

L. T. Gardiner, T. Sawa, and M. Fujimoto. Numerical Simulations of the Magellanic System - Part One - Orbits of the Magellanic Clouds and the Global Gas Distribution. *MNRAS*, 266:567, February 1994. doi: 10.1093/mnras/266.3.567.

F. F. Gardner and J. B. Whiteoak. The Polarization of Cosmic Radio Waves. *ARA&A*, 4: 245, 1966. doi: 10.1146/annurev.aa.04.090166.001333.

G. Giovannini, L. Feretti, M. Girardi, F. Govoni, M. Murgia, V. Vacca, and J. Bagchi. A giant radio halo in the low luminosity X-ray cluster Abell 523. *A&A*, 530:L5, June 2011. doi: 10.1051/0004-6361/201116930.

O. Goldshmidt and Y. Rephaeli. Turbulent generation of intracluster magnetic fields and Faraday rotation measurements. *ApJ*, 411:518–528, July 1993. doi: 10.1086/172853.

J. L. Gómez, A. P. Marscher, S. G. Jorstad, I. Agudo, and M. Roca-Sogorb. Faraday Rotation and Polarization Gradients in the Jet of 3C 120: Interaction with the External Medium and a Helical Magnetic Field? *ApJ*, 681:L69, July 2008. doi: 10.1086/590388.

Gopal-Krishna and P. J. Wiita. Extragalactic radio sources with hybrid morphology: implications for the Fanaroff-Riley dichotomy. *A&A*, 363:507–516, November 2000.

K. N. Gourgouliatos, J. Braithwaite, and M. Lyutikov. Structure of magnetic fields in intracluster cavities. *MNRAS*, 409:1660–1668, December 2010. doi: 10.1111/j.1365-2966.2010.17410.x.

F. Govoni, K. Dolag, M. Murgia, L. Feretti, S. Schindler, G. Giovannini, W. Boschin, V. Vacca, and A. Bonafede. Rotation measures of radio sources in hot galaxy clusters. *A&A*, 522:A105, November 2010. doi: 10.1051/0004-6361/200913665.

F. Govoni, M. Murgia, G. Giovannini, V. Vacca, and A. Bonafede. The large-scale diffuse radio emission in A781. *A&A*, 529:A69, May 2011. doi: 10.1051/0004-6361/201016042.

D. Guidetti, R. A. Laing, M. Murgia, F. Govoni, L. Gregorini, and P. Parma. Structure of the magnetoionic medium around the Fanaroff-Riley Class I radio galaxy 3C 449. *A&A*, 514:A50, May 2010. doi: 10.1051/0004-6361/200913872.

D. Guidetti, R. A. Laing, A. H. Bridle, P. Parma, and L. Gregorini. Ordered magnetic fields around radio galaxies: evidence for interaction with the environment. *MNRAS*, 413:2525–2544, June 2011. doi: 10.1111/j.1365-2966.2011.18321.x.

D. Guidetti, R. A. Laing, J. H. Croston, A. H. Bridle, and P. Parma. The magnetized medium around the radio galaxy B2 0755+37: an interaction with the intragroup gas. *MNRAS*, 423:1335–1350, June 2012. doi: 10.1111/j.1365-2966.2012.20961.x.

L. M. Haffner, R. J. Reynolds, S. L. Tufte, G. J. Madsen, K. P. Jaehnig, and J. W. Percival. The Wisconsin Hα Mapper Northern Sky Survey. *ApJS*, 149:405–422, December 2003. doi: 10.1086/378850.

A. M. Hammond, T. Robishaw, and B. M. Gaensler. A New Catalog of Faraday Rotation Measures and Redshifts for Extragalactic Radio Sources. *ArXiv e-prints*, September 2012.

J. L. Han, R. N. Manchester, A. G. Lyne, G. J. Qiao, and W. van Straten. Pulsar Rotation Measures and the Large-Scale Structure of the Galactic Magnetic Field. *ApJ*, 642:868–881, May 2006. doi: 10.1086/501444.

P. J. Hancock, T. Murphy, B. M. Gaensler, A. Hopkins, and J. R. Curran. Compact continuum source finding for next generation radio surveys. *MNRAS*, 422:1812–1824, May 2012. doi: 10.1111/j.1365-2966.2012.20768.x.

P. Haves. Polarization parameters of 183 extragalactic radio sources. *MNRAS*, 173:553–568, December 1975.

R. F. Haynes, U. Klein, S. R. Wayte, R. Wielebinski, J. D. Murray, E. Bajaja, D. Meinert, U. R. Buczilowski, J. I. Harnett, A. J. Hunt, R. Wark, and L. Sciacca. A radio continuum study of the Magellanic Clouds. I - Complete multi-frequency maps. *A&A*, 252: 475–486, December 1991.

G. Heald, R. Braun, and R. Edmonds. The Westerbork SINGS survey. II Polarization, Faraday rotation, and magnetic fields. *A&A*, 503:409–435, August 2009. doi: 10.1051/0004-6361/200912240.

S. F. Helsdon and T. J. Ponman. The intragroup medium in loose groups of galaxies. *MNRAS*, 315:356–370, June 2000. doi: 10.1046/j.1365-8711.2000.03396.x.

P. Hickson. Systematic properties of compact groups of galaxies. *ApJ*, 255:382–391, April 1982. doi: 10.1086/159838.

A. S. Hill, L. M. Haffner, and R. J. Reynolds. Ionized Gas in the Smith Cloud. *ApJ*, 703: 1832–1838, October 2009. doi: 10.1088/0004-637X/703/2/1832.

J. V. Hindman, F. J. Kerr, and R. X. McGee. A Low Resolution Hydrogen-line Survey of the Magellanic System. II. Interpretation of Results. *Australian Journal of Physics*, 16:570, 1963. doi: 10.1071/PH630570.

J. Holt, C. N. Tadhunter, R. M. González Delgado, K. J. Inskip, J. Rodriguez Zaurin, B. H. C. Emonts, R. Morganti, and K. A. Wills. The properties of the young stellar populations in powerful radio galaxies at low and intermediate redshifts. *MNRAS*, 381: 611–639, October 2007. doi: 10.1111/j.1365-2966.2007.12140.x.

T. Hovatta, M. L. Lister, M. F. Aller, H. D. Aller, D. C. Homan, Y. Y. Kovalev, A. B. Pushkarev, and T. Savolainen. MOJAVE: Monitoring of Jets in Active Galactic Nuclei with VLBA Experiments. VIII. Faraday Rotation in Parsec-scale AGN Jets. *AJ*, 144: 105, October 2012. doi: 10.1088/0004-6256/144/4/105.

E. Hummel and R. Beck. Magnetic fields in interacting galaxies: NGC 2276. *A&A*, 303: 691, November 1995.

W. Jaffe. Clusters of Galaxies and Radio Sources. In D. L. Jauncey, editor, *Radio Astronomy and Cosmology*, volume 74 of *IAU Symposium*, page 305, 1977.

R. Jansson and G. R. Farrar. A New Model of the Galactic Magnetic Field. *ApJ*, 757:14, September 2012. doi: 10.1088/0004-637X/757/1/14.

M. Johnston-Hollitt, C. P. Hollitt, and R. D. Ekers. Statistical Analysis of Extra-galactic Rotation Measures. In B. Uyaniker, W. Reich, and R. Wielebinski, editors, *The Magnetized Interstellar Medium*, pages 13–18, February 2004.

C. Jones and W. Forman. The structure of clusters of galaxies observed with Einstein. *ApJ*, 276:38–55, January 1984. doi: 10.1086/161591.

D. H. Jones, M. A. Read, W. Saunders, M. Colless, T. Jarrett, Q. A. Parker, A. P. Fairall, T. Mauch, E. M. Sadler, F. G. Watson, D. Burton, L. A. Campbell, P. Cass, S. M. Croom, J. Dawe, K. Fiegert, L. Frankcombe, M. Hartley, J. Huchra, D. James, E. Kirby, O. Lahav, J. Lucey, G. A. Mamon, L. Moore, B. A. Peterson, S. Prior, D. Proust, K. Russell, V. Safouris, K.-I. Wakamatsu, E. Westra, and M. Williams. The 6dF Galaxy Survey: final redshift release (DR3) and southern large-scale structures. *MNRAS*, 399:683–698, October 2009. doi: 10.1111/j.1365-2966.2009.15338.x.

P. A. Jones and W. B. McAdam. The structure of southern extragalactic radio sources. *ApJS*, 80:137–203, May 1992. doi: 10.1086/191662.

J. F. Kaczmarek, C. R. Purcell, B. M. Gaensler, N. M. McClure-Griffiths, and J. Stevens. Detection of a Coherent Magnetic Field in the Magellanic Bridge through Faraday Rotation. *MNRAS*, January 2017. doi: 10.1093/mnras/stx206.

C. R. Kaiser, A. P. Schoenmakers, and H. J. A. Röttgering. Radio galaxies with a 'double-double' morphology - II. The evolution of double-double radio galaxies and implications for the alignment effect in FRII sources. *MNRAS*, 315:381–394, June 2000. doi: 10.1046/j.1365-8711.2000.03431.x.

P. M. W. Kalberla, N. M. McClure-Griffiths, D. J. Pisano, M. R. Calabretta, H. A. Ford, F. J. Lockman, L. Staveley-Smith, J. Kerp, B. Winkel, T. Murphy, and K. Newton-McGee. GASS: the Parkes Galactic all-sky survey. II. Stray-radiation correction and second data release. *A&A*, 521:A17, October 2010. doi: 10.1051/0004-6361/200913979.

H. Kang, D. Ryu, R. Cen, and D. Song. Shock-heated Gas in the Large-Scale Structure of the Universe. *ApJ*, 620:21–30, February 2005. doi: 10.1086/426931.

N. G. Kantharia, S. Ananthakrishnan, R. Nityananda, and A. Hota. GMRT observations of the group Holmberg 124: Evolution by tidal forces and ram pressure? *A&A*, 435: 483–496, May 2005. doi: 10.1051/0004-6361:20042261.

P. Kharb, D. C. Gabuzda, C. P. O'Dea, P. Shastri, and S. A. Baum. Rotation Measures Across Parsec-Scale Jets of Fanaroff-Riley Type I Radio Galaxies. *ApJ*, 694:1485–1497, April 2009. doi: 10.1088/0004-637X/694/2/1485.

C. C. Kirkpatrick, B. R. McNamara, and K. W. Cavagnolo. Anisotropic Metal-enriched Outflows Driven by Active Galactic Nuclei in Clusters of Galaxies. *ApJ*, 731:L23, April 2011. doi: 10.1088/2041-8205/731/2/L23.

S. S. Komissarov and A. G. Gubanov. Relic radio galaxies: evolution of synchrotron spectrum. *A&A*, 285:27–43, May 1994.

C. G. Kotanyi and R. D. Ekers. Radio galaxies with dust lanes. *A&A*, 73:L1–L3, March 1979.

H. Kotarba, S. J. Karl, T. Naab, P. H. Johansson, K. Dolag, H. Lesch, and F. A. Stasyszyn. Simulating Magnetic Fields in the Antennae Galaxies. *ApJ*, 716:1438–1452, June 2010. doi: 10.1088/0004-637X/716/2/1438.

P. P. Kronberg. Intergalactic Magnetic Fields, and Some Connections with Cosmic Rays. *Space Sci. Rev.*, 75:387–399, January 1996. doi: 10.1007/BF00195047.

P. P. Kronberg, H. Lesch, and U. Hopp. Magnetization of the Intergalactic Medium by Primeval Galaxies. *ApJ*, 511:56–64, January 1999. doi: 10.1086/306662.

P. P. Kronberg, Q. W. Dufton, H. Li, and S. A. Colgate. Magnetic Energy of the Intergalactic Medium from Galactic Black Holes. *ApJ*, 560:178–186, October 2001. doi: 10.1086/322767.

P. P. Kronberg, M. L. Bernet, F. Miniati, S. J. Lilly, M. B. Short, and D. M. Higdon. A Global Probe of Cosmic Magnetic Fields to High Redshifts. *ApJ*, 676:70–79, March 2008. doi: 10.1086/527281.

P. P. Kronberg, R. V. E. Lovelace, G. Lapenta, and S. A. Colgate. Measurement of the Electric Current in a kpc-scale Jet. *ApJ*, 741:L15, November 2011. doi: 10.1088/2041-8205/741/1/L15.

R. M. Kulsrud, R. Cen, J. P. Ostriker, and D. Ryu. The Protogalactic Origin for Cosmic Magnetic Fields. *ApJ*, 480:481, May 1997. doi: 10.1086/303987.

R. A. Laing. Magnetic fields in extragalactic radio sources. *ApJ*, 248:87–104, August 1981. doi: 10.1086/159132.

R. A. Laing. The sidedness of jets and depolarization in powerful extragalactic radio sources. *Nature*, 331:149–151, January 1988. doi: 10.1038/331149a0.

R. A. Laing and A. H. Bridle. Dynamical models for jet deceleration in the radio galaxy 3C 31. *MNRAS*, 336:1161–1180, November 2002. doi: 10.1046/j.1365-8711.2002.05873.x.

R. A. Laing, A. H. Bridle, P. Parma, and M. Murgia. Structures of the magnetoionic media around the Fanaroff-Riley Class I radio galaxies 3C31 and Hydra A. *MNRAS*, 391:521–549, December 2008. doi: 10.1111/j.1365-2966.2008.13895.x.

A. Lauberts. *ESO/Uppsala survey of the ESO(B) atlas*. 1982.

J. P. Leahy. Small-scale variations in the Galactic Faraday rotation. *MNRAS*, 226:433–446, May 1987. doi: 10.1093/mnras/226.2.433.

N. Lehner, J. C. Howk, F. P. Keenan, and J. V. Smoker. Metallicity and Physical Conditions in the Magellanic Bridge. *ApJ*, 678:219-233, May 2008. doi: 10.1086/529574.

R. Liu, G. Pooley, and J. M. Riley. Spectral ageing in a sample of 14 high-luminosity double radio sources. *MNRAS*, 257:545–571, August 1992. doi: 10.1093/mnras/257.4.545.

A. Lobo Gomes, A. M. Magalhães, A. Pereyra, and C. V. Rodrigues. A New Optical Polarization Catalog for the Small Magellanic Cloud: The Magnetic Field Structure. *ApJ*, 806:94, June 2015. doi: 10.1088/0004-637X/806/1/94.

A. M. Magalhaes, N. Loiseau, C. V. Rodrigues, and V. Piirola. . In R. Beck, R. Wielebinski, and P. P. Kronberg, editors, *Galactic and Intergalactic Magnetic Fields*, volume 140 of *IAU Symposium*, page 255, 1990.

M. Mahmud, C. P. Coughlan, E. Murphy, D. C. Gabuzda, and D. R. Hallahan. Connecting magnetic towers with Faraday rotation gradients in active galactic nuclei jets. *MNRAS*, 431:695–709, May 2013. doi: 10.1093/mnras/stt201.

R. N. Manchester. Structure of the Local Galactic Magnetic Field. *ApJ*, 188:637–644, March 1974. doi: 10.1086/152757.

S. A. Mao, B. M. Gaensler, S. Stanimirović, M. Haverkorn, N. M. McClure-Griffiths, L. Staveley-Smith, and J. M. Dickey. A Radio and Optical Polarization Study of the Magnetic Field in the Small Magellanic Cloud. *ApJ*, 688:1029-1049, December 2008. doi: 10.1086/590546.

S. A. Mao, B. M. Gaensler, M. Haverkorn, E. G. Zweibel, G. J. Madsen, N. M. McClure-Griffiths, A. Shukurov, and P. P. Kronberg. A Survey of Extragalactic Faraday Rotation at High Galactic Latitude: The Vertical Magnetic Field of the Milky Way Toward the Galactic Poles. *ApJ*, 714:1170–1186, May 2010. doi: 10.1088/0004-637X/714/2/1170.

S. A. Mao, N. M. McClure-Griffiths, B. M. Gaensler, M. Haverkorn, R. Beck, D. McConnell, M. Wolleben, S. Stanimirović, J. M. Dickey, and L. Staveley-Smith. Magnetic Field Structure of the Large Magellanic Cloud from Faraday Rotation Measures of Diffuse Polarized Emission. *ApJ*, 759:25, November 2012. doi: 10.1088/0004-637X/759/1/25.

D. S. Mathewson and V. L. Ford. The Magnetic-Field Structure of the Magellanic Clouds. *ApJ*, 160:L43, April 1970a. doi: 10.1086/180520.

D. S. Mathewson and V. L. Ford. Polarization measurements of stars in the Magellanic Clouds. *AJ*, 75:778–784, September 1970b. doi: 10.1086/111024.

D. S. Mathewson, V. L. Ford, M. P. Schwarz, and J. D. Murray. . In W. B. Burton, editor, *The Large-Scale Characteristics of the Galaxy*, volume 84 of *IAU Symposium*, pages 547–556, 1979.

T. Mauch, T. Murphy, H. J. Buttery, J. Curran, R. W. Hunstead, B. Piestrzynski, J. G. Robertson, and E. M. Sadler. SUMSS: a wide-field radio imaging survey of the southern sky - II. The source catalogue. *MNRAS*, 342:1117–1130, July 2003. doi: 10.1046/j.1365-8711.2003.06605.x.

N. M. McClure-Griffiths, D. J. Pisano, M. R. Calabretta, H. A. Ford, F. J. Lockman, L. Staveley-Smith, P. M. W. Kalberla, J. Bailin, L. Dedes, S. Janowiecki, B. K. Gibson, T. Murphy, H. Nakanishi, and K. Newton-McGee. Gass: The Parkes Galactic All-Sky Survey. I. Survey Description, Goals, and Initial Data Release. *ApJS*, 181:398–412, April 2009. doi: 10.1088/0067-0049/181/2/398.

N. M. McClure-Griffiths, G. J. Madsen, B. M. Gaensler, D. McConnell, and D. H. F. M. Schnitzeler. Measurement of a Magnetic Field in a Leading Arm High-velocity Cloud. *ApJ*, 725:275–281, December 2010. doi: 10.1088/0004-637X/725/1/275.

S. L. McGee, M. L. Balogh, R. G. Bower, A. S. Font, and I. G. McCarthy. The accretion of galaxies into groups and clusters. *MNRAS*, 400:937–950, December 2009. doi: 10.1111/j.1365-2966.2009.15507.x.

B. R. McNamara, F. Kazemzadeh, D. A. Rafferty, L. Bîrzan, P. E. J. Nulsen, C. C. Kirkpatrick, and M. W. Wise. An Energetic AGN Outburst Powered by a Rapidly Spinning Supermassive Black Hole or an Accreting Ultramassive Black Hole. *ApJ*, 698:594–605, June 2009. doi: 10.1088/0004-637X/698/1/594.

J. Meaburn. Young Star Formation in the Magellanic HI Bridge. *MNRAS*, 223:317, November 1986. doi: 10.1093/mnras/223.2.317.

T. K. Menon. Radio properties of spiral galaxies in high-density groups. *MNRAS*, 274: 845–852, June 1995.

B. Y. Mills, O. B. Slee, and E. R. Hill. . *Australian Journal of Physics*, 13:676, December 1960. doi: 10.1071/PH600676.

N. Mizuno, E. Muller, H. Maeda, A. Kawamura, T. Minamidani, T. Onishi, A. Mizuno, and Y. Fukui. Detection of Molecular Clouds in the Magellanic Bridge: Candidate Star Formation Sites in a Nearby Low-Metallicity System. *ApJ*, 643:L107–L110, June 2006. doi: 10.1086/505298.

R. Morganti, N. E. B. Killeen, and C. N. Tadhunter. The Radio Structures of Southern 2-JY Radio Sources. *MNRAS*, 263:1023, August 1993.

J. S. Mulchaey and A. I. Zabludoff. The Properties of Poor Groups of Galaxies. II. X-Ray and Optical Comparisons. *ApJ*, 496:73–92, March 1998. doi: 10.1086/305356.

J. S. Mulchaey, D. S. Davis, R. F. Mushotzky, and D. Burstein. The Intragroup Medium in Poor Groups of Galaxies. *ApJ*, 456:80, January 1996. doi: 10.1086/176629.

J. S. Mulchaey, D. S. Davis, R. F. Mushotzky, and D. Burstein. An X-Ray Atlas of Groups of Galaxies. *ApJS*, 145:39–64, March 2003. doi: 10.1086/345736.

E. Muller, L. Staveley-Smith, W. Zealey, and S. Stanimirović. High-resolution HI observations of the Western Magellanic Bridge. *MNRAS*, 339:105–124, February 2003. doi: 10.1046/j.1365-8711.2003.06147.x.

E. Muller, S. Stanimirović, E. Rosolowsky, and L. Staveley-Smith. A Statistical Investigation of H I in the Magellanic Bridge. *ApJ*, 616:845–856, December 2004. doi: 10.1086/425154.

K. Murase, S. Inoue, and S. Nagataki. Cosmic Rays above the Second Knee from Clusters of Galaxies and Associated High-Energy Neutrino Emission. *ApJ*, 689:L105, December 2008. doi: 10.1086/595882.

B. Nikiel-Wroczyński, M. Soida, M. Urbanik, R. Beck, and D. J. Bomans. Intergalactic magnetic fields in Stephan's Quintet. *MNRAS*, 435:149–157, October 2013a. doi: 10.1093/mnras/stt1263.

B. Nikiel-Wroczyński, M. Soida, M. Urbanik, M. Weżgowiec, R. Beck, D. J. Bomans, and B. Adebahr. Radio continuum observations of the Leo Triplet at 2.64 GHz. *A&A*, 553:A4, May 2013b. doi: 10.1051/0004-6361/201321089.

N. E. D. Noël, B. C. Conn, J. I. Read, R. Carrera, A. Dolphin, and H.-W. Rix. The MAGellanic Inter-Cloud (MAGIC) project - II. Slicing up the Bridge. *MNRAS*, 452: 4222–4235, October 2015. doi: 10.1093/mnras/stv1614.

C. A. Norman and S. Ikeuchi. The disk-halo interaction - Superbubbles and the structure of the interstellar medium. *ApJ*, 345:372–383, October 1989. doi: 10.1086/167912.

N. Oppermann, H. Junklewitz, G. Robbers, M. R. Bell, T. A. Enßlin, A. Bonafede, R. Braun, J. C. Brown, T. E. Clarke, I. J. Feain, B. M. Gaensler, A. Hammond, L. Harvey-Smith, G. Heald, M. Johnston-Hollitt, U. Klein, P. P. Kronberg, S. A. Mao, N. M. McClure-Griffiths, S. P. O'Sullivan, L. Pratley, T. Robishaw, S. Roy, D. H. F. M. Schnitzeler, C. Sotomayor-Beltran, J. Stevens, J. M. Stil, C. Sunstrum, A. Tanna, A. R. Taylor, and C. L. Van Eck. An improved map of the Galactic Faraday sky. *A&A*, 542: A93, June 2012. doi: 10.1051/0004-6361/201118526.

N. Oppermann, H. Junklewitz, M. Greiner, T. A. Enßlin, T. Akahori, E. Carretti, B. M. Gaensler, A. Goobar, L. Harvey-Smith, M. Johnston-Hollitt, L. Pratley, D. H. F. M. Schnitzeler, J. M. Stil, and V. Vacca. Estimating extragalactic Faraday rotation. *A&A*, 575:A118, March 2015. doi: 10.1051/0004-6361/201423995.

S. P. O'Sullivan, S. Brown, T. Robishaw, D. H. F. M. Schnitzeler, N. M. McClure-Griffiths, I. J. Feain, A. R. Taylor, B. M. Gaensler, T. L. Landecker, L. Harvey-Smith, and E. Carretti. Complex Faraday depth structure of active galactic nuclei as revealed by broad-band radio polarimetry. *MNRAS*, 421:3300–3315, April 2012. doi: 10.1111/j.1365-2966.2012.20554.x.

S. P. O'Sullivan, I. J. Feain, N. M. McClure-Griffiths, R. D. Ekers, E. Carretti, T. Robishaw, S. A. Mao, B. M. Gaensler, J. Bland-Hawthorn, and Ł. Stawarz. Thermal Plasma in the Giant Lobes of the Radio Galaxy Centaurus A. *ApJ*, 764:162, February 2013. doi: 10.1088/0004-637X/764/2/162.

F. N. Owen and R. A. Laing. CCD surface photometry of radio galaxies. I - FR class I and II sources. *MNRAS*, 238:357–378, May 1989.

F. N. Owen and R. A. White. Surface photometry of radio galaxies. II - Cluster sources. *MNRAS*, 249:164–171, March 1991.

P. Parma, M. Murgia, H. R. de Ruiter, and R. Fanti. The lives of FR I radio galaxies. *New AR*, 46:313–325, May 2002. doi: 10.1016/S1387-6473(01)00201-9.

R. A. Perley, J. W. Dreher, and J. J. Cowan. The jet and filaments in Cygnus A. *ApJ*, 285:L35–L38, October 1984. doi: 10.1086/184360.

R. A. Perley, C. J. Chandler, B. J. Butler, and J. M. Wrobel. The Expanded Very Large Array: A New Telescope for New Science. *ApJ*, 739:L1, September 2011. doi: 10.1088/2041-8205/739/1/L1.

V. Ptuskin. Cosmic ray transport in the Galaxy. In *Journal of Physics Conference Series*, volume 47 of *Journal of Physics Conference Series*, pages 113–119, October 2006. doi: 10.1088/1742-6596/47/1/014.

M. E. Putman, L. Staveley-Smith, K. C. Freeman, B. K. Gibson, and D. G. Barnes. The Magellanic Stream, High-Velocity Clouds, and the Sculptor Group. *ApJ*, 586:170–194, March 2003. doi: 10.1086/344477.

D. Raimann, T. Storchi-Bergmann, H. Quintana, R. Hunstead, and L. Wisotzki. Stellar populations in a complete sample of local radio galaxies. *MNRAS*, 364:1239–1252, December 2005. doi: 10.1111/j.1365-2966.2005.09665.x.

M. Ramella, M. J. Geller, A. Pisani, and L. N. da Costa. The UZC-SSRS2 Group Catalog. *AJ*, 123:2976–2984, June 2002. doi: 10.1086/340357.

M. J. Rees. The origin and cosmogonic implications of seed magnetic fields. *QJRAS*, 28: 197–206, September 1987.

M. Reuland, W. van Breugel, W. de Vries, M. A. Dopita, A. Dey, G. Miley, H. Röttgering, B. Venemans, S. A. Stanford, M. Lacy, H. Spinrad, S. Dawson, D. Stern, and A. Bunker. Metal-Enriched Gaseous Halos around Distant Radio Galaxies: Clues to Feedback in Galaxy Formation. *AJ*, 133:2607–2623, June 2007. doi: 10.1086/516571.

R. J. Reynolds. Ionized disk/halo gas - Insight from optical emission lines and pulsar dispersion measures. In H. Bloemen, editor, *The Interstellar Disk-Halo Connection in Galaxies*, volume 144 of *IAU Symposium*, pages 67–76, 1991.

R. J. Reynolds, N. C. Sterling, and L. M. Haffner. Detection of a Large Arc of Ionized Hydrogen Far above the Cassiopeia OB6 Association: A Superbubble Blowout into the Galactic Halo? *ApJ*, 558:L101–L104, September 2001. doi: 10.1086/323638.

A. S. G. Robotham, P. Norberg, S. P. Driver, I. K. Baldry, S. P. Banford, A. M. Hopkins, J. Liske, J. Loveday, A. Merson, and J. A. Peacock. Galaxy and Mass Assembly (GAMA): the GAMA galaxy group catalogue (G^3Cv1). *MNRAS*, 416:2640–2668, October 2011. doi: 10.1111/j.1365-2966.2011.19217.x.

L. Rudnick and K. M. Blundell. Lowering Inferred Cluster Magnetic Field Strengths: The Radio Galaxy Contributions. *ApJ*, 588:143–154, May 2003. doi: 10.1086/373891.

D. J. Saikia and C. J. Salter. Polarization properties of extragalactic radio sources. *ARA&A*, 26:93–144, 1988. doi: 10.1146/annurev.aa.26.090188.000521.

L. Saripalli, R. Subrahmanyan, and N. Udaya Shankar. A Case for Renewed Activity in the Giant Radio Galaxy J0116-473. *ApJ*, 565:256–264, January 2002. doi: 10.1086/324600.

R. J. Sault and T. J. Cornwell. The Hamaker-Bregman-Sault Measurement Equation. In G. B. Taylor, C. L. Carilli, and R. A. Perley, editors, *Synthesis Imaging in Radio Astronomy II*, volume 180 of *Astronomical Society of the Pacific Conference Series*, page 657, 1999.

R. J. Sault, P. J. Teuben, and M. C. H. Wright. . In R. A. Shaw, H. E. Payne, and J. J. E. Hayes, editors, *Astronomical Data Analysis Software and Systems IV*, volume 77 of *Astronomical Society of the Pacific Conference Series*, page 433, 1995.

R. T. Schilizzi and W. B. McAdam. Observations of extended sources at 408 MHz. I - The radio structures. *MmRAS*, 79:1–73, 1975.

T. Schmidt. Polarization measurements and magnetic field structure within the Magellanic Clouds. *A&A*, 6:294–308, June 1970.

T. Schmidt. Starlight polarization in the Magellanic Cloud regions. *A&AS*, 24:357–378, April 1976.

D. H. F. M. Schnitzeler. The latitude dependence of the rotation measures of NVSS sources. *MNRAS*, 409:L99–L103, November 2010. doi: 10.1111/j.1745-3933.2010.00957.x.

D. H. F. M. Schnitzeler and K. J. Lee. Finding a faint polarized signal in wide-band radio data. *MNRAS*, 466:378–391, April 2017. doi: 10.1093/mnras/stw3104.

A. P. Schoenmakers, A. G. de Bruyn, H. J. A. Rottgering, and H. van der Laan. Radio galaxies with a 'double-double' morphology - III. The case of B1834+620. *MNRAS*, 315:395–406, June 2000. doi: 10.1046/j.1365-8711.2000.03432.x.

H. Seta, M. S. Tashiro, and S. Inoue. Suzaku Detection of Thermal X-Ray Emission Associated with the Western Radio Lobe of Fornax A. *PASJ*, 65:106, October 2013. doi: 10.1093/pasj/65.5.106.

P. R. Shapiro and G. B. Field. Consequences of a New Hot Component of the Interstellar Medium. *ApJ*, 205:762–765, May 1976. doi: 10.1086/154332.

Y. Shen, J. S. Mulchaey, S. Raychaudhury, J. Rasmussen, and T. J. Ponman. Differences in the AGN Populations of Groups and Clusters: Clues to AGN Evolution. *ApJ*, 654: L115–L118, January 2007. doi: 10.1086/511030.

M. Simard-Normandin, P. P. Kronberg, and S. Button. The Faraday rotation measures of extragalactic radio sources. *ApJS*, 45:97–111, January 1981. doi: 10.1086/190709.

A. Simionescu, N. Werner, H. Böhringer, J. S. Kaastra, A. Finoguenov, M. Brüggen, and P. E. J. Nulsen. Chemical enrichment in the cluster of galaxies Hydra A. *A&A*, 493: 409–424, January 2009. doi: 10.1051/0004-6361:200810225.

O. B. Slee. Radio sources observed with the Culgoora circular array. *Australian Journal of Physics*, 48:143–186, 1995. doi: 10.1071/PH950143.

O. B. Slee, E. M. Sadler, J. E. Reynolds, and R. D. Ekers. Parsecscale Radio Cores in Early Type Galaxies. *MNRAS*, 269:928, August 1994. doi: 10.1093/mnras/269.4.928.

J. V. Smoker, F. P. Keenan, A. G. Polatidis, C. J. Mooney, N. Lehner, and W. R. J. Rolleston. CO and optical observations of the Magellanic Bridge. *A&A*, 363:451–454, November 2000.

M. Soida, M. Urbanik, and R. Beck. The magnetic field in the perturbed spiral galaxy NGC 4254. *A&A*, 312:409–418, August 1996.

D. D. Sokoloff, A. A. Bykov, A. Shukurov, E. M. Berkhuijsen, R. Beck, and A. D. Poezd. Depolarization and Faraday effects in galaxies. *MNRAS*, 299:189–206, August 1998. doi: 10.1046/j.1365-8711.1998.01782.x.

L. S. Sparke and J. S. Gallagher, III. *Galaxies in the Universe*. Cambridge University Press, February 2007.

V. Springel, C. S. Frenk, and S. D. M. White. The large-scale structure of the Universe. *Nature*, 440:1137–1144, April 2006. doi: 10.1038/nature04805.

J. M. Stil, A. R. Taylor, and C. Sunstrum. Structure in the Rotation Measure Sky. *ApJ*, 726:4, January 2011. doi: 10.1088/0004-637X/726/1/4.

G. G. Stokes. On the Change of Refrangibility of Light. 142:463–562, 1852. doi: 10.1098/rstl.1852.0022.

R. Subrahmanyan, R. W. Hunstead, N. L. J. Cox, and V. McIntyre. SGRS J0515-8100: A Fat-Double Giant Radio Galaxy. *ApJ*, 636:172–180, January 2006. doi: 10.1086/497956.

K. Subramanian. Magnetizing the universe. *ArXiv e-prints*, February 2008.

S. Subramanian and A. Subramaniam. Depth estimation of the Large and Small Magellanic Clouds. *A&A*, 496:399–412, March 2009. doi: 10.1051/0004-6361/200811029.

M. Sun. Hot gas in galaxy groups: recent observations. *New Journal of Physics*, 14(4): 045004, April 2012. doi: 10.1088/1367-2630/14/4/045004.

M. Sun, G. M. Voit, M. Donahue, C. Jones, W. Forman, and A. Vikhlinin. Chandra Studies of the X-Ray Gas Properties of Galaxy Groups. *ApJ*, 693:1142–1172, March 2009. doi: 10.1088/0004-637X/693/2/1142.

X.-H. Sun and W. Reich. The Galactic halo magnetic field revisited. *Research in Astronomy and Astrophysics*, 10:1287–1297, December 2010. doi: 10.1088/1674-4527/10/12/009.

X. H. Sun, L. Rudnick, T. Akahori, C. S. Anderson, M. R. Bell, J. D. Bray, J. S. Farnes, S. Ideguchi, K. Kumazaki, T. O'Brien, S. P. O'Sullivan, A. M. M. Scaife, R. Stepanov, J. Stil, K. Takahashi, R. J. van Weeren, and M. Wolleben. Comparison of Algorithms for Determination of Rotation Measure and Faraday Structure. I. 1100-1400 MHz. *AJ*, 149:60, February 2015. doi: 10.1088/0004-6256/149/2/60.

C. N. Tadhunter, R. Morganti, S. di Serego-Alighieri, R. A. E. Fosbury, and I. J. Danziger. Optical Spectroscopy of a Complete Sample of Southern 2-JY Radio Sources. *MNRAS*, 263:999, August 1993.

M. Tashiro, K. Makishima, and H. Kaneda. ASCA Measurements of Field-Particle Energy Distribution in Radio Lobes. *Advances in Space Research*, 25:751–756, 2000. doi: 10.1016/S0273-1177(99)00834-0.

A. R. Taylor, J. M. Stil, and C. Sunstrum. A Rotation Measure Image of the Sky. *ApJ*, 702:1230–1236, September 2009. doi: 10.1088/0004-637X/702/2/1230.

G. Trinchieri, J. Sulentic, W. Pietsch, and D. Breitschwerdt. Stephan's Quintet with XMM-Newton. *A&A*, 444:697–710, December 2005. doi: 10.1051/0004-6361:20052910.

R. B. Tully. Galaxy Groups: A 2MASS Catalog. *AJ*, 149:171, May 2015. doi: 10.1088/0004-6256/149/5/171.

P. H. van Cittert. Die Wahrscheinliche Schwingungsverteilung in Einer von Einer Lichtquelle Direkt Oder Mittels Einer Linse Beleuchteten Ebene. *Physica*, 1 (1):201, 1934. ISSN 0031-8914. doi: http://dx.doi.org/10.1016/S0031-8914(34)90026-4. URL http://www.sciencedirect.com/science/article/pii/S0031891434900264.

S. van Velzen, H. Falcke, P. Schellart, N. Nierstenhöfer, and K.-H. Kampert. Radio galaxies of the local universe. All-sky catalog, luminosity functions, and clustering. *A&A*, 544:A18, August 2012. doi: 10.1051/0004-6361/201219389.

A. Walker. The Distances of the Magellanic Clouds. *Post-Hipparcos Cosmic Candles*, 237:125, 1999. doi: 10.1007/978-94-011-4734-7-8.

J. V. Wall and R. T. Schilizzi. Variations in emission spectrum over southern radio sources of large angular extent. *MNRAS*, 189:593–600, November 1979. doi: 10.1093/mnras/189.3.593.

E. Waxman and A. Loeb. Fluctuations in the Radio Background from Intergalactic Synchrotron Emission. *ApJ*, 545:L11–L14, December 2000. doi: 10.1086/317326.

S. R. Wayte. Structure of the interstellar medium in the Magellanic Clouds. *ApJ*, 355: 473–495, June 1990. doi: 10.1086/168782.

G. Wegner, M. Bernardi, C. N. A. Willmer, L. N. da Costa, M. V. Alonso, P. S. Pellegrini, M. A. G. Maia, O. L. Chaves, and C. Rité. Redshift-Distance Survey of Early-Type Galaxies: Spectroscopic Data. *AJ*, 126:2268–2280, November 2003. doi: 10.1086/378959.

I. K. Wehus, U. Fuskeland, and H. K. Eriksen. The Effect of Systematics on Polarized Spectral Indices. *ApJ*, 763:138, February 2013. doi: 10.1088/0004-637X/763/2/138.

M. Wenger, F. Ochsenbein, D. Egret, P. Dubois, F. Bonnarel, S. Borde, F. Genova, G. Jasniewicz, S. Laloë, S. Lesteven, and R. Monier. The SIMBAD astronomical database. The CDS reference database for astronomical objects. *A&AS*, 143:9–22, April 2000. doi: 10.1051/aas:2000332.

W. E. Wilson, R. H. Ferris, P. Axtens, and et al. The Australia Telescope Compact Array Broad-band Backend: description and first results. *MNRAS*, 416:832–856, September 2011. doi: 10.1111/j.1365-2966.2011.19054.x.

S. Wykes, J. H. Croston, M. J. Hardcastle, J. A. Eilek, P. L. Biermann, A. Achterberg, J. D. Bray, A. Lazarian, M. Haverkorn, R. J. Protheroe, and O. Bromberg. Mass entrainment and turbulence-driven acceleration of ultra-high energy cosmic rays in Centaurus A. *A&A*, 558:A19, October 2013. doi: 10.1051/0004-6361/201321622.

C. K. Xu, N. Lu, J. J. Condon, M. Dopita, and R. J. Tuffs. Physical Conditions and Star Formation Activity in the Intragroup Medium of Stephan's Quintet. *ApJ*, 595: 665–684, October 2003. doi: 10.1086/377445.

H. Xu, H. Li, D. C. Collins, S. Li, and M. L. Norman. Evolution and Distribution of Magnetic Fields from Active Galactic Nuclei in Galaxy Clusters. I. The Effect of Injection Energy and Redshift. *ApJ*, 725:2152–2165, December 2010. doi: 10.1088/0004-637X/725/2/2152.

F. Zernike. The concept of degree of coherence and its application to optical problems. *Physica*, 5:785–795, August 1938. doi: 10.1016/S0031-8914(38)80203-2.

E. G. Zweibel. The growth of magnetic fields prior to galaxy formation. *ApJ*, 329:L1–L4, June 1988. doi: 10.1086/185164.

A

BLIND POLARISED SOURCE FINDING WITH PRE-CABB ATCA IN THE SMC-WING

We present the source finding results from our reduction of archival ATCA observations of the SMC-Wing. The HI data were analysed and presented by Muller et al. (2003). We calibrated and imaged the continuum data to a common resolution of $110.6'' \times 83.95''$ across the 13 frequency bins, covering a total frequency range of $1336 - 1432$ MHz. We create a total intensity multi-frequency synthesis image of the entire region and employ the source-finding algorithm 'AEGEAN' (Hancock et al. 2012) was used to identify all total intensity sources above 8σ. We identify 700 unresolved and partially resolved sources in our field of view. In order to create the polarised spectra corresponding to each total intensity source, we create an aperture mask corresponding to the size and shape of an ellipse fit to continuum source. RM-synthesis and RM-clean (Heald et al. 2009) were then run on the corresponding spectra extracted from the 13 frequency channels. A source as considered to be polarised if it returned an FDF with a peak 3σ above the measured uncertainty in the Stokes Q and U images.

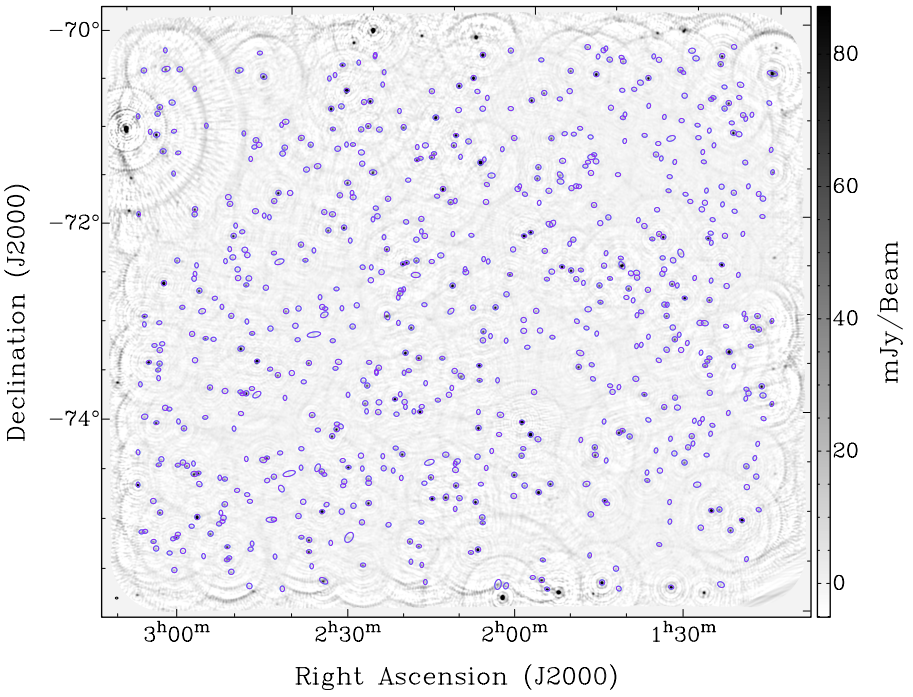

(a) Total intensity

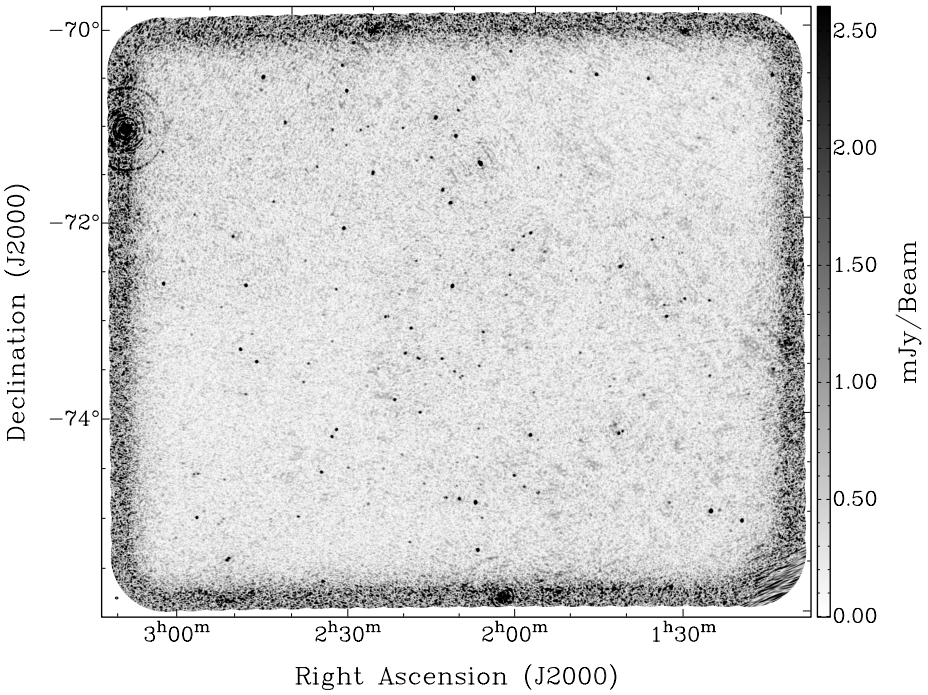

(b) Total polarised intensity

Figure A.1: Band-averaged total intensity (a) and polarised intensity (b) channel maps of the entire SMC-Wing region. Purple annotations mark the position of all source detections above 8σ in total intensity. The synthesised beam is shown in the lower lefthand corner.

Table A.1: Table of parameter values for all total intensity sources above 8σ from Figure A.1(a), as identified with AEGEAN. Column 1 gives the source name, columns 2 and 3 list the position in R.A. and Dec, as identified as the middle of the centroid-fit to Stokes I. Column 4 gives the total flux extracted for each source, with the mean polarised RMS given in column 5. Th polarised flux associated with each total intensity source is listed in column 6. Finally, Column 7 identifies if a peak in the Faraday depth spectrum could be identified for this source.

Name	R.A.	Dec.	S_I (mJy)	σ_{QU} (mJy/beam)	S_{PI} (mJy)	Detect?
024614.0-702011.88	46:14.0	-70:20:11.88	20.547	2.026	0.003	n
013500.3-702205.07	35:00.3	-70:22:05.07	12.515	1.292	0.001	n
014009.2-702815.51	40:09.2	-70:28:15.51	15.312	1.089	0.001	n
013619.1-702859.97	36:19.1	-70:28:59.97	90.711	0.930	0.001	n
024916.8-703025.53	49:16.8	-70:30:25.53	31.536	1.960	0.002	n
023433.2-703044.85	34:33.2	-70:30:44.85	23.954	1.561	0.001	n
024630.4-703206.13	46:30.4	-70:32:06.13	59.707	1.246	0.002	n
015315.0-703224.94	53:15.0	-70:32:24.94	33.093	1.189	0.001	n
015056.9-703235.30	50:56.9	-70:32:35.30	10.437	1.087	0.001	n
013932.1-703246.59	39:32.1	-70:32:46.59	15.740	0.853	0.001	n
024447.9-703343.44	44:47.9	-70:33:43.44	32.242	1.158	0.001	n
015115.3-703349.11	51:15.3	-70:33:49.11	15.665	1.049	0.001	n
013622.4-703414.27	36:22.4	-70:34:14.27	64.078	0.756	0.001	n
014452.0-703444.82	44:52.0	-70:34:44.82	10.788	0.898	0.001	n
012945.2-703453.09	29:45.2	-70:34:53.09	168.922	1.744	0.009	y
014409.8-703631.18	44:09.8	-70:36:31.18	14.914	0.824	0.001	n
020254.8-703654.66	02:54.8	-70:36:54.66	37.398	1.167	0.005	y
014853.8-703720.49	48:53.8	-70:37:20.49	15.748	0.840	0.001	n
015152.1-703759.43	51:52.1	-70:37:59.43	9.301	0.883	0.001	n
022003.8-703826.58	20:03.8	-70:38:26.58	15.676	1.191	0.001	n
022006.3-703915.84	20:06.3	-70:39:15.84	15.724	1.183	0.001	n
015022.1-703921.79	50:22.1	-70:39:21.79	27.501	0.857	0.001	n
014838.2-703941.31	48:38.2	-70:39:41.31	34.643	0.769	0.001	n
020626.7-703956.12	06:26.7	-70:39:56.12	261.520	1.175	0.001	n
023722.5-704008.17	37:22.5	-70:40:08.17	48.867	1.114	0.001	n
014119.3-704117.17	41:19.3	-70:41:17.17	37.796	0.713	0.001	n
015901.1-704214.26	59:01.1	-70:42:14.26	14.674	0.970	0.001	n
022212.5-704239.00	22:12.5	-70:42:39.00	22.990	1.092	0.001	n
014056.8-704243.59	40:56.8	-70:42:43.59	16.266	0.707	0.001	n
022416.3-704322.39	24:16.3	-70:43:22.39	92.758	1.189	0.004	y
013331.1-704520.73	33:31.1	-70:45:20.73	24.111	0.721	0.001	n
023424.0-704557.57	34:24.0	-70:45:57.57	87.207	1.018	0.010	y

Table A.1 continued...

Name	R.A.	Dec.	S_I (mJy)	σ_{QU} (mJy/beam)	S_{PI} (mJy)	Detect?
024318.0-704731.30	43:18.0	-70:47:31.30	37.851	1.003	0.001	n
015513.2-704815.23	55:13.3	-70:48:15.23	57.387	0.707	0.002	y
013530.0-704821.26	35:30.0	-70:48:21.26	11.506	0.681	0.000	n
014515.7-704844.13	45:15.7	-70:48:44.13	115.613	0.729	0.006	y
015156.0-704916.71	51:56.0	-70:49:16.71	140.441	0.749	0.006	y
022519.4-704928.83	25:19.4	-70:49:28.83	18.343	1.056	0.002	n
021902.7-704942.47	19:02.7	-70:49:42.47	11.810	0.889	0.001	n
022604.9-705123.75	26:05.0	-70:51:23.75	19.601	1.045	0.001	n
014614.4-705214.30	46:14.4	-70:52:14.30	15.220	0.660	0.001	n
013326.7-705329.67	33:26.7	-70:53:29.67	9.851	0.718	0.001	n
024625.2-705346.35	46:25.2	-70:53:46.35	30.424	0.988	0.001	n
012932.1-705348.71	29:32.1	-70:53:48.71	13.435	1.293	0.001	n
020736.7-705440.82	07:36.7	-70:54:40.82	272.174	0.925	0.025	y
024804.6-705520.56	48:04.6	-70:55:20.56	48.376	1.164	0.001	n
013643.8-705603.25	36:43.8	-70:56:03.25	35.195	0.676	0.002	y
014657.0-705650.68	46:57.0	-70:56:50.68	16.952	0.662	0.000	n
014025.3-705718.32	40:25.3	-70:57:18.32	11.486	0.698	0.000	n
013658.8-705721.02	36:58.8	-70:57:21.02	32.039	0.674	0.001	n
021918.0-705728.44	19:18.0	-70:57:28.44	16.545	0.834	0.001	n
013440.6-705803.46	34:40.6	-70:58:03.46	79.389	0.652	0.001	n
014828.3-705809.42	48:28.3	-70:58:09.42	8.397	0.649	0.001	n
025101.0-705826.56	51:01.0	-70:58:26.56	48.068	2.506	0.002	n
024830.0-705909.86	48:30.0	-70:59:09.86	40.647	1.238	0.001	n
020927.2-705937.91	09:27.2	-70:59:37.91	145.121	0.829	0.002	n
022357.0-705947.05	23:57.0	-70:59:47.05	1176.006	1.064	0.010	y
015512.6-710112.85	55:12.6	-71:01:12.85	13.751	0.689	0.001	n
013506.8-710155.50	35:06.8	-71:01:55.50	36.587	0.625	0.001	n
021259.5-710251.27	12:59.5	-71:02:51.27	35.360	0.843	0.001	n
013130.9-710304.62	31:30.9	-71:03:04.62	7.100	0.788	0.001	n
013811.3-710305.38	38:11.3	-71:03:05.38	17.548	0.627	0.001	n
015829.2-710312.91	58:29.2	-71:03:12.91	52.812	0.752	0.001	n
020706.6-710319.32	07:06.6	-71:03:19.32	14.920	0.824	0.001	n
013236.9-710413.90	32:36.9	-71:04:13.90	30.684	0.681	0.001	n
013212.6-710613.67	32:12.6	-71:06:13.67	9.372	0.736	0.001	n
014453.4-710620.24	44:53.4	-71:06:20.24	5.208	0.643	0.001	n
015625.7-710630.46	56:25.7	-71:06:30.46	12.868	0.733	0.001	n
020549.7-710718.79	05:49.7	-71:07:18.79	10.676	0.792	0.001	n
022059.8-710733.75	20:59.8	-71:07:33.75	122.837	0.895	0.001	n
022149.7-710756.92	21:49.7	-71:07:56.92	30.867	0.903	0.001	n
020003.9-710807.60	00:03.9	-71:08:07.60	106.805	0.786	0.001	n
024950.3-710938.02	49:50.2	-71:09:38.02	32.374	1.525	0.004	n
022448.0-710940.48	24:48.0	-71:09:40.48	35.901	0.943	0.002	n
014944.9-710950.28	49:44.9	-71:09:50.28	18.079	0.634	0.001	n

Table A.1 continued...

Name	R.A.	Dec.	S_I (mJy)	σ_{QU} (mJy/beam)	S_{PI} (mJy)	Detect?
013356.2-711014.29	33:56.2	-71:10:14.29	13.329	0.666	0.000	n
022607.2-711039.53	26:07.2	-71:10:39.53	159.370	0.971	0.002	n
024230.2-711155.80	42:30.2	-71:11:55.80	33.568	0.990	0.001	n
024646.6-711157.72	46:46.6	-71:11:57.72	23.706	1.035	0.001	n
024904.2-711208.10	49:04.2	-71:12:08.10	129.705	1.282	0.001	n
014243.2-711217.61	42:43.2	-71:12:17.61	7.157	0.678	0.001	n
014026.2-711314.96	40:26.2	-71:13:14.96	9.025	0.665	0.001	n
014751.7-711321.27	47:51.7	-71:13:21.27	6.697	0.637	0.000	n
020245.2-711353.38	02:45.1	-71:13:53.38	12.447	0.735	0.001	n
020625.1-711414.88	06:25.1	-71:14:14.88	15.722	0.801	0.001	n
021717.0-711449.27	17:17.0	-71:14:49.27	17.395	0.800	0.001	n
013818.3-711449.62	38:18.3	-71:14:49.62	16.638	0.634	0.001	n
020933.7-711504.44	09:33.7	-71:15:04.44	18.385	0.864	0.003	y
014805.5-711531.84	48:05.5	-71:15:31.84	25.699	0.663	0.001	n
023212.2-711609.73	32:12.2	-71:16:09.73	31.623	0.941	0.004	y
013331.9-711615.18	33:32.0	-71:16:15.18	102.739	0.672	0.000	n
013247.5-711637.05	32:47.5	-71:16:37.05	10.950	0.670	0.001	n
013641.3-711711.17	36:41.3	-71:17:11.17	6.608	0.672	0.001	n
023245.6-711749.62	32:45.6	-71:17:49.62	12.025	0.951	0.001	n
021232.8-711939.84	12:32.8	-71:19:39.84	216.392	0.889	0.012	y
023748.4-712015.15	37:48.4	-71:20:15.15	27.182	0.970	0.001	n
013759.0-712236.23	37:59.0	-71:22:36.23	8.081	0.694	0.002	n
012818.8-712258.03	28:18.8	-71:22:58.03	11.485	1.302	0.001	n
024836.3-712317.57	48:36.3	-71:23:17.57	60.353	1.137	0.003	n
022126.4-712319.48	21:26.4	-71:23:19.48	68.329	0.839	0.002	n
022607.1-712335.82	26:07.1	-71:23:35.82	57.823	0.879	0.003	n
015334.8-712421.70	53:34.8	-71:24:21.70	16.223	0.668	0.001	n
022225.0-712508.27	22:25.1	-71:25:08.27	35.746	0.854	0.003	y
021648.3-712514.66	16:48.3	-71:25:14.66	61.672	0.861	0.003	y
014503.0-712519.19	45:03.0	-71:25:19.19	15.322	0.634	0.000	n
014132.3-712522.65	41:32.3	-71:25:22.65	8.927	0.668	0.001	n
023619.3-712531.74	36:19.3	-71:25:31.74	39.123	0.922	0.001	n
022000.9-712555.56	20:00.9	-71:25:55.56	28.325	0.786	0.001	n
024641.5-712559.51	46:41.5	-71:25:59.51	31.923	0.979	0.001	n
013550.3-712603.58	35:50.3	-71:26:03.58	7.312	0.684	0.000	n
023020.8-712724.51	30:20.9	-71:27:24.51	45.289	0.939	0.001	n
015421.6-712819.34	54:21.6	-71:28:19.34	14.675	0.750	0.001	n
015534.4-712823.92	55:34.4	-71:28:23.92	9.947	0.731	0.001	n
023558.5-712848.16	35:58.5	-71:28:48.16	12.207	0.952	0.001	n
015207.8-712923.62	52:07.8	-71:29:23.62	6.584	0.648	0.001	n
014309.5-712932.07	43:09.5	-71:29:32.07	7.667	0.730	0.001	n
023638.1-712940.98	36:38.1	-71:29:40.98	12.863	0.949	0.002	n
014735.7-713008.29	47:35.7	-71:30:08.29	5.457	0.657	0.001	n

Table A.1 continued...

Name	R.A.	Dec.	S_I (mJy)	σ_{QU} (mJy/beam)	S_{PI} (mJy)	Detect?
020954.9-713109.31	09:54.9	-71:31:09.31	199.722	0.843	0.009	y
013710.8-713117.48	37:10.8	-71:31:17.48	6.695	0.683	0.001	n
015717.5-713142.80	57:17.5	-71:31:42.80	59.352	0.769	0.001	n
022912.1-713215.34	29:12.1	-71:32:15.34	40.033	0.893	0.001	n
023239.5-713223.74	32:39.5	-71:32:23.74	36.785	0.948	0.001	n
020212.2-713229.41	02:12.2	-71:32:29.41	28.734	0.806	0.001	n
013125.0-713343.50	31:25.0	-71:33:43.50	22.956	0.655	0.001	n
022427.5-713406.02	24:27.5	-71:34:06.02	10.794	0.895	0.002	n
022337.0-713423.87	23:37.0	-71:34:23.87	31.963	0.850	0.001	n
020815.6-713500.69	08:15.6	-71:35:00.69	24.573	0.830	0.001	n
023301.1-713600.05	33:01.1	-71:36:00.05	18.076	0.901	0.001	n
022540.2-713621.23	25:40.2	-71:36:21.23	17.514	0.814	0.001	n
014317.6-713635.39	43:17.6	-71:36:35.39	31.942	0.667	0.001	n
012738.4-713643.63	27:38.4	-71:36:43.63	51.332	1.369	0.003	n
023718.8-713653.08	37:18.8	-71:36:53.08	8.759	0.937	0.002	n
021360.0-713711.43	14:00.0	-71:37:11.43	15.623	0.809	0.001	n
013652.3-713721.14	36:52.3	-71:37:21.14	14.166	0.643	0.001	n
021012.6-713724.33	10:12.6	-71:37:24.33	73.395	0.837	0.001	n
021505.5-713804.66	15:05.5	-71:38:04.66	12.630	0.840	0.001	n
024744.3-713824.06	47:44.3	-71:38:24.06	29.256	0.957	0.001	n
014232.4-713843.81	42:32.4	-71:38:43.81	6.708	0.662	0.001	n
020346.2-713944.33	03:46.2	-71:39:44.33	11.915	0.826	0.001	n
022233.0-713944.55	22:33.0	-71:39:44.55	15.332	0.784	0.001	n
014042.1-713952.53	40:42.1	-71:39:52.53	8.149	0.673	0.001	n
015129.6-714025.84	51:29.5	-71:40:25.84	23.700	0.733	0.001	n
015149.7-714200.37	51:49.7	-71:42:00.37	11.642	0.739	0.001	n
021252.5-714230.83	12:52.6	-71:42:30.83	45.279	0.804	0.001	n
015111.0-714434.40	51:11.0	-71:44:34.40	12.136	0.738	0.001	n
021310.7-714442.31	13:10.7	-71:44:42.31	67.749	0.831	0.003	y
020920.9-714447.68	09:20.9	-71:44:47.68	14.722	0.844	0.001	n
021441.8-714513.96	14:41.8	-71:45:13.96	24.118	0.802	0.001	n
015215.2-714523.73	52:15.2	-71:45:23.73	12.828	0.706	0.000	n
015539.9-714539.14	55:39.9	-71:45:39.14	26.141	0.652	0.000	n
021509.6-714609.46	15:09.6	-71:46:09.46	79.161	0.822	0.002	n
022832.4-714616.76	28:32.4	-71:46:16.76	29.658	0.892	0.003	y
020610.2-714628.54	06:10.2	-71:46:28.54	12.397	1.000	0.001	n
022232.2-714653.91	22:32.2	-71:46:53.91	24.427	0.796	0.001	n
023003.2-714741.80	30:03.2	-71:47:41.80	22.346	0.933	0.001	n
015233.8-714806.21	52:33.8	-71:48:06.21	14.841	0.707	0.002	n
013031.5-714814.29	30:31.5	-71:48:14.29	6.593	0.779	0.001	n
020638.5-714822.76	06:38.5	-71:48:22.76	721.250	0.963	0.025	y
014109.4-714933.10	41:09.4	-71:49:33.10	11.921	0.704	0.001	n
015852.1-715026.46	58:52.1	-71:50:26.46	58.460	0.642	0.003	y

Table A.1 continued...

Name	R.A.	Dec.	S_I (mJy)	σ_{QU} (mJy/beam)	S_{PI} (mJy)	Detect?
013404.1-715117.82	34:04.1	-71:51:17.82	10.896	0.705	0.001	n
014806.9-715144.10	48:07.0	-71:51:44.10	7.647	0.679	0.000	n
012859.3-715156.48	28:59.3	-71:51:56.48	14.311	0.950	0.001	n
015145.4-715209.51	51:45.4	-71:52:09.51	19.448	0.760	0.002	n
022108.7-715250.57	21:08.7	-71:52:50.57	85.850	0.815	0.006	y
013218.8-715349.25	32:18.8	-71:53:49.25	29.714	0.742	0.001	n
012819.3-715423.03	28:19.3	-71:54:23.03	13.452	1.012	0.001	n
015552.3-715438.53	55:52.3	-71:54:38.53	35.755	0.645	0.001	n
013601.2-715511.67	36:01.2	-71:55:11.67	7.922	0.693	0.001	n
020509.4-715631.36	05:09.4	-71:56:31.36	20.863	0.867	0.001	n
015856.1-715728.08	58:56.1	-71:57:28.08	63.771	0.689	0.001	n
022439.5-715818.86	24:39.5	-71:58:18.86	74.971	0.791	0.001	n
014105.5-715827.80	41:05.5	-71:58:27.80	23.529	0.731	0.001	n
015547.7-715845.13	55:47.7	-71:58:45.13	13.125	0.694	0.001	n
021627.1-715848.59	16:27.1	-71:58:48.59	15.818	0.829	0.001	n
024057.2-715851.54	40:57.2	-71:58:51.54	13.577	0.910	0.001	n
013845.5-715916.84	38:45.5	-71:59:16.84	9.771	0.743	0.001	n
025317.8-715927.28	53:17.8	-71:59:27.28	83.711	2.055	0.004	n
023407.6-720025.66	34:07.6	-72:00:25.66	103.546	0.929	0.001	n
015338.2-720103.01	53:38.2	-72:01:03.01	9.897	0.751	0.001	n
015315.8-720111.97	53:15.8	-72:01:11.97	8.303	0.776	0.001	n
023233.4-720119.70	32:33.4	-72:01:19.70	8.728	0.827	0.001	n
013335.8-720213.90	33:35.8	-72:02:13.90	6.455	0.743	0.001	n
020546.3-720216.57	05:46.3	-72:02:16.57	19.964	0.833	0.001	n
015415.3-720233.66	54:15.3	-72:02:33.66	19.206	0.676	0.001	n
013559.7-720254.74	35:59.7	-72:02:54.74	10.629	0.836	0.001	n
020117.6-720259.49	01:17.6	-72:02:59.49	8.228	0.728	0.001	n
024539.5-720302.84	45:39.5	-72:03:02.84	77.736	0.865	0.001	n
024050.6-720317.24	40:50.6	-72:03:17.24	35.914	0.835	0.001	n
013759.7-720325.25	37:59.7	-72:03:25.25	9.445	0.761	0.001	n
020133.7-720440.79	01:33.7	-72:04:40.79	12.096	0.765	0.001	n
022409.5-720458.43	24:09.5	-72:04:58.43	7.910	0.831	0.001	n
021145.0-720501.33	11:45.0	-72:05:01.33	185.770	0.941	0.005	y
015718.6-720502.29	57:18.6	-72:05:02.29	27.755	0.695	0.001	n
023450.3-720515.80	34:50.3	-72:05:15.80	37.442	0.903	0.003	y
013150.3-720518.67	31:50.3	-72:05:18.67	8.334	0.727	0.000	n
012758.6-720534.04	27:58.6	-72:05:34.04	16.737	1.072	0.001	n
022550.7-720549.77	25:50.8	-72:05:49.77	32.174	0.817	0.001	n
024549.5-720612.15	45:49.5	-72:06:12.15	28.519	0.887	0.002	n
013617.9-720722.08	36:17.9	-72:07:22.08	9.036	0.771	0.001	n
022402.6-720744.40	24:02.6	-72:07:44.40	27.877	0.810	0.001	n
020033.9-720751.84	00:33.9	-72:07:51.84	14.819	0.773	0.001	n
021234.5-720932.12	12:34.5	-72:09:32.12	14.853	0.870	0.001	n

Table A.1 continued...

Name	R.A.	Dec.	S_I (mJy)	σ_{QU} (mJy/beam)	S_{PI} (mJy)	Detect?
021918.2-721003.71	19:18.2	-72:10:03.71	32.053	0.848	0.001	n
023731.5-721006.15	37:31.5	-72:10:06.15	26.826	0.881	0.001	n
014222.1-721117.06	42:22.1	-72:11:17.06	11.172	0.735	0.001	n
015102.3-721213.40	51:02.3	-72:12:13.40	29.743	0.732	0.001	n
021005.6-721241.23	10:05.6	-72:12:41.23	11.746	0.837	0.001	n
013438.9-721245.49	34:39.0	-72:12:45.49	11.241	0.731	0.001	n
015834.7-721257.79	58:34.7	-72:12:57.79	6.209	0.776	0.001	n
020552.3-721321.03	05:52.3	-72:13:21.03	18.613	0.827	0.002	n
021043.6-721326.15	10:43.6	-72:13:26.15	54.886	0.880	0.007	y
023625.1-721337.68	36:25.1	-72:13:37.68	9.232	0.848	0.001	n
023543.6-721502.58	35:43.6	-72:15:02.58	7.792	0.834	0.001	n
022102.4-721530.62	21:02.4	-72:15:30.62	16.250	0.843	0.001	n
022809.0-721532.37	28:09.0	-72:15:32.37	30.780	0.898	0.001	n
024029.1-721723.71	40:29.1	-72:17:23.71	10.211	0.889	0.001	n
022702.8-721724.10	27:02.8	-72:17:24.10	39.736	0.914	0.002	n
013014.2-721832.71	30:14.2	-72:18:32.71	6.877	0.829	0.001	n
014446.6-721907.24	44:46.6	-72:19:07.24	6.464	0.737	0.001	n
014856.8-721914.40	48:56.8	-72:19:14.40	22.731	0.751	0.001	n
022052.8-722040.04	20:52.8	-72:20:40.04	16.978	0.833	0.001	n
013438.8-722123.08	34:38.8	-72:21:23.08	9.963	0.778	0.001	n
013238.2-722138.63	32:38.2	-72:21:38.63	21.316	0.783	0.001	n
023941.8-722150.51	39:41.8	-72:21:50.51	22.524	0.880	0.001	n
014352.3-722223.23	43:52.3	-72:22:23.23	19.275	0.746	0.001	n
022130.3-722226.20	21:30.3	-72:22:26.20	8.709	0.862	0.001	n
014959.7-722315.53	49:59.7	-72:23:15.53	9.225	0.770	0.001	n
024057.4-722334.49	40:57.4	-72:23:34.49	86.505	0.969	0.004	y
021449.1-722336.05	14:49.0	-72:23:36.05	22.752	0.803	0.001	n
013452.9-722444.05	34:52.9	-72:24:44.05	100.978	0.744	0.001	n
021656.5-722506.71	16:56.5	-72:25:06.71	14.247	0.854	0.001	n
015634.6-722532.23	56:34.6	-72:25:32.23	14.369	0.825	0.001	n
015701.9-722613.42	57:01.9	-72:26:13.42	24.311	0.829	0.001	n
014143.2-722621.43	41:43.1	-72:26:21.43	40.762	0.771	0.001	n
022535.5-722623.49	25:35.5	-72:26:23.49	99.444	0.868	0.008	y
022747.7-722714.26	27:47.7	-72:27:14.26	71.056	0.886	0.001	n
013422.4-722720.04	34:22.4	-72:27:20.04	8.461	0.750	0.001	n
014105.8-722750.79	41:05.8	-72:27:50.79	119.228	0.761	0.002	y
014235.7-722959.57	42:35.7	-72:29:59.57	43.652	0.776	0.003	y
021452.0-723125.79	14:52.0	-72:31:25.79	9.640	0.807	0.000	n
024144.7-723130.35	41:44.7	-72:31:30.35	7.593	0.889	0.001	n
015934.4-723145.68	59:34.4	-72:31:45.68	193.530	0.909	0.005	y
024913.7-723257.83	49:13.7	-72:32:57.83	42.436	0.883	0.001	n
023940.3-723320.79	39:40.3	-72:33:20.79	13.094	0.939	0.001	n
021028.3-723333.35	10:28.3	-72:33:33.35	10.619	0.801	0.001	n

Table A.1 continued...

Name	R.A.	Dec.	S_I (mJy)	σ_{QU} (mJy/beam)	S_{PI} (mJy)	Detect?
022007.3-723408.66	20:07.3	-72:34:08.66	10.979	0.800	0.001	n
020029.6-723408.75	00:29.6	-72:34:08.75	420.350	0.872	0.003	y
020752.5-723423.79	07:52.5	-72:34:23.79	13.937	0.823	0.001	n
021424.1-723426.70	14:24.1	-72:34:26.70	21.702	0.855	0.001	n
023147.0-723432.61	31:47.0	-72:34:32.61	43.711	0.806	0.001	n
022451.4-723451.65	24:51.4	-72:34:51.65	9.329	0.812	0.001	n
015334.9-723456.68	53:34.9	-72:34:56.68	23.937	0.702	0.001	n
021535.8-723633.18	15:35.8	-72:36:33.18	17.538	0.822	0.001	n
013824.7-723635.45	38:24.7	-72:36:35.45	23.493	0.736	0.001	n
023925.0-723651.50	39:25.0	-72:36:51.50	12.437	0.929	0.001	n
024128.4-723656.10	41:28.4	-72:36:56.10	21.069	0.892	0.001	n
015404.0-723742.83	54:04.0	-72:37:42.83	8.136	0.777	0.001	n
023540.3-723750.09	35:40.3	-72:37:50.09	22.264	0.832	0.001	n
024640.6-723810.22	46:40.6	-72:38:10.22	7.654	0.878	0.001	n
024234.6-723835.47	42:34.6	-72:38:35.47	7.332	0.886	0.001	n
023003.3-723902.55	30:03.3	-72:39:02.55	6.275	0.884	0.001	n
013229.2-723957.84	32:29.2	-72:39:57.84	232.837	0.759	0.001	n
014051.3-724100.37	40:51.3	-72:41:00.37	16.025	0.752	0.000	n
013921.8-724143.70	39:21.8	-72:41:43.70	11.627	0.716	0.001	n
021946.6-724145.27	19:46.6	-72:41:45.27	79.785	0.837	0.001	n
014851.9-724153.55	48:51.9	-72:41:53.55	11.012	0.725	0.001	n
020159.2-724256.76	01:59.2	-72:42:56.76	17.518	0.799	0.004	y
015730.5-724304.74	57:30.6	-72:43:04.74	34.973	0.840	0.002	n
024705.5-724320.66	47:05.5	-72:43:20.66	8.817	0.889	0.001	n
023502.5-724345.22	35:02.5	-72:43:45.22	15.841	0.826	0.001	n
014643.2-724402.56	46:43.2	-72:44:02.56	28.610	0.753	0.001	n
012957.6-724431.64	29:57.6	-72:44:31.64	6.077	0.759	0.001	n
023122.5-724437.89	31:22.5	-72:44:37.89	43.221	0.877	0.002	n
024102.8-724454.81	41:02.8	-72:44:54.81	13.911	0.957	0.001	n
025137.2-724523.94	51:37.2	-72:45:23.94	416.867	1.010	0.011	y
024719.3-724608.92	47:19.3	-72:46:08.92	10.514	0.882	0.001	n
021212.7-724656.65	12:12.7	-72:46:56.65	19.988	0.792	0.001	n
014027.6-724812.01	40:27.6	-72:48:12.01	11.776	0.736	0.001	n
014629.3-724836.16	46:29.3	-72:48:36.16	143.585	0.778	0.003	y
020607.9-724922.62	06:07.9	-72:49:22.62	9.281	0.816	0.001	n
021540.6-724941.23	15:40.6	-72:49:41.23	55.821	0.842	0.002	n
014900.1-724949.02	49:00.1	-72:49:49.02	30.175	0.756	0.001	n
024108.8-725023.53	41:08.8	-72:50:23.53	13.545	1.000	0.001	n
021330.9-725038.23	13:30.9	-72:50:38.23	19.265	0.872	0.001	n
021704.6-725043.16	17:04.5	-72:50:43.16	102.483	0.861	0.001	n
020528.6-725048.92	05:28.6	-72:50:48.92	8.946	0.837	0.001	n
013339.0-725054.72	33:39.0	-72:50:54.72	6.938	0.746	0.001	n
013601.1-725054.84	36:01.1	-72:50:54.84	7.235	0.846	0.001	n

Table A.1 continued...

Name	R.A.	Dec.	S_I (mJy)	σ_{QU} (mJy/beam)	S_{PI} (mJy)	Detect?
014038.9-725059.19	40:38.9	-72:50:59.19	16.534	0.762	0.001	n
021735.8-725127.80	17:35.8	-72:51:27.80	116.478	0.883	0.001	n
023937.8-725131.48	39:37.8	-72:51:31.48	12.575	0.924	0.001	n
022321.6-725212.37	23:21.6	-72:52:12.37	13.987	0.803	0.001	n
014417.2-725218.85	44:17.2	-72:52:18.85	19.354	0.752	0.001	n
015456.1-725222.85	54:56.1	-72:52:22.85	179.043	0.732	0.001	n
022207.9-725239.61	22:07.9	-72:52:39.61	6.860	0.779	0.001	n
013121.2-725242.06	31:21.3	-72:52:42.06	10.878	0.760	0.000	n
014505.4-725301.75	45:05.4	-72:53:01.75	10.232	0.752	0.001	n
015214.8-725343.53	52:14.8	-72:53:43.53	34.922	0.760	0.001	n
024651.4-725413.65	46:51.4	-72:54:13.65	83.602	0.815	0.001	n
015337.6-725421.44	53:37.6	-72:54:21.44	108.638	0.760	0.002	n
014410.4-725516.50	44:10.4	-72:55:16.50	19.538	0.787	0.001	n
024006.8-725523.48	40:06.8	-72:55:23.48	49.474	0.993	0.008	y
020845.7-725544.86	08:45.7	-72:55:44.86	10.575	0.847	0.001	n
015622.4-725553.84	56:22.4	-72:55:53.84	15.840	0.750	0.001	n
022042.4-725558.26	20:42.4	-72:55:58.26	16.795	0.819	0.001	n
013905.3-725628.28	39:05.3	-72:56:28.28	69.859	0.739	0.001	n
013820.0-725704.57	38:20.0	-72:57:04.57	9.572	0.756	0.001	n
014760.0-725731.55	48:00.0	-72:57:31.55	38.035	0.729	0.001	n
020840.2-725739.96	08:40.2	-72:57:39.96	16.843	0.827	0.001	n
020220.1-725842.44	02:20.1	-72:58:42.44	65.000	0.864	0.003	y
021550.4-725849.63	15:50.4	-72:58:49.63	14.639	0.812	0.001	n
023723.6-725849.92	37:23.6	-72:58:49.92	18.180	0.877	0.001	n
015248.8-725940.01	52:48.8	-72:59:40.01	37.477	0.695	0.002	n
024451.0-730037.49	44:51.0	-73:00:37.49	16.261	0.821	0.001	n
022218.4-730039.63	22:18.4	-73:00:39.63	9.877	0.785	0.001	n
015701.5-730045.88	57:01.5	-73:00:45.88	33.406	0.738	0.001	n
015146.2-730141.20	51:46.2	-73:01:41.20	9.061	0.695	0.000	n
014226.2-730206.57	42:26.2	-73:02:06.57	30.212	0.792	0.001	n
014926.1-730226.74	49:26.1	-73:02:26.74	64.624	0.796	0.001	n
024939.6-730233.74	49:39.6	-73:02:33.74	29.893	0.747	0.002	n
014512.4-730239.14	45:12.4	-73:02:39.14	68.915	0.762	0.001	n
013328.9-730306.04	33:28.9	-73:03:06.04	65.730	0.728	0.003	y
025512.7-730314.34	55:12.7	-73:03:14.34	77.533	1.257	0.001	n
013702.8-730414.33	37:02.8	-73:04:14.33	163.094	0.833	0.004	y
022719.2-730430.08	27:19.2	-73:04:30.08	15.237	0.731	0.003	y
021034.0-730559.20	10:34.0	-73:05:59.20	139.351	0.873	0.015	y
024401.5-730639.56	44:01.5	-73:06:39.56	10.505	0.782	0.002	n
024656.4-730715.31	46:56.4	-73:07:15.31	21.820	0.686	0.001	n
021738.3-730735.18	17:38.4	-73:07:35.18	12.652	0.813	0.001	n
021801.5-730749.22	18:01.5	-73:07:49.22	13.888	0.794	0.001	n
012616.6-730750.97	26:16.6	-73:07:50.97	50.623	0.975	0.001	n

Table A.1 continued...

Name	R.A.	Dec.	S_I (mJy)	σ_{QU} (mJy/beam)	S_{PI} (mJy)	Detect?
012815.8-730801.98	28:15.9	-73:08:01.98	12.029	0.776	0.001	n
025529.0-730817.40	55:29.0	-73:08:17.40	13.009	1.265	0.001	n
014524.7-730823.94	45:24.7	-73:08:23.94	10.616	0.777	0.001	n
022947.1-730841.56	29:47.1	-73:08:41.56	6.988	0.750	0.001	n
012406.7-730908.46	24:06.7	-73:09:08.46	67.655	1.522	0.001	n
025319.4-730917.13	53:19.5	-73:09:17.13	15.019	0.867	0.001	n
014424.0-730944.41	44:24.0	-73:09:44.41	6.556	0.771	0.001	n
013925.0-730957.39	39:25.0	-73:09:57.39	6.808	0.809	0.001	n
021811.9-730958.03	18:11.9	-73:09:58.03	50.451	0.803	0.002	n
013949.9-731001.50	39:49.9	-73:10:01.50	36.556	0.790	0.003	y
012751.9-731100.49	27:51.9	-73:11:00.49	15.032	0.832	0.001	n
020246.4-731117.25	02:46.4	-73:11:17.25	23.232	0.782	0.002	n
021828.6-731228.39	18:28.6	-73:12:28.39	7.703	0.797	0.001	n
014905.7-731254.94	49:05.7	-73:12:54.94	52.086	0.752	0.001	n
024252.2-731310.86	42:52.2	-73:13:10.86	37.717	0.678	0.001	n
023302.9-731424.77	33:02.9	-73:14:24.77	18.160	0.706	0.001	n
022935.7-731458.53	29:35.7	-73:14:58.53	18.341	0.714	0.001	n
012639.9-731504.20	26:39.9	-73:15:04.20	59.314	0.971	0.001	n
023453.0-731504.46	34:53.0	-73:15:04.46	39.514	0.695	0.001	n
022434.1-731550.16	24:34.1	-73:15:50.16	12.553	0.679	0.001	n
012546.1-731603.83	25:46.1	-73:16:03.83	62.536	1.144	0.002	n
022911.3-731610.62	29:11.3	-73:16:10.62	14.378	0.688	0.001	n
014305.1-731620.45	43:05.1	-73:16:20.45	18.738	0.748	0.001	n
022645.0-731651.10	26:45.0	-73:16:51.10	7.636	0.668	0.001	n
013919.3-731656.43	39:19.3	-73:16:56.43	61.800	0.840	0.006	y
021443.1-731737.82	14:43.1	-73:17:37.82	11.692	0.779	0.000	n
013032.3-731741.10	30:32.3	-73:17:41.10	28.743	0.747	0.001	n
015048.3-731759.69	50:48.3	-73:17:59.69	11.259	0.705	0.001	n
013340.7-731759.78	33:40.7	-73:17:59.78	22.968	0.755	0.001	n
024045.1-731814.91	40:45.1	-73:18:14.91	7.707	0.647	0.001	n
013422.0-731817.11	34:22.0	-73:18:17.11	12.900	0.760	0.001	n
014337.5-731846.36	43:37.5	-73:18:46.36	8.390	0.745	0.001	n
020420.2-731935.49	04:20.2	-73:19:35.49	97.515	0.725	0.001	n
020736.7-731952.19	07:36.7	-73:19:52.19	42.897	0.763	0.001	n
022923.8-732001.27	29:23.8	-73:20:01.27	20.578	0.664	0.001	n
024855.4-732012.76	48:55.4	-73:20:12.76	25.320	0.650	0.001	n
015822.6-732101.64	58:22.6	-73:21:01.64	26.397	0.724	0.001	n
021052.4-732204.47	10:52.4	-73:22:04.47	16.566	0.762	0.001	n
025329.0-732237.42	53:29.0	-73:22:37.42	12.741	0.726	0.000	n
025438.7-732239.47	54:38.6	-73:22:39.47	20.995	0.846	0.001	n
022013.5-732337.28	20:13.5	-73:23:37.28	66.798	0.793	0.002	n
013813.2-732341.11	38:13.2	-73:23:41.11	15.910	0.763	0.001	n
024704.5-732425.99	47:04.5	-73:24:25.99	61.895	0.632	0.001	n

Table A.1 continued...

Name	R.A.	Dec.	S_I (mJy)	σ_{QU} (mJy/beam)	S_{PI} (mJy)	Detect?
023727.1-732442.73	37:27.1	-73:24:42.73	16.325	0.637	0.001	n
023345.8-732455.10	33:45.8	-73:24:55.10	10.629	0.653	0.000	n
024557.5-732554.66	45:57.5	-73:25:54.66	10.254	0.639	0.000	n
015219.9-732602.38	52:19.9	-73:26:02.38	10.385	0.713	0.001	n
024012.8-732605.10	40:12.7	-73:26:05.10	39.618	0.685	0.002	n
025359.9-732612.32	53:59.9	-73:26:12.32	31.993	0.782	0.001	n
020010.0-732701.86	00:10.0	-73:27:01.86	11.927	0.753	0.001	n
012628.9-732714.79	26:28.9	-73:27:14.79	43.410	0.927	0.001	n
013708.9-732739.21	37:08.9	-73:27:39.21	8.713	0.705	0.001	n
021837.0-732826.72	18:37.0	-73:28:26.72	8.992	0.759	0.001	n
022523.0-732853.36	25:23.0	-73:28:53.36	27.275	0.658	0.001	n
015051.1-732949.90	50:51.1	-73:29:49.90	13.685	0.743	0.001	n
013742.3-733050.53	37:42.3	-73:30:50.53	59.682	0.732	0.001	n
014136.9-733122.17	41:36.9	-73:31:22.17	6.263	0.734	0.001	n
023110.9-733141.08	31:10.9	-73:31:41.08	8.982	0.664	0.000	n
021644.5-733141.87	16:44.5	-73:31:41.87	80.450	0.769	0.005	y
013547.9-733201.35	35:47.9	-73:32:01.35	7.549	0.714	0.001	n
025555.5-733210.90	55:55.5	-73:32:10.90	174.435	0.980	0.002	n
014917.4-733246.92	49:17.4	-73:32:46.92	6.794	0.755	0.001	n
012929.6-733312.34	29:29.6	-73:33:12.34	209.246	0.729	0.002	n
015741.5-733313.81	57:41.4	-73:33:13.81	9.812	0.754	0.001	n
023340.0-733347.67	33:40.0	-73:33:47.67	14.681	0.649	0.000	n
020006.3-733352.55	00:06.3	-73:33:52.55	12.222	0.723	0.001	n
025424.3-733428.43	54:24.3	-73:34:28.43	44.109	0.781	0.001	n
024208.9-733430.86	42:08.9	-73:34:30.86	119.392	0.661	0.005	y
020604.5-733446.47	06:04.5	-73:34:46.47	69.326	0.762	0.003	y
022829.6-733641.68	28:29.6	-73:36:41.68	22.081	0.638	0.002	y
013335.7-733643.95	33:35.7	-73:36:43.95	7.295	0.715	0.001	n
024909.6-733645.75	49:09.6	-73:36:45.75	13.775	0.643	0.001	n
013634.6-733655.01	36:34.6	-73:36:55.01	11.119	0.714	0.001	n
014233.0-733657.79	42:33.0	-73:36:57.79	9.602	0.739	0.001	n
015548.0-733701.36	55:48.0	-73:37:01.36	19.710	0.739	0.001	n
020501.0-733742.91	05:01.0	-73:37:42.91	10.558	0.727	0.000	n
013843.0-733800.49	38:43.0	-73:38:00.49	25.560	0.734	0.001	n
014314.3-733804.82	43:14.3	-73:38:04.82	9.649	0.735	0.001	n
025448.2-733811.68	54:48.2	-73:38:11.68	38.377	0.753	0.000	n
013214.7-733902.77	32:14.7	-73:39:02.77	33.743	0.752	0.001	n
020240.0-734021.37	02:40.0	-73:40:21.37	8.368	0.727	0.001	n
020608.0-734022.11	06:08.0	-73:40:22.11	31.668	0.721	0.002	n
013228.8-734123.89	32:28.8	-73:41:23.89	39.046	0.750	0.001	n
012828.3-734141.28	28:28.3	-73:41:41.28	9.502	0.737	0.001	n
025458.5-734314.17	54:58.5	-73:43:14.17	9.914	0.775	0.001	n
024001.9-734346.96	40:01.9	-73:43:46.96	542.877	0.653	0.007	y

Table A.1 continued...

Name	R.A.	Dec.	S_I (mJy)	σ_{QU} (mJy/beam)	S_{PI} (mJy)	Detect?
015928.7-734405.37	59:28.7	-73:44:05.37	11.446	0.719	0.002	n
013242.5-734416.27	32:42.5	-73:44:16.27	45.905	0.728	0.002	n
025748.9-734431.60	57:48.9	-73:44:31.60	12.454	1.499	0.001	n
013941.2-734515.21	39:41.2	-73:45:15.21	9.475	0.713	0.001	n
015130.8-734541.23	51:30.8	-73:45:41.23	22.111	0.739	0.002	n
021745.0-734722.24	17:45.0	-73:47:22.24	153.332	0.747	0.004	y
023221.6-734902.97	32:21.6	-73:49:02.97	61.819	0.646	0.003	y
013147.3-734946.16	31:47.3	-73:49:46.16	17.616	0.802	0.003	y
023815.8-734953.60	38:15.8	-73:49:53.60	27.279	0.642	0.001	n
022753.7-735017.63	27:53.7	-73:50:17.63	20.015	0.622	0.000	n
012349.5-735037.76	23:49.4	-73:50:37.76	104.048	1.062	0.001	n
021545.8-735054.20	15:45.7	-73:50:54.20	82.688	0.750	0.003	y
021214.0-735128.07	12:14.0	-73:51:28.07	51.199	0.729	0.004	y
022317.6-735204.10	23:17.6	-73:52:04.10	19.546	0.772	0.000	n
014940.2-735230.82	49:40.2	-73:52:30.82	22.920	0.712	0.001	n
023504.4-735405.03	35:04.4	-73:54:05.03	9.359	0.637	0.000	n
022826.0-735406.64	28:26.0	-73:54:06.64	17.860	0.627	0.001	n
023712.2-735417.96	37:12.2	-73:54:17.96	51.687	0.623	0.001	n
012600.4-735419.69	26:00.4	-73:54:19.69	20.025	0.821	0.001	n
015136.3-735425.04	51:36.3	-73:54:25.04	80.346	0.718	0.001	n
024738.1-735520.10	47:38.1	-73:55:20.10	54.950	0.603	0.001	n
022153.6-735552.98	21:53.6	-73:55:52.98	33.799	0.747	0.002	n
012322.7-735607.96	23:22.6	-73:56:07.96	33.210	1.111	0.001	n
020638.8-735610.14	06:38.8	-73:56:10.14	232.138	0.716	0.002	y
012535.2-735637.87	25:35.1	-73:56:37.87	19.312	0.859	0.002	n
022218.2-735811.55	22:18.2	-73:58:11.55	8.805	0.765	0.001	n
014249.5-735831.73	42:49.5	-73:58:31.73	21.648	0.748	0.000	n
021721.4-735839.60	17:21.4	-73:58:39.60	31.933	0.737	0.001	n
022217.3-735856.18	22:17.3	-73:58:56.18	7.427	0.779	0.001	n
024528.3-735905.01	45:28.3	-73:59:05.01	15.987	0.587	0.001	n
021024.5-735932.83	10:24.5	-73:59:32.83	27.784	0.756	0.003	y
021806.4-735948.61	18:06.4	-73:59:48.61	9.735	0.773	0.001	n
012551.8-740008.43	25:51.8	-74:00:08.43	9.095	0.829	0.001	n
012149.1-740012.32	21:49.1	-74:00:12.32	64.964	1.610	0.001	n
024121.3-740017.32	41:21.3	-74:00:17.32	18.067	0.660	0.001	n
023325.1-740026.24	33:25.1	-74:00:26.24	10.556	0.646	0.002	y
013124.2-740039.17	31:24.2	-74:00:39.17	25.290	0.737	0.001	n
024310.1-740112.49	43:10.1	-74:01:12.49	30.028	0.628	0.001	n
014918.6-740114.99	49:18.6	-74:01:14.99	14.150	0.714	0.001	n
025451.8-740222.22	54:51.8	-74:02:22.22	13.606	0.684	0.001	n
024252.2-740237.11	42:52.2	-74:02:37.11	17.675	0.634	0.001	n
024219.5-740240.96	42:19.5	-74:02:40.96	121.396	0.648	0.002	y
020923.8-740255.76	09:23.8	-74:02:55.76	55.273	0.721	0.001	n

Table A.1 continued...

Name	R.A.	Dec.	S_I (mJy)	σ_{QU} (mJy/beam)	S_{PI} (mJy)	Detect?
022420.5-740308.54	24:20.5	-74:03:08.54	14.787	0.647	0.001	n
025417.5-740339.08	54:17.5	-74:03:39.08	16.508	0.656	0.000	n
014637.1-740430.56	46:37.1	-74:04:30.56	15.788	0.740	0.002	n
024044.9-740433.03	40:44.9	-74:04:33.03	13.374	0.664	0.001	n
014514.9-740450.71	45:15.0	-74:04:50.71	7.021	0.745	0.000	n
025812.3-740500.54	58:12.3	-74:05:00.54	20.229	1.155	0.001	n
020350.7-740520.23	03:50.7	-74:05:20.23	13.807	0.711	0.001	n
020635.5-740525.67	06:35.5	-74:05:25.67	63.116	0.677	0.001	n
022348.3-740623.99	23:48.3	-74:06:23.99	61.959	0.663	0.001	n
021450.9-740651.17	14:50.9	-74:06:51.17	10.960	0.719	0.001	n
013632.1-740659.28	36:32.1	-74:06:59.28	33.100	0.741	0.000	n
014116.1-740734.06	41:16.1	-74:07:34.06	74.459	0.692	0.003	y
014609.1-740812.41	46:09.1	-74:08:12.41	13.472	0.723	0.001	n
023632.7-740901.09	36:32.8	-74:09:01.09	5.719	0.640	0.001	n
021051.4-741010.63	10:51.4	-74:10:10.63	8.783	0.742	0.001	n
025638.6-741014.60	56:38.6	-74:10:14.60	81.500	0.823	0.001	n
012237.9-741016.64	22:37.9	-74:10:16.64	19.966	1.255	0.003	n
012806.4-741103.01	28:06.4	-74:11:03.01	7.968	0.754	0.001	n
022651.7-741119.94	26:51.7	-74:11:19.94	5.645	0.631	0.000	n
015811.5-741154.44	58:11.5	-74:11:54.44	19.330	0.741	0.002	n
025315.8-741228.66	53:15.8	-74:12:28.66	7.068	0.646	0.001	n
013558.4-741254.85	35:58.4	-74:12:54.85	11.442	0.775	0.001	n
021849.7-741306.36	18:49.7	-74:13:06.36	8.350	0.746	0.001	n
024906.0-741313.81	49:06.0	-74:13:13.81	25.933	0.602	0.001	n
013800.4-741352.28	38:00.4	-74:13:52.28	42.796	0.726	0.001	n
021118.3-741429.12	11:18.3	-74:14:29.12	15.622	0.722	0.001	n
024334.2-741441.76	43:34.2	-74:14:41.76	9.481	0.613	0.000	n
021939.1-741600.58	19:39.2	-74:16:00.58	184.193	0.855	0.005	y
025237.6-741720.37	52:37.6	-74:17:20.37	46.793	0.688	0.001	n
022417.8-741726.60	24:17.8	-74:17:26.60	50.634	0.675	0.000	n
022210.1-741727.37	22:10.1	-74:17:27.37	10.889	0.772	0.001	n
021302.5-741738.30	13:02.5	-74:17:38.30	26.657	0.738	0.001	n
013153.9-741738.55	31:53.9	-74:17:38.55	5.891	0.715	0.001	n
021811.6-741807.97	18:11.6	-74:18:07.97	13.997	0.763	0.001	n
013305.9-741931.82	33:05.9	-74:19:31.82	5.756	0.710	0.000	n
013214.5-742019.00	32:14.5	-74:20:19.00	5.863	0.733	0.001	n
013013.5-742024.69	30:13.5	-74:20:24.69	21.854	0.759	0.001	n
021805.6-742114.38	18:05.6	-74:21:14.38	9.304	0.742	0.001	n
021533.8-742124.98	15:33.8	-74:21:24.98	12.357	0.776	0.001	n
023239.6-742143.44	32:39.6	-74:21:43.44	41.671	0.606	0.001	n
022410.2-742231.04	24:10.2	-74:22:31.04	7.868	0.651	0.001	n
014012.3-742308.21	40:12.3	-74:23:08.21	9.853	0.718	0.001	n
024459.0-742321.96	44:59.0	-74:23:21.96	6.956	0.603	0.001	n

Table A.1 continued...

Name	R.A.	Dec.	S_I (mJy)	σ_{QU} (mJy/beam)	S_{PI} (mJy)	Detect?
022222.0-742332.82	22:22.1	-74:23:32.82	25.594	0.677	0.001	n
021648.6-742413.46	16:48.6	-74:24:13.46	11.247	0.748	0.001	n
021550.3-742432.27	15:50.3	-74:24:32.27	177.462	0.782	0.004	y
020645.3-742516.24	06:45.3	-74:25:16.24	12.417	0.701	0.001	n
021932.7-742530.18	19:32.7	-74:25:30.18	11.635	0.684	0.001	n
030022.1-742542.76	00:22.1	-74:25:42.76	19.623	1.668	0.002	n
013017.7-742549.98	30:17.7	-74:25:49.98	7.989	0.799	0.001	n
012247.0-742631.26	22:47.0	-74:26:31.26	6.977	1.033	0.001	n
020318.3-742648.75	03:18.3	-74:26:48.75	27.769	0.703	0.001	n
014703.3-742712.82	47:03.4	-74:27:12.82	12.493	0.794	0.001	n
022856.0-742851.05	28:56.0	-74:28:51.05	13.698	0.575	0.001	n
013309.1-742916.31	33:09.1	-74:29:16.31	37.258	0.719	0.001	n
022821.7-743031.10	28:21.7	-74:30:31.10	7.786	0.631	0.000	n
015952.7-743056.54	59:52.7	-74:30:56.54	943.319	0.763	0.001	n
023200.0-743124.88	32:00.0	-74:31:24.88	12.144	0.601	0.001	n
014402.0-743139.28	44:01.9	-74:31:39.28	67.610	0.871	0.003	y
022903.2-743202.25	29:03.2	-74:32:02.25	101.799	0.639	0.005	y
013623.6-743252.94	36:23.6	-74:32:52.94	8.544	0.829	0.001	n
014432.9-743306.41	44:32.9	-74:33:06.41	92.269	0.860	0.006	y
025701.4-743319.36	57:01.4	-74:33:19.36	25.030	0.767	0.001	n
013247.2-743343.60	32:47.3	-74:33:43.60	8.083	0.754	0.001	n
014250.0-743444.73	42:50.0	-74:34:44.73	44.713	0.821	0.001	n
020642.6-743512.20	06:42.6	-74:35:12.20	139.447	0.711	0.002	y
012248.0-743533.66	22:48.0	-74:35:33.66	8.125	0.990	0.001	n
022951.2-743607.88	29:51.2	-74:36:07.88	87.842	0.659	0.005	y
025736.4-743620.54	57:36.4	-74:36:20.54	33.274	0.810	0.000	n
013328.1-743631.52	33:28.1	-74:36:31.52	30.048	0.773	0.001	n
025347.4-743807.32	53:47.4	-74:38:07.32	26.843	0.637	0.001	n
015827.2-743828.09	58:27.2	-74:38:28.09	565.635	0.784	0.008	y
025440.4-743904.25	54:40.4	-74:39:04.25	31.705	0.693	0.001	n
020326.9-743906.96	03:26.9	-74:39:06.96	19.044	0.745	0.001	n
013023.5-743924.62	30:23.5	-74:39:24.62	10.365	0.812	0.001	n
015028.1-743954.37	50:28.1	-74:39:54.37	9.237	0.812	0.002	n
025210.8-744006.26	52:10.8	-74:40:06.26	9.339	0.660	0.001	n
025315.5-744040.09	53:15.6	-74:40:40.09	45.938	0.676	0.001	n
015715.7-744112.11	57:15.7	-74:41:12.11	28.834	0.822	0.001	n
013825.8-744124.95	38:25.8	-74:41:24.95	9.088	0.770	0.000	n
013528.2-744136.47	35:28.2	-74:41:36.47	15.412	0.778	0.001	n
012352.6-744140.14	23:52.6	-74:41:40.14	43.763	0.892	0.001	n
023455.0-744147.14	34:55.0	-74:41:47.14	10.815	0.656	0.001	n
023820.7-744241.10	38:20.7	-74:42:41.10	14.616	0.635	0.001	n
024348.7-744316.64	43:48.6	-74:43:16.64	8.460	0.645	0.001	n
014810.0-744344.93	48:10.0	-74:43:44.93	69.828	0.768	0.001	n

Table A.1 continued...

Name	R.A.	Dec.	S_I (mJy)	σ_{QU} (mJy/beam)	S_{PI} (mJy)	Detect?
024031.4-744436.31	40:31.4	-74:44:36.31	83.461	0.659	0.001	n
030129.1-744522.57	01:29.1	-74:45:22.57	156.157	1.825	0.001	n
024110.6-744533.04	41:10.6	-74:45:33.04	29.024	0.639	0.001	n
013341.1-744611.37	33:41.1	-74:46:11.37	45.927	0.778	0.001	n
025221.5-744634.38	52:21.5	-74:46:34.38	86.852	0.675	0.002	n
021955.5-744635.21	19:55.4	-74:46:35.21	22.167	0.686	0.001	n
025141.9-744637.31	51:41.9	-74:46:37.31	96.018	0.657	0.002	y
012201.1-744640.09	22:01.1	-74:46:40.09	21.474	1.011	0.001	n
015932.1-744728.48	59:32.1	-74:47:28.48	34.222	0.741	0.001	n
014758.4-744828.43	47:58.4	-74:48:28.43	75.892	0.793	0.001	n
020433.9-744933.29	04:33.9	-74:49:33.29	7.476	0.688	0.001	n
022532.8-744951.77	25:32.8	-74:49:51.77	8.463	0.650	0.001	n
021854.1-745034.19	18:54.1	-74:50:34.19	89.353	0.689	0.002	n
022203.6-745111.60	22:03.6	-74:51:11.60	8.787	0.679	0.001	n
014610.1-745113.99	46:10.1	-74:51:13.99	9.355	0.816	0.001	n
021156.7-745148.52	11:56.7	-74:51:48.52	26.697	0.689	0.001	n
022832.2-745149.77	28:32.2	-74:51:49.77	19.607	0.671	0.001	n
015945.6-745157.99	59:45.6	-74:51:57.99	44.593	0.679	0.001	n
024827.1-745201.23	48:27.1	-74:52:01.23	7.911	0.654	0.001	n
020651.2-745310.07	06:51.2	-74:53:10.07	17.583	0.678	0.002	y
024741.6-745320.12	47:41.6	-74:53:20.12	40.816	0.691	0.002	n
025151.9-745324.56	51:51.9	-74:53:24.56	22.631	0.630	0.001	n
023517.9-745329.87	35:17.9	-74:53:29.87	8.160	0.672	0.001	n
013724.3-745330.11	37:24.4	-74:53:30.11	10.763	0.798	0.001	n
012311.0-745422.53	23:11.0	-74:54:22.53	11.525	0.832	0.001	n
023240.0-745447.33	32:40.0	-74:54:47.33	11.010	0.697	0.001	n
013925.8-745550.01	39:25.8	-74:55:50.01	7.653	0.759	0.001	n
021008.2-745611.58	10:08.2	-74:56:11.58	29.893	0.669	0.001	n
023718.5-745612.50	37:18.5	-74:56:12.50	9.107	0.691	0.001	n
022741.3-745622.69	27:41.3	-74:56:22.69	120.024	0.664	0.002	y
021436.6-745622.94	14:36.6	-74:56:22.94	13.299	0.710	0.001	n
023949.3-745648.87	39:49.3	-74:56:48.87	31.710	0.678	0.001	n
023203.3-745722.85	32:03.3	-74:57:22.85	50.232	0.702	0.006	y
021027.8-745735.04	10:27.8	-74:57:35.04	10.355	0.671	0.001	n
025940.2-745735.25	59:40.2	-74:57:35.25	17.682	0.983	0.001	n
022529.4-745757.55	25:29.4	-74:57:57.55	6.842	0.661	0.001	n
024058.5-745834.87	40:58.6	-74:58:34.87	8.906	0.655	0.001	n
013108.6-745835.47	31:08.6	-74:58:35.47	16.094	0.807	0.001	n
022201.2-745841.20	22:01.2	-74:58:41.20	22.191	0.663	0.001	n
023142.4-745922.73	31:42.4	-74:59:22.73	25.590	0.698	0.001	n
020525.5-750010.62	05:25.5	-75:00:10.62	11.250	0.734	0.001	n
022031.0-750029.53	20:31.0	-75:00:29.53	8.118	0.671	0.000	n
013913.2-750039.91	39:13.2	-75:00:39.91	41.741	0.785	0.001	n

Table A.1 continued...

Name	R.A.	Dec.	S_I (mJy)	σ_{QU} (mJy/beam)	S_{PI} (mJy)	Detect?
021024.9-750124.68	10:24.9	-75:01:24.68	22.849	0.688	0.001	n
024602.1-750138.12	46:02.1	-75:01:38.12	14.923	0.655	0.001	n
020050.7-750359.92	00:50.7	-75:03:59.92	93.083	0.728	0.004	y
022434.4-750428.03	24:34.4	-75:04:28.03	38.092	0.667	0.001	n
023852.3-750449.64	38:52.3	-75:04:49.64	9.440	0.694	0.001	n
022834.4-750503.01	28:34.4	-75:05:03.01	20.580	0.672	0.000	n
024430.6-750517.26	44:30.6	-75:05:17.26	11.118	0.633	0.001	n
021914.8-750520.33	19:14.8	-75:05:20.33	7.279	0.709	0.001	n
025858.7-750530.68	58:58.7	-75:05:30.68	65.304	0.870	0.001	n
021425.3-750539.93	14:25.3	-75:05:39.93	67.931	0.729	0.001	n
012035.5-750635.39	20:35.5	-75:06:35.39	23.280	1.057	0.001	n
014901.1-750659.80	49:01.1	-75:06:59.80	37.306	0.834	0.001	n
022437.9-750709.30	24:37.9	-75:07:09.30	16.457	0.680	0.001	n
022847.9-750730.21	28:47.9	-75:07:30.21	11.330	0.671	0.000	n
015453.4-750830.83	54:53.4	-75:08:30.83	82.795	0.722	0.001	n
024822.7-750845.98	48:22.7	-75:08:45.98	37.972	0.678	0.001	n
021531.1-750914.16	15:31.1	-75:09:14.16	13.767	0.712	0.002	n
024413.8-750942.66	44:13.8	-75:09:42.66	14.217	0.654	0.001	n
020616.2-751013.95	06:16.2	-75:10:13.95	14.666	0.704	0.002	n
015906.2-751025.90	59:06.2	-75:10:25.90	32.754	0.746	0.002	n
021020.9-751103.45	10:20.9	-75:11:03.45	84.633	0.705	0.001	n
012655.0-751122.14	26:55.0	-75:11:22.14	54.866	0.956	0.002	n
013510.4-751201.16	35:10.4	-75:12:01.16	8.232	0.796	0.003	y
012811.5-751254.14	28:11.5	-75:12:54.14	253.120	0.928	0.020	y
025311.0-751316.74	53:11.0	-75:13:16.74	335.739	0.703	0.005	y
024914.8-751335.85	49:14.8	-75:13:35.85	7.251	0.681	0.001	n
015645.2-751409.14	56:45.2	-75:14:09.14	169.543	0.745	0.002	n
030237.7-751431.64	02:37.8	-75:14:31.64	32.709	1.472	0.001	n
030202.3-751445.98	02:02.3	-75:14:45.98	36.111	1.266	0.001	n
023535.2-751448.77	35:35.2	-75:14:48.77	14.390	0.650	0.001	n
012256.9-751506.71	22:56.9	-75:15:06.71	604.062	0.918	0.013	y
014546.4-751617.57	45:46.4	-75:16:17.57	133.280	0.780	0.001	n
024857.9-751700.36	48:57.9	-75:17:00.36	13.690	0.682	0.002	n
020049.6-751711.19	00:49.6	-75:17:11.19	20.666	0.706	0.001	n
014523.5-751755.55	45:23.6	-75:17:55.55	15.900	0.792	0.001	n
025422.4-751809.84	54:22.4	-75:18:09.84	13.632	0.695	0.000	n
023148.6-751814.92	31:48.6	-75:18:14.92	12.451	0.689	0.001	n
021202.4-751819.24	12:02.4	-75:18:19.24	89.598	0.709	0.002	n
021417.7-751855.63	14:17.7	-75:18:55.63	205.729	0.697	0.000	n
020948.2-751856.34	09:48.2	-75:18:56.34	41.350	0.704	0.005	y
024914.0-751904.09	49:14.0	-75:19:04.09	14.768	0.689	0.001	n
022451.1-751936.39	24:51.1	-75:19:36.39	94.559	0.696	0.002	n
024950.5-752008.97	49:50.5	-75:20:08.97	19.643	0.675	0.001	n

Table A.1 continued...

Name	R.A.	Dec.	S_I (mJy)	σ_{QU} (mJy/beam)	S_{PI} (mJy)	Detect?
022723.2-752036.06	27:23.1	-75:20:36.06	20.261	0.679	0.001	n
025652.0-752110.62	56:52.0	-75:21:10.62	20.240	0.711	0.001	n
020706.8-752117.48	07:06.9	-75:21:17.48	141.744	0.763	0.017	y
030103.8-752205.41	01:03.8	-75:22:05.41	38.521	0.935	0.001	n
023238.6-752209.45	32:38.6	-75:22:09.45	336.594	0.682	0.000	n
012430.0-752242.08	24:30.0	-75:22:42.08	69.514	0.837	0.002	n
025712.3-752253.82	57:12.3	-75:22:53.82	86.312	0.714	0.001	n
024045.1-752302.17	40:45.1	-75:23:02.17	19.518	0.674	0.001	n
024110.9-752308.20	41:10.9	-75:23:08.20	13.074	0.688	0.001	n
023638.0-752312.86	36:38.0	-75:23:12.86	24.061	0.668	0.003	y
025746.9-752318.16	57:46.9	-75:23:18.16	11.470	0.708	0.001	n
022924.5-752329.03	29:24.5	-75:23:29.03	10.851	0.694	0.001	n
013441.3-752402.72	34:41.3	-75:24:02.72	9.484	0.793	0.001	n
012926.4-752435.53	29:26.4	-75:24:35.53	22.718	0.786	0.001	n
025131.6-752504.84	51:31.6	-75:25:04.84	60.222	0.669	0.001	n
014753.5-752535.66	47:53.5	-75:25:35.66	26.410	0.787	0.002	n
021031.7-752538.82	10:31.7	-75:25:38.82	18.402	0.684	0.001	n
030053.7-752645.87	00:53.7	-75:26:45.87	27.982	0.934	0.001	n
020600.2-753053.31	06:00.2	-75:30:53.31	40.701	0.716	0.002	y
022611.8-753117.04	26:11.8	-75:31:17.04	24.322	0.660	0.001	n
025851.8-753126.48	58:51.8	-75:31:26.48	12.081	0.804	0.001	n
025635.4-753205.48	56:35.4	-75:32:05.48	13.458	0.718	0.001	n
021613.8-753322.90	16:13.8	-75:33:22.90	29.325	0.723	0.001	n
022146.3-753357.77	21:46.3	-75:33:57.77	13.297	0.662	0.001	n
020554.3-753418.10	05:54.4	-75:34:18.10	51.964	0.724	0.001	n
024908.3-753507.76	49:08.3	-75:35:07.76	76.769	0.698	0.001	n
024456.4-753555.38	44:56.4	-75:35:55.38	9.398	0.689	0.001	n
023634.2-753629.77	36:34.2	-75:36:29.77	35.750	0.637	0.001	n
025321.8-753755.43	53:21.8	-75:37:55.43	7.493	0.752	0.001	n
012058.7-753817.89	20:58.7	-75:38:17.89	19.050	1.577	0.001	n
023519.7-753845.82	35:19.7	-75:38:45.82	84.635	0.650	0.001	n
013555.9-753907.16	35:55.9	-75:39:07.16	25.902	0.824	0.001	n
024520.6-753908.37	45:20.6	-75:39:08.37	14.269	0.741	0.001	n
022834.3-753954.40	28:34.3	-75:39:54.40	15.250	0.685	0.001	n
024909.9-754202.22	49:09.9	-75:42:02.22	49.895	0.805	0.004	y
023143.8-754210.12	31:43.8	-75:42:10.12	8.054	0.715	0.001	n
025841.2-754228.93	58:41.2	-75:42:28.93	29.147	1.019	0.001	n
024932.7-754301.74	49:32.7	-75:43:01.74	44.471	0.823	0.005	y
021817.1-754502.40	18:17.1	-75:45:02.40	60.402	0.735	0.002	y
023534.2-754559.42	35:34.2	-75:45:59.42	86.263	0.711	0.001	n
024124.8-754605.95	41:24.8	-75:46:05.95	12.017	0.735	0.001	n
021647.3-754813.22	16:47.3	-75:48:13.22	53.589	0.738	0.001	n
020640.4-755052.52	06:40.4	-75:50:52.52	224.635	0.829	0.011	y

Table A.1 continued...

Name	R.A.	Dec.	S_I (mJy)	σ_{QU} (mJy/beam)	S_{PI} (mJy)	Detect?
024912.4-755053.13	49:12.4	-75:50:53.13	25.935	1.152	0.001	n
014729.1-755101.55	47:29.1	-75:51:01.55	31.292	0.973	0.001	n
020753.3-755244.12	07:53.3	-75:52:44.12	45.234	0.848	0.001	n
023524.1-755512.10	35:24.1	-75:55:12.10	7.431	0.960	0.001	n
015528.2-755604.25	55:28.2	-75:56:04.25	49.769	0.969	0.001	n
012425.2-755703.97	24:25.2	-75:57:03.97	21.625	2.713	0.004	n
014245.7-755728.34	42:45.7	-75:57:28.34	21.814	1.316	0.001	n
021815.5-755738.40	18:15.5	-75:57:38.40	22.831	0.899	0.001	n
022634.3-755745.64	26:34.3	-75:57:45.64	45.226	0.999	0.001	n
021624.4-755955.38	16:24.4	-75:59:55.38	29.570	0.960	0.001	n
024631.9-760132.17	46:31.9	-76:01:32.17	16.602	2.137	0.001	n
013251.5-760406.80	32:51.5	-76:04:06.80	171.726	3.012	0.012	y
023337.9-760501.23	33:37.9	-76:05:01.23	86.170	1.803	0.006	y
024057.4-760635.34	40:57.4	-76:06:35.34	10.993	2.509	0.002	n
014455.8-760659.88	44:55.8	-76:06:59.88	207.090	2.589	0.003	n
015704.3-760714.62	57:04.3	-76:07:14.62	30.939	1.809	0.002	n
015528.2-760828.04	55:28.2	-76:08:28.04	87.775	2.299	0.004	n
014154.3-760934.32	41:54.3	-76:09:34.32	18.788	3.210	0.012	y
021553.7-761036.92	15:53.7	-76:10:36.92	23.222	1.986	0.003	n
020307.0-761221.55	03:07.0	-76:12:21.55	32.070	2.597	0.003	n
020142.0-761305.92	01:42.0	-76:13:05.92	18.043	2.884	0.004	n
015425.7-761351.93	54:25.7	-76:13:51.93	139.511	3.276	0.012	y

B

POLARISATION PARAMETER AND UNCERTAINTY MAPS FOR NGC 612

In Section §3.6, we have argued that each of the single-component polarisation models discussed in this work offer similar goodness-of-fit to the observed polarisation spectra. Below, we present each of the parameter maps returned from our model-fitting routine. The agreement in parameter values between all models adds credence to the data validity. We point out that the major discrepancies between the parameter maps lie in the maps of Faraday depth, in that in the case of internal Faraday rotation, the total Faraday depth is equal to two times the observed Faraday rotation ($\phi = \frac{1}{2}$RM).

We also present the corresponding uncertainty maps represent the average of the 1σ deviations of the walkers above and below the resultant best-fit (σ_+ and σ_-, respectively).

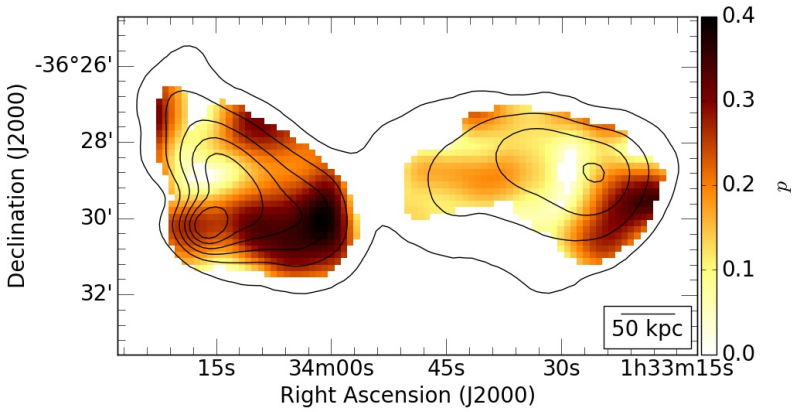

(a) p_0

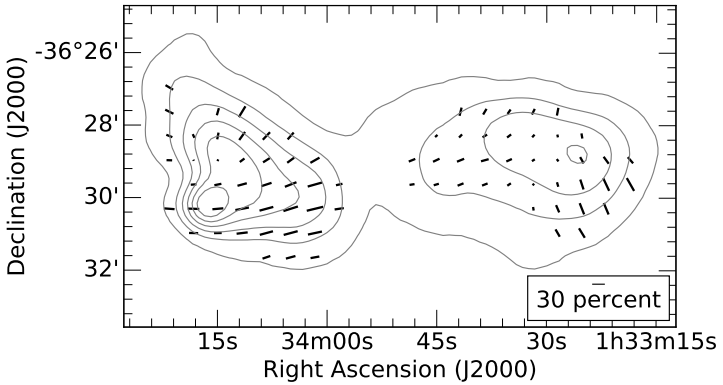

(b) ψ_0

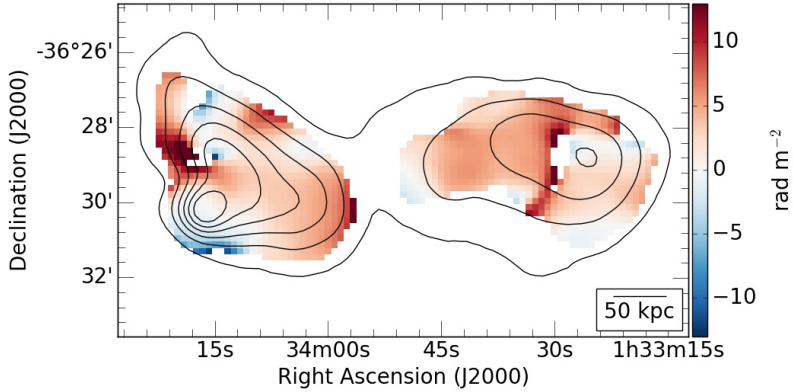

(c) ϕ

Figure B.1: Faraday thin parameter maps showing intrinsic polarisation (a), intrinsic polarisation angle (b) and Faraday depth (c). The length of each vector in Figure (c) represents the corresponding polarisation fraction at that location. Each subfigure has a scale bar in the lower righthand corner. Total intensity contours mark $25 - 400$ mJy/beam every 75 mJy/beam.

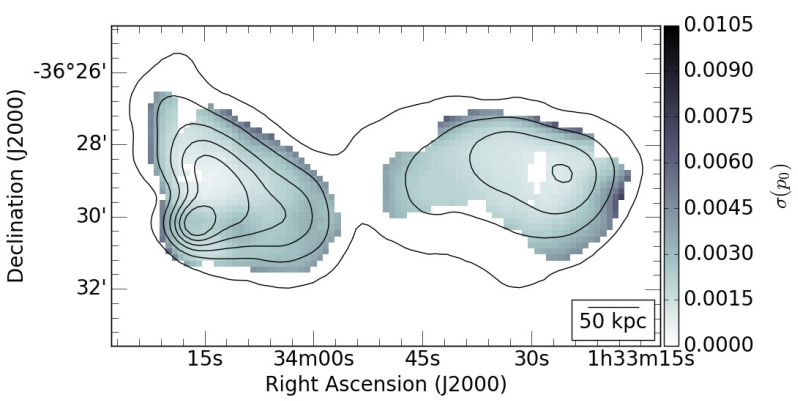

(a) $\sigma(p_0)$

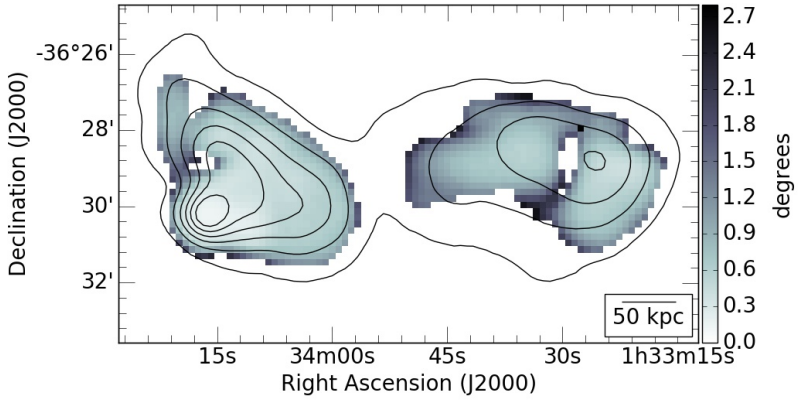

(b) $\sigma(\psi_0)$

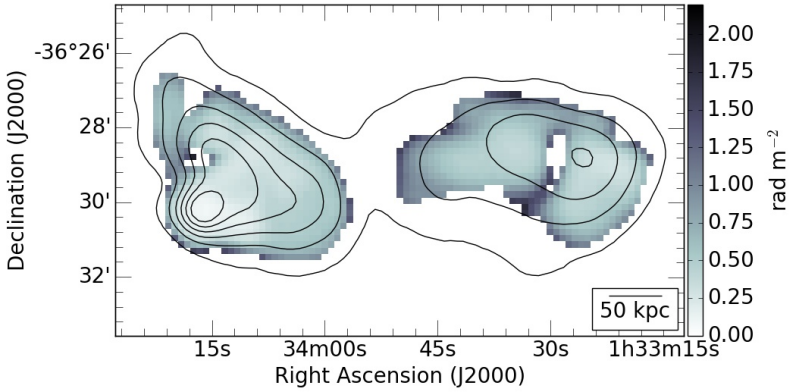

(c) $\sigma(\phi)$

Figure B.2: Uncertainty maps for a Faraday thin model. Maps shown correspond to uncertainty in intrinsic polarisation fraction (a), uncertainty in intrinsic polarisation angle, in degrees (b), and uncertainty in Faraday depth (c). Each subfigure has a scale bar in the lower righthand corner. Total intensity contours mark $25 - 400$ mJy/beam every 75 mJy/beam.

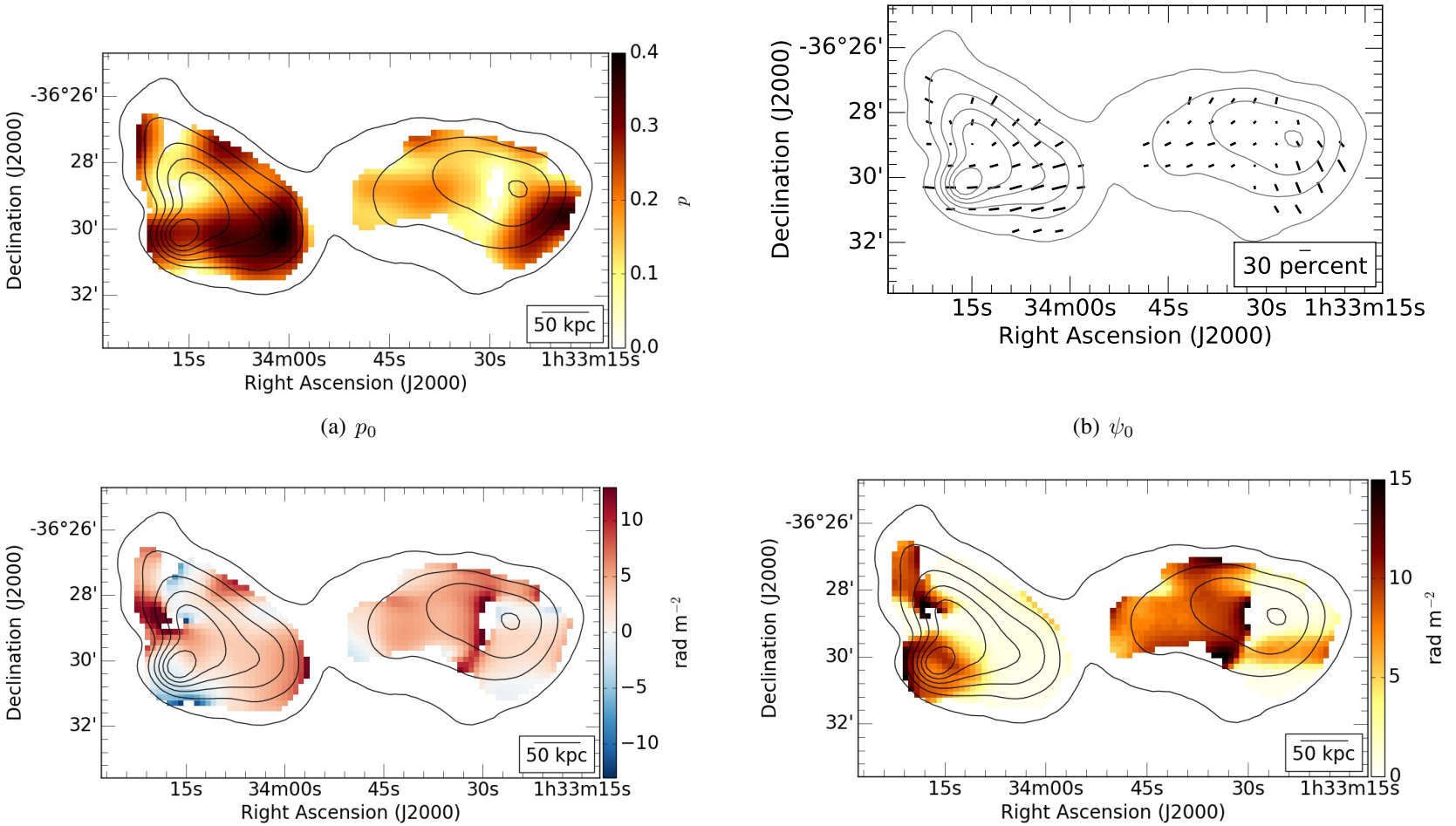

(a) p_0

(b) ψ_0

(c) ϕ

(d) σ_ϕ

Figure B.3: EFD parameter maps showing intrinsic polarisation (a), intrinsic polarisation angle (b), Faraday depth (c) and Faraday dispersion. The length of each vector in Figure (c) represents the corresponding polarisation fraction at that location. Each subfigure has a scale bar in the lower righthand corner. Total intensity contours mark $25 - 400$ mJy/beam every 75 mJy/beam.

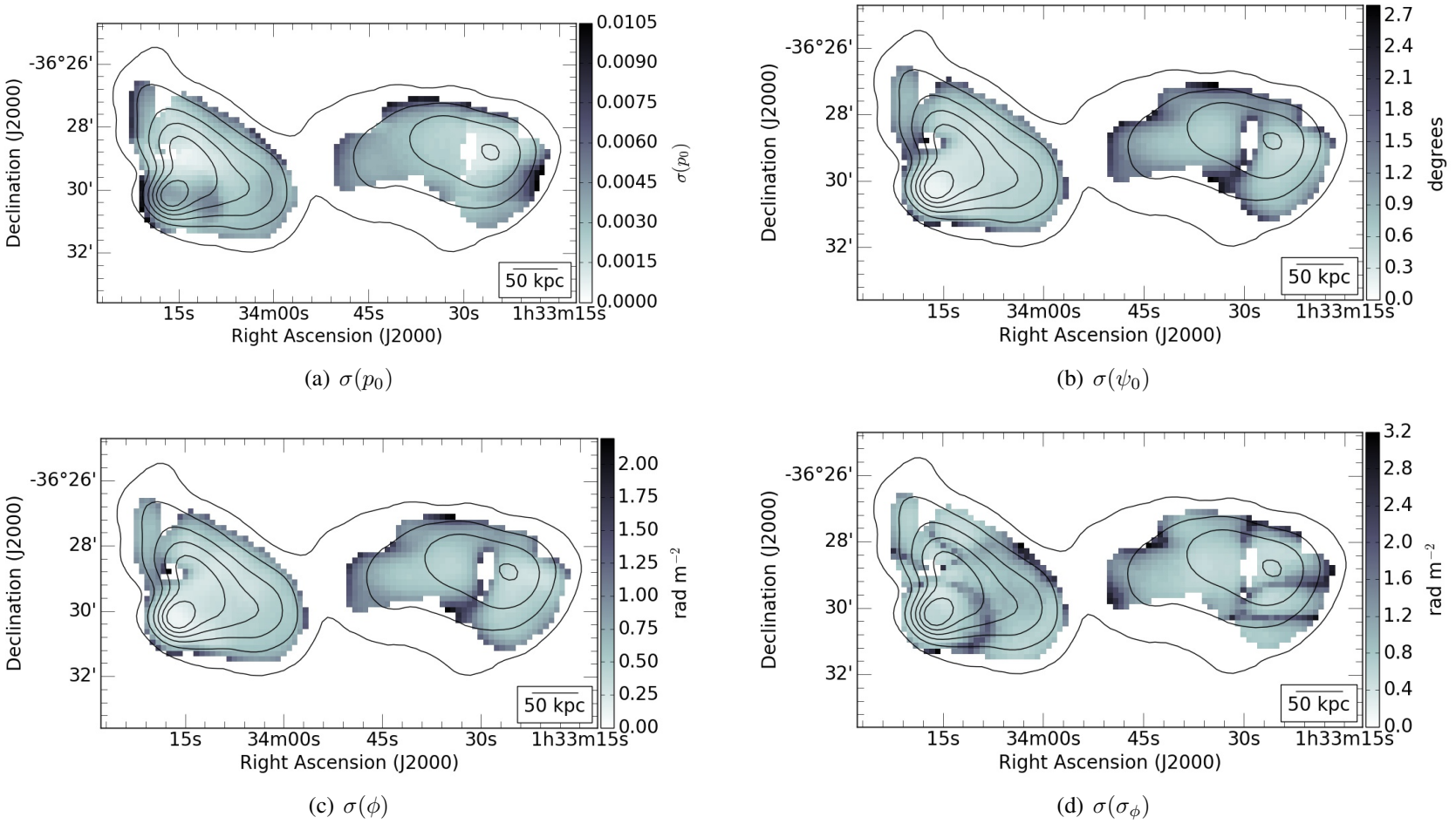

(a) $\sigma(p_0)$

(b) $\sigma(\psi_0)$

(c) $\sigma(\phi)$

(d) $\sigma(\sigma_\phi)$

Figure B.4: Uncertainty maps pertaining to the EFD polarisation model. The figures shown represent uncertainty in intrinsic polarisation (a), uncertainty in the intrinsic polarisation angle (b), uncertainty in Faraday depth (c) and uncertainty in the Faraday dispersion (d). Each subfigure has a scale bar in the lower righthand corner. Total intensity contours mark $25 - 400$ mJy/beam every 75 mJy/beam.

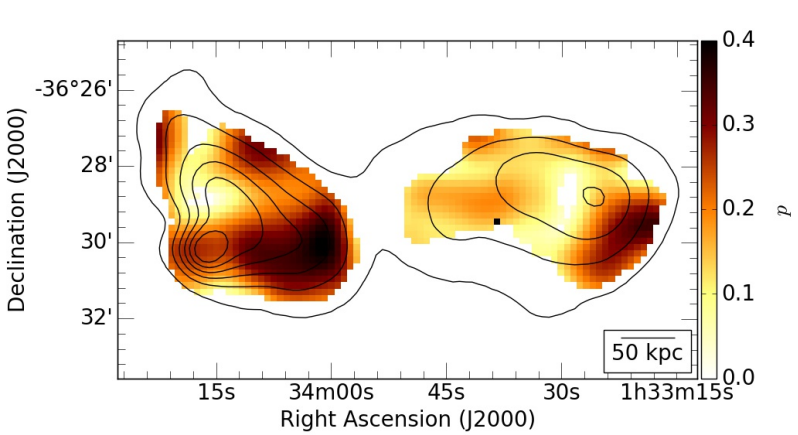

(a) p_0

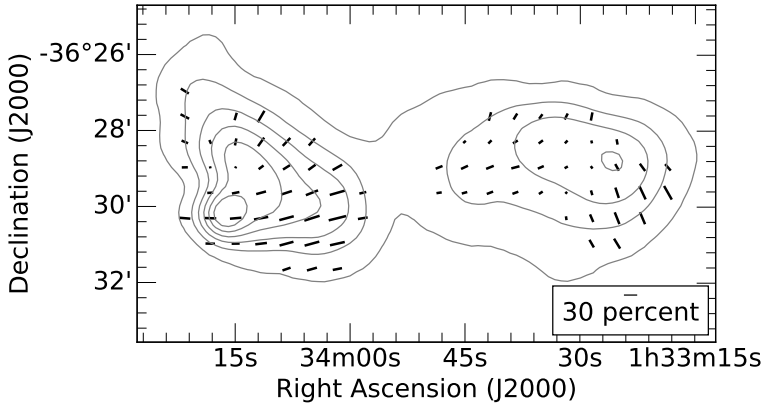

(b) ψ_0

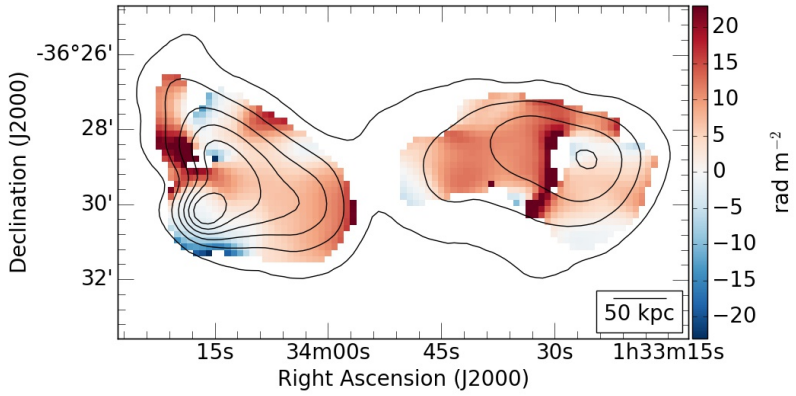

(c) ϕ

Figure B.5: Parameter maps corresponding to the DFR polarisation model showing intrinsic polarisation (a), intrinsic polarisation angle (b) and Faraday depth (c). The length of each vector in Figure (c) represents the corresponding polarisation fraction at that location. Each subfigure has a scale bar in the lower righthand corner. Total intensity contours mark $25 - 400$ mJy/beam every 75 mJy/beam.

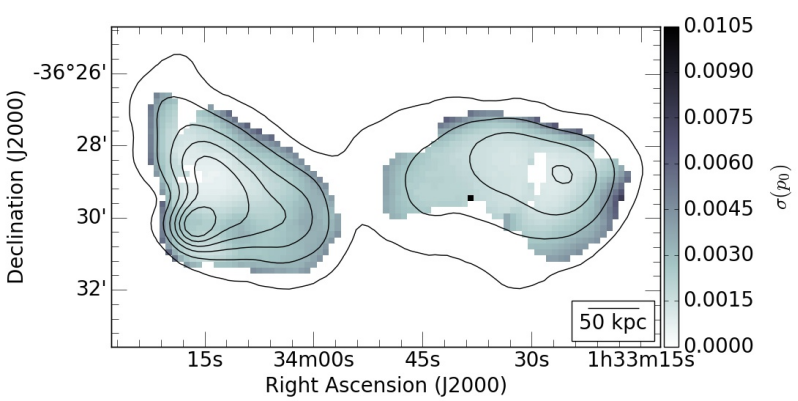

(a) $\sigma(p_0)$

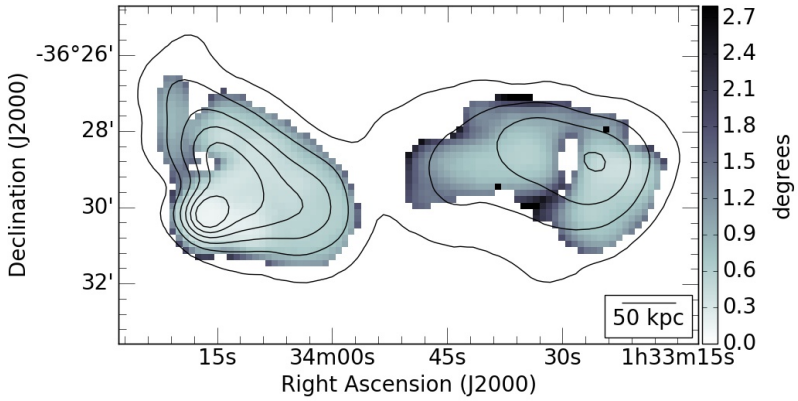

(b) $\sigma(\psi_0)$

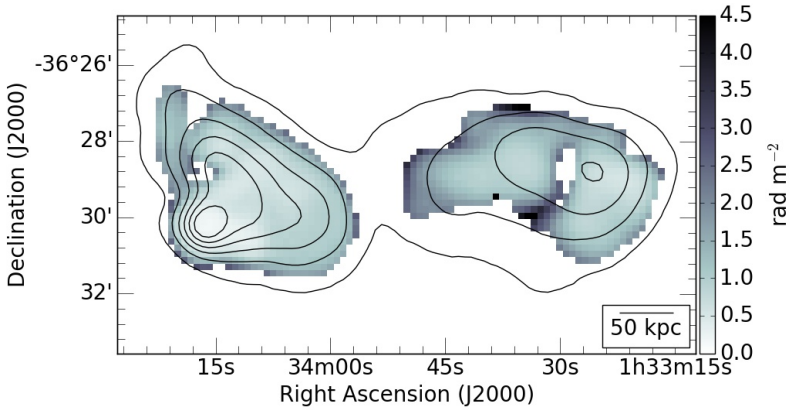

(c) $\sigma(\phi)$

Figure B.6: Parameter uncertainty maps corresponding to the DFR polarisation model. Uncertainties shown are for intrinsic polarisation (a), intrinsic polarisation angle (b) and Faraday depth (c). The length of each vector in Figure (c) represents the corresponding polarisation fraction at that location. Each subfigure has a scale bar in the lower righthand corner. Total intensity contours mark $25 - 400$ mJy/beam every 75 mJy/beam.

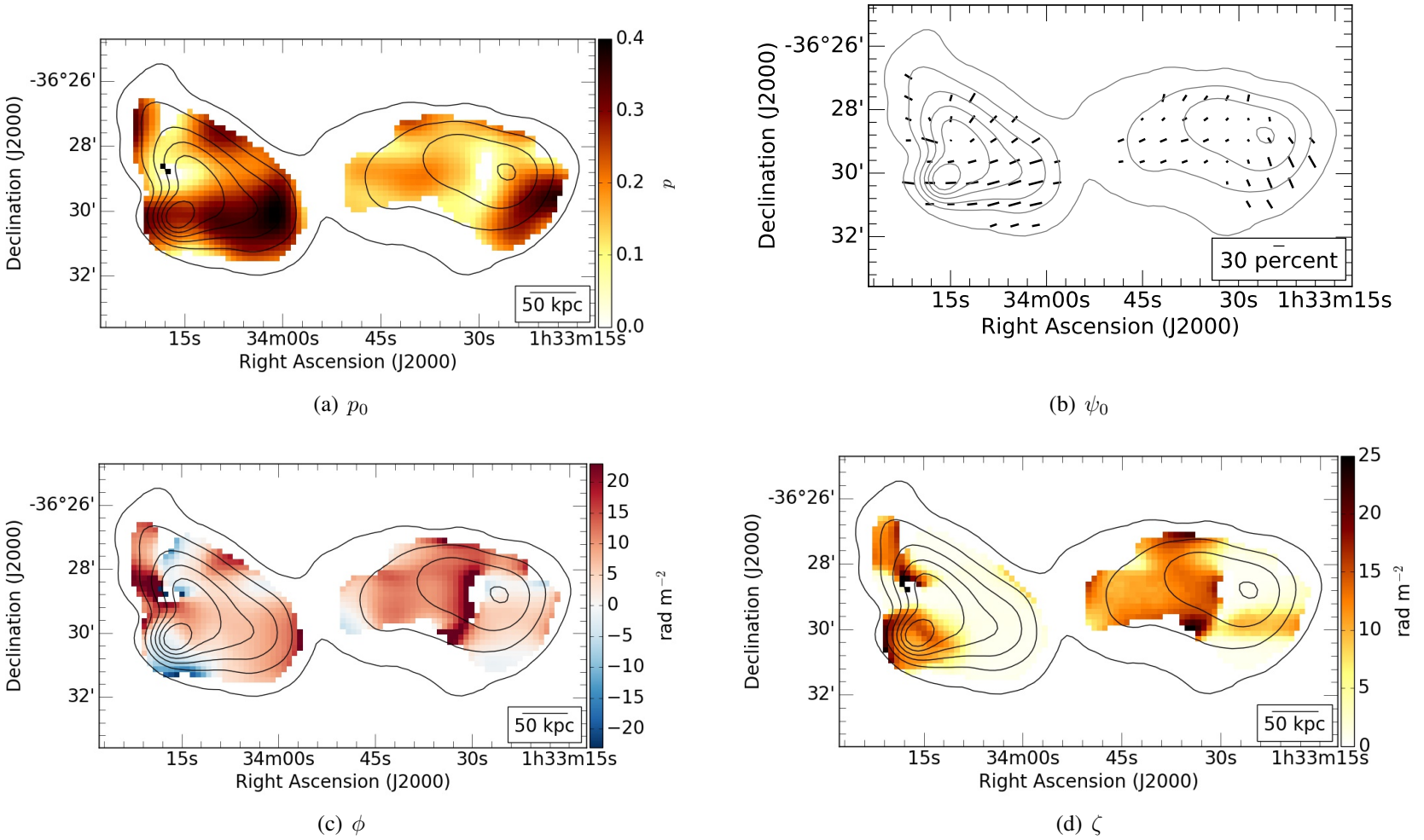

(a) p_0

(b) ψ_0

(c) ϕ

(d) ζ

Figure B.7: Parameter maps corresponding to the IFD polarisation model showing intrinsic polarisation (a), intrinsic polarisation angle (b), Faraday depth (c) and internal Faraday dispersion (d). The length of each vector in Figure (c) represents the corresponding polarisation fraction at that location. Each subfigure has a scale bar in the lower righthand corner. Total intensity contours mark $25 - 400$ mJy/beam every 75 mJy/beam.

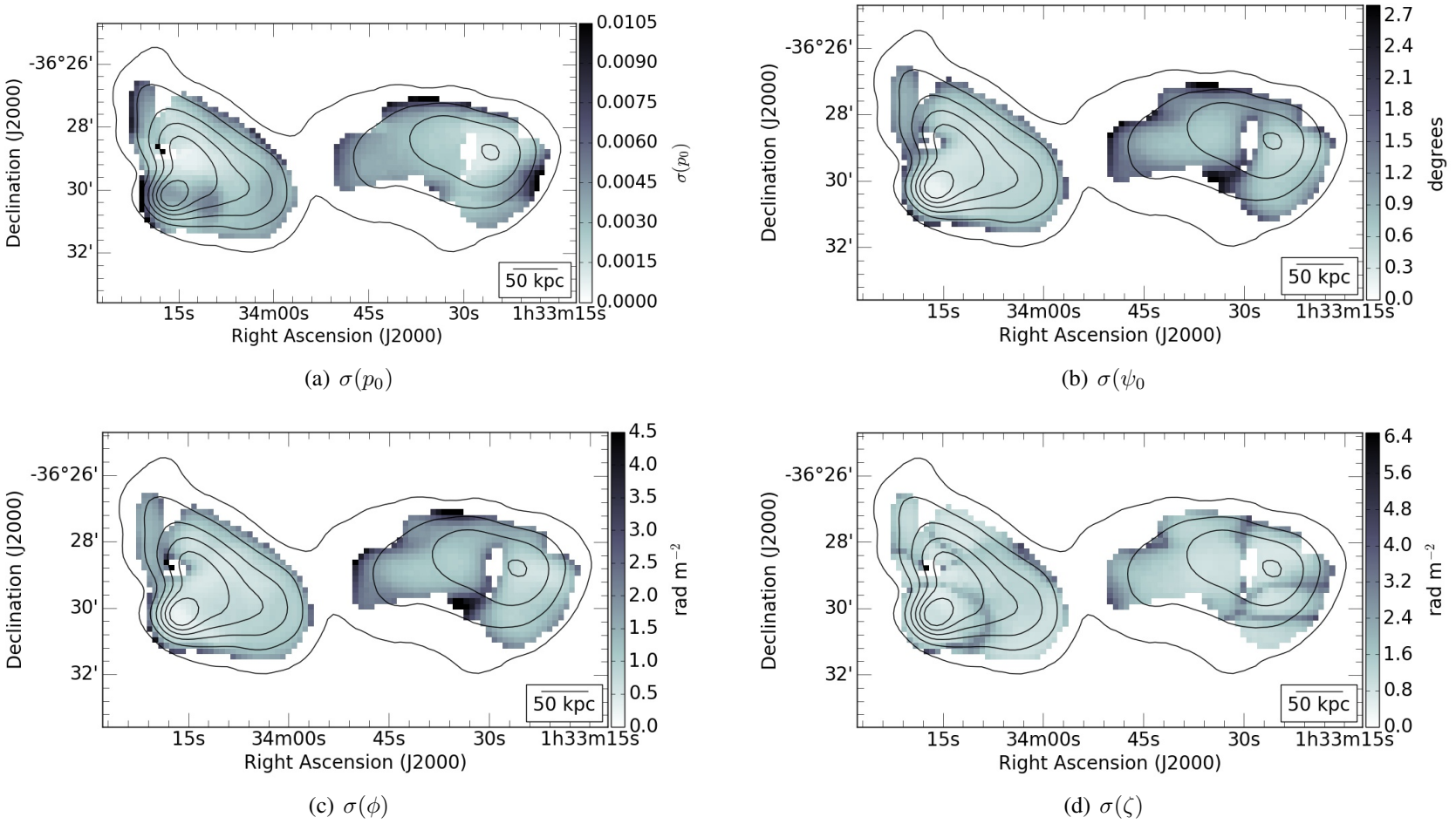

(a) $\sigma(p_0)$

(b) $\sigma(\psi_0$

(c) $\sigma(\phi)$

(d) $\sigma(\zeta)$

Figure B.8: Parameter uncertainty maps corresponding to the IFD polarisation model. Uncertainties shown are for intrinsic polarisation (a), intrinsic polarisation angle (b), Faraday depth (c) and Faraday dispersion (d). The length of each vector in Figure (c) represents the corresponding polarisation fraction at that location. Each subfigure has a scale bar in the lower righthand corner. Total intensity contours mark $25 - 400$ mJy/beam every 75 mJy/beam.

C

UNCERTAINTY PARAMETER MAPS FOR MSH 05−3*13*

In Chapter 4, we discuss the resultant parameter maps from $q - u$ fitting to an EFD model (§1.4.1). Here, we present the corresponding uncertainty to each fit polarisation parameter. We plot the average uncertainty of the positive and negative RMS values (σ_+ and σ_-, respectively) of the final MCMC walkers.

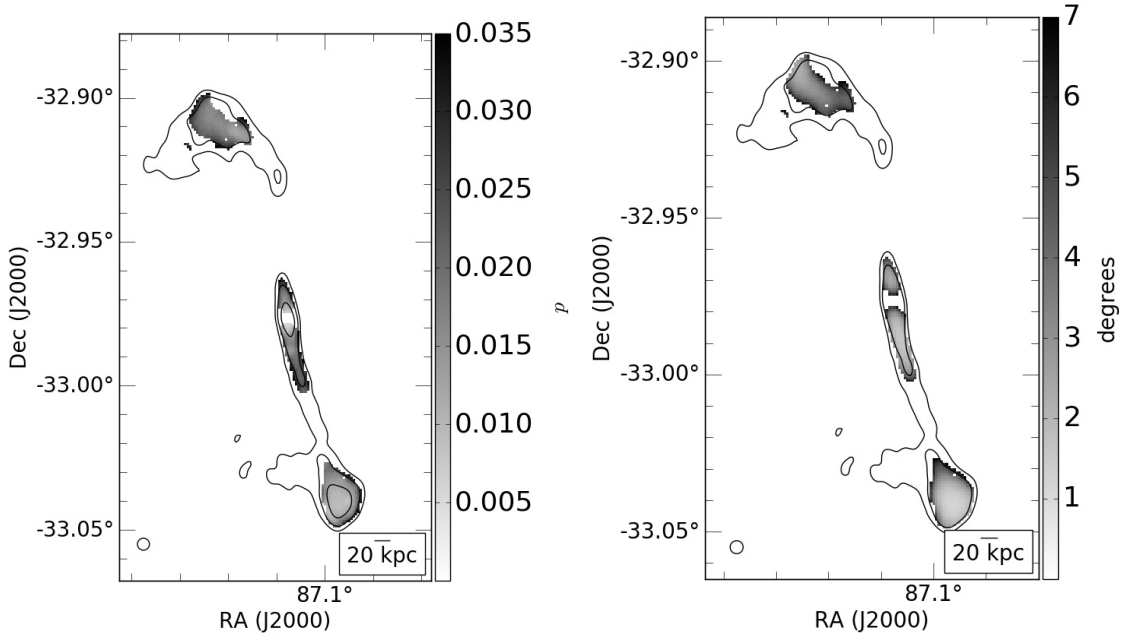

(a) Uncertainty in p_0

(b) Uncertainty in Ψ_0

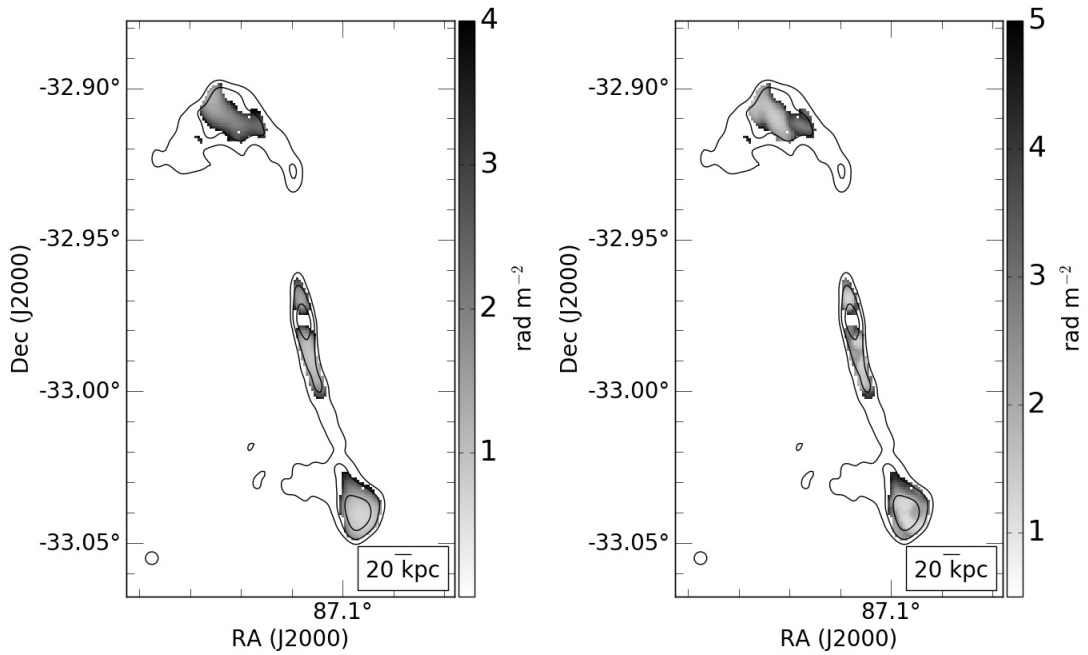

(c) Uncertainty in ϕ_{obs}

(d) Uncertainty in σ_ϕ

Figure C.1: Maps of uncertainty in polarisation parameter values, as calculated from our $q-u$ fitting routine. Black contours trace total intensity levels of $4, 8$ and 16 mJy/beam. Our synthesised beam is shown in the lower lefthand corner and a scale bar is given in the lower right.